Electrical properties of diamond nanostructures

Mose Bevilacqua

Diamond Electronics Group
London Centre for Nanotechnology
University College London
2010

A thesis presented for the degree of Doctor of Philosophy

Declaration

The work in this thesis is the results of research carried out at University College London, London Centre for Nanotechnology, Diamond Electronics Group, London. I declare it to be my own work unless referenced to the contrary in the text.

Abstract

Nanocrystalline diamond films (NCD) can potentially be used in a large variety of applications such as electrochemical electrodes, tribology, cold cathodes, and corrosion resistance.

A thorough knowledge of the electrical properties of NCD films is therefore critical to understand and predict their performance in various applications.

In the present work the electrical properties of NCD films were analysed using Impedance Spectroscopy and Hall Effect measurements. Impedance Spectroscopy permits to identify and single out the conduction paths within the films tested. Such conduction paths can be through grain interiors and/or grain boundaries. Hall measurements, carried out on Boron-doped NCD, permits determination of the mobility of the films. Specific treatments were devised to enhance the properties of the NCD films studied.

Detonation nanodiamond (DND) is becoming an increasingly interesting material. It is already used as abrasive material or component for coatings [1], but its potential applications can extend far beyond these. It is therefore essential to understand the structure and electrical properties of DND in order to exploit the full potential of this material.

In the present work, electrical properties of DND were studied using Impedance Spectroscopy. The results obtained suggest that DND could be used to manufacture devices able to work as Ammonia detectors.

Another major area of study in this work was ultra-violet diamond photodetectors. Using high quality CVD single-crystal diamond, UV photodetection devices were built using standard lithographic techniques. Following the application of heat treatments, the photoconductive properties of these devices were highly enhanced. The devices represent the state-of-the-art UV diamond photodetectors.

References

[1] Baidakova M. and Vul A, Journal of Physics D: Applied Physics **40** (2007) 6300

Table of Contents

Relevant Publications

1. Bevilacqua M., Tumilty N., Mitra C., Ye H., Feygelson T., Butler J.E. and Jackman R.B., *Nanocrystalline diamond as an electronic material: an impedance spectroscopic and Hall effect tudy*, Journal of Applied Physics, **107** (2010) 033716

2. Bevilacqua M., Chaudhary A. and Jackman R.B., *The influence of Ammonia on the electrical properties of detonation nanodiamond*, Journal of Applied Physics, **106** (2009) 12

3. Bevilacqua M and Jackman R.B*., Extreme sensitivity displayed by single crystal diamond deep ultraviolet photoconductive devices*, Applied Physics Letters, **95** (2009) 24

4. Bevilacqua M., Tumilty N., Chaudhary A., Ye H., Butler J.E. and Jackman R.B*., Nanocrystalline diamond as a dielectric for SOD applications*, Material Research Society Symposium Proceedings, **1039** (2008) 235

5. Bevilacqua M., Patel S., Chaudhary, A., Ye H. and Jackman R.B., *Electrical properties of aggregated detonation nanodiamond*, Applied Physics Letters, **93** (2008) 13

6. Ye H. Tumilty N., Bevilacqua M., Curat S., Nesladek M., Bazin B., Bergonzo, P. and Jackman R.B., *Electronic properties of homoepitaxial (111) highly Boron doped diamond films,* Journal of Applied Physics, **103** (2008) 5

Acknowledgements

A PhD thesis is a work of art: it is the expression of the creativity of the author, together with all its positive and negative sides. Behind the many lines of a PhD thesis there are many painful and ecstatic moments, just like behind any art piece. So, whoever will happen to read this, quite unlikely I expect, must know that every line is the fruit of much intellectual as well as emotional effort.

During my climb towards completion I cannot say whether I loved or hated reading for a PhD; it was a very unsettling situation, similar to walking blindfold along a busy road.

The difficulties met along this road were not just relegated to the realm of science, but even more to my own character. Dealing with a scientific field I had never stumbled upon before, dealing with people holding a different vision than mine and having to drop many preconceptions about research was very painful but nonetheless educative as almost nothing else so far. There was no choice but trying to be more humble and accepting things as they came along, as most of the time were beyond control anyway.

Having reached the end of my climb I cannot do anything but give my heartfelt thanks to whoever I happen to have met and interacted along the way, as each experience, positive and negative, revealed (and keeps on revealing) itself as a life lesson.

And by the way, standing on what I believed it to be the top, I start realising it is not the top at all, as up there between the clouds there are higher peaks waiting to be climbed.

I dedicate this thesis to everyone met during these four years, impossible to name them all, as well as to those who will meet difficulties during the course of their PhD: many people have been there and experienced the same problems before, so take heart and go ahead!

Getting my feet back on earth, there are some people I would like to thank in particular: my supervisor Prof. Richard Jackman for his invaluable help with the analysis of the experimental data presented in this thesis. His great wit and experience are very much appreciated and treasured. He has also been a very sincere and compassionate friend who has indeed given me support on many occasions, not only scientific.

I would also like to thank my colleagues and friends Dr. Stephane Curat, Dr. Haitao Ye, Dr. Niall Tumilty, Mr. Rezal Ahmad, Mrs. Aysha Chaudhary (her help with proof-reading and styling this thesis is appreciated), Mr. Robert Edgington, Mr. Joseph Welch and Miss Carolina Parada for the many scientific (and non-scientific…) discussions that proved to be a source of inspiration and insight. We are a wonderful group and I do not look forward to when we will have to part for different directions.

I would also like to thank Mr. Steve Etienne, Mr. Kevin Lee, Mr. Mike Creswell and Mr. Alan Sasnovski for their assistance during the time spent working in the LCN clean room.
Dr. Robert McKeag is also thanked for his assistance with setting up the monochromator in the LCN lab and his experience with ultra-violet light diamond photodetectors.
I also wish to extend my gratitude to Ms. Tatyana Feygelson and Prof. James E. Butler of the Naval Research Laboratory, Washington DC, USA for providing the diamond films upon which a great part of this work was based.
The UK Engineering and Physical Sciences Research Council (EPSRC) is also acknowledged for its financial support.
I would like to thank my girlfriend Rachel (a.k.a. Dr. Rui Liao) for her constant loving support and great patience, without which I would have found it very difficult to complete this thesis.
And finally I would like to thank my parents and family, who were for me like the North Star is for the lost traveler.

Chapter 1

Introduction

Diamond is a material unlike any other in nature. Properties such as extreme hardness, high resistance to corrosion, high thermal conductivity, low coefficient of friction and transparency, make diamond a very attractive material for a wide array of applications in industry.

However, diamond is found in scarce quantity in nature so considerable effort has been exerted in trying to grow high-quality synthetic diamond. Chemical Vapour Deposition (CVD) represents the state-of-the-art technique to produce high-quality single-crystal diamond films.

The main limitation to the application of single-crystal diamond in industry is its size, as it is unfeasible to grow large CVD diamond substrates as yet. Research has therefore been aimed at circumventing this problem, and a remarkable achievement was the production of polycrystalline diamond (PCD). Polycrystalline diamond is diamond grown on silicon substrates, which is readily available in large wafers and thus represents a potential candidate for industrial applications, as it can retain most of the characteristics of single-crystal CVD diamond. A typical feature of PCD is the size of its grain boundaries, which can be chosen according to the parameters of growth recipes. Polycrystalline diamond bearing nanometre-scale grains is known as “nanocrystalline diamond” (NCD).

Chapter 2 reports on diamond’s structure, growth, properties and applications.

It is a journey from the sub-nanometric scale, where basic quantum mechanics is used as tool of investigation, proceeding to the microscopic and macroscopic scale, where classical physics takes over.

The chapter begins with a brief description of the carbon atom along with its three types of hybridization, moving then on reviewing the principal characteristics of diamond’s lattice. It then accounts for all possible ways in which diamond can be formed, naturally and artificially. As for artificial diamond the “High-Pressure-High-Temperature” (HPHT) and “Chemical Vapour Deposition” (CVD) methods of growing diamond are presented.

Further to the growth techniques, the main features of polycrystalline diamond films (PCD) are reported, ranging from microcrystalline (MCD), to nanocrystalline (NCD) to ultra-nanocrystalline (UNCD). Particular attention is given to how grain boundaries influence the properties of the films.

The structure of detonation nanodiamond (DND) and its various methods of manufacture are also reported.
The chapter's final section presents diamond's applications, focusing in particular on the use of CVD diamond as a deep ultra-violet photodetector. Despite an extensive literature on the use of homoepitaxial single-crystal layers grown on natural or HPHT substrates as photoconductive devices, the direct use of a CVD grown single crystal did not attracted much attention.

Chapter 3 describes the main experimental and characterization techniques employed during the course of the present work. Impedance Spectroscopy, which was used extensively throughout all the experimental work, is fully reviewed. Theoretical models that further clarify the validity of the method are also described.
Other experimental techniques utilized include Hall effect measurements, Atomic Force Microscopy, Fourier Transfer Infrared Spectroscopy, metal deposition, photolithography and wet-etching.

Chapter 4 describes the type of nanocrystalline films used in the present work, kindly provided by Naval Research Laboratories, (Washington DC, USA), was grown using a novel seeding technique that led to the production of particularly dense films.
The chapter reports on Impedance Spectroscopy measurements carried out on these dense intrinsic films at different temperatures, revealing its good dielectric properties. Following an annealing treatment, the insulating character of the films was further enhanced and stabilised.
Hall Effect measurements were also carried out in conjunction with Impedance Spectroscopy on films grown in the same fashion but lightly doped with boron. Hall data were used to calculate the mobility for those films, which was found to be remarkably high.

Chapter 5 shows the results of Impedance Spectroscopy measurements carried out on Detonation Nanodiamond, revealing it to be a near-to-ideal dielectric material.
Exposure of DND to ammonia fumes was followed by further Impedance Spectroscopy and Fourier Transfer Infrared Spectroscopy in order to reveal the changes occurred in the electrical conduction paths, as well as the mode in which radical groups bonded with the grain clusters.

Chapter 6 describes the performance of deep ultraviolet (UV) diamond photodetectors made on commercially supplied CVD-grown single-crystal and fabricated by the author.
The performance of these devices is studied through the analysis of the photocurrent generated upon illumination ranging from infrared to deep ultra-violet.
Following the application of passivation treatments, it is shown how the surface of this type of single-crystal diamond was subsequently modified and the performance of the devices greatly enhanced, resulting in extreme levels of sensitivity to deep UV radiation while maintaining good UV-to-visible-light discrimination and dark-current levels.

Chapter 7 summarises the results achieved with the present work, and briefly outlines future work needed to further prove the feasibility of NCD as a high-quality dielectric, of DND as a material to build sensors and CVD single-crystal diamond as an efficient material to build highly sensitive deep UV photoconductive devices.

Chapter 2

Structure, Growth, Properties and Applications

2.1 Introduction

The word “diamond” comes from the ancient Greek “adamas”, which means unbreakable. Diamonds feature more predominantly than any other gemstones in the history and cultural heritage of the human race [2.1]. They were prized for their scarcity for centuries and they remain nowadays a symbol of wealth and prestige. Although they were mined for the first time in India more than 4000 years ago, the modern diamond era commenced in 1866, when large diamond deposit were discovered in South Africa, attracting the attention of European prospectors.

Apart from its appeal as a gemstone, diamond possesses outstanding properties such extreme hardness, low coefficient of friction, chemical inertness, and high thermal conductivity. A selection of these properties is presented in table 2.1.

Extreme mechanical hardness and wear resistance
Highest bulk modulus (1200 GN/m2)
Lowest compressibility
Very low thermal expansion coefficient at room temperature
Broad optical transparency from the deep ultraviolet to the far infrared
Highest sound propagation velocity (17.5 km/s)
Excellent electrical insulator (room temperature resistivity ca. 100 TΩ cm
Very resistant to chemical corrosion
Biologically compatible

Table 2.1: Selection of diamond properties [2.2]

With such remarkable properties, diamond is now used in several applications within mechanical industry (e.g. cutting and polishing tools), as well as in electronics (e.g. high power switches, ultra violet light detectors).

2.2 The carbon atom

The Carbon atom is composed of a nucleus of six protons and six, seven or eight neutrons surrounded by six electrons.

As determined by Schrödinger, the behavior of the electrons in their movement around the nucleus is governed by the specific rules of standing waves; no electron in an atom or a molecule can be accurately located. The electron wave function Ψ establishes the probability of an electron being located in a given volume with the nucleus being the origin of the coordinate system. Mathematically speaking, this function has a finite value anywhere in space, but the value of the function becomes negligible at a distance of a few angstroms from the nucleus. [2.3] These rules state that, in any given atom, the electrons are found in a series of energy levels called "orbitals", which are distributed around the nucleus. These orbitals are well defined and, in-between them, large ranges of intermediate energy levels are not available (or forbidden) to the electrons since the corresponding frequencies do not allow a standing wave [2.4]. In any orbital no more than two electrons can be present at the same time and these must have opposite spins, as stated in the Pauli's exclusion principle.

The electron configuration of carbon, that is, the arrangement of the electrons in each orbital, is described as: $1s^1\ 2s^2\ 2p^2$. The notation ls^* refers to the three quantum numbers necessary to define an orbital, the number "1" referring to the K or first shell (principal quantum number). The letter "s" refers to the sub-shell "s" (angular momentum number) and the superscript numeral "2" refers to the number of electrons in that sub-shell. There is only one orbital (the s orbital) in the K shell, which can never have more than two electrons. These two electrons, which have opposite spin, are the closest to the nucleus and have the lowest possible energy. The filled K shell is completely stable and its two electrons do not take part in any bonding. The next two terms, $2s^2$ and $2p^2$ refer to the four electrons in the L shell. The L shell, when filled, can never have more than eight electrons. The L-shell electrons belong to two different sub-shells, the s and the p, and the 2s and the 2p electrons have different energy levels (the number "2" referring to the L or second shell, and the letters "s" and "p" to the orbitals or sub-shells). The two 2s electrons have opposite spin and the two 2p electrons parallel spin.

In any given atom, the electrons located in the outer orbital are the only ones available for bonding to other atoms. These electrons are called the valence electrons. In the case of the carbon atom, the valence electrons are the two 2p orbitals. Carbon in this state would then be divalent, since only these two electrons are available for bonding [2.4].

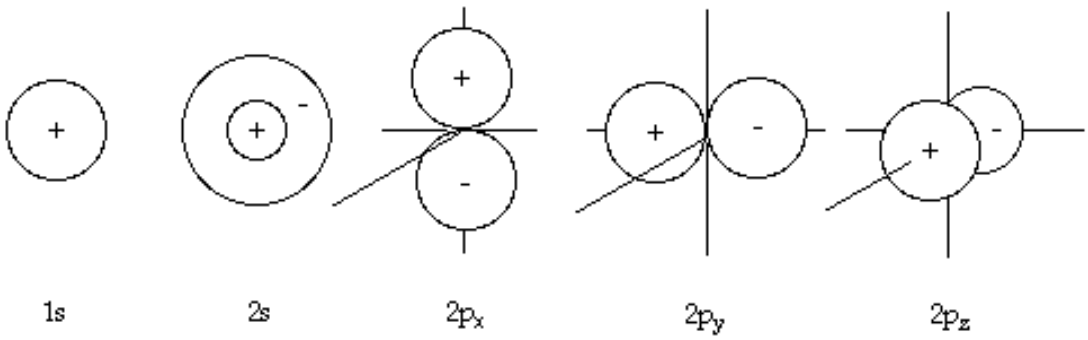

Figure 2.1: Schematic representation of the s and p orbital [2.4]

2.2.1 Hybridization sp^3, sp^2, and sp

The concept of "orbital hybridization" was developed by Linus Pauling soon after the description of the hydrogen molecule by the valence bond theory. These concepts were applied to an issue of specific concern to organic chemistry, the tetrahedral orientation of the bonds to tetra-coordinate carbon. The electronic configuration of a carbon atom in its ground state is not consistent with a simple rationalisation of the tetrahedral bonding at carbon. Pauling suggested that the four atomic orbitals 2s, $2p_x$, $2p_y$, and $2p_z$ are replaced by a set of four equivalent hybrid orbitals, designated sp^3 [2.5]. In other words, the structure of the carbon atom must be altered to a state with four valence electrons instead of two, each in a separate orbital and each with its spin uncoupled from the other electrons. This alteration occurs as a result of the formation of hybrid atomic orbitals, in which the arrangement of the electrons of the L shell of the atom in the ground state is modified as one of the 2s electron is promoted to the higher orbital 2p as shown in figure 1.2. These new orbitals are called hybrid since they combine the 2s and the 2p orbitals. They are labeled sp^3 since they are formed from one s orbital and three p orbitals [2.4].

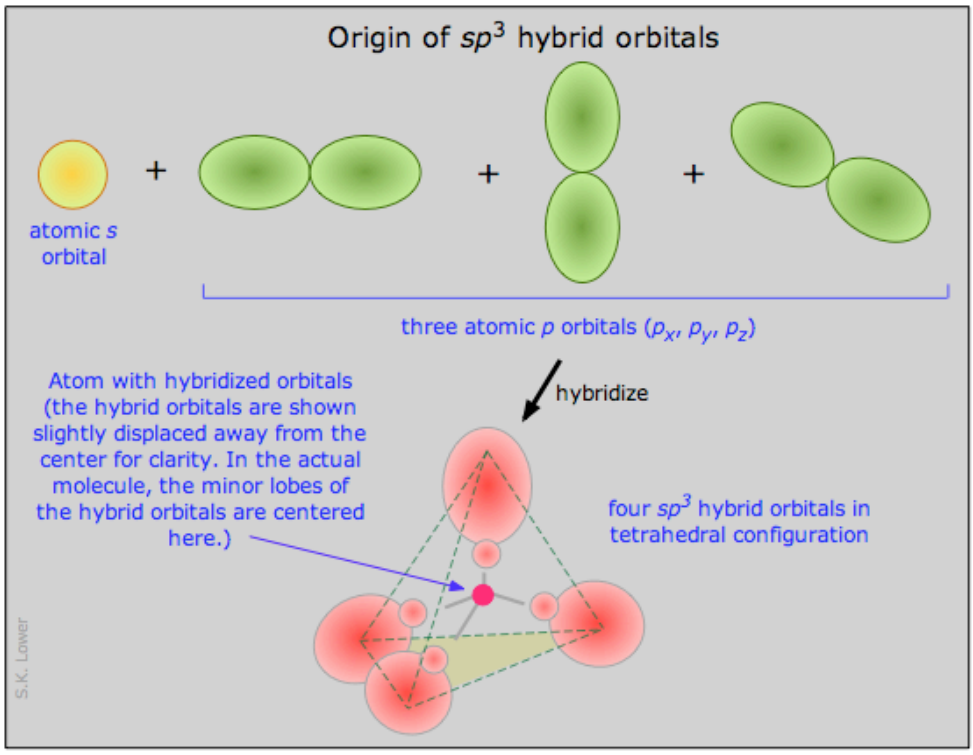

Figure 2.2: sp^3 hybridization [2.6]

The energy required to accomplish the sp^3 hybridization and raise the carbon atom from the ground state to the corresponding valence state V_4 is 2.38 eV. This hybridization is possible only because the required energy is more than compensated by the energy decrease associated with forming bonds with other atoms. The four hybrid sp^3 orbitals form a regular tetrahedron (a solid with four plane faces) with equal angles to each other of 109° 28' and length of 1.544 Å [2.7]. The four sp^3 valence electrons of the hybrid carbon atom, together with the small size of the atom, result in strong covalent bonds (7.36 eV). By convention, a directional or stereo-specific orbital such as the sp^3 is called a σ (sigma) orbital, and the bond a σ bond. The diamond lattice consists of sp^3-bonded carbon [2.4].

In addition to the sp^3-tetragonal hybrid orbital, two other orbitals complete the series of electronic building blocks of all carbon allotropes and compounds: the sp^2 and the sp orbitals. The mechanism of the sp^2 hybridization is somewhat different from that of the sp^3 hybridization. The arrangement of the electrons of the L shell of the atom in the ground state is modified as one of the 2s electrons is promoted and combined with two of the 2p orbitals (hence the designation sp^2), to form three sp^2 orbitals and an unhybridized free (or delocalized) p orbital electron as shown in figure 1.3.

The three identical sp^2 orbital form a 120° and are 1.41 Å long. Like the sp^3 bond, the sp^2 bond is covalent. It is a strong bond, because of the three sp^2 valence electrons and the small size of the atom, and like the sp^3 orbital, the sp^2 orbital is directional and is called a σ (sigma) orbital, and the bond a σ bond [2.4].

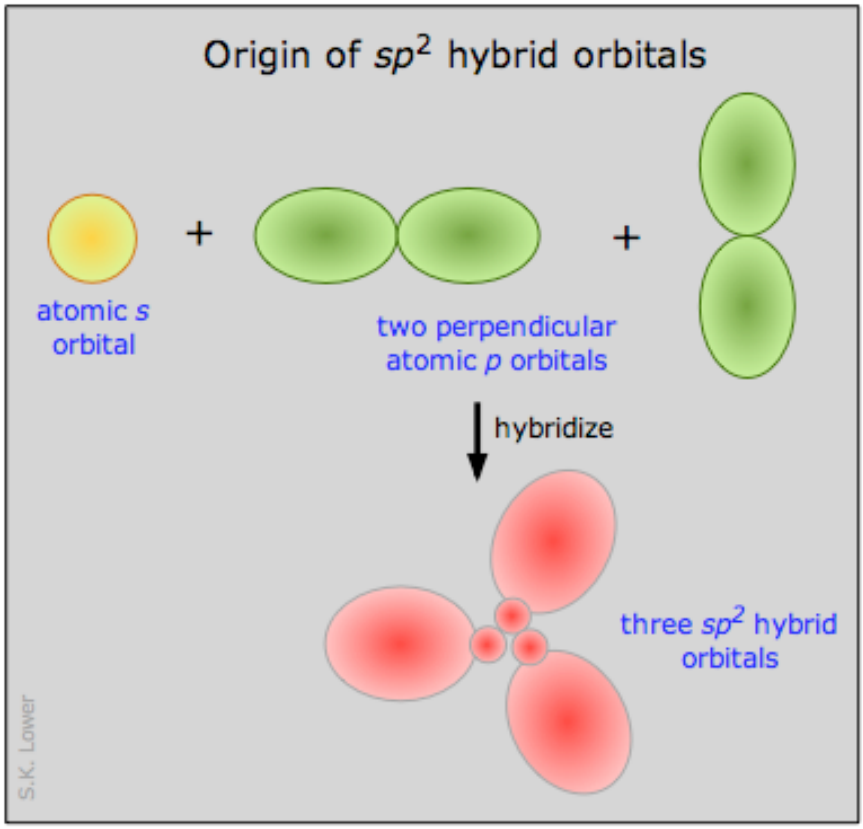

Figure 2.3: sp^2 hybridization [2.6]

Each sp^2 hybridized carbon atom combines with three other sp^2 hybridized atoms to form a series of hexagonal structures, all located in parallel planes. The free delocalized electron is oriented perpendicularly to this plane (figure 2.4). Unlike the σ, it is non-symmetrical and is called by convention a π (pi) orbital and is available to form a subsidiary π bond. A graphite lattice is arranged as schematically represented in figure 2.4.

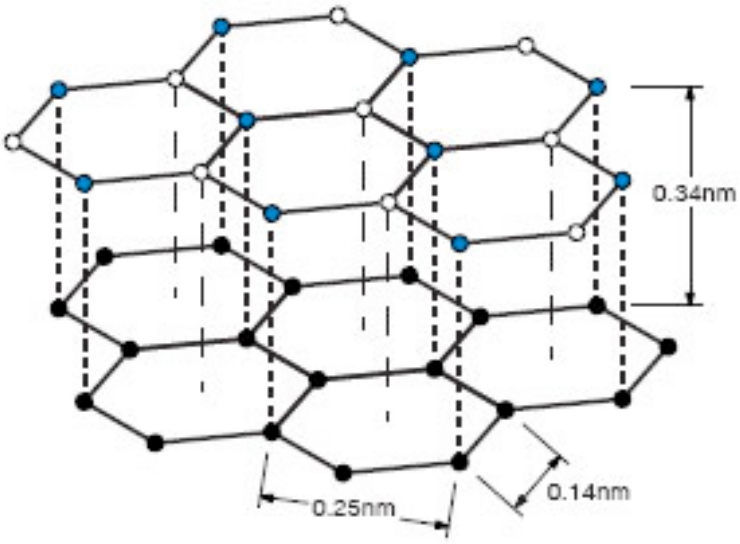

Figure 2.4: Graphite lattice [2.8]

The sp orbital (known as a diagonal orbital) is a merger of an s and a p orbital. It consists of two sp orbitals that form an angle of 180° due to the mutual repulsion. The bond is a σ bond and has high strength. The sp orbitals account for two of the electrons of the carbon atom. The other two valence electrons are free, delocalized π orbital electrons, which are available to form subsidiary π bonds in a manner similar to the sp^2 hybridization. An example of molecule having sp bonds is Beryllium hydride (BeH_2), represented in figure 2.5, a chemical compound typically used in rocket fuel [2.9]. Acetilene (C_2H_2) is another example.

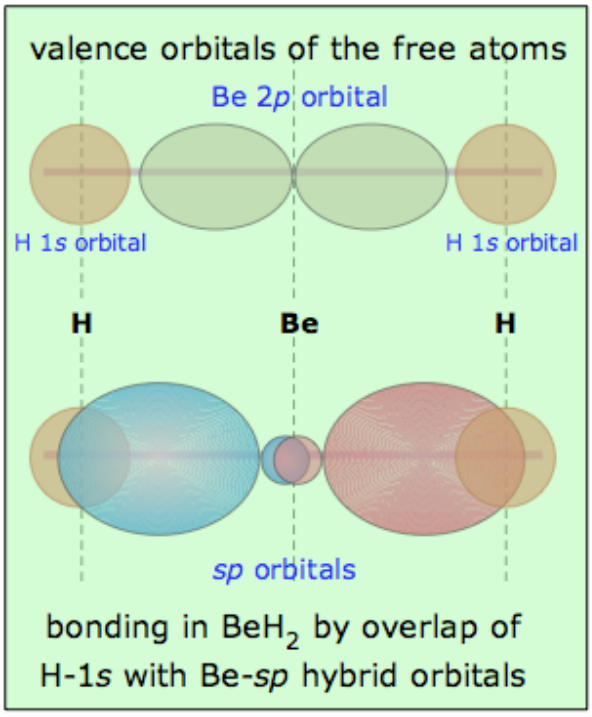

Figure 2.5: sp hybridization [2.6]

A particular carbon polymorph will be formed under a specific set of condition of pressure and temperature; the phase diagram of carbon reproduced in figure 2.6 relates these conditions to the particular polymorph.

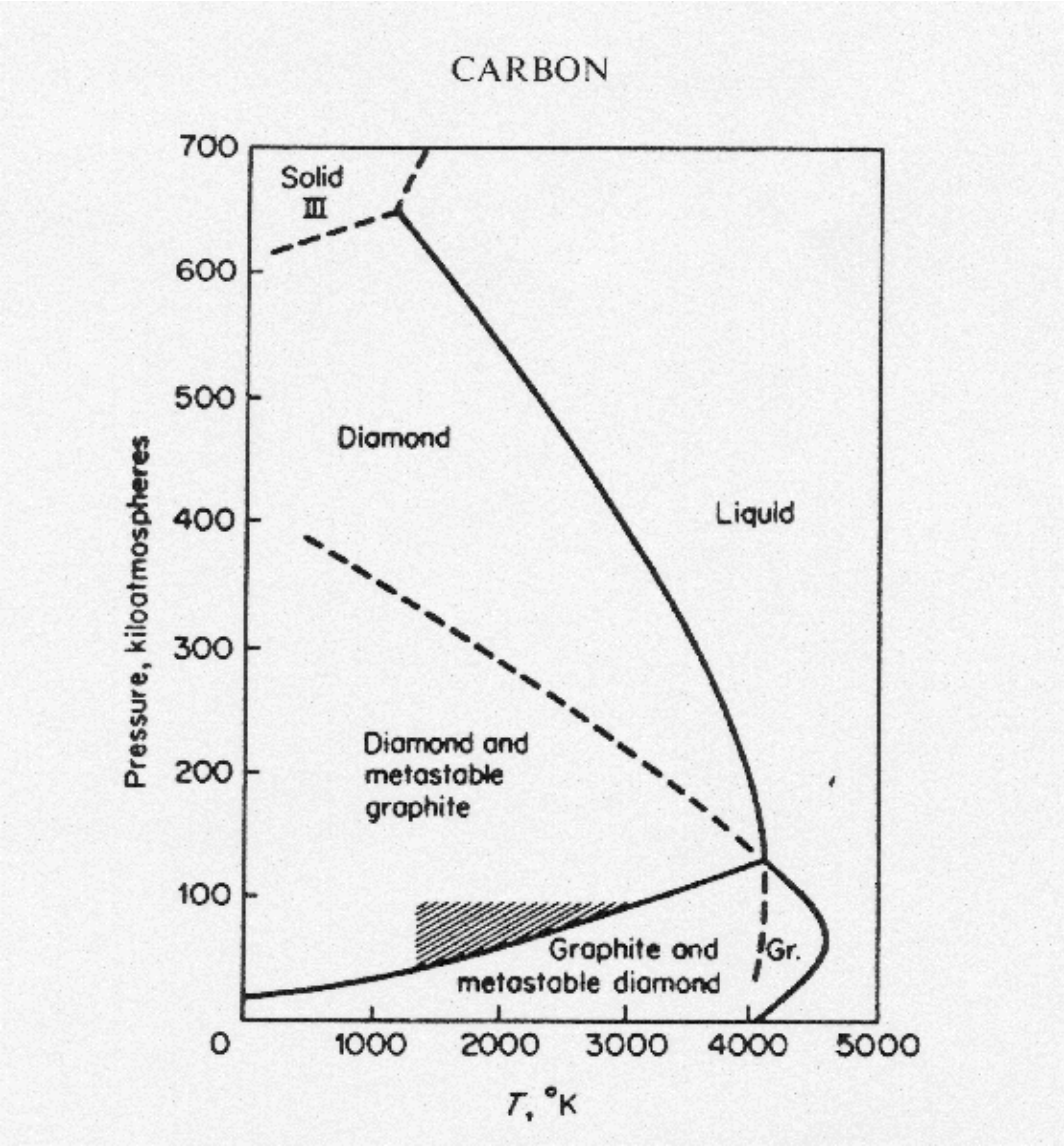

Figure 2.6: Phase diagram of Carbon [2.10]

2.2.2 Diamond lattice

Diamond can exist as a metastable phase under conditions of low pressure and temperature, which are calculated to favour the graphite phase. The reason for this is that although the bonding energy of graphite is 2.1 kJ/mol lower than that for diamond [2.11], the strong covalent bonds of diamond have to be broken, requiring an energy of 711 kJ/mol, which is the equivalent of approximately 1620°C at room pressure. Therefore, after formation diamond can persist indefinitely in a metastable phase under normal conditions.

The crystal structure of diamond is a face-centred cubic (FCC) lattice, with eight atoms per unit cell, with its cubic edge-length being 3.567 Å at 0°C.

Within the cubic lattice there are three crystallographic planes of carbon atoms that can be used to describe its structure: the family of planes {100}, {110} and {111} [2.12].

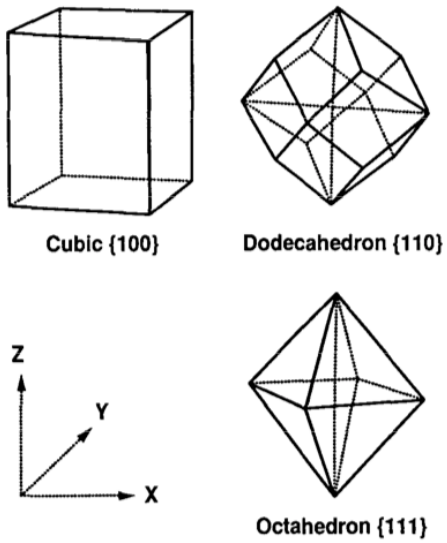

Figure 2.7: Major crystal forms of diamond [2.4]

Figure 2.8: A three-dimensional cubic crystal with {100}, {110} and {111} faces [2.12]

The planes of atoms impart different degrees of abrasiveness or ease of polishing depending on which orientation is presented to the work piece. The softest polishing direction in the {100} plane is the <100> direction, whereas the hardest is the <111> direction in the {111} plane [2.12].

2.3 Classification of Diamond

Diamonds have been historically classified into four categories according to their optical absorption properties, which are determined by impurities of nitrogen-, boron- and hydrogen-related defects as listed in table 2.2.

Robertson and co-authors [2.13] realised that diamond's absorption of deep ultraviolet radiation fell into two categories: those with an absorption cut-off at wavelengths greater than 300 nm, the most prevalent, were designated as "type I", whereas those with a 225 nm threshold were designated as "type II".

Type I includes diamonds having nitrogen as the main impurity, at a concentration of up to 1%. If the nitrogen atoms are arranged in pairs or larger aggregates, they do not affect the diamond's colour (type Ia, about 98% of natural diamond). If the nitrogen atoms are instead dispersed throughout the crystal in isolated sites, they confer to the diamond an intense yellow or brown colour (type Ib). Type Ib diamonds contain paramagnetic active nitrogen as substitutional impurities. While the type Ib diamonds are rarely formed in nature, most synthetic diamonds belong to this group. The presence of nitrogen within the diamond lattice has a critical effect on its optical and electronic properties due to both its role in the creation of photon absorption and carrier recombination centres and to its effects in compensating acceptors [2.15].

Type II includes diamonds with almost no nitrogen impurity. Diamonds with the highest purity are type IIa, exhibiting the intrinsic semiconducting properties with a wide band gap of 5.47 eV. Type IIb diamonds are naturally boron doped, and show p-type conductivity due to an acceptor level introduced by the substitutional boron located at 0.35-0.38 eV above the valence band.

Type	Origin	Impurities
Ia	98% of all natural diamonds	Approximately 0.1 % nitrogen in small aggregates
Ib	Rare in nature (< 0.1 %). Includes most high-pressure synthetic diamonds	Nitrogen 0.05 % in lattice
IIa	Rare in nature	Few parts per million of nitrogen. Usually clear
IIb	Extremely rare in nature. Produced by high-pressure synthesis	Less nitrogen than IIa. Becomes semiconducting by boron doping. Blue in colour

Table 2.2: Classification of single crystal natural diamond [2.4]

2.4 Natural diamond

Natural diamond is thought to have formed over 990 million years ago between 140 and 200 km from the Earth surface, where temperatures ranges between 900°C and 1400°C and pressures between 45 and 60 kbar [2.16, 2.17]. Kimberlite, a form of solidified lava, is the principal diamond-bearing ore. Volcanic eruptions bring diamond to accessible regions within the Earth's crust, where they can be extracted. In a typical mine such as the Premier Mine near Pretoria, South Africa, one hundred tons of kimberlite produce an average of thirty-two carats of diamond (6.4 g) [2.4]. Naturally occurring diamonds of extraterrestrial origin have occasionally been found in small quantities within meteorites [2.18], which are the remaining parts of supernovae stars.

2.5 HPHT synthesis of diamond

High-pressure high-temperature (HPHT) techniques attempt to recreate the actual geological conditions occurring 150 km deep in the Earth's mantle that led to the formation of natural diamond. The process involves the use of large presses to generate a pressure of 5 GPa and a temperature of 1500°C. The two most common HPHT methods are the BELT system and its Russian counterpart, the BARS system [2.19].

The BELT system is used by, among others, De Beers and General Electric, and it consists of a huge hydraulic press with anvils and a ring-shaped structure (hence its name "belt"). Diamond seeds are placed at the bottom of the press. The internal part is then heated by a tubular graphite heater, generating temperatures above 1400°C that melt the solvent metal. The molten metals dissolve the high purity carbon source, which is then transported to the diamond seeds and precipitate.

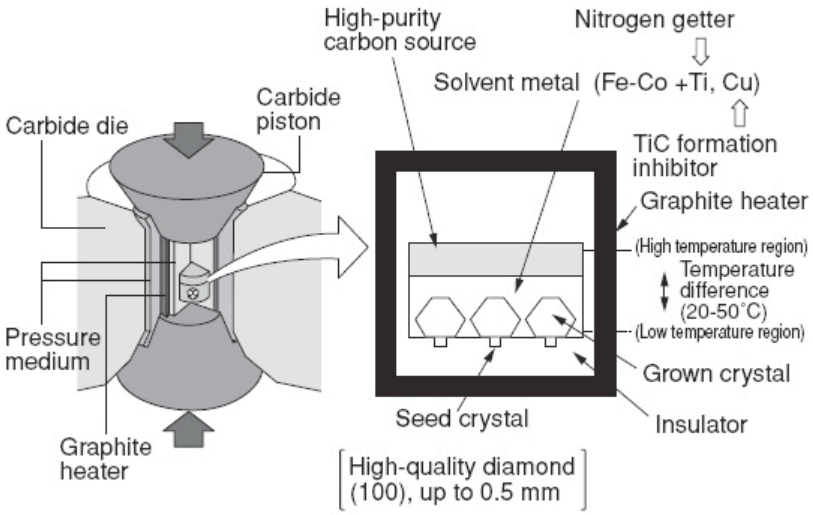

Figure 2.9: Schematic representation of a Belt type HPHT press [2.19]

The BARS system, developed at the Russian Academy of Sciences in Novosibirsk, consists of up to eight outer anvils with a spherical outer shape to which pressure is applied, and six inner anvils to multiply the pressure to the sample [2.20].

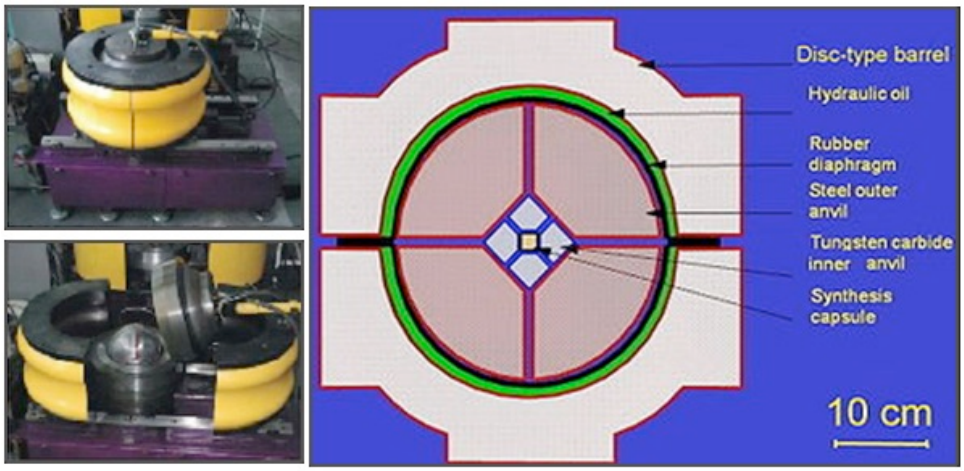

Figure 2.10: BARS press [2.20]

A third type of press design is the cubic press, which is typically smaller than a BELT press and can achieve pressures and temperatures of 70 kbar/inch^2 and 2500°C respectively, achieving diamond formation faster.

HPHT synthesis accounts for approximately 90% of the worldwide market in diamond for industrial applications [2.21]. The main disadvantage of this technique is the lack of facility for detailed process control, which precludes control over the ultimate lattice

location of any impurities introduced and sets an upper limit on crystallite size (10 mm) due to the rapid cooling inherent in the process (long range re-ordering of the constituents atoms is inhibited) [2.21].

2.6 CVD synthesis of diamond

Chemical Vapour Deposition (CVD) is a process in which a precursor gas mixture of 0.5 – 5% methane in hydrogen is thermally dissociated within a reactor either by means of a hot filament (HFCVD) or electric discharge over a substrate at temperatures between 600°C and 1000°C. Several CVD processes based on these two methods are presently in use. The four most important are: high-frequency (glow) plasma, plasma arc, thermal CVD and combustion synthesis (oxy-acetylene torch). Their main characteristics are summarized in table 2.3.

Activation method	Process	Substrate deposition rate	Temperature control	Main product
Glow-discharge plasma	Microwave RF	Low (0.1-10 μm/h)	Good	Coating
Arc plasma	DC arc, RF arc	High (50-1000 μm/h)	Poor plates	Coating
Thermal	Hot-filament	Low (0.1-10 μm/h)	Good plates	Coating
Combustion	Torch	High	Poor	Coating powder

Table 2.3: Characteristics of diamond deposition processes [2.4]

The deposition mechanism consists of a complex interaction of many factors. Adsorption, diffusion, and reaction of various species occur on the substrate surface, leading to the nucleation of diamond particles, suppression of graphite carbon, and ultimately the growth of a continuous diamond film.

Although homoepitaxial growth is possible on diamond seed crystals, the techniques in table 2.3 give rise to the growth of polycrystalline films when nucleated on non-diamond substrates. The polycrystallinity results from the formation of separate nuclei that eventually coalesce to form a continuous film. The nucleation rate and the adhesion vary with the nature of the substrate and appear to be related to the ability of the substrate to form an intermediate carbide. Surface treatments such as etching or mechanical working (scratching with diamond powder or diamond polish) help promote adhesion. [2.4].

2.6.1 Gas-phase nucleation

Diamond can be nucleated homogeneously in the gas phase. Matsumoto and Matsui [2.22] suggested that hydrocarbon cage molecules such as adamantane, bicyclooctane, tetracyclopentadecane and dodecahedrane are possible embryos for homogeneous nucleation of diamond. However, thermodynamic equilibrium calculations revealed that such low-molecular-weight hydrocarbons were not stable at high temperatures (over 600°C) in the harsh environment associated with CVD diamond [2.23]. A limited number of experiments have been conducted to examine homogeneous nucleation of diamond in the gas phase at atmospheric and sub-atmospheric pressures [2.24]. The number of diamond particles collected from the gas phase is very small compared with typical nucleation densities observed on different substrate surfaces. Therefore, the homogeneous nucleation mechanism cannot account for the large variation of nucleation densities observed on different substrate materials. The nuclei formed in the gas phase may reach the growing surface and increase the surface nucleation density.

2.6.2 Surface nucleation

Diamond has the highest surface energies among any known materials. The growth process in CVD polycrystalline diamond films typically shows several stages [2.25]: (a) incubation period; (b) 3-D surface nucleation; (c) termination of nucleation and 3-D growth of nuclei to grains; (d) faceting and coalescence of individual grains and formation of continuous film; and (e) growth of continuous film. Two criteria must be satisfied for 'spontaneous' (non-epitaxial) surface nucleation: (a) carbon saturation of the substrate surface and (b) the presence of high-energy sites (unsaturated valences). Diamond nucleation on non-diamond substrates is generally supposed to occur mostly on an intermediate layer of diamond-like amorphous carbon, metal carbides or graphite formed at the substrate surface owing to chemical interactions between the activated gaseous species and the surface during the incubation period [2.25]. Furthermore, such intermediate layers provide nucleation sites for diamond crystallite growth, enhancing diamond nucleation density on non-diamond substrates and giving an opportunity for controlling the morphology, orientation and texture of diamond films. The thickness of inter-layers ranges from several angstroms, to nanometers, up to even a few micrometers. The representative nucleation mechanisms proposed in published literature are summarized in figure 2.11 [2.25].

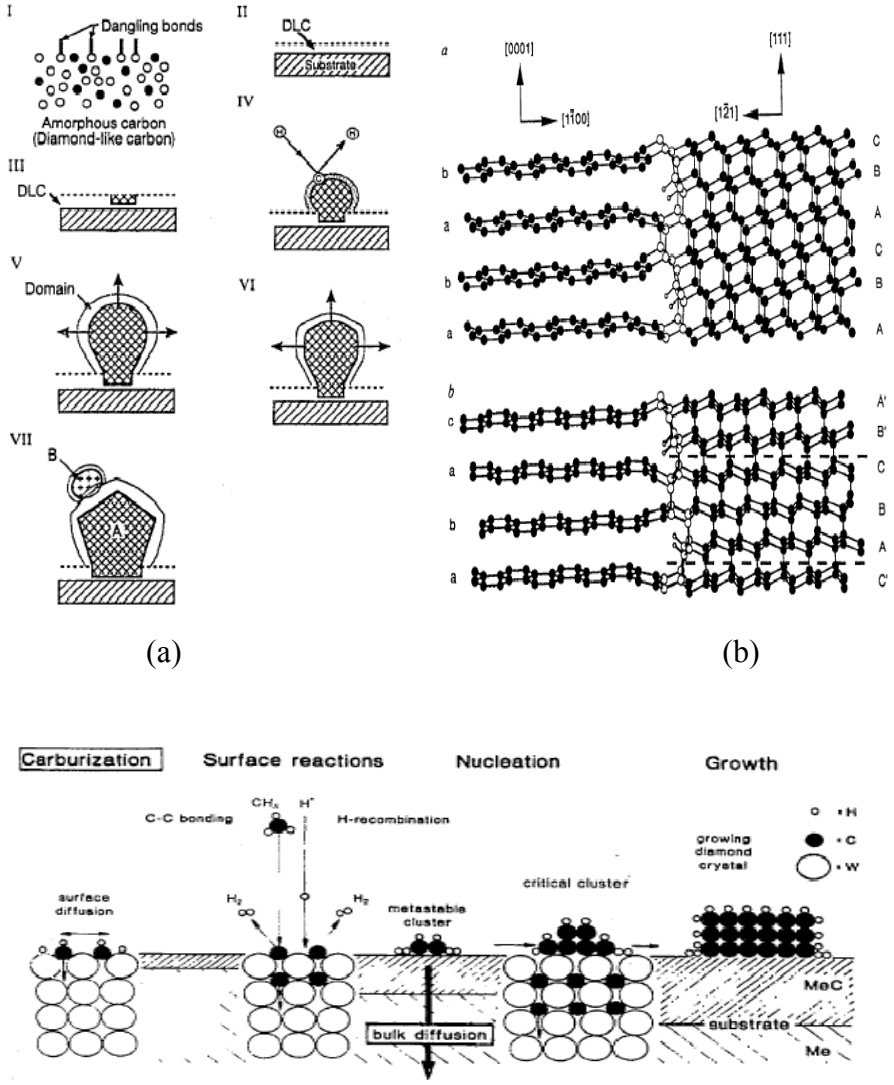

Figure 2.11: Summary of nucleation mechanisms thought to account for nucleation of diamond on most substrate: (a) On a DLC interlayer: (I) formation of carbide clusters, bonding change from sp^1 to sp^2; (II) sp^2 converts to sp^3, (III) amorphouse phase crystallises; (IV-VI) growth and faceting of diamond crystals; (VII) secondary nucleation and growth. (b) On a graphite interlayer: Condensation of graphite followed by hydrogenation of the {100} prism planes along edges of graphite particles; diamond nucleation at emerging stacking fault - almost perfect interface. Upper: cubic diamond on perfect hexagonal graphite, lower: twinned diamond nucleus adjoining a graphite stacking fault. Twin boundaries: dash lines, H-atoms: open circles, C-atoms: solid circles. (c) On a carbide interlayer: Carburisation consumes available C to form carbide surface; C surface concentration below diamond nucleation minimum; carbide layer thickness increases; C transport rate decreases, C surface concentration increases; diamond nucleus forms when either surface C concentration reaches critical level or C cluster attains critical size [2.25].

Singh [2.24] provided direct evidence for the formation of a diamond-like amorphous carbon layer, in which small nanocrystalline diamonds were embedded on copper TEM grids, and large diamond crystallites were observed to grow from these nanocrystallites. It was suggested that the diamond nanocrystallites formed as a result of direct transformation of a-C into diamond, with the intermediate layer providing nucleation sites. Figure 2.11 (a) depicts the detailed nucleation mechanism proposed on the basis of the experimental observations.

In step I, carbon clusters are formed on the substrate surface, and a change in the bonding structure from sp^1 to sp^2 takes place. In step II, sp^2-bonded carbon atoms are converted into a relatively stable network of sp^3-bonded carbon. At the same time, etching of unstable phases (sp and sp^2), which is ten times faster than etching of stable phase (sp^3), promotes and stabilizes the sp^3 phase. In step III, a bonding state in the carbon network transits from a disordered domain to diamond. Carbon atoms added into the surface (step IV) diffuse inwards by a solid-state diffusion process. Once a diamond microcrystal reaches a critical size (step V), it will acquire a faceted crystallographic shape characterized by defects (VI). In step VII, secondary nucleation takes place.

Several experiments on Ni, Pt in hot filament chemical vapour deposition (HFCVD) [2.26], on Si [2.27], and Cu [2.28] in microwave plasma enhanced chemical vapour deposition (MPECVD) provided direct evidence for the formation of graphite on the substrates prior to diamond nucleation. On the basis of these experimental results, Lambrecht and co-authors [2.29] proposed a detailed nucleation mechanism, as shown schematically in figure 2.2(b). It was suggested that graphite initially condenses on the substrate surface and the {100} prism planes are subsequently hydrogenated. Diamond nuclei grow preferentially on the prism planes of graphite, with kinetically preferential nucleation at the emerging graphite stacking faults, and with an almost perfect interface between graphite and the diamond nuclei. Etching of graphite occurs simultaneously during diamond nucleation. Atomic hydrogen terminates the dangling surface bonds and stabilizes sp^3 nuclei with repect to sp^2 nuclei. Lambrecht et al [2.29] stated this detailed nucleation mechanism is the dominant channel for the spontaneous nucleation of new independent diamond crystals in the absence of pre-existing diamond seeds.

Badzian [2.30] suggested that diamond nucleation on Si proceeds by the formation of a β-SiC buffer layer, followed by nucleation on the surface of the silicon carbide. This is supported by many growth experiments performed either on diamond particles/films on Si substrate in HFCVD and MPCVD [2.31], which showed that the Si surface was indeed

transformed to SiC leading to diamond growth with diamond nucleation occurring on a SiC intermediate layer.

A recent AFM study [2.32] provided further evidence for the formation of SiC. The formation of a Mo carbide layer in the initial stage of diamond film deposition was reported in DC arc discharge CVD [2.33] and MPCVD [2.34]. The growth rate of SiC was much lower than that of MoC. Diamond nanocrystallites were observed after 1 minute, and no further carbide layer growth was detected once the interface was covered with diamond. Wolter and co-authors [2.35] conducted systematic studies of diamond growth on carbide-forming refractory metals, and observed that diamond nucleation occurred only after the formation of a thin carbide layer. Lux and Haubner [2.36] subsequently proposed a model to elucidate the mechanism governing the nucleation process on a carbide-forming substrate as shown in figure 2.11 (c). It was suggested that carbon dissolved into the substrate initially, resulting in the formation of a stable carbide. Diamond nucleation is believed to occur on the carbide layer when the carbon concentration on the surface reaches its saturation value.

Lux and Haubner [2.36] also compared the time evolution of diamond nucleation densities on Ti, Hf, Nb, Ta, Mo and W, and found that the difference in the nucleation densities was related to the diffusion of carbon in the respective substrates. The incubation period for nucleation is the shortest on metal that can most rapidly achieve a super-saturation of carbon on the surfaces.

The growth of the nuclei first leads to the formation of individual, rapidly growing crystals [2.37, 2.38]. The nuclei form either single or polycrystals exhibit re-entrant corners, growth spirals and growth steps for easy atomic attachment in order to avoid the need of surface nucleation. Once a population of such individual crystals has started to grow and the optimal nucleation density in accordance with the surface diffusion rate has established the minimum distances between the next neighbours, no further individual nuclei are formed. It has been shown that during the early growth stages small crystals can be dissolved again if the bulk diffusion rate of carbon into the substrate is high enough [2.25]. The density of the nuclei is never so high that a layer can form directly. The individual crystals grow in all directions until they touch and form the layer. The growth rates of individual crystal diameters are, of course, much higher than the increase in layer thickness. The total weight gain per unit surface and time becomes, however, higher once the layer is formed [2.39].

2.7 Properties of Diamond

2.7.1 Thermal properties

Impurity-free diamond possesses the highest thermal conductivity among any other solid at room temperatures and approximately five times that of copper [2.4]. Lattice vibration (that is, a flow of phonons) occurs in diamond when the carbon atoms are excited by a source of energy. Since carbon atoms are small, have low mass and are tightly and isotropically bonded to each other, the energies required to make these atoms vibrate are large, occurring at high frequencies [2.40]. As a result, at ordinary temperatures, few atomic vibrations are present to impede the passage of thermal waves and thermal conductivity is unusually high. However, inclusions within the cubic structure, crystallite boundaries, lattice defects and vacancy sites lower the conductivity from its theoretical value.

Diamond exhibits very high values of electrical breakdown field and intrinsic resistivity. The low relative dielectric permittivity and possible negative electron affinity of diamond also stand out among other semiconducting materials [2.4].

Temperature (K)	**Specific heat (J/mol)**
300	6.195
1800	24.7
3000	26.3
	Effective Debye Temperature (K)
0	2220
273-1100	1860
	Thermal conductivity (W/m K)
80 (type Ia)	2000-4000
80 (type Iia)	17000
293 (type (Ia)	600-1000
293 (type Iia)	2000-2100
	Linear thermal expansion (K^-6)
193	0.4
293	0.8
400-1200	1.5-4.8

Table 2.4: thermal properties of diamond [2.4]

2.7.2 Optical properties

Pure diamond (never found in nature and not yet synthesized) would have only two intrinsic absorption bands [2.41, 2.42]:

- An ultraviolet absorption due to the electron transition across the bandgap, corresponding to a wavelength of 230 nm.
- An infrared absorption related to the creation of phonons and the intrinsic multi-phonon absorption.

Impurities and lattice defects constitute obstacles to the free flow of photons. Lattice vacancies may considerably alter the valence bands and cause electrons to be excited by a much smaller amount of energy that would normally be required in a perfect lattice.

Type	Optical absorption bands
Ia	IR: 6-13 μm UV: < 225 nm
Ib	IR: 6-13 μm UV: < 225 nm
Iia	Closer to ideal crystal. No absorption in the range < 1332 cm-1. Continuous absorption below 5.4 eV
Iib	IR: no significant absorption from 2.5-25 μm. UV: absorption at 237 nm

Table 2.5: optical absorption of diamond by type [2.41, 2.42]

2.8.3 Electronic properties

The band structure of bulk crystalline material is a consequence of the effect of the Pauli Exclusion Principle on the overlapping wavefunctions of each electron of each atom in the lattice. Band structure calculations are based upon a quantum mechanical analysis of the effects on a free electron of the periodic potential that it experiences because of interactions with atom nuclei, core electrons and valence electrons [2.43]. The bandgap energy E_g for diamond was calculated to be 5.40 eV by Painter and co-authors [2.44], agreeing well with empirical results reported elsewhere [2.45] of 5.47 eV and 5.49 eV.

With such a high bandgap energy, pure single-crystal diamond is one of the best solid electrical insulators [2.46]. The high strength of the electron bond makes it unlikely that an electron would be exited out of the valence band. Pure diamond possesses a resistivity greater than 10^{18} Ω m; however, as with optical properties, the presence of impurities can alter its electronic state and the inclusion of graphite bonds will considerable decrease the resistivity and render the material useless for electronic applications.

Resistivity	type I and most type Iia: 10^18 Ωm Type IIb: 1000-100000 Ωm
Dielectric constant at 300 K	5.7
Dielectric strength	10 MV/cm
Saturated electron velocity	2.7^7 cm.s
Carrier mobility	electron: 2200 cm^2/Vs
	hole: 1600 cm^2/Vs

Table 2.6: electronic properties of diamond [2.4]

Particularly important for semiconducting applications is the carrier mobility, μ, describing the ease with which a charge carrier can move through a semiconductor under the force arising from an electric field [2.47]:

$$\mu = q \tau_m / m^* \qquad (2.1)$$

where q is the electronic charge, τ_m is the mean free time between scattering collisions and m^* is the effective carrier mass (that is, the mass that a particle seems to carry in the classical model of transport in a crystal).

The carrier mobility is of critical importance in the design of electronic devices as it determines the conductivity σ of a sample:

$$\sigma = q (n\mu_n + p\mu_p) \qquad (2.2)$$

where n and p are the respective electron and hole densities.

Impurity scattering will be the dominant influence on τ_m at lower temperatures, whereas lattice scattering will be dominant at higher temperatures. The overall mobility is the sum of these components μ_l and μ_I, respectively, according to the Matthieson rule [2.48]:

$$\mu^{-1} = \mu^{-1}_{l} + \mu^{-1}_{i} \quad (2.3)$$

Another fundamental parameter is the saturated carrier velocity. Under high bias the drift velocity of carriers in a semiconductor can become comparable to their thermal velocity, at which point any additional energy imparted to the carriers by the electric field will be lost to lattice as heat, increasing scattering events [2.47]. This situation sets an upper limit on the speed of devices that can be quantified by this parameter.

2.8.4 Mechanical properties

Diamond is the hardest known material, and therefore it is difficult to measure its hardness as only another diamond can be used as an indenter. The values of hardness obtained ranges from 5,700 to 10,400 kg/mm^2 [2.4]. Major mechanical properties of diamond are reported in table 2.7 [2.49].

Property	Diamond	Alumina
Density (g/cm^3)	3.52	3.98
Young's modulus (Gpa)	910-1250	380-400
Compression strength (Gpa)	8.68-16.53	2.75
Knoop hardness (kg/mm^2)	overall: 5700-10400 (111) plane: 7500-10400 (100) plane: 6900-9600	2000-2100
Poisson's ratio	0.10-0.16	0.22
Coefficient of friction	In air: 0.05-0.1 In vacuum: near 1	

Table 2.7: Mechanical properties of diamond compared to alumina [2.49]

2.8.5 Chemical properties

Natural diamond and single-crystal synthetic diamond is generally inert to most chemical environments. However in a pure oxygen atmosphere it starts to “oxidise” at 250°C, with the reaction becoming fast at temperatures above 600°C. As diamond is composed of carbon, the by-product of full oxidation is carbon dioxide and therefore it does not passivate the diamond surface. At room pressure and temperature oxygen is adsorbed on diamond surface following exposure after a certain period of time. Oxygen is chemisorbed on diamond surface up to a temperature of 144°C [2.50].

Like oxygen, hydrogen is also chemisorbed on the surface of diamond but not until a temperature of 400°C.

Diamond can be etched by strong oxidisers such as sodium and potassium nitrates at temperatures above 500°C, by fluxes of sodium and potassium chlorates and by molten hydroxides.

At approximately 1000°C it reacts with carbide forming materials such as Iron, Cobalt, Nickel, Aluminium and Tantalum.

In the case of diamond polycrystalline films, the structure of grain boundaries, and the concentration of impurities at the boundary affect diamond chemical properties [2.4].

2.8 Doping of diamond

The covalent bonds of carbon atoms in diamond are extremely strong and short [2.51], making diamond an excellent insulator with a band gap of 5.4 eV at room temperature. Moreover, properties such as extraordinary intrinsic carrier mobility high thermal conductivity, radiation hardness, chemical inertness and high break-down field make it highly desirable for the production of conductive material by doping [2.52].

However, as opposite to Silicon and other common semi-conductor materials, its extremely compact diamond lattice does not favour the presence of substitutional impurities. Consequently only few species can be used as dopant for diamond, the most common of which include boron, nitrogen and phosphorous.

2.8.1 P-type doping

Boron is the ideal dopant species for diamond due to the relative simplicity with which it can be diffused or implanted into the diamond bulk and due to its low activation energy.

Boron-doped diamond exists in nature (type IIb) and behaves as a p-type semiconductor. Boron is also the most conspicuously successful among the chemical species that can be incorporated in sufficient concentrations in diamond.

Diamond may be doped with boron using gas-phase growth such as high-pressure-high-temperature (HPHT) and chemical vapour deposition (CVD). Boron-doped HPHT diamond was first reported by Wentorf and co-authors [2.53] by adding boron to the metal catalyst during synthesis. The solvent catalyst usually contains species that getter nitrogen in order to stop its incorporation and to prevent these atoms from compensating the boron. However, contamination of the diamond by nitrogen and by the catalyst cannot be completely eliminated and the films obtained tend to be over-doped or of poor quality.

Boron can also be added to the gas mixture during CVD growth by adding boron-

containing molecules in either a microwave (MW) or in a hot filament (HF) reactor [2.51]. Teraji and co-authors, [2.54] reporting on boron-doped films grown by means of MPCVD (on type Ib substrates) recorded through Hall measurements that the estimated acceptor densities N_A increased with the boron-to-carbon (B/C) ratio in the gas phase. The correspondent boron activation energy decreased from 0.36 eV at lower concentrations to 0.29 eV at the highest, consistently with previous reports [2.55]. The correspondent Hall mobility recorded by the authors is remarkably high, the highest of which being of 1620 cm^2V/s at 290 K and 2750 cm^2V/s at 215 K for the sample with a B/C ratio of 0.5 ppm. However, the presence of compensating impurities and defects introduced during CVD growth limits the doping efficiency and carrier mobilities.

Using type Ib synthetic diamond, Yamanaka and co-authors [obtained boron-doped films with a Hall mobility as high as 1840 cm^2/Vs at carrier concentration of 2.3×10^{14} cm^{-3} and temperature of 290 K increasing to 3370 cm^2/Vs at carrier concentration of 7.2×10^{9} cm^{-3} and temperature of 170 K [2.56].

Diamond can be doped with boron also by means of ion-implantation. In this technique, electric fields in accelerators are used to confer high momentum to the boron atoms that are then implanted into the diamond bulk. The characteristic mass and energy of the accelerated boron atoms determine their penetration depth into the bulk. The advantage of this technique is given by the precise control with which dopants can be injected into the material, but the residual bulk damage left by the implantation process is a limiting factor for the mobilities of the doped films; in fact, these defects can lower the temperature at which the diamond-to-graphite conversion is initiated [2.57]. Prins [2.58] has proposed a scheme for implantation and annealing of diamond, which is based on implanting boron to low doses (below the graphitization limit) into diamond held at low temperature followed by rapid annealing (CIRA). Fontaine and co-authors [2.57] took the CIRA approach a step further by devising a special in-situ rapid heating step at 1050^0C for 10 minutes followed by a further anneal at 1450^0C for 10 minutes. The substrates used were type IIa diamond. After the first annealing step the mobility was recorded to be 220 cm^2V/s and the boron activation energy 0.35 eV; after the second annealing step the mobility increased to 385 cm^2V/s and the activation energy 0.34 eV.

As for other Group-III potential dopant species, theory predicts that as the atomic number increases, so the acceptor level associated with the on-site substitutional impurity moves deeper into the band-gap [2.59]. Such deep levels are clearly of no practical importance, due to the high energy required to electrically activate those species.

2.8.2 N-type doping

Nitrogen is commonly present in diamond in various aggregated forms, but does not lead to a shallow donor level [2.52]. The localization of the nitrogen donor electron is accompanied by the formation of a very deep donor level, usually quoted at around E_a = -1.7 eV [Goss 8]. Such a deep level is of no value for the manufacture of n-type semiconductors, with a room temperature ionization fraction that of approximately zero.

Another candidate for n-type doping of diamond is phosphorous, which is not though to relax in a similar fashion to nitrogen and leads to a shallower donor level. The donor level is experimentally reported to be at E_a = -0.6 eV, remaining still deep for room temperature ionization [2.60].

Koizumi and co-authors [2.61] reported on successful doping of diamond with phosphorous. Posphine (PH_3) was added to the gas phase of diamond during growth by means of microwave plasma assisted chemical vapor deposition. The substrate used for growth was HPHT type Ib diamond. A lower methane concentration (~0.15%) and a higher substrate temperature (~950 ^{0}C) than usual were required to obtain higher crystalline perfection for the phosphorous doping. For a sample grown with the ratio PH_3/CH_4 equal to 1000 ppm, the phosphorous concentration was calculated to be about 2.5×10^{19} cm^{-3}. The Hall mobility was measured over a temperature range, with the highest value of 23 cm^{2}V/s corresponding to the highest temperature at which was tested (227 ^{0}C). This low mobility value was considered by the authors due to the scattering of conducting electron by a large number of un-ionized phosphorous atoms as much as to crystal defects [2.61]. The activation energy of the carriers was calculated to be 0.43 eV at approximately 125 ^{0}C.

More recently, Katagiri and co-authors [2.62] showed that lightly phosphorous-doped diamond (type Ib) with high crystalline perfection could be successfully obtained.

At a phosphorous concentration of 7×10^{16} cm^{-3} the maximum Hall mobility recorded was 410 cm^2/Vs, and at a lower concentration of 5×10^{15} cm^{-3} the Hall mobility became 660 cm^2/Vs. In both cases measurements were taken at room temperature.

Despite the search for other n-type dopants, currently phosphorus is the only plausible conventional n-type diamond dopant. In particular, recent studies [2.63, 2.64] have suggested that sulfur (S) or eventually a S–B complex can act as an n-type dopant in diamond, but they have not been widely confirmed and the role of sulfur in n-type diamond doping is not fully understood. Spectroscopic investigations of S-doped CVD diamond films could not confirm the shallow character of sulfur dopant and found only

deep gap states related to sulfur in S-doped CVD diamond [2.65].

Of the alternative dopants, lithium and sodium have been predicted to have shallow donor levels when in interstitial positions in diamond [2.66] and have been the subject of significant experimental interest [2.67, 2.68-2.71]. However, despite expectations of Li being a shallow donor [2.66] most experimental studies have found Li doped samples to be either highly resistive or electrically inactive.

In spite of a significant number of experimental studies, especially for lithium, the results are not always in agreement with each other. For example, the position of the lithium donor level in diamond is unclear, with some studies finding a shallow level [2.72] while others find impurity levels at 0.8–0.9 eV [2.68,] and 1.5 eV [2.68, 2.73].

Recently, Ueda and co-authors [2.74] investigated beryllium-doped diamond (type Ib). As for the Beryllium-doped films obtained by means of ion implantation, despite a carrier concentration of 10^{19} cm^{-3}, the authors were not able to determine the carrier concentration and mobility by means of Hall measurements due to the extremely high resistivity of the films. However, theoretical studies conducted by Yan and co-authors [2.75] suggested that beryllium- and magnesium-doped diamond could be n-type semiconductor.

2.9 Polycrystalline diamond

2.9.1 The role of grain boundaries in polycrystalline diamond

It is important to understand the structure and composition of the grain boundaries in order to better understand the detrimental effects they have on diamond films.

Photothermal Deflection Spectroscopy measures the change in the refractive index of a material due to heating by light [2.76]. This technique permits measurement of absorbances down to 10^{-5} level. It is employed when high accuracy absorbance measurements are required, and therefore it is ideal for the study of deep defects on a ppm scale. This technique has been amply reviewed in previous works [2.76, 2.77].

Photothermal Deflection Spectroscopy studies conducted on thin polycrystalline films (0.25 – 1.6 μm) by Zammit and co-authors [2.78] in the spectral range 0.25 – 3.5 μm into the sub gap region of diamond (4.4 – 0.35 eV) revealed optical absorption levels that were three or four orders of magnitude larger than in bulk IIa diamond (not reported).

Figure 4.3 represents a plot of the absorption coefficient β against the band gap energy, where β is the ratio of the light transmitted through a material I, and the light incident I_0 (as according to the Beer-Lambert law).

The absorption coefficient in figure 2.12 increased along with the methane concentration.

The authors attributed the defects causing the sub band gap energy levels to sp^2 carbon, whose concentration (along with the size of their sites) increased along with the methane content during the growth process.

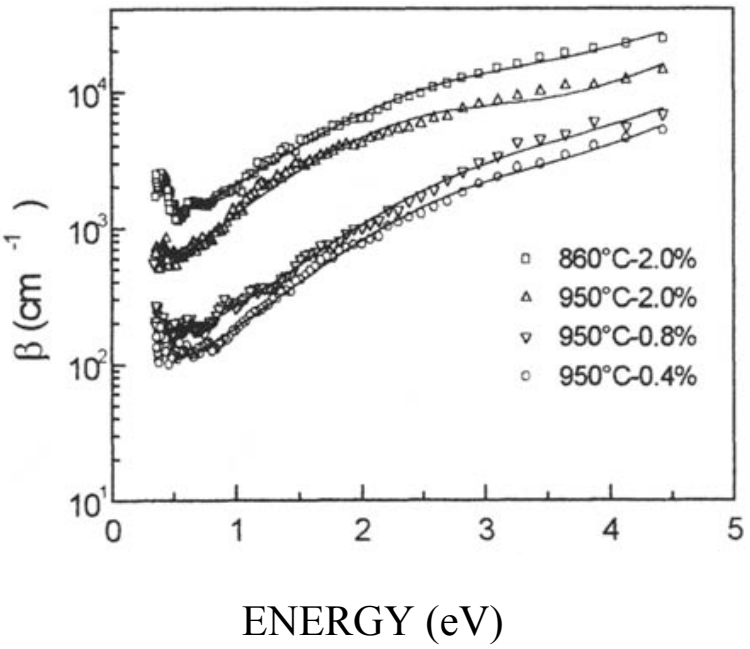

Figure 2.12: sub gap absorption spectra for diamond thin film [2.78]

Hearne and co-authors [2.79] backed the conclusions reached by Zammit and o-authors. Dark conductivity measurements performed on polycrystalline diamond samples, with characteristics summarized in table 2.8, were carried out to gain an insight into the conduction mechanisms within the material.

Sample	H2:CH4:O2 (sccm)	Microwave power (kW)	T (C)	P (Torr)	Thickness (µm)	Dark conductivity
A	150:2.5:0	5	725	118	277	1.7 eV
B	100:4.75:0	4.5	815	116	136	< 610 K: grain boundary related > 610 K: 1.8 eV activation
C	155.7:6.3:0	4.5	750	115	260	< 450 K: grain boundary related > 450 K: 1.2 eV activation

Table 2.8: Summary of sample growth parameters and characterization data [2.79]

A constant activation energy of 1.7 eV was measured with sample A, whose origin is attributed by the authors to electronic levels associated with Nitrogen impurities within the diamond grains. However, for sample B and C the dark conduction was thought to have a contribution not only from the grains but also from the grain boundaries. In particular, below 600 K (that is, at temperatures more relevant for potential applications of devices built with this material) the activation energy showed a strong dependence with temperature, which the authors thought to be caused by a band tail extending into the band gap, an effect typically observed in disordered materials, which in the current case was attributed to the grain boundaries in the polycrystalline diamond [2.79]. Table 4.2 and figure 2.13 summarize the results of the authors' study.

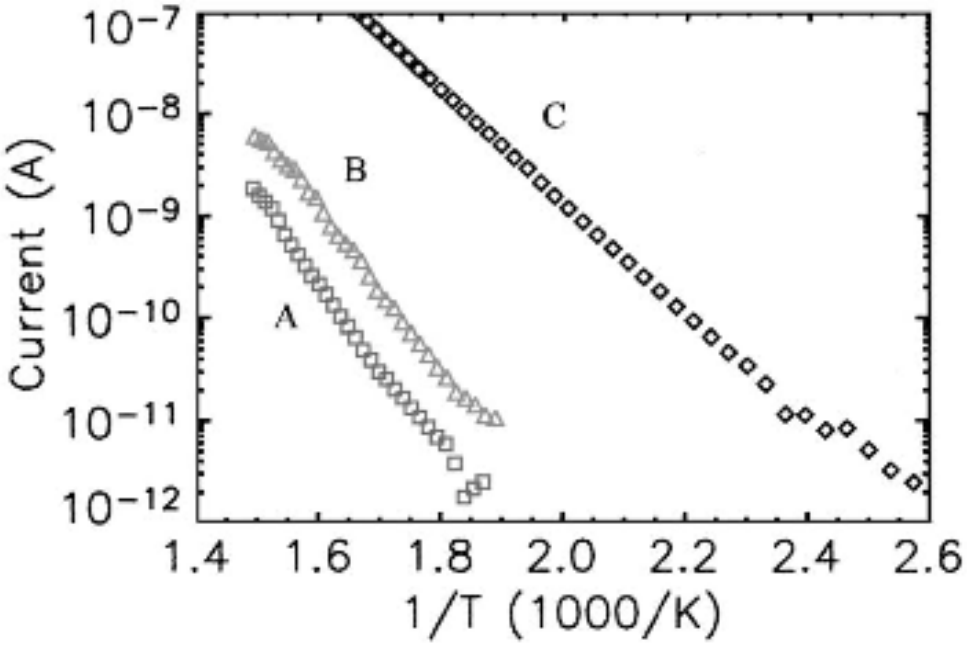

Figure 2.13: Arrhenius plots of dark conductivity for sample A, B and C at an electric field of 2 kV/cm [2.79]

Nesladek and co-authors [2.77] observed that despite the fact that the charge-carrier mobilities in some homoepitaxially grown CVD diamond films had approached values recorded in natural diamond, tested devices built with such polycrystalline materials performed modestly. Therefore the nature of the non-diamond materials in polycrystalline films needs to be understood. As seen above, such non-diamond material is mainly concentrated at the grain boundaries in polycrystalline diamond.

Nesladek and co-authors [2.77] confirmed the conclusions by Zammit and Hearne [2.78] by showing the existence of a sub-gap continuum absorption that is not observed in natural

diamond, starting below 1 eV, that is, at approximately 1 eV from the valence band. The technique utilized by the authors to record their results was also in this case Photothermal Deflection Spectroscopy (figure 2.14).

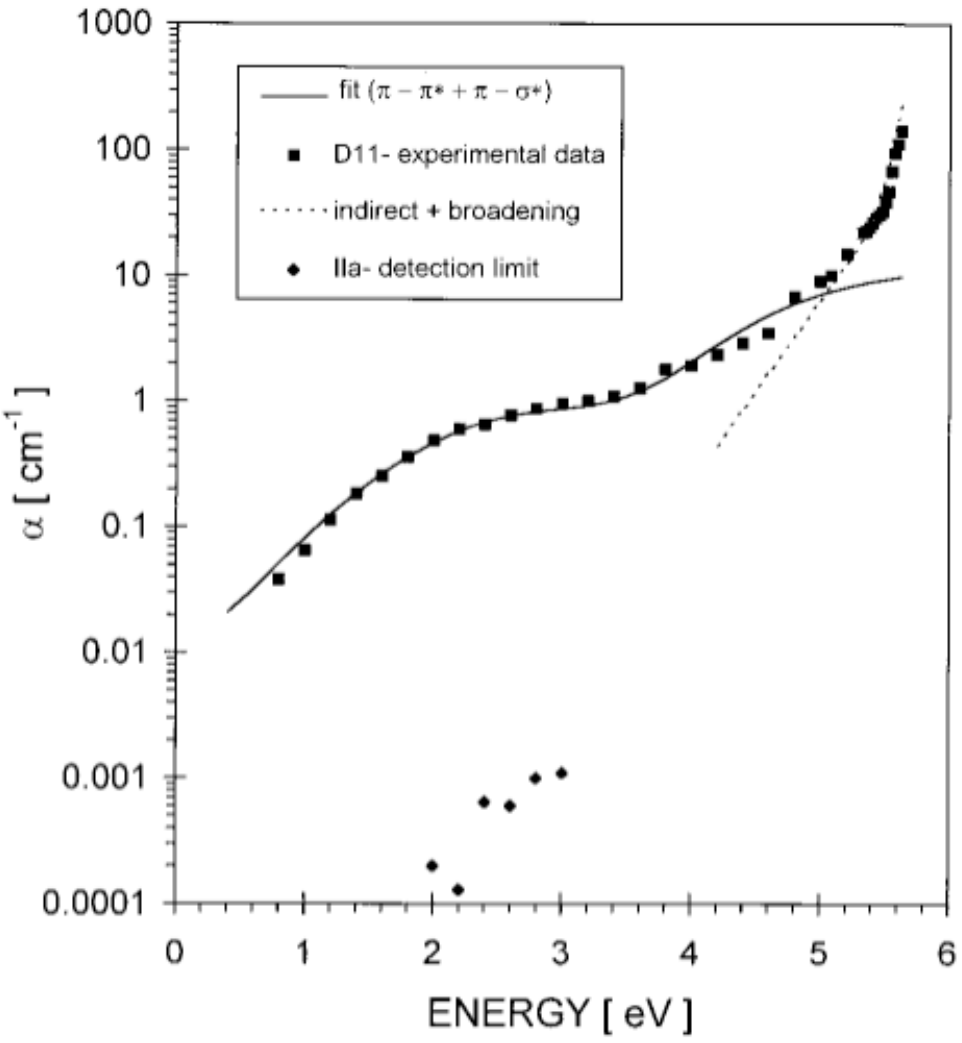

Figure 2.14: The spectral dependence of the optical absorption coefficient α obtained from PDS measurements for the polycrystalline material tested by the authors (D11) and for the bulk IIa diamond sample (investigated only in the range 1 – 3 eV) [2.77]

Having taken into account a model developed by Robertson and O'Reilly [2.80] and Bredas and Street [2.81] for amorphous Carbon, Nesladek and co-authors proposed a model [2.77], in which a π - π^* band-type transition is responsible for the observed absorption. In a graphite lattice three electrons form sp^2 bonds to neighbouring Carbon atoms (σ bonds) and one electron forms a π orbital perpendicular to the σ bonds (figure 2.15).

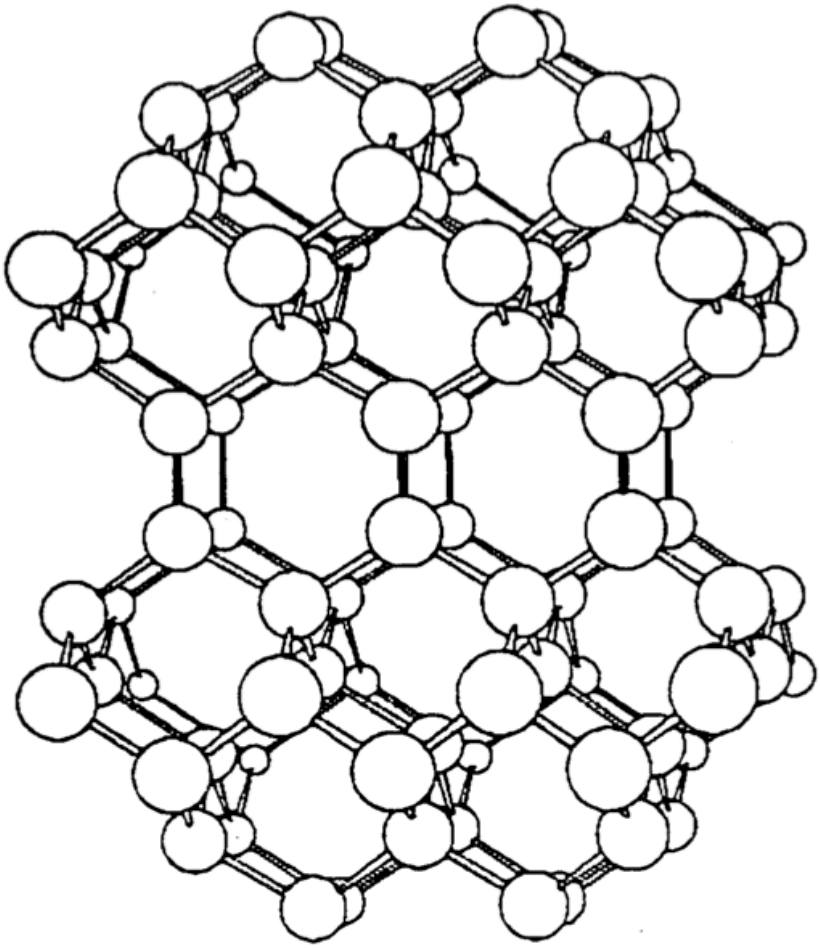

Figure 2.15: Schematic drawing of a graphite lattice [2.81]

The π bonds are weaker than σ bonds and therefore closer to the Fermi level. Due to disorder, π and σ bands are broadened. Assuming a Gaussian distribution for the filled π and the empty π^* and that the distribution of the filled σ and empty σ^* decrease exponentially towards the centre of the band gap [2.82], figure 2.16 schematically shows the dominant transitions responsible for the optical absorption seen above in figure 4.5. Σ represents the valence band and Σ^* the conduction band in type IIa diamond.

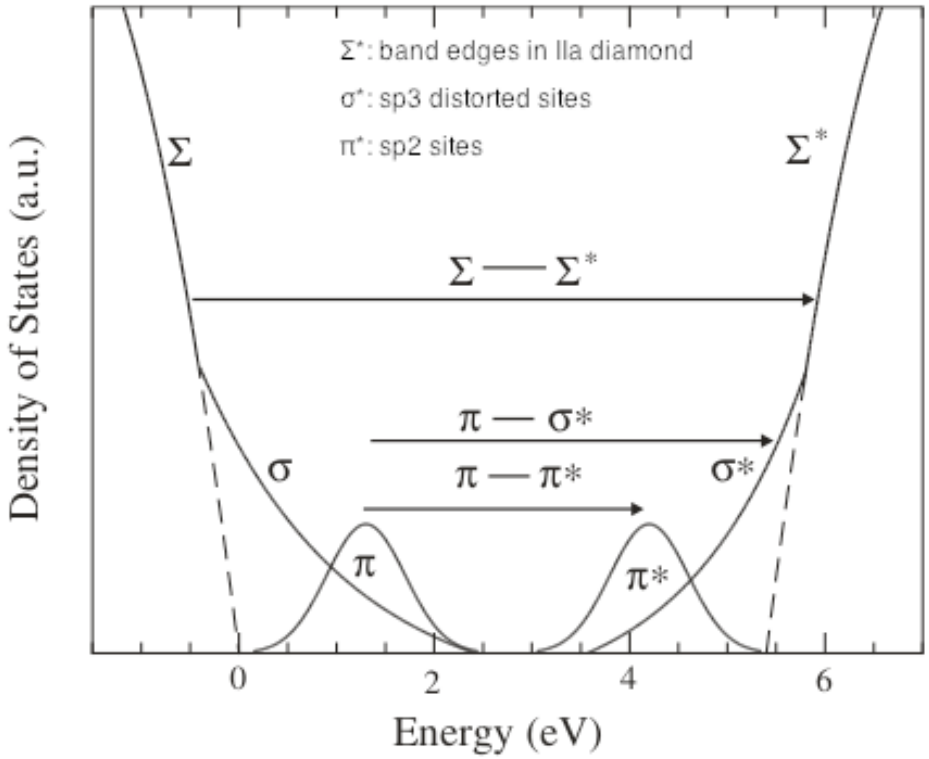

Figure 2.16: Schematic model of the density of states in the gap of CVD diamond. The π and π^* bands are due to the presence of amorphous Carbon region [2.77]

As well as to the π - π^* transition, a π - σ^* transition is also reported. This transition occurs as a consequence of sufficient bond-angle distortion due to the immersion of sp^2 atoms in sp^3 environment [2.77].

The empty π^* and σ^* states at grain boundaries are traps for electrons and the filled π and σ states are traps for holes. A graphite lattice consists of in-plane bonded six-membered hexagonal rings with 120° bonding angle between each carbon. A diamond lattice consists of 109.5° tetragonally bonded carbon. The incorporation of graphite rings within the diamond structure would cause an extremely large distortion, so the authors proposed that such amorphous carbon is located mainly in grain boundaries [2.82].

The Σ - Σ^* transition corresponds to the fundamental absorption in type IIa diamond.

In grain boundaries carrier transport occurs by thermal activated hopping (all the Carbon electrons are within π bonds).

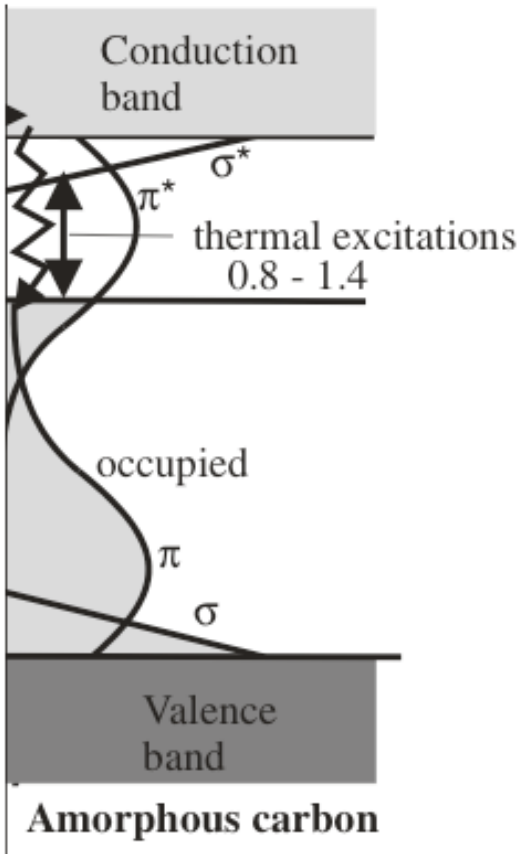

Figure 2.17: Schematic model of the density of states representative of the properties of CVD diamond at grain boundaries. Photo-generated electrons are trapped in anti-bonding π^* and σ^* where transport takes place by thermal activated hopping. Holes are trapped in the bulk grains. To establish thermodynamic equilibrium, electrons and holes have to overcome an energy barrier of about 1.4 eV [2.82]

UV photodetectors analysed by Nebel [2.82] with polycrystalline diamond showed persistent photocurrent effects as a function of temperature. Annealing at 750°C for 30 minutes was performed before UV illumination (emitting photons at 5.5 eV) was initiated. It is activated with approximately 0.85 eV in the low and 1.47 eV in the high temperature regimes (figure 2.17). As the temperature increases, electrons are photo-ejected until all traps are empty.

One approach to overcome the grain boundary problem is the growth of films with ever-increasing crystal sizes, leading to reduction of grain boundary densities.

Hammersberg and co-authors [2.83] investigated the photocurrent mobility × lifetime products ($\mu\tau$) and free-carrier lifetimes of a number of CVD polycrystalline diamond samples having different grain size and nitrogen content (table 2.9). A study of $\mu\tau$ products permitted the discrimination of the quality of the diamond films; the higher μ and τ, the higher the quality of the diamond film.

Sample	Average grain size (µm)	Average growth size (µm)	Average nucleation size (µm)	Average thickness (µm)	Nitrogen content (cm^3)
1	25	34	15	95	< 4×10^4
2	32	54	9	227	< 4×10^4
3	39	49	29	202	10^15 - 10^16
4	48	52	44	225	10^15 - 10^16
5	110	113	107	98	< 4×10^4

Table 2.9: Technical data for the samples investigated by the authors [2.83]

Their work focused on investigating how the grain size and therefore grain boundaries influence the mobilities and lifetimes of the samples. The relatively large variation in grain size (25 µm to 110 µm) made it possible to single out effects due to lifetime limiting trapping and recombination centres inside the grain from effects caused by defect centres at the grain boundaries.

In fact, at low photo-generated carrier densities, $< 10^{13}$ cm^{-3}, the effective free carrier lifetimes is in the sub-nanosecond to nanosecond range due to intra-grain trapping and recombination centres. However, at high carrier densities, $>10^{13}$ cm^{-3}, the intra-grain centres become saturated so that the effective lifetime becomes predominantly given by carrier diffusion to, and recombination at, the defects related to the grain boundaries [2.83].

To characterize the material, two different electro-optical techniques were used, a $\mu\tau$ product measurement commonly referred to as 'charge collection distance' (CCD) and a photoconductive decay (PCD) technique. In the CCD technique a uniform electric field E = V/D is applied to a semiconductor exposed to radiation (figure 2.18), where V is the voltage applied and D is the thickness of the semiconductor material at which extremes the field E is applied. In the current case, metal contacts are deposited at the growth and nucleation side of the diamond sample, where E is applied. Electron-hole pairs are generated, and due to E they drift towards the anode and cathode respectively (charge trappings and recombination might prevent some of the carriers to be collected by the electrodes).

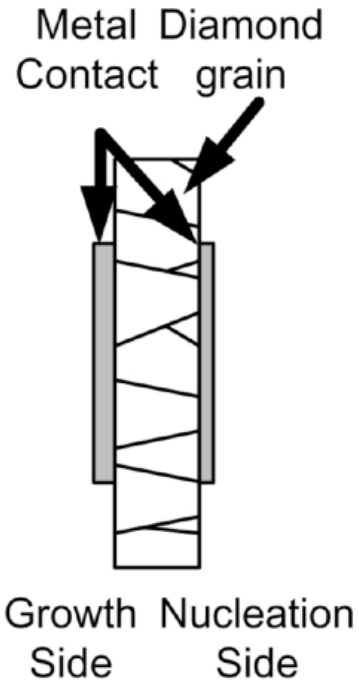

Figure 2.18: Contact geometry as devised by Hammersberg and co-authors [2.83]

The charge collection distance is defined as:

$$\delta = (\lambda_e + \lambda_h) = (\mu_e \tau_e E + \mu_h \tau_h E)$$

where λE is the mean free distances for charge carriers, μ is the mobility and τ is the carrier lifetime before being trapped.

The collection efficiency

$$\eta = (L_e + L_h) / D$$

obtained following photocurrent measurements, in which monochromatic light with a pulse of 10 μs (longer than both transit time and carrier lifetimes) was focused on either the cathode or the anode, is equalled to a theoretical value described by the Hecht model [2.84]:

$$\eta = \frac{\lambda_h + \lambda_e}{D} - \frac{[\lambda_h^2 e^{-D/\lambda_h}(e^{G/\lambda_h} - 1) + \lambda_e^2(1 - e^{-G/\lambda_e})]}{DG}$$

$\mu_e\tau_e$ or $\mu_h\tau_h$ can be extrapolated by either illuminating the anode or the cathode or by reversing the applied bias voltage.

CCD experiments showed that the $\mu\tau$ product is decreasing along with the average grain size and increasing nitrogen content, as figure 2.19 shows.

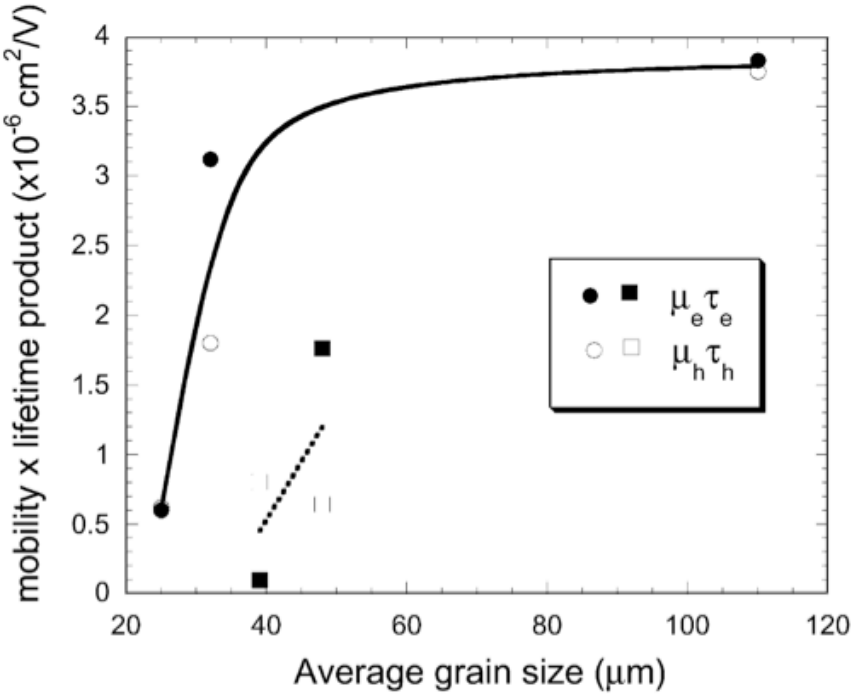

Figure 2.19: Summary of the extracted experimental results from the $\mu\tau$ product measurements [4.5]. The circular symbols indicate the samples 1, 2 and 5, with a N content $< 4 \times 10^{14}$ cm^{-3}, and the squares the samples 3 and 4, with N content $10^{15} – 10^{16}$ cm^{-3} [2.83]

In the PCD technique electron-hole pairs are generated by optical excitation; by laser light with a wavelength of 266 nm. Excitation is then interrupted and the decay of the carrier lifetimes is measured by monitoring the photocurrent decay.

PCD measurements showed that samples with larger grain boundaries have an overall longer effective lifetime than samples with a high density of grain boundaries.

The authors remarked the importance of large grain size and low Nitrogen content to obtain high $\mu\tau$ products and therefore high quality polycrystalline diamond.

The disadvantage with large grain sizes polycrystalline diamond (figure 2.20) is that such films become unreasonably thick and not suited for integration with micro- and nano-scale device technology. Flat surfaces are in fact highly desirable, as photolithographic techniques are difficult to carry out on rough surfaces.

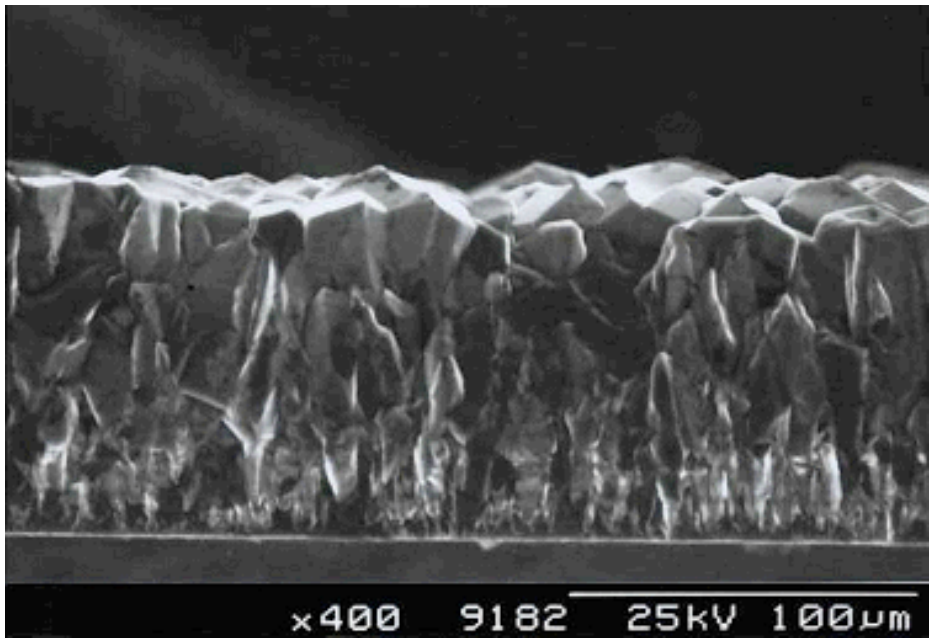

Figure 2.20: scanning electron microscope image of a cross-section of typical microcrystalline diamond film [2.2]

Nanocrystalline diamond (NCD) films, in which the grains are less than 100 nm in diameter (figure 2.21), can be produced with film thicknesses of only tens of nanometres overcoming the problem of integration, but clearly leading to an even higher level of grain boundary density than in the case of microcrystalline diamond materials [2.85, 2.86, 2.87, 2.88]. Nesladek [2.77] showed that films with the highest sub gap absorption were very finely grained with an increased surface of grain boundaries. A Raman spectroscopy study performed reported an increased amount of sp^2 Carbon in these films.

The properties of NCD are thus influenced in a directly proportional relation to the fraction of π-bonded Carbon atoms that make up the grain boundaries, that is, to the nanocrystallite sizes. A 10% Carbon fraction at the grain boundaries is associated with an average crystallite size of approximately 3 nm, whereas a 1% fraction is associated to 30 nm and 0.1% to 300 nm.

The presence of sp^2-bonded dimers and chain segments and sp^3-hybridized dangling bonds in the grain boundary introduces states in the perfect-crystal bandgap. However, because of the lack of spatial connectivity among these sp^2-bonded defects, the associated gap states do not form a continuous graphite-like π-band but are localized. The electrical conductivity cannot therefore be expected to be metallic as in graphite. However, the possibility of transitions between the localized electronic gap states suggests a relatively low effective energy gap in the grain boundary region, making NCD a non-ideal dielectric.

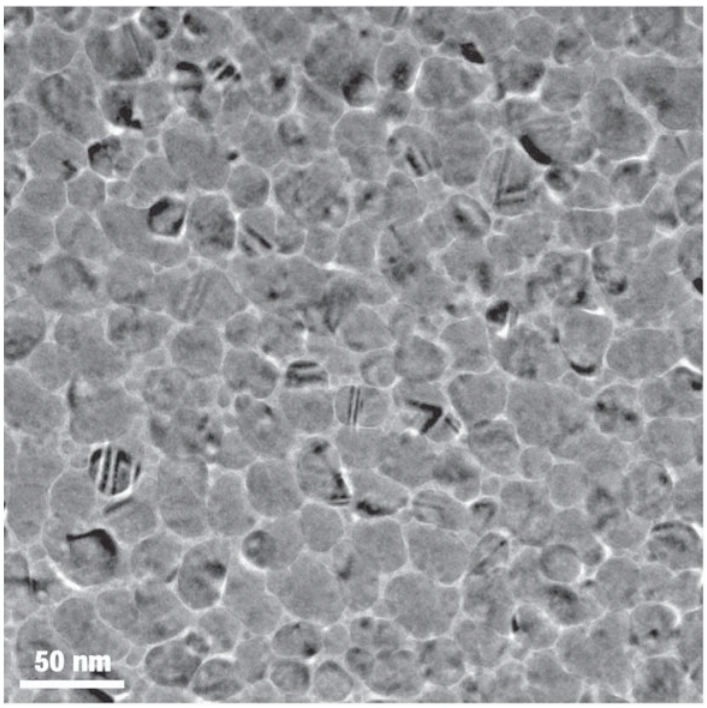

Figure 2.21: scanning electron microscope image of the surface of typical NCD [2.88]

Even smaller grain sizes are evident in so-called 'ultra-nanocrystalline diamond (UNCD)' (figure 2.22), where inert gas incorporation into the CVD growth environment leads to a material with structure of the order of 5 nm [2.89].

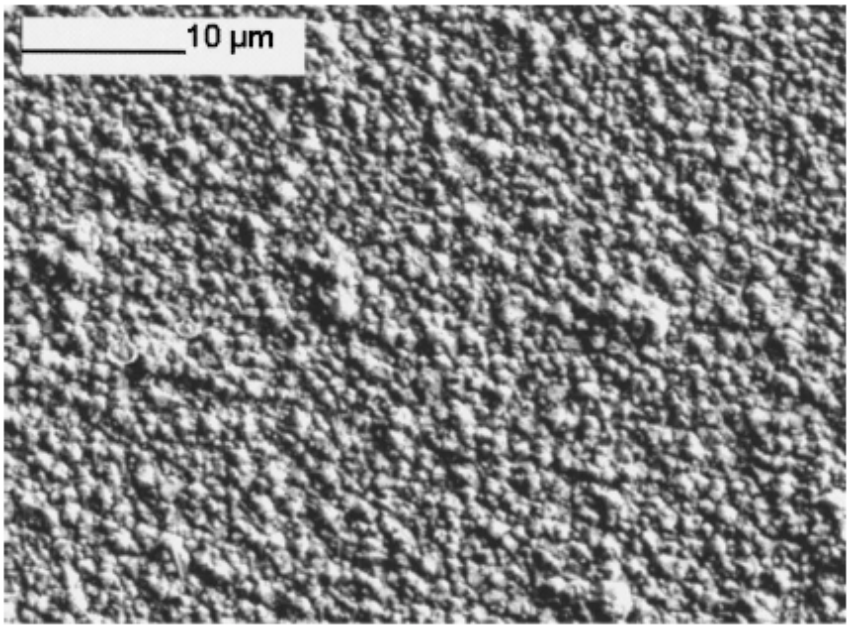

Figure 2.22: scanning electron microscope image of typical UNCD [2.89]

UNCD has been shown to be an effective dielectric: In UNCD films, Diamond films produced with 5% and 6% hydrogen concentration in the plasma yielded a low value of permittivity. The reason is that when hydrogen is added to the Ar/CH_4 gas mixture in the growth process more atomic hydrogen (which is a strong etcher of graphitic Carbon) is generated. Moreover, hydrogen is incorporated into the grain boundaries where it saturates sp^2 carbon dangling bonds and resulting in an increased resistivity [2.90].

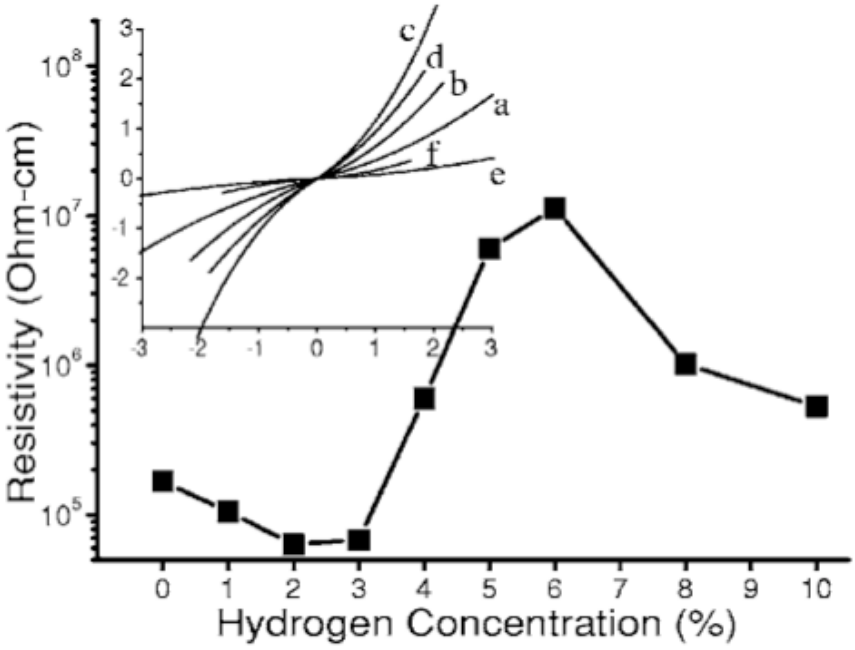

Figure 2.23: Schematic plotting of CVD-diamond-thin-film resistivity as a function of Hydrogen percentage in the gas mixture during film growth. Inset: I-E curves measured from test structure with diamond thin films deposited in microwave plasmas with (a) 0%, (b) 1%, (c) 2%, (d) 3%, (e) 5% and (f) 10% Hydrogen in the Ar/CH_4 gas mixture (x axis: electric field, V/μm, y axis: current, 10^{-4} A) [2.90]

UNCD is also a good n-type semiconductor when nitrogen is additionally used during CVD.

Hall measurements performed by Williams and co-authors over a range of temperature [2.91] showed that the activation energy of nitrogen-doped UNCD films decreased with added nitrogen in the gas phase, and is below 10 meV for nitrogen gas phase concentrations above 10%. Theoretical modelling has demonstrated that nitrogen in the gas phase promotes π-bonded states within the grain boundaries. The predicted density of states also shows the Fermi level is situated close to the valence band for films grown without nitrogen. As nitrogen is added, the increase in conductivity manifests due to the high density of states within the band gap due to π-bonding at the grain boundaries [2.91].

2.9.2 Boron-doped nanocrystalline diamond

NCD is difficult to dope: the dense lattice of single-crystal diamond, having the highest atomic concentration of $n_C = 1{,}763\times10^{23}$ atoms/cm^3, makes it inherently difficult to dope as other elements are not easily incorporated in a substitutional manner. In the presence of grain boundaries such as those found in NCD, it might be argued that doping would be even more difficult since impurity atoms may prefer to reside in the grain boundaries as opposed to taking up substitutional position within the restrictive volume of diamond lattice. Therefore, applications of NCD as a material for the fabrication of semiconducting devices are limited [2.92].

Only boron has been extensively used to successfully dope diamond. The electrical conductivity of a number of boron-doped NCD samples with different boron concentration was analysed by Borst and Weis [2.93] by carrying out Hall measurements. The characteristic of the films and the results are showed in table 2.10 and figure 2.24, respectively.

Sample	Fitted acceptor concentration (cm^-3)	Activation energy (eV)	Maximum Hall mobility (cm^2 V/s)
1	10^18	0.35	256
2	2×10^18	0.34	164
3	2×10^19	0.24	65
4	5×10^19	0.1	16
5	8×10^19	0.02	4
6	3×10^20	~ 0	4

Table 2.10: Fitted acceptor concentrations n_a, activation energies E_a and the maximum of the Hall mobility $\mu_{H,\,max}$ for six different Boron-doped homoepitaxial layers [2.93]

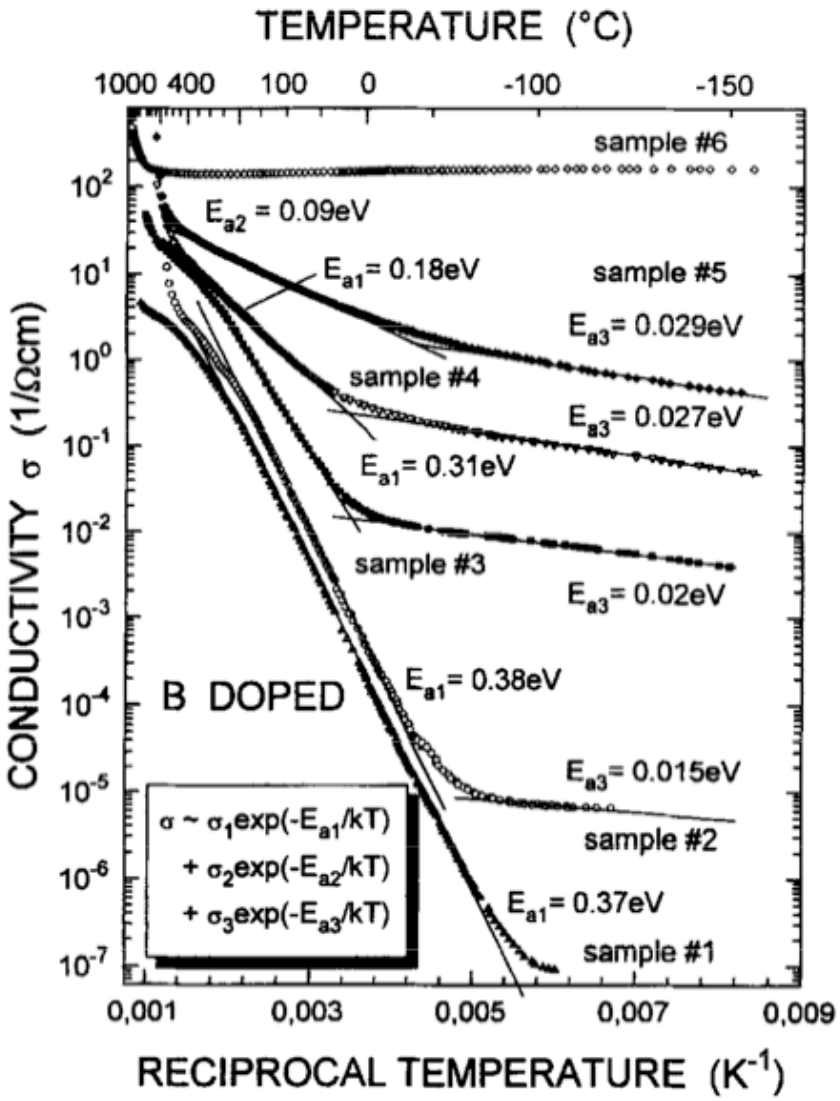

Figure 2.24: Measured electrical conductivity σ of eight different Boron-doped homoepitaxial Hall bar layers as a function of reciprocal temperature, plotted on a semi-logarithmic scale. The decomposition of the inset defines the activation energies of conductivity E_{a1}, E_{a2}, and E_{a3}. This relation was used for the fit represented by the solid curves. The Boron concentrations were determined by SIMS and are given in the inset [2.93]

The conduction of Boron-doped films follows the general relationship [2.94]:

$$\sigma = \sigma_1\text{^}(-E_{a1}/kT) + \sigma_2\text{^}(-E_{a2}/kT) + \sigma_3\text{^}(-E_{a3}/kT)$$

where E_{a1} is the activation energy due to the acceptor ionisation (valence band conduction), E_{a2} is an activation energy due to the motion of carriers over neutral acceptors and E_{a3} is an activation energy due to the transition of holes from occupied to unoccupied acceptor (hopping conduction).

As can be seen from figure 2.24, E_{a1} depends from the Boron concentration in the film. A possible explanation is the formation of an impurity band found in heavily doped synthetic

single crystals. The value of 0.35 eV for E_{a1} drops dramatically as the doping level exceeds 5×10^{18} cm^{-3}.

To date, most boron-doped NCD films that have been reported contain high levels of dopant such that they are near metallic in nature [2.93 – 2.95]. Moreover, Nesladek [2.96] reported 420 nm thick Boron-doped NCD films ($n_A = 1.54 \times 10^{21}$ cm^{-3}) becoming superconductive at a temperature of 1.66 K.

Whilst these films may be useful, for example, as conductive electrodes for electrochemical applications [2.97, 2.98], they cannot be used for active diamond electronic devices.

2.10 Nanodiamond

Several other diamond structures with critical sizes at the nanometric level were observed, which are referred to as “nanodiamond”.

Experimental evidence shows the existence of two major groups of nanodiamond structures. One group includes nanodiamond nuclei observed when conventional processes of micro- and macro-diamond growth were interrupted in their early stage; the purpose was to gain insight into the diamond nucleation process.

Another group includes nanodiamond structures that are the product of synthesis methods [2.99, 2.100], one of which is detonation.

Shenderova and co-authors [2.100] classified various forms of nanodiamond according to the dimensionality of the diamond constituents along with their synthesis condition, summarized in table 2.11(a) and 2.11(b).

Nanodiamond form	Typical size	Characteristics	Details of synthesis
0-Dimensional			
Isolated particles			
1. Formed in gas phase	1-450 nm	Abundant twin forms with star-like morphology	Low-P CVD microwave plasma flow reactor; mix of CH2Cl2
2. Presolar nano-diamond	0.2-10 nm	Twin microstructure similar to that of CVD growth from gas phase	majority of these structures formed by CVD-type process
3. Detonation nanodiamond (ultradispersed diamond-UDD)	2-10 nm	Mostly planar twin forms, presence of dislocations; different functional groups	Conversion of carbon-containing explosives into ND during detonation explosion. ND extracted after several purification steps
4. ND formed by shock wave compression of carbon onions	5-10 nm		50 Gpa pressure
ND nucleated on a surface			
1. Nucleation on Si	2-6 nm	Nucleates on a step	Bias assisted hot filament CVD of Ch4/H2 on Si
Formation by irradiation of carbon species			
1. ND nucleation from energetic species within amorphous carbon matrix on surface of Si	5-10 nm		Biased CVD plasma of CH4/H2 or direct ion beam deposition using hydrocarbons, H, Ar
2. ND within SiC at ion beam bombardment by C ions	2-5 nm	Epitaxial diamond grains formed at depth o150 nm in SiC	Bombardment by 60 keV C ions at 900 C
3. ND within graphite by ion irradiation	7.5 nm	Highly ordered single crystals; twinned crystals; multiply-twinned crystals	sheets of fine-grain polycrystalline graphite were bombarded at 20 C with 350 MeV Kr ions
4. e-beam conversion of carbon onions to ND	up to 100 nm		1.2 MeV electron irradiation at irradiation temperatures above 900 K

Table 2.11(a): Classification of diamond nanostructures according to their characteristic size and synthesis condition [2.100]

Nanodiamond form	Typical size	Characteristics	Details of synthesis
1-Dimensional			
1. Diamond nanorods	40-40 in diameter		Selective etching of CVD diamond films
2. Diamond filaments	sub- and micron dia., consist of UDD	Tangled networks of filaments	UDD assembly in colloids or laser ablation of UDD pellets
3-Dimensional			
1. Ultrananocrystalline diamond (UNCD), CVD grown films	2-5 nm grains	Compact, pure phase of diamond, sp2 grain boundaries, 2-4 Angstrom wide	Microwave activated plasma CVD using carbon/rare gas
2. Carbide derived carbon structured diamond films	5 nm	Wide variety of diamond polytypes; nanoporosity	Chlorination of SiC and metal carbides at 1000 C
3. Nanocomposite material from UDD bonded by pyrocarbon	4-5 nm	Diamond grains are bonded by a pyricarbon matrix 2-8 Angstrom thick	Nanodiamond powder placed in a container of a particulr shape had been bonded by pyrocarbon formed by means of Methane decomposition through the entire volume of diamond powder
4. Polycrystalline diamond powder synthesized by shock wave process	Bimodal size distribution: 1-4nm and 10-160 nm	Nanograins sinter to micron size particles	ND formed by shock wave compression of carbon materials (graphite, carbon black, etc.) mixed with metal powder - Du Pont' syntheis

Table 2.11(b): Classification of diamond nanostructures according to their characteristic size and synthesis condition [2.100]

One such material, often referred to as ‘detonation nanodiamond’ (DND), consists of polycrystalline diamond powder produced by shock synthesis. The shock waves generated from the detonation of suitable explosives create high pressure and high temperature in confined volumes for a sufficient time interval to achieve partial conversion of graphite into nanometer-sized diamond grains [2.100].

There are two main methods by which detonation synthesis is employed to produce nanodiamond grains. The first method consists in detonating a mixture of carbon-containing material together with explosives. Diamond formation occurs both within the carbon-containing particles and by condensation of carbon atoms of the explosives. Detonation is performed either in air or in inert atmosphere relative to the product of synthesis [2.101]. Nanodiamond grains synthesised in inert atmosphere consist of a diamond cubic phase of no more than 20 nm in size, whereas nanodiamond grains synthesized in air are about 8nm. In both cases the size of the grains formed are comparable to the particle sizes of the precursor carbon material. After purification, the nanodiamond particles are typically utilized in polishing applications [2.101].

In the second method no carbon-containing material is used and therefore diamond clusters are formed exclusively from carbon atoms contained in the explosive material (figure 2.25).

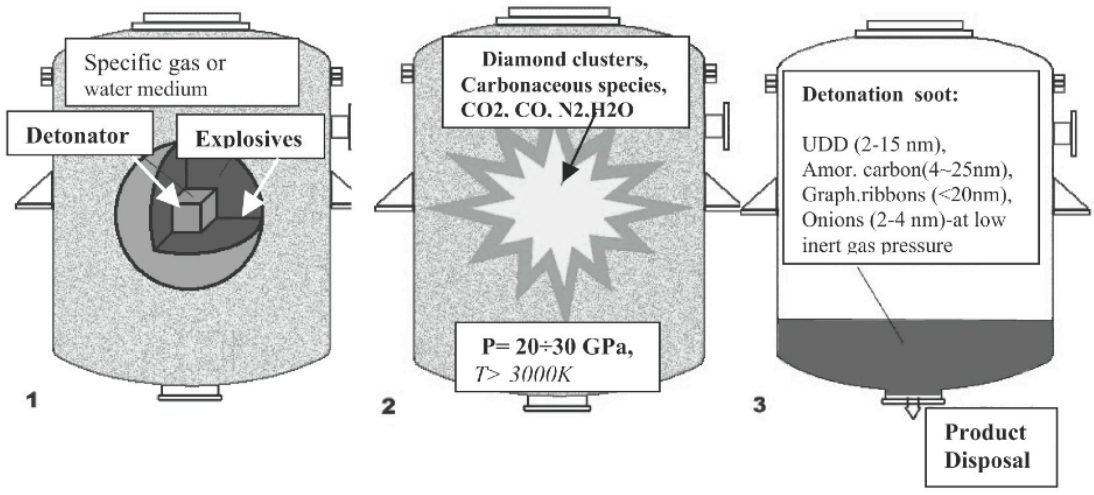

Figure 2.25: Schematic illustration of the synthesis of nanodiamond from carbon-containing explosives [2.100].

The typical mixture of explosive consists of TNT (2-methyl-1,3,5-trinitrobenzene) and hexogen in a 60/40 to 70/30 proportion [2.101]. Detonation can occur in inert atmosphere (N_2, CO_2, Ar, referred to as 'dry'), water or ice (referred to as 'wet').

When detonation occurs, the initial shock compresses the explosive material of the mixture causing it to heat and chemically decompose, releasing a large amount of energy in a fraction of a microsecond (figure 2.26, 2.27). Temperatures between 3000 and 4000 K and pressures between 20 and 30 GPa propagate through the material; such temperature and pressure values lie in the region of thermal stability of the diamond in the phase diagram of carbon (figure 2.26), and this is what accounts for the formation of diamond crystals directly from the carbon of explosives in the course of the explosion [2.101].

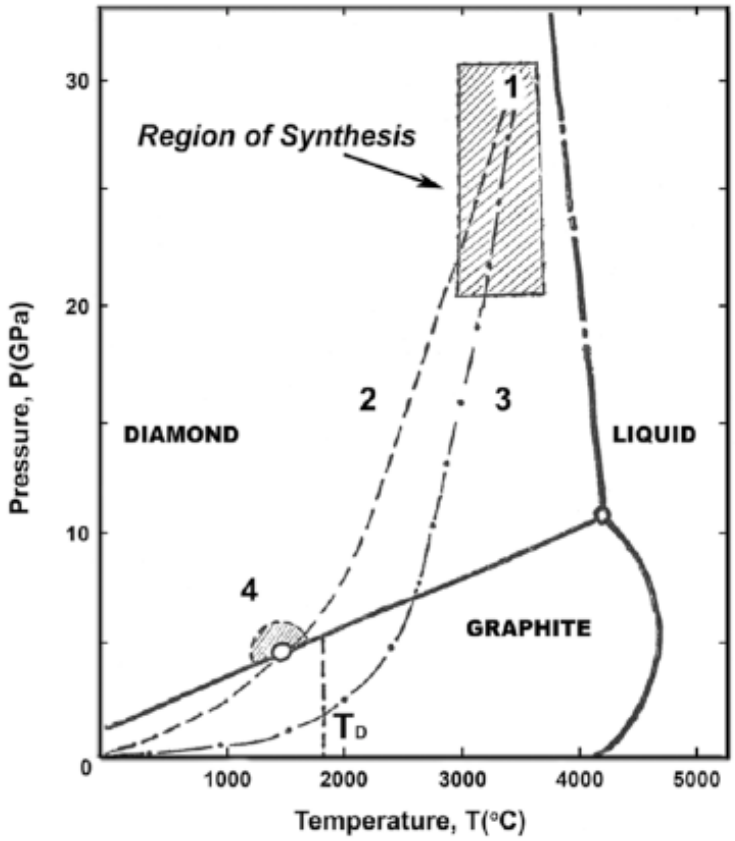

Figure 2.26: P-T phase diagram for carbon showing the regions for nanodiamond syntheses. P-T conditions for detonation synthesis and kinetics of cooling of detonation products (1) are shown for wet (2) and dry (3) synthesis [2.101]

It is important to highlight that the detonation of the explosive mixture occurs in a non-oxidising environment. The mixture has a negative oxygen balance, that is, the oxygen content is lower than the stoichiometric value so that 'excess' carbon is present in the system. This condition is fundamental for the formation of nanodiamond grains [2.100, 2.101].

The kinetics of the process represents the dominant factor responsible for crystallisation. Following detonation, temperature and pressure drop rapidly and fall within a region where diamond is thermodynamically unstable and the diamond-graphite reverse-transition can occur. However the higher the cooling rate, the lower is the time the products of detonation synthesis spend in the region of thermodynamic instability [2.101]. As a consequence, the sp^2/sp^3 ratio within the nanodiamond can vary along with the cooling rate, affecting greatly its properties.

The nanodiamond grains contain impurities that can be divided into four groups: (1) water-soluble ionized species, (2) chemically bonded to diamond surface, such as salt forms of functional surface groups, (3) water insoluble (metals, oxides, carbides, salts), and (4) incorporated into the diamond lattice and encapsulated. By using methods of purification it is possible to eliminate 40 to 95% of impurities belonging to the first three groups, whereas it is not possible to remove the fourth group impurities by chemical methods. Acid purification at high temperatures is largely utilized as it is very efficient with the removal of all impurities of the first three groups. For this purpose, nitric acid is mainly used; the reaction with detonation forms intermediates containing alcohol and ketone groups, which are always left on the surface of the particles:

$$C + HNO_3 \rightarrow C–O–NO_2 + H_2O \rightarrow C–OH + \text{oxidation} \rightarrow C=O \quad [2.101]$$

Addition of water is necessary to eliminate the acidic media. Nanodiamond powders consist of different form of carbon (80 to 89%, 90% to 97% of which being a mix of diamond and 3% to 10% non-diamond carbon), nitrogen (2% to 3%), hydrogen (0.5% to 1.5%), oxygen (up to 10%) and incombustible residue (0.5% to 8%) [2.100].

The primary ultra-disperse diamond particles, assumed here to be spherical for simplicity, have a diameter of approximately 4 nm. However, as it can be seen from figure 2.27 and 2.28, the diamond product of detonation synthesis shows a glutinous structure. To minimise surface energy, the primary ultra-disperse particles coalesce to form larger clusters of 20 to 30 nm in diameter. The strength of such aggregates was found to be surprisingly high [2.102] and impossible to break by means of ultrasound processing [2.101]. Only by applying a technique called stirred-media milling were Osawa and co-authors able to obtain a suspension consisting of primary 4 nm grains [2.101, 2.102]. Clusters of primary grains form, in turn, larger weakly bonded aggregates of the order of one micron [2.100]. It is likely that the aggregate structure includes bucky diamond particles to form a composite assembly (schematically showed in figure 2.29) containing

diamond particles with a more or less pronounced graphitic shell, soot structures and also graphitic ribbon-like structures. The graph in figure 2.30 summarizes the process of agglutination of nanodiamond particles. Properties of the collective aggregates are reported in table 2.12.

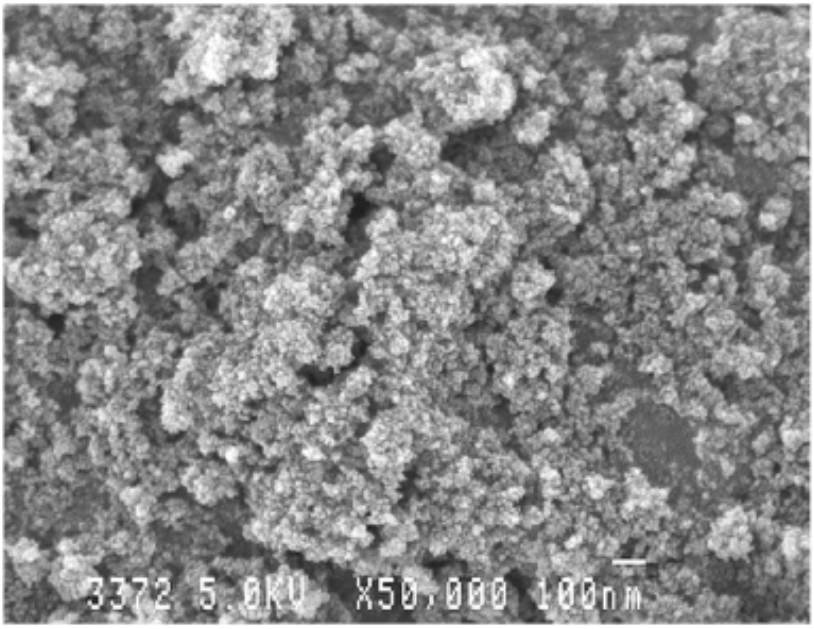

Figure 2.27: SEM micrograph of detonation nanodiamond, in which glutinous structure is evident [2.101]

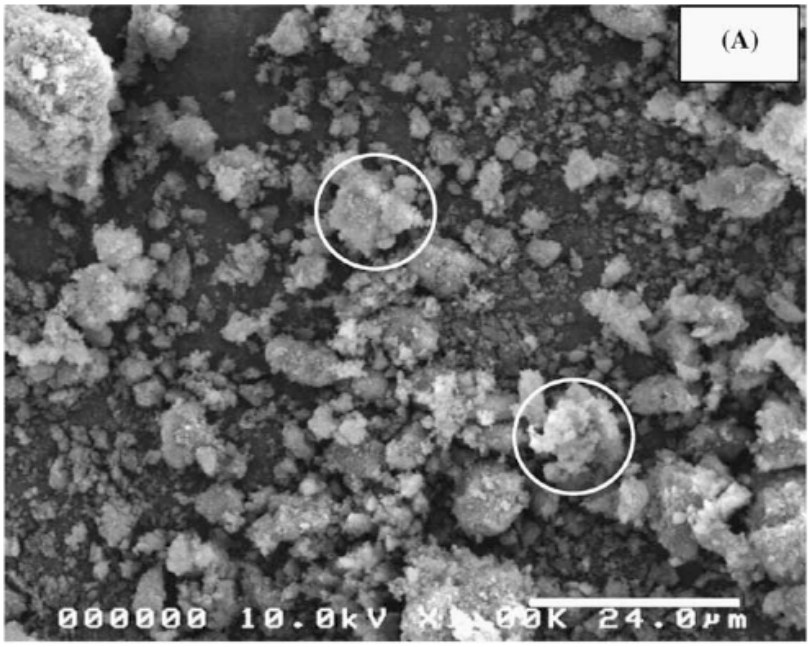

Figure 2.28: SEM micrograph of detonation nanodiamond. The white circles indicate typical aggregation [2.102]

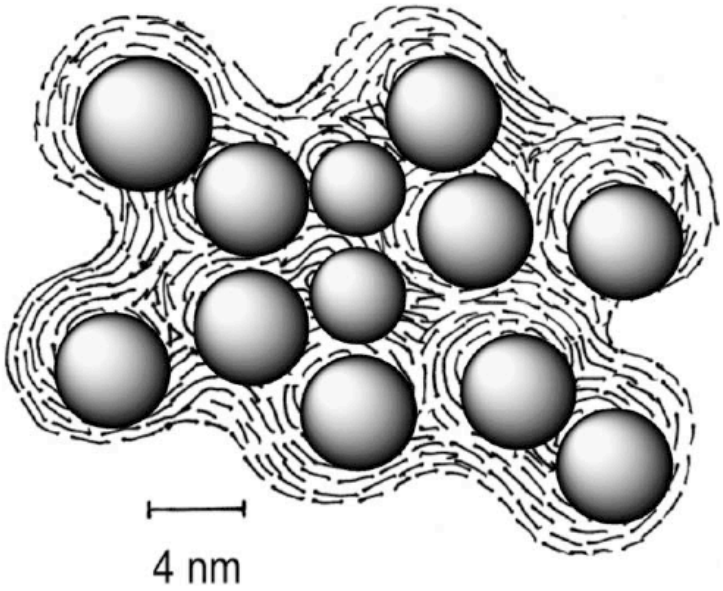

Figure 2.29: Simplified model of core aggregate in nanodiamond. Primary particles are represented by spheres embedded in the aggregate structure of soot [2.102]

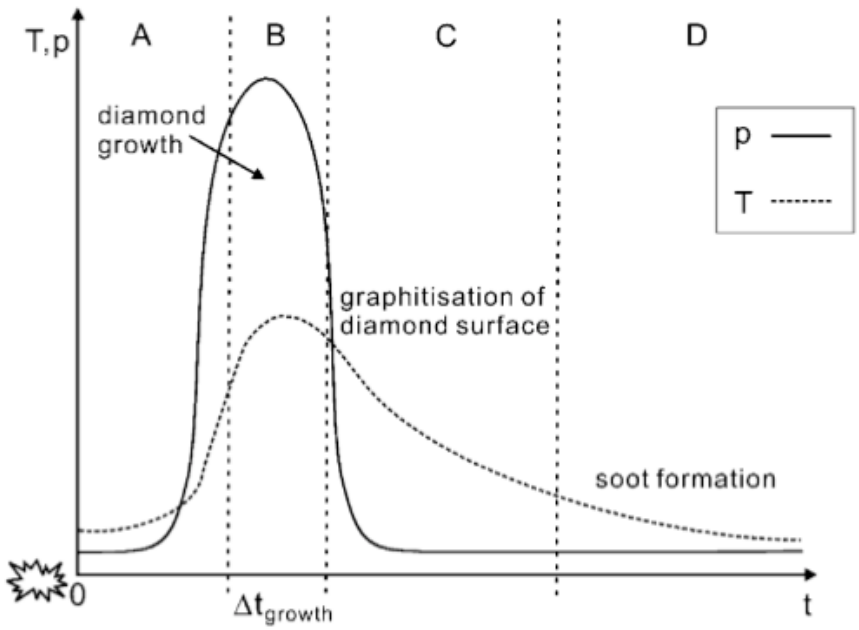

Figure 2.30: Events taking place after detonation of the explosive mixture [2.102]

Structure	Cubic (a=0.3573 nm)
Density	3.30 g/cm^3
Particle size	2-20 nm
Average monocrystal size	4.3 nm
Size of uncrushable aggregates	20-50 nm
Specific surface area	300-400 m^2/g
Pore volume in powder	0.3-1 sm^3/g
Density of dislocation	1.8×10^17
Composition (%)	C (93.2-100); O (0-6.8)
Initial air oxidation temperature (depends on purity)	430 C
Initial vacuum graphitization temperature	1100-1200 C
Resistivity	7.7×10^9 Ωm
Refractive index	~ 2.55 (at λ=580 nm)

Table 2.12: Properties of agglomerated ultradisperse detonation nanodiamond [2.100]

A recent study conducted by Panich and co-authors [2.103] provided similar information confirming the fractal structure of detonation nanodiamond discussed above, also reconciling with theoretical models [2.104]. According to Panich and co-authors [2.103], nanodiamond structures consist of three parts: the central core (primary particles) made up of sp^3-hybridized carbon, a fullerene-like shell of sp^2 carbon partially covering the core particles, which are, in turn, bound by hydrogen and oxygen atoms and give rise to functional groups that saturate the dangling bonds.

Stumm and Drubold [2.105] investigated the optical absorption of amorphous diamond-like films, showing that a decrease in the sp^2 fraction should bring about an increase in the bandgap optical width. In other reports [2.106 – 2.108] it was shown that the value of absorbance of nanodiamond layers deposited from an aqueous suspension exceeded by several orders of magnitude those of diamond single-crystal in the same spectral range. Therefore, the strong absorption found by Stumm and Drabold provides more evidence to the nanodiamond model discussed above.

On the other hand, in the study of Alam and Belobrov [2.109] on nanodiamond no sp^2 carbon was detected. The authors concluded that only 30% of bonds on nanodiamond are nondistorded sp^3 bonds and the remaining 70% are distorted but still with sp^3 hybridization.

2.11 Applications of diamond

The microstructure, mechanical and electrical properties of diamond films offer many opportunities for applications in areas such as tribology, electro-emitting cold cathodes, microelectromechanical systems (MEMS), surface acoustic wave devices (SAW), electrochemical electrodes, and conformal coatings.

As potential applications of CVD diamond are continuously discovered, it may be expected that the ultimate economic impact of this emerging technology on space and commercial areas outstrip that of high-temperature superconductors with more immediate applications [2.110].

Possible areas for the utilization of diamond thin films are listed in table 2.13.

Function	Field of application	Feature	Impact to industries
High Temperature semi-conductor	♦ Automobile & aircraft engines ♦ Household appliances	Heat resistant	♦ High reliability above 100°C
High frequency power transistor	♦ Microwave wireless LAN ♦ High speed transistor ♦ High speed data processing	High breakdown field, High carrier mobility, High saturation velocity	♦ GHz band microwave amplification
High voltage transistor	♦ Electric power control	High breakdown field	♦ Smaller equipment
Electron emission	♦ Flat panel display	Negative electron affinity	♦ Displays of low energy consumption
Light emission	♦ Light emission and laser of blue & UV ♦ White luminescence ♦ Light source for printer	Wide band gap	♦ Ultra capacity photo recording, light source for medical inspection ♦ Large-size display ♦ Compact printer
Radiation sensing	♦ Digital X-ray image recording ♦ Nuclear reactor control	Radiation hard	♦ Medical application of X-ray ♦ Maintenance of nuclear power plant
Light detection	♦ Fire flame detection ♦ UV monitoring	Wide band gap	♦ Detection of accidents ♦ Environment measurement
Pressure sensing	♦ High sensitive distortion/pressure sensor at high temperature	High piezoresistivity, heat resistant	♦ High sensitivity monitoring
Temperature measurement	♦ High sensitive radiation detector	Wide band gap	♦ Optimal combustion control of automobile engines ♦ Maintenance of nuclear plant
IR window	♦ IR window	High transparency	♦ environment measurement
Thermal propagation	♦ Heat sink	High thermal conductivity	♦ High reliable microwave module

Table 2.13: Industrial applications of CVD diamond films [2.111]

2.11.1 Deep ultra-violet light photodetectors

As seen above, diamond's electrical properties make it an ideal material for deep UV detection. However, since diamond is not naturally available in large quantities, devices will have to be manufactured out of artificial diamond, whose photoconductive properties need to be outstanding. There have been previous attempts at manufacturing diamond photodetectors that are sensitive to deep UV radiation. Landstrass and co-workers [2.112] investigated homoepitaxial single crystal layers grown by chemical vapour deposition (CVD) methods onto natural diamond substrates. The insulating properties of diamond suggest that simple photoconductive devices can be constructed, which will display low dark currents without the need for reverse-biased p-n junctions. Devices with an interdigitated planar electrode configuration (35 μm gaps, 10 μm electrode widths) illuminated with 6.1 eV pulsed laser were used to determine that photoconductive mobilities as high as 3500 cm^2 / Vs could be measured in the epitaxial layer, comparable to the best type IIa natural gemstones (figure 2.31 and 2.32). The carrier lifetimes of 220 ps are only marginally lower than typical. No spectral response measurements were reported in this case.

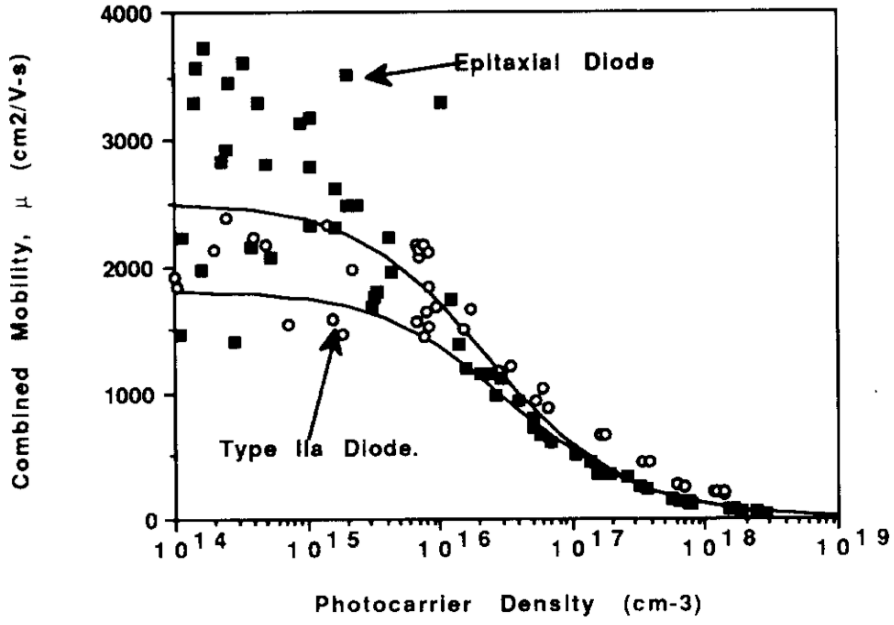

Figure 2.31: Photoconductivity mobility vs. carrier density as adjusted by modulating the UV light intensity of a 6.1 eV pulsed laser [2.112]

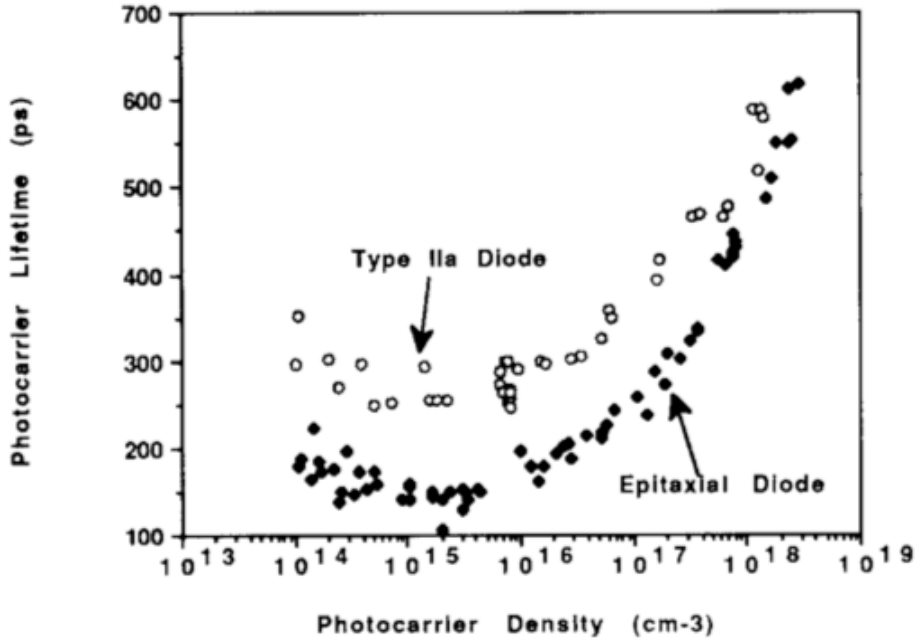

Figure 2.32: Epitaxial diamond and natural diamond photoconductor diode lifetime vs. carrier density as adjusted by modulating the UV light intensity of a 6.1 eV pulsed laser [2.112]

More recently, Liao and Koide [2.113] fabricated photoconductive devices using an interdigitated planar metal-semiconductor-metal (MSM) structure on epitaxial layers grown by CVD on an HPHT type Ib substrate (10 μm spacing, 10 μm electrodes).

The authors compared the performance of an 'as-fabricated' device (MSM-PD) and of a similar device after anneal at 600°C in an argon environment. Time-resolved response was obtained using an ArF excimer laser with a wavelength of 193 nm and a pulse width of 10 ns.

When tested under a bias of 20 V, both devices show the highest sensitivity at 210 nm, with a discrimination of five orders of magnitude in the case of the as-fabricated device and nearly eight in the case of the annealed device. A weak photo-response at wavelengths larger than 500 nm was also observed.

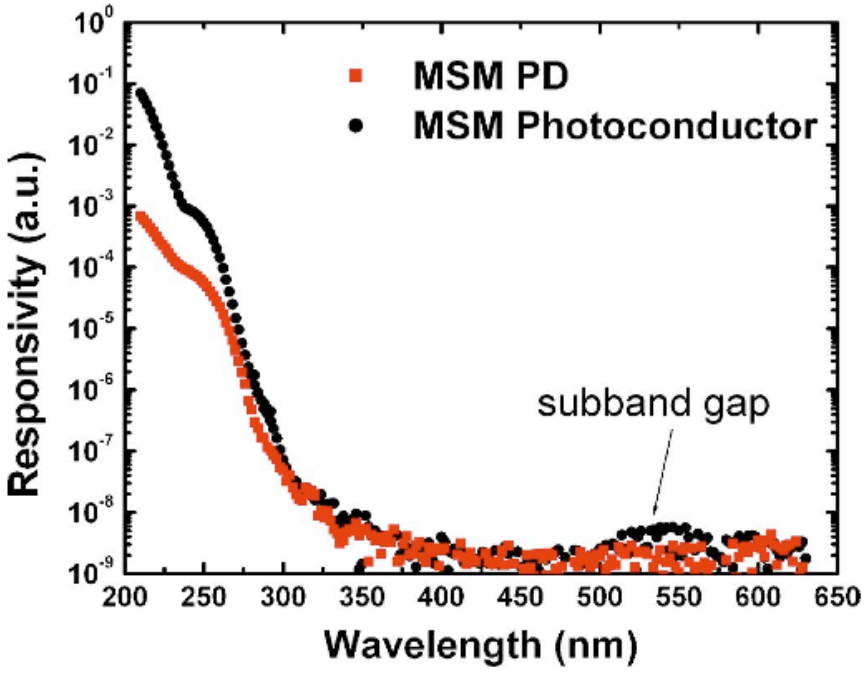

Figure 2.33: Spectral photoresponses measured from the MSM-PD and the photoconductor. The spectra are normalized by the photon flux [2.113]

Excellent spectral resolution was achieved as devices were tested under a bias of 3 V, being 10^8 between deep UV (220 nm) with a responsivity of around 6 A/W, indicating a Gain of 33, assuming the external quantum efficiency is unity.

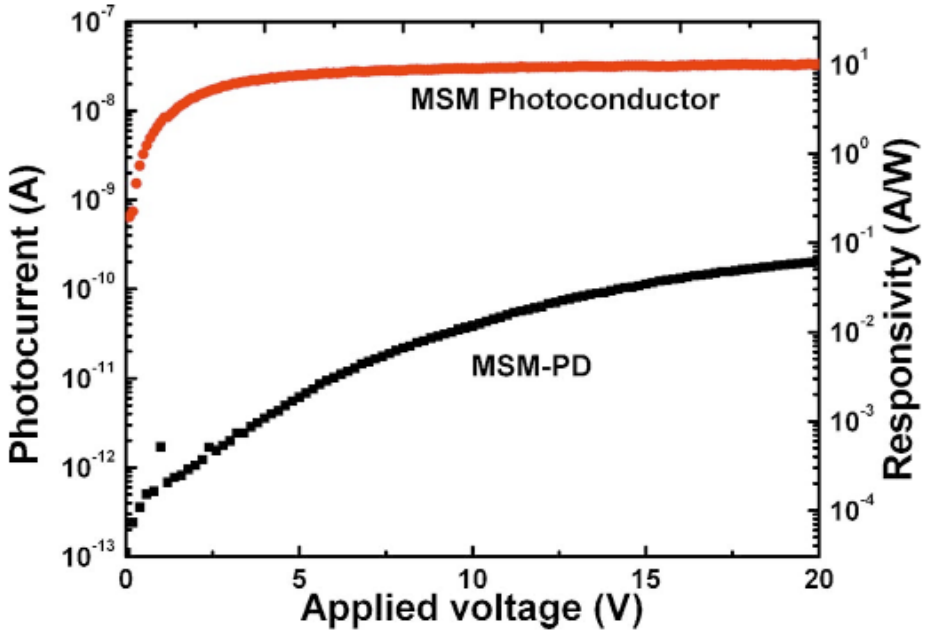

Figure 2.34: Current-voltage characteristics of the photoconductor in comparison with a typical MSM-PD during 220 nm illumination [2.113]

In terms of the realisation of a commercially useful device, polycrystalline CVD grown diamond films (PCD) have been investigated by McKeag *et al* [2.114] using an interdigitated planar MSM configuration with 20 μm gaps, a dimension that is closely related to the grain size of the material in that plane, chosen in order to minimize the deleterious effects of grain boundaries within the polycrystalline material. Electrodes were 20 μm thick in order to ensure a satisfactory photo-collection area.

The authors compared the performance of an as-fabricated device to a similar device subjected to a series of anneal steps first in methane then in air with the aim of passivating the device surface. Devices were exposed to monochromatic light, whose source was a 150 W Xenon lamp.

Whilst the defective polycrystalline diamond meant that 'as-fabricated' photoconductive structures performed poorly, the use of post-growth defect passivation treatments dramatically improved device performance. Discrimination between deep UV light (220 nm) and visible wavelengths exceeded a factor of 10^6, ultra-low dark currents were observed and a deep UV sensitivity of around 0.6 A/W was reported (figure 2.35).

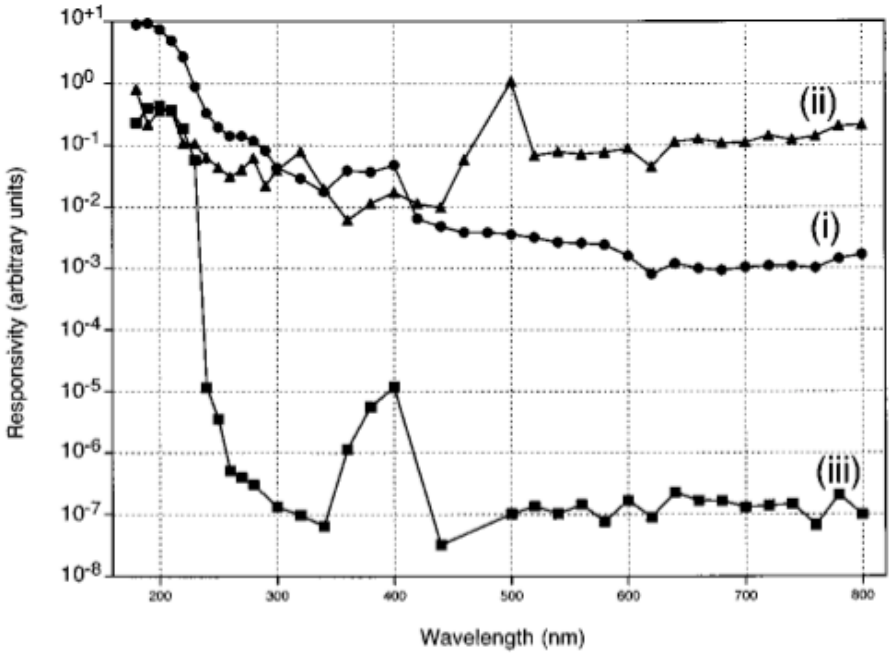

Figure 2.35: Spectral responsitivity of photoconductive device (i) as-fabricated, (ii) following methane annealing, and (iii) after methane and air annealing [2.114]

Similar performance levels with PCD without the use of similar defect passivation treatments were not achieved; Binari and co-authors [2.115] produced a metal-semiconductor-metal (MSM) UV photodetector made of type IIa natural diamond, type Ib synthetic diamond and polycrystalline diamond. The MSM structure consisted of two 500

nm thick, 2.5 mm long and 0.3 mm wide evaporated Aluminium stripes. The separation between the stripes was 0.35 mm. For wavelengths from 130 to 230 nm, a vacuum ultraviolet system comprising of a 150 W Deuterium lamp and two monochromators with an adjustable bandpass filter and a CsTe photocathode was used. In the 200-700 nm wavelength range a 500 W Hg/Xe lamp, 10-25 nm bandpass filter and a calibrated Si photodetector were used. Devices were tested under a 100 V bias (figure 2.36).

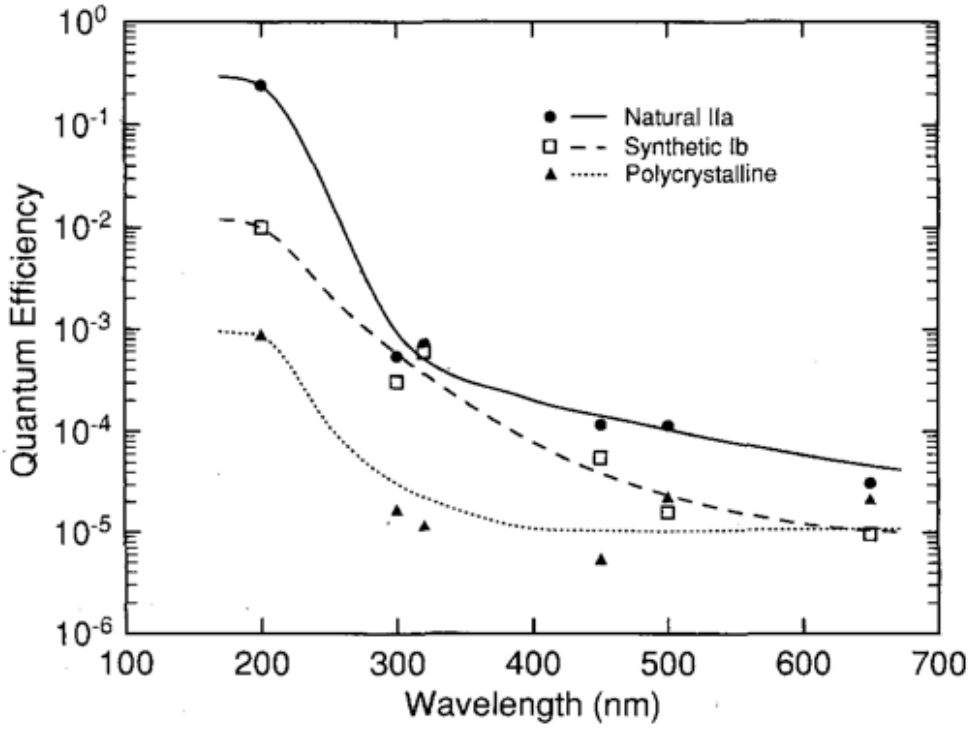

Figure 2.36: Quantum efficiencies of MSM detectors fabricated in type IIa natural diamond, type Ib synthetic diamond, and polycrystalline diamond tested under a bias of 100 V [2.115]

At a wavelength of 200 nm, the quantum efficiency for the polycrystalline device remains at 0.09%. The authors do not mention any anneal treatment given to the substrate before or after the deposition of the metal electrodes.

Polyakov and co-authors [2.116] investigated the photoresponse of planar detectors fabricated from freestanding polycrystalline films. Devices consisted of an interdigitated array of 20-50 μm Nickel contacts with 20-50 μm spacing. The performance of as-fabricated devices was compared to similar devices that were annealed in air at 450°C for 30 minutes before the deposition of the metal electrodes. Devices were tested in the wavelength range of 200-700 nm under a bias voltage of 9 V (Figure 2.37).

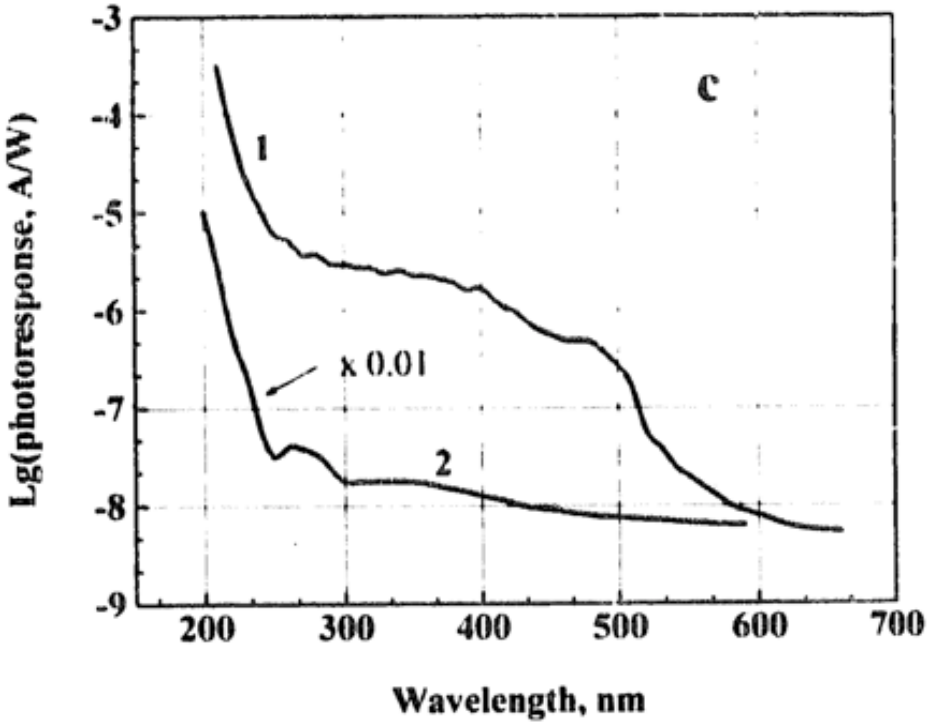

Figure 2.37: Photoresponse of the planar (1) and sandwich (2) photoconductive UV detectors (both biased at 9 V) plotted as function of illumination wavelength [2.116]

Devices showed a low dark current < 10 pA and a high spectral discrimination, a 10^4 higher response to 200 nm than to visible (600 nm) wavelength. According to the authors, annealing in air decreased the defect density within the polycrystalline diamond substrates by more than an order of magnitude and strongly increased the spectral discrimination of the planar detectors. The results obtained by these devices remains of a lower standard compared to the work of McKeag as discussed above.

In the work of Leveufre and co-authors [2.117], planar photoconductive devices were fabricated from 200 μm thick polycrystalline diamond films, which were subsequently cleaned by a thermal and a chemical treatment to remove the surface conductive layer caused by hydrogen-terminated bonds and graphitic components. The treatment consisted of anneal at 500°C in air atmosphere for 1 hour followed by immersion in a sulfochromic solution for 10 minutes and rinsed in a solution of aqua regia for 5 minutes.

Devices consisted of Ti/Au electrodes (100 μm thick), separated by a 200 μm distance. Good ohmic contacts were thus realised and tested by IV measurement.

Photodetectors were tested using over-gap (193 nm and 213 nm) as well as sub-gap (266 nm) nanosecond laser irradiation (figure 2.38).

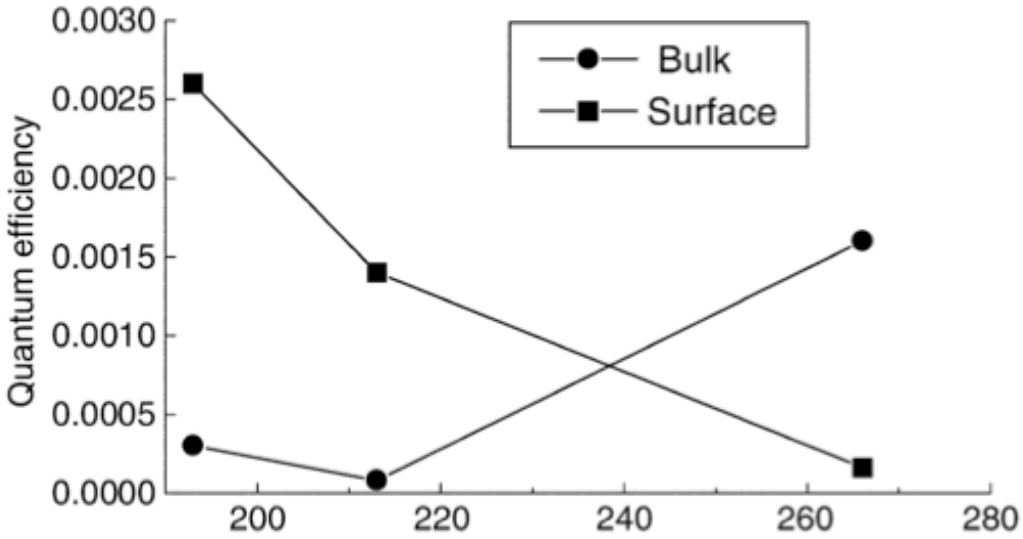

Figure 2.38: Comparison of quantum efficiency of surface and BCs as a function of laser wavelengths (193, 213 and 266 nm) for a field of 10 kV/cm [2.117]

A quantum efficiency of approximately 0.0026 was obtained during the 193 nm irradiation, in contrast with irradiation at 213 nm and 266 nm, which is lower. The results are consistent with those analyzed before, despite not being as successful as the work of McKeag.

McKeag presented further enhancements in the use of defect passivation treatments [2.118]. On this occasion, the authors fabricated planar photoconductive devices consisting in interdigitated electrodes with a 40 μm pitch, and approximately 20 μm spacing. Three different kinds of polycrystalline diamond substrates were used: type I, 280 μm thick with 40-60 μm grain size; type II, 110 μm thick with 20-40 μm grain size; type III, 70 μm thick with 10-30 μm grain size. Following fabrication, the devices were given heat treatments in Methane ambient followed by treatment in air, the same treatment that the authors had used in their work discussed previously. The photoresponse of the devices was recorded at bias between 1 V and 50 V. External quantum efficiencies as high as 10^5 were obtained (figure 2.39).

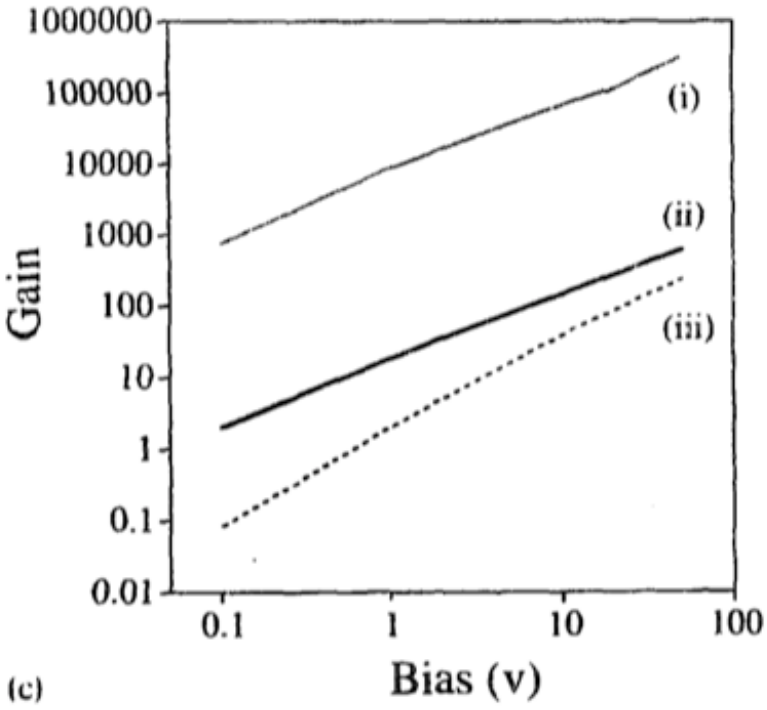

Figure 2.39: Photoconductive gain (external quantum efficiency) plotted as a function of bias level for devices fabricated from sample types I-III [2.118]

Carrying on further the work of McKeag, Lansley and co-authors [2.119], photodetector devices consisting of interdigitated metal layers on 100 μm thick polycrystalline diamond films, with grains between 20 μm and 40 μm were fabricated. After fabrication, multiple 1-hour-long Methane treatments (700°C) were carried out followed by a 1-hour-long air treatment (400°C). Spectral response (bias level: 10 V) for a range of devices that had received between one and nine methane-air treatments were recorded (figure 2.40).

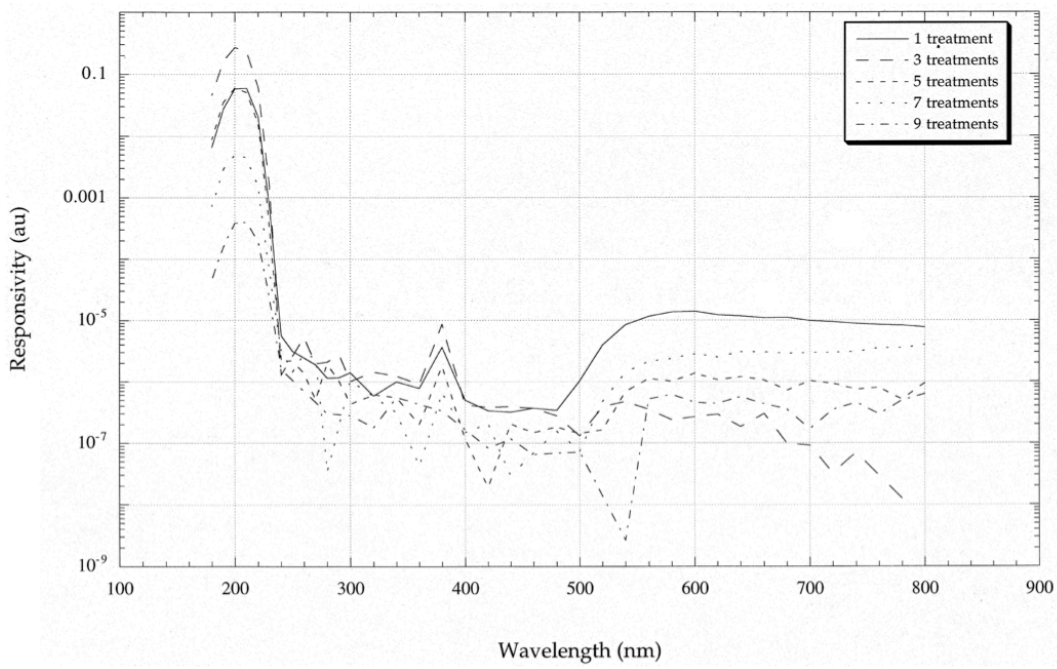

Figure 2.40: Responsitivity plotted against illumination wavelength for devices that had received between one and nine Methane-Air treatments [2.119]

The responsivity of all devices is dramatically higher at wavelengths shorter than the band-gap edge (225 nm). Devices that did not undergo the methane-air heat treatment did not display the sharp cut off in responsivity at wavelengths lower than 225 nm. The highest responsitivity is recorded with devices that underwent three heat treatments; this number gives also the lowest visible light response level.

The authors also investigated the speed of the response of these devices. In the case of the single treatment device, the turn off period is tens of seconds; devices that received five treatments showed their turn-off period to be less than 1 ms. Devices that received between 1 and 5 heat treatments displayed turn-off speed in between these two extremes. Devices that had been treated more than five times showed no further increase in the turn-off speed. Devices that underwent five treatments were then illuminated with a 193 nm laser pulses at 100 Hz (figure 2.41).

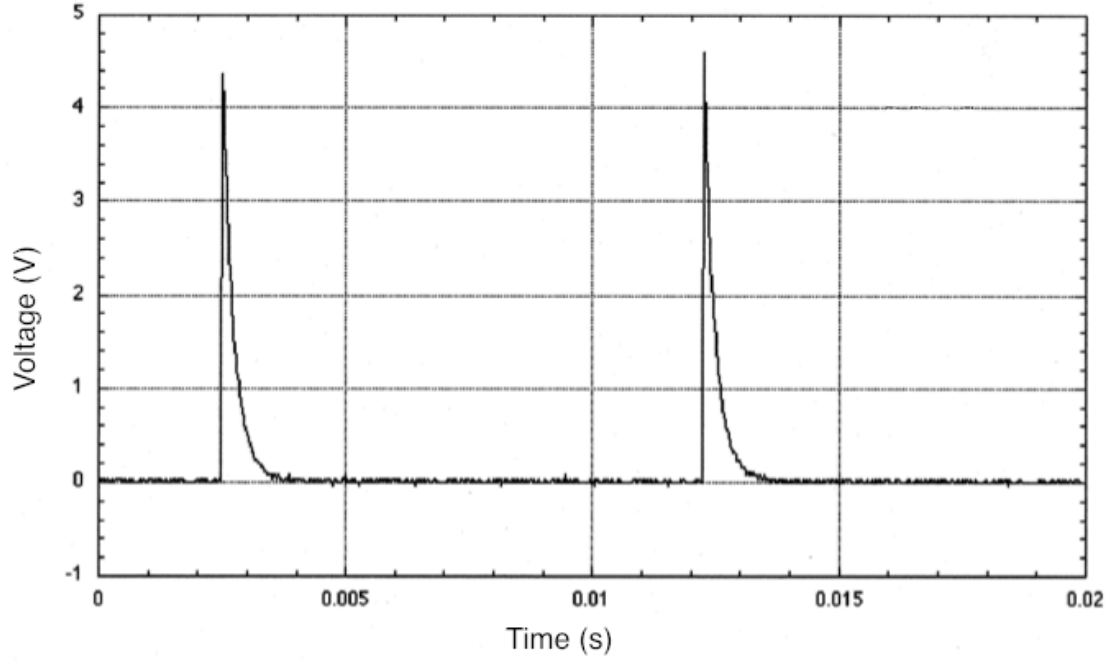

Figure 2.41: Operation of the device with 100 Hz excimer laser radiation pulse frequency [2.119]

It is possible to estimate from the space between the peaks that the device could be operated, fully turning off after each pulse, at 1 kHz, a frequency that is required for state-of-the-art excimer laser applications at this wavelength.

Single crystal diamond (SCD) grown by CVD methods has recently become a commercially available material. Element Six has managed to produce high quality CVD single crystal diamond for electrochemical, optical, thermal and mechanical applications, which include high power lasers, water jet cutting equipment and electrochemistry instruments. Research is aimed at finding further potential applications in the high-energy physics field, high frequency electronics, radiation detection and sensing applications [2.120].

The availability of such outstanding material together with the knowledge of previous successful work discussed above with the use of polycrystalline diamond for deep UV photodection, contributed in awakening interest in the use of CVD single crystal diamond for the fabrication of UV photodetectors. HPHT single crystal diamond has been extensively used to fabricate UV photoconductive devices. The work of Balducci and co-authors [2.121, 2.122] reports on planar photoconductive devices realised using homo-epitaxial 150 μm thick diamond films grown on a low cost (100) HPHT diamond substrate. The devices consisted of interdigitated Aluminium non-ohmic contacts with a 20 μm inter-electrode distance. Prior to electrode deposition, diamond substrates were annealed in air at

500°C in order to oxidize the surface and remove the surface hydrogen conductive layer present in the as-grown material. Devices, tested under a bias of 100 V, showed a good performance when exposed to laser radiation within the 210-1200 nm wavelength range. Four orders of magnitude variation was measured when moving across the band gap wavelength of 225 nm. Such a drop increased by up to six orders of magnitude when the UV to visible rejection ratio is considered.

External quantum efficiency (EQE) values, measured at 220 nm for different bias voltages, remained lower than 0.25.

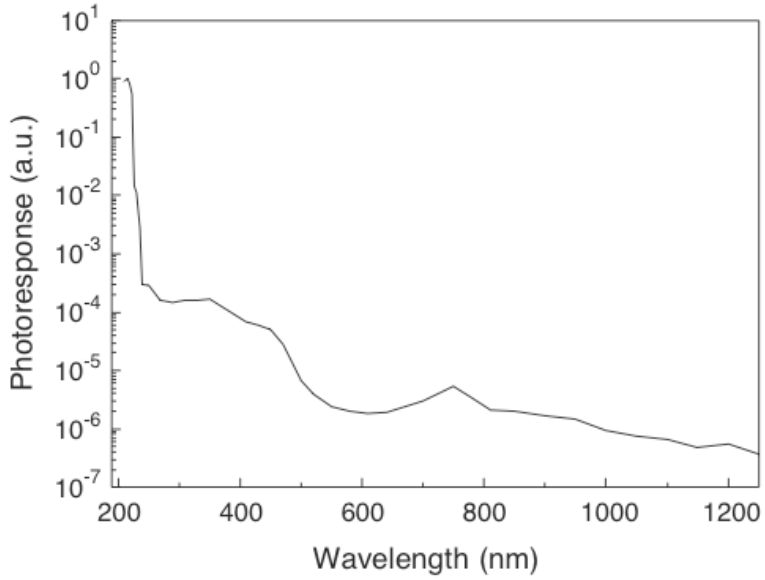

Figure 2.42: Normalized responsitivity as a function of the incident laser radiation wavelength, under a bias of 100 V [2.121, 2.122]

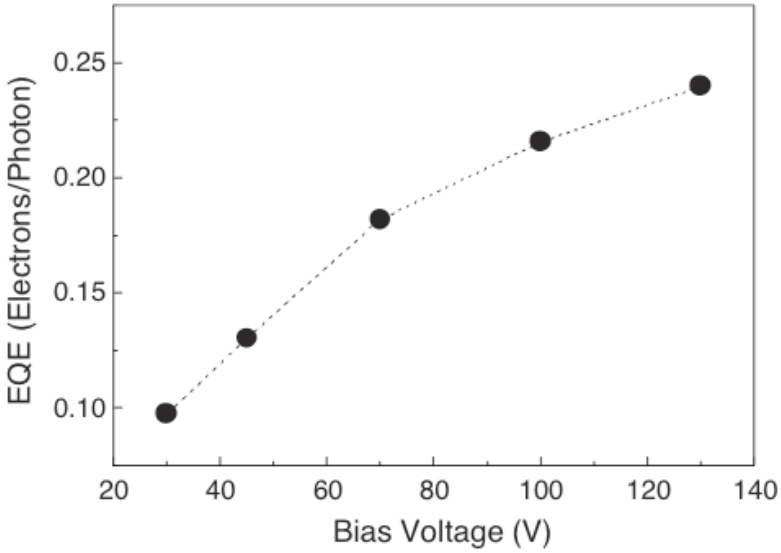

Figure 2.43: External quantum efficiency (EQE) as a function of the bias voltage for a fixed wavelength of 220 nm [2.121, 2.122]

Teraji and co-authors [2.123] used undoped homoepitaxial diamond (100) films grown on mechanically polished HPHT substrates. Titanium films capped with Gold were deposited on the 20 μm thick diamond to give a planar device comprising interdigitated electrodes. Three electrode patterns with different spacings of 20 μm (photodetector P1), 50 μm (photodetector P2) and 100 μm (photodetector P3) were used. Photocurrents were measured under the bias voltage of up to 7 V. The best result was obtained when the spectral photo response of the P2 device was measured (monochromatic light from a Xenon lamp was used). Photo responsitivity at 400 nm visible light was found to be at least four orders of magnitude smaller than for 220 nm UV light.

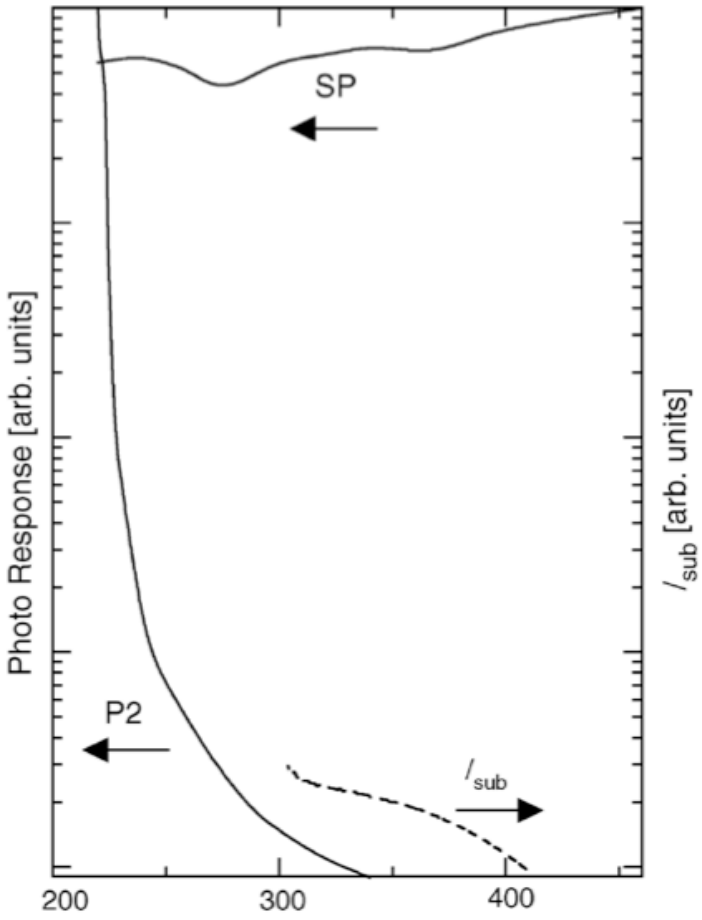

Figure 2.44: Spectral response of the DBP P2 and silicon photodetector (SP) in the wavelength range between 220 and 470 nm. Bias voltage was 7 V for the P2 and 5 V for the SP [2.123]

The work of Brescia and co-authors [2.124] reports on photodection devices built with single-crystal homoepitaxial CVD diamond films (4 μm-thick) grown on a HPHT (001) Ib-type diamond substrate. Due to the small size of the homoepitaxial sample (2.5×2.5 mm^2), the planar photoconductive device consisted simply of a 1 mm Gold disk with an open 40 μm gap along the diameter. To analyse the sensitivity of the device as a function of the

wavelength, current measurements were carried out under calibrated illumination transients. The device was tested under a field intensity of 5 V/μm and 1 V/μm. The highest EQE obtained exceeded 100 but the same device displayed a non-optimal solar blindness (figure 2.45).

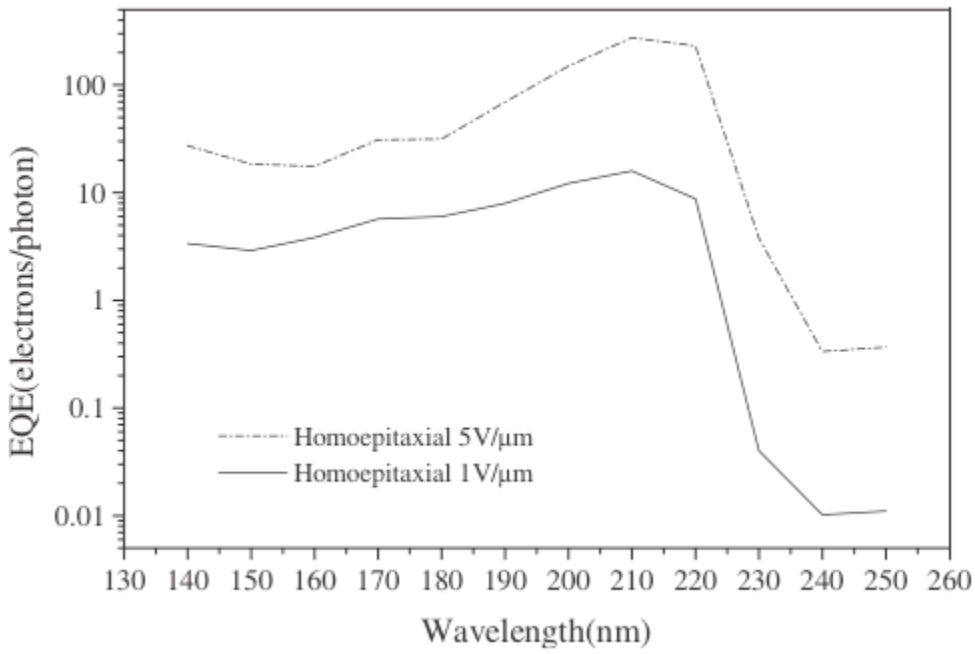

Figure 2.45: External quantum efficiency of the homoepitaxial photoconductor at two different electric fields [2.124]

Iwakaji and co-authors [2.128] fabricated UV stack-type detectors (figure 2.46) using high-quality Boron-doped homoepitaxial diamond layers that were sequentially grown on a HPHT type-Ib (100) substrate. In order to form contacts to the Boron-doped layer, a small area of the top undoped layer was completely etched out. A diamond dip structure was fabricated in the top undoped layer with a patterned Platinum plasma coplanar mask by means of Oxygen ECR. The width of each coplanar mask strip was 5 μm and the gap between two adjacent strips was 10 μm. 100 nm thick Ti electrodes and 100 nm thick TiN caps were deposited on the diamond surface as Ohmic contacts to the boron-doped layer.

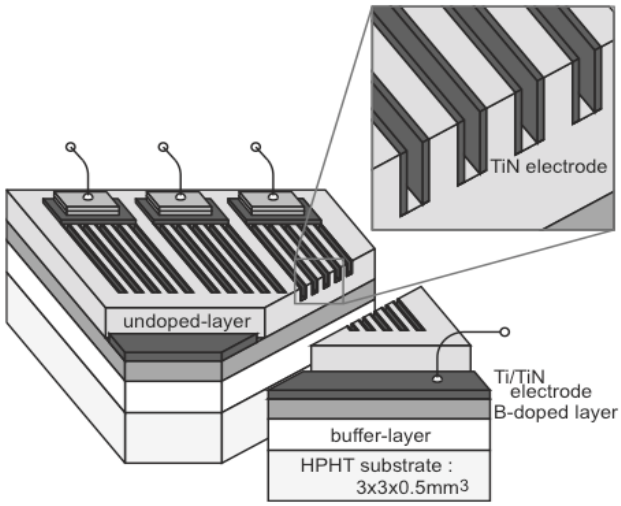

Figure 2.46: Schematic diagram of the stacked-structure detector fabricated by Iwakaji and co-authors. The film thicknesses of buffer, Boron-doped, and top undoped layers are approximately 16, 9 and 48 μm, respectively [2.125]

The performance of the photodetectors was studied for UV light monochromatized from a 150 W Deuterium lamp in the wavelength region from 190 to 550 nm. The photoresponse spectrum of the detector was taken at a bias of 30 V. This detector yielded a high responsivity of 325 mA/W at wavelengths around 210 nm and had a cut-off wavelength of 225 nm and the out-of-band rejection (at 210-240 nm) of more than four orders of magnitude (figure 2.47).

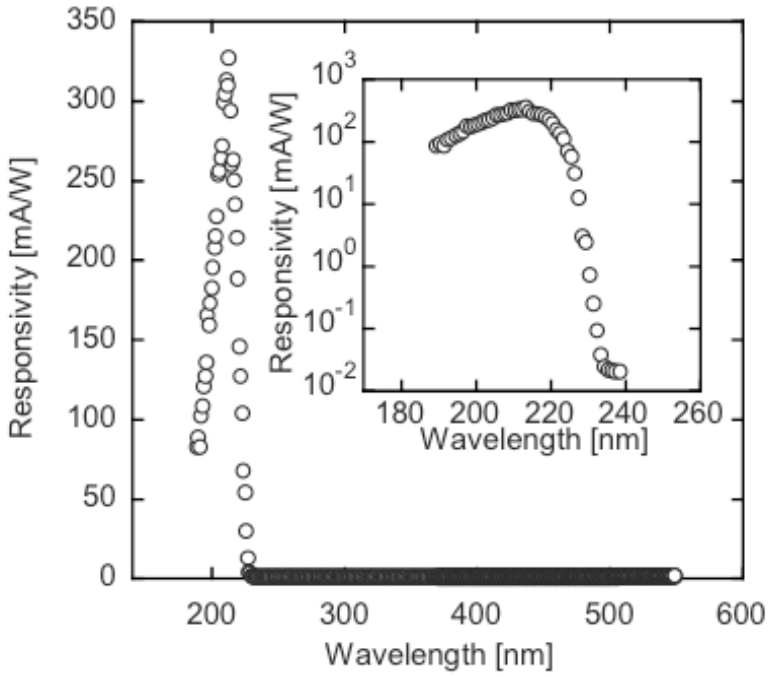

Figure 2.47: Spectral responsitivity of the diamond-based detector in the wavelength ranges of 190-550 nm, for a 30 V applied bias voltage. The inset shows the responsitivity in the vacuum-ultraviolet (VUV) region in the logarithm scale [2.125]

Direct use of a CVD grown single crystal has attracted little attention.

This present work describes the fabrication of devices made on commercially supplied single crystal diamond (SCD), and shows how the defect passivation treatments that were employed can be used to modify the surface of this form of SCD resulting in extreme levels of sensitivity to deep UV whilst maintaining good UV-to-visible-light discrimination and dark-current levels.

2.11.2 Gas-sensor devices

Solid-state sensors offer advantages over gas or liquid-based techniques in terms of size and ability to integrate into demanding environments. Diamond, which can be considered as a wide band-gap-energy (5.5 eV) semiconductor capable of supporting high carrier mobilities, high electric-field breakdown strength and the highest thermal conductivity of any material [2.126], is of considerable interest as a platform for chemical sensors. The physical and chemically robust nature of diamond means that it can be deployed within harsh environments. Acoustic wave devices have been produced, as well as sensors based on electrochemical processes [2.127, 2.128].

Diamond surfaces can display strongly differing electrical properties depending on the chemical nature of the surface-terminating groups present. For example, hydrogenated surfaces may be highly conductive, whilst oxygen-termination removes this conductivity [2.129, 2.130].

Looi and co-authors [2.129, 2.130] showed that CVD-grown polycrystalline diamond surfaces can display p-type conductivity. In their study they measured the sheet resistivity and carrier concentration of polycrystalline films, following annealing in air at different temperatures and time, by means of Hall Effect measurements. The films studied were 300 μm thick with top surface grains between 20 and 40 μm. No impurity dopants were intentionally added during the growth of the films. Figure 2.50 and 2.51 summarize the authors' findings.

Annealing at 60°C over a prolonged period of time proved to have little effect on the films sheet resistivity and carrier concentration. However, at higher temperature the films resistivity and carrier concentration rose in the former and fell in the latter, and then stabilised after a certain time interval.

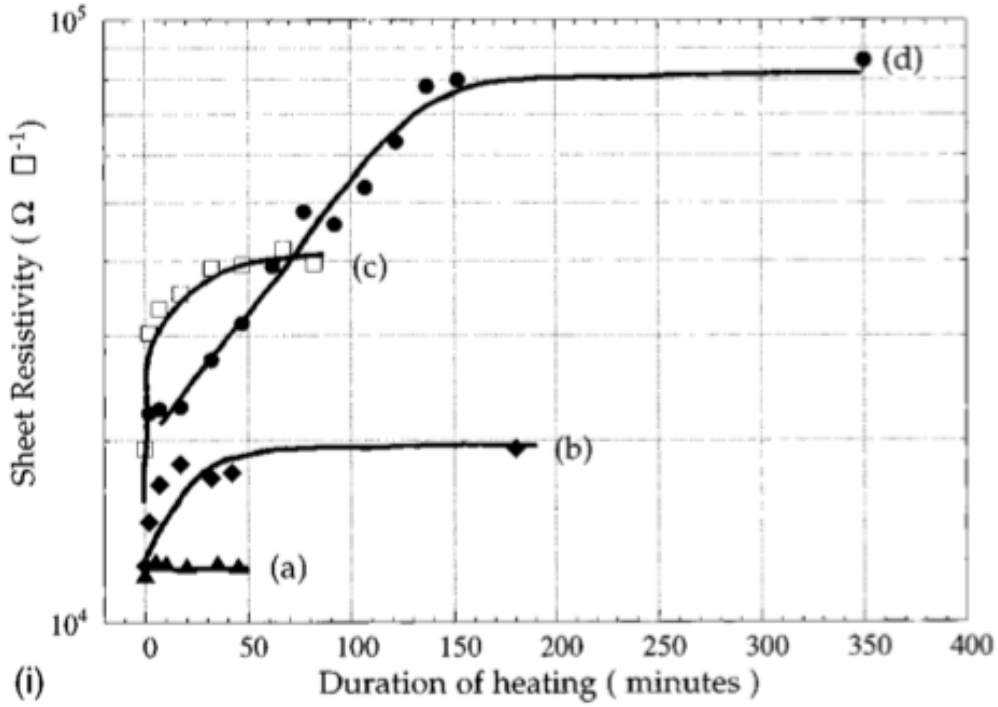

Figure 2.48: Changes in sheet resistivity for different duration of heating at 60°C (a), 100°C (b), 150° (c), 200°C (d) [2.129]

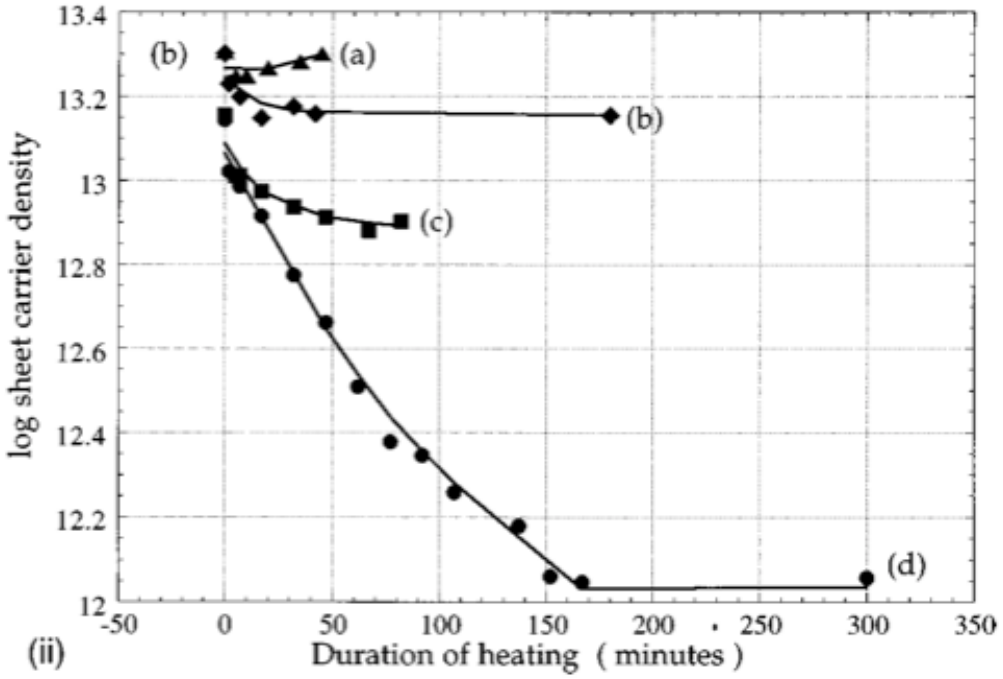

Figure 2.49: Changes in the sheet carrier concentration (cm^{-2}) for different duration of heating at 60°C (a), 100°C (b), 150° (c), 200°C (d) [2.129]

It was thought that hydrogen within the first 20 nm from the surface caused such p-type conductivity as it leads to the formation of shallow acceptor states within the band gap [2.131, 2.132]. This effect can be used to produce highly rectifying, low-leakage current, Schottky-barrier diodes [2.129]. These observations, when considered alongside the reversible nature of chemical changes to diamond surfaces (since the diamond lattice itself is so strongly bonded) have led to interest in the direct detection of chemical species by monitoring electrical changes to the diamond surface.

Some years ago, Sung Gi and co-workers [2.133] showed that polycrystalline diamond films, grown by a chemical vapour deposition (CVD) method, showed decreased surface conductivity in the presence of ammonia, whilst increasing in the presence of oxidising gases (such as NO_2). Diamond films were placed inside a closed container filled with gases; the resistance of the films was measured by a two-point probe method (figure 2.50).

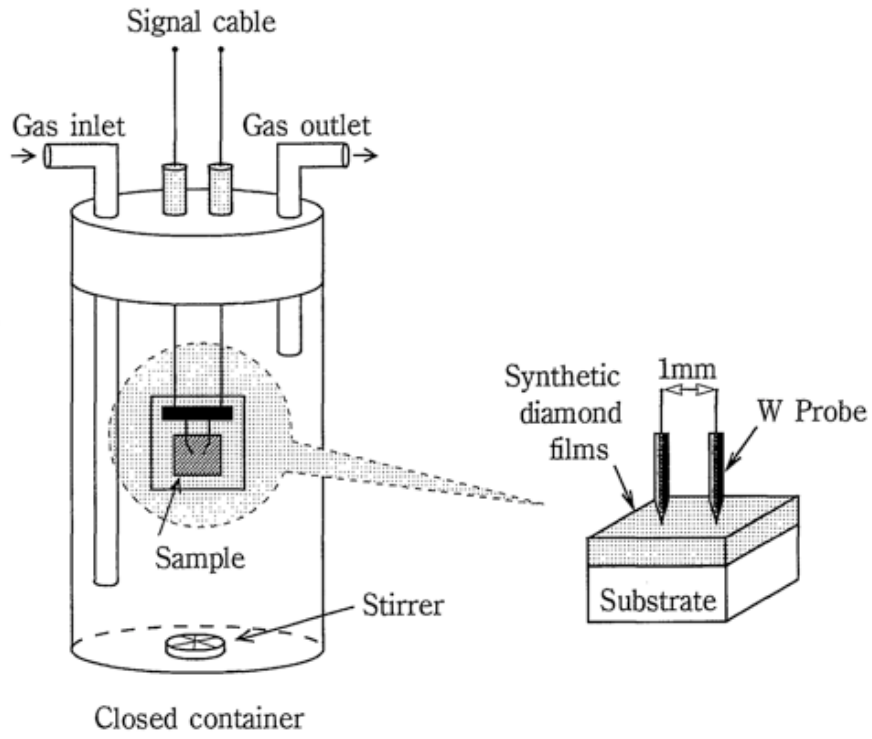

Figure 2.50: Schematic representation of equipment used to measure electrical resistance of diamond film surface [2.133]

When exposed to nitrogen dioxide (NO_2), the resistance of the film decreased approximately one order of magnitude within two minutes. When the film was subsequently exposed to ammonium hydroxide (NH_4OH) the resistance increased three orders of magnitude (figure 2.52). The authors suggested the possibility of building diamond NO_2 detectors due to the rapid change of surface conductivity following exposure [2.133].

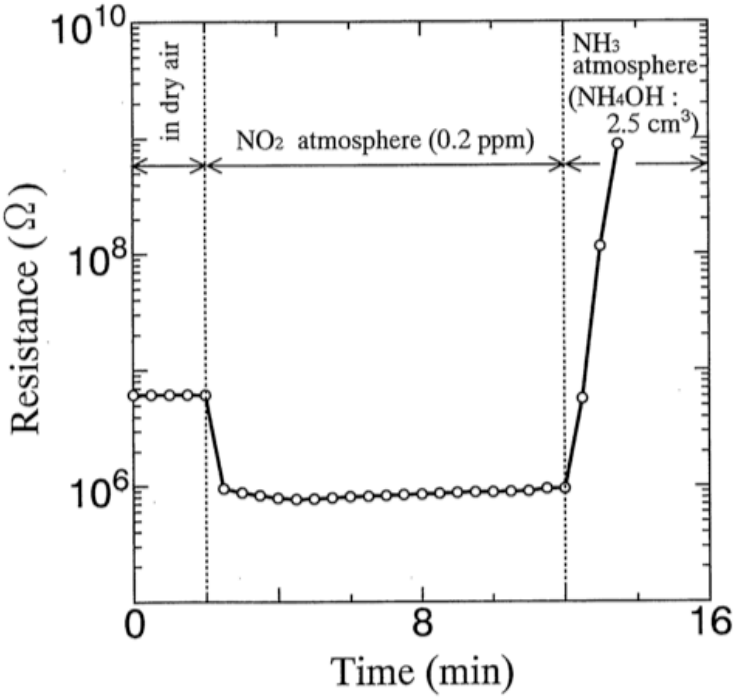

Figure 2.51: Dependence of resistance of diamond film surfaces terminated by Hydrogen atoms on time [2.133]

More recently, an attempt to increase the sensitivity of this approach to usable levels was reported by Wang and co-authors [2.134]. Polycrystalline CVD diamond films were plasma-etched to produce an array of micron-scale cone structures, which were subsequently hydrogenated. The conical shape had a high aspect ratio, and therefore the effective sensing area was maximized [2.135].

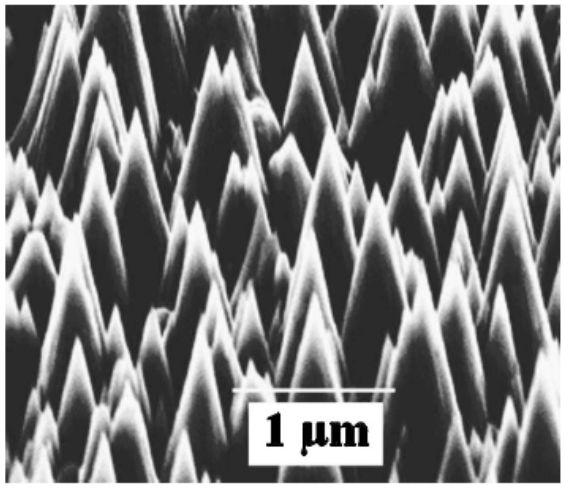

Figure 2.52: SEM image of as-formed diamond nanocone arrays [2.135]

1 ml of NO_2 and ammonia (NH_3) respectively were injected into Teflon containers with a volume size of approximately 10,000 ml. Electrical measurements were performed at room temperature; a bias of 5 V was applied to silver-paint electrical contacts on the surface of

the sample. Following hydrogenation in H_2 atmosphere, the surface conductivity increased by approximately four orders of magnitude, showing the formation of a surface-conductive layer. The structures were capable of sensing both NO_2 and NH_3 gases through surface electrical changes caused by the oxidising or reducing species.

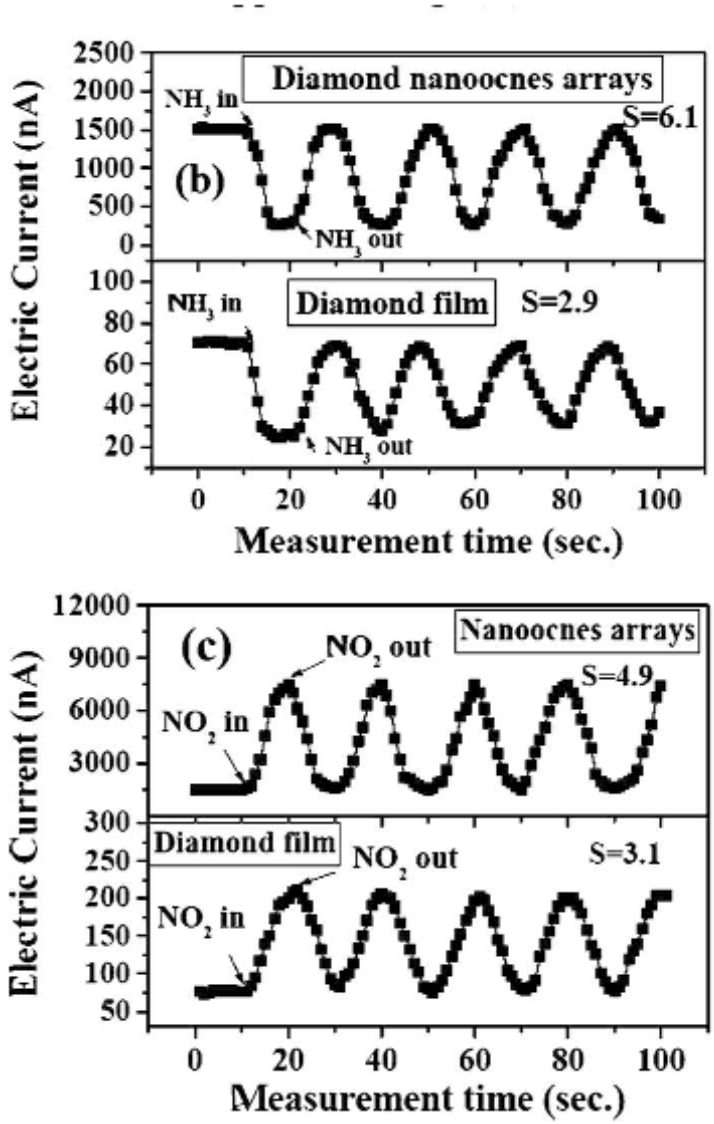

Figure 2.53: Current vs. measurement time (I-t) plots of hydrogenated diamond film and diamond nanocone arrays at room temperature for NH_3 (b) and NO_2 (c) diluted in air [2.135]

Figure 2.54 shows a current decrease by 6.1 times with the diamond nanocone array and 2.9 times with diamond film in NH_3/air atmosphere, whereas it increases by 4.9 and 3.1 times respectively in NO_2/air atmosphere [2.135].

References

[2.1] Ward, F., *Diamonds. Bethesda*, MD: Gem. (1998)

[2.2] May P., Philosophical Transactions: Mathematical, Physical and Engineering properties, **358**, 1766, (2000)

[2.3] Wehr M., III, *Physics of the Atom,* Addison-Wesley Publishing Co, Reading, MA (1978)

[2.4] Pierson H.O., *Handbook of Carbon, Graphite, Diamond and Fullerenes: properties, processing and applications,* Noyes Publications, New Jersey (1993)

[2.5] Carey F.A. and Sundberg R.J., *Advanced Chemistry: Structure and mechanisms*, 4th ed., Copyrighted Material (2000)

[2.6] http://www.chem1.com/acad/webtext/chembond/cb06.html.

[2.7] Shriver D.F. *et al.*, *Inorganic Chemistry*, 2nd ed., Oxford University Press, Oxford (1996)

[2.8] *Atomic Resolution Images In Air Of Highly Ordered Pyrolytic Graphite (HOPG) Using STM Equipment.* Available at: http://www.azonano.com/details.asp?ArticleID=1858

[2.9] Patnaik P., *Handbook of Inorganic Chemicals*, McGraw-Hill (2002)

[2.10] Cotton F.A., *Basic Inorganic Chemistry*, 3rd ed., Copyrighted Material (1995)

[2.11] Edwards I.A.S., *Introduction to Carbon Science*, ed. H. Marsh, Butterworth, London (1989)

[2.12] From Element Six L.t.d., available at: http://www.e6cvd.com

[2.13] Robertson F.R.S., Fox, J.J. and Martin E., Philosphical Transaction of the Royal Society of London, **A232**, 463 (1934)

[2.14] Walker J., *Optical absorption and luminescence in diamond*, Rep. Prog. Phys. **42**, 1605 (1979)

[2.15] Sonoda S., Won J.H., Yagi H., Hatta A., Ito T. and Hiraki A., Applied Physics Letters, **70**, 2574 (1997)

[2.16] Woods G.S., *Properties and Growth of Diamond*, ed. G. Davies, INSPEC, London, UK, (1994)

[2.17] Banfield J., *Diamonds and Diamond simulants,* Lecture notes for "Geology 306" at University of Winsconsin-Madison, USA, available at www.geology.wisc.edu

[2.18] Wilks J. And Wilks E., *Properties and Applications of Diamond*, Butterworth-Heinemann, Oxford (1991)

[2.19] (2007) *HPHT-High Pressure High Temperature,* available at: http://www.diamondlab.org/80-hpht_synthesis.htm

[2.20] (2009) *HPHT-High Pressure High Temperature*, available at: http://memorialdiamonds.co.uk/?page_id=110

[2.21] National Materials Advisory Board, *Status and Applications of Diamond and Diamond-like Materials: an emerging technology,* NMAB-445, National Academy Press, Washington, USA (1990)

[2.22] Matsumoto S. and Matsui Y., Journal of Material Science **18** (1983) 1785

[2.23] Seino Y. and Nagai S., Journal of Material Science. **12** (1993) 324

[2.24] Singh J. and Vellaikal M., Journal of Applied Physics **73** (1993) 2831

[2.25] Liu H. and Dandy D.S., Diamond and Related Materials **4** (1995) 1173

[2.26] Belton D.N. and Schmieg S.J., Surface Science **233** (1990) 131

[2.27] Waite M.M. and Shah S.I., Applied Physics Letters **60** (1992) 2344

[2.28] Ong TP, Xiong F., Chang R.P.H. and White C.W., Applied Physics Letters **60** (1992) 2083

[2.29] Lambrecht W.R.L., Choone H.L., Segall B., Angus C., Zhidan L. and Sunkara M., Nature **364** (1993) 607

[2.30] Badzian A.R. and Badzian T., Surface and Coatings Technology **36** (1988) 283

[2.31] Wolter S.D. and Glass J.T., J. Applied Physics Letters **77** (1995) 5119

[2.32] George M.A, Journal of Applied Physics Letters **76** (1994) 4099

[2.33] Smolin A.A. Raichenko V.G., Pimenov S.M., Kononenko T.V. and Loubnin E.N. Applied Physics Letters **62** (1993) 3449

[2.34] Meilunas R., Wong M.S., Sheng K.C. Chang R.P.H. and Van Duyne R.P., Applied Physics Letters **54** (1989) 2204

[2.35] Wolter S.D., Stoner B.R. and Glass J.T., Applied Physics Letters **62** (1993) 1215

[2.36] Lux B. and Haubner R., in *Diamond and Diamond-like Films and Coatings*, eds. Clausing R.E., Horton L.L., Augus J.C. and Koidl P., Plenum Press, New York (1991)

[2.37] Angus J.C., Wang Y. and Sunkara M., Annual Review of Material Science **21** (1991) 221

[2.38] Belton D.N. and Schmieg S.J., Thin Solid Films **212** (1992) 68

[2.39] Wild C., Koidl P., Muller-Serbert W., Walcher H., Kohl R., Herres N., Locher R., Samlenski R. and Brenn R., Diamond and Related Materials **2** (1993) 158

[2.40] Davies G., *Diamond*, Adam Hilger Ltd., Bristol, UK (1984)

[2.41] Seal M. and van Enckevort W., *Diamond Optics* (Feldman A. and Holly S. eds.), 69:144-152, SPIE (1988)

[2.42] Lettington A.H., *Applications of Diamond Films and Related Materials* (Tzeng Y. Et al. eds.), 703-710, Elsevier Science Publishers (1991)

[2.43] Fong C.Y. *et al.*, *Diamond: Electronic properties and applications*, ed. Pan L.S. and Kania D.R., Kluwer Academic Press, MA, USA (1995)

[2.44] Painter G.S., Ellis D.E. and Lubinsky R., Physical Review **B4**, 3610 (1971)

[2.45] Mainwood A., *Properties and Growth of Diamond*, ed. Davies G., INSPEC, London, UK

[2.46] Davies G., *Diamond Optics* (Feldman A. and Holly S. eds.), 969:165-184, SPIE (1988)

[2.47] Streetman B.G., *Solid State Electronic Devices*, Prentice-Hall, New Jersey (1990)

[2.48] Pan L.S., Kania D.R., Pianetta P., Ager III J.W. and Han S., Journal of Applied Physics **73**, (1993) 2888

[2.49] Field J.E., *The Properties of Diamond* (Field JE ed.), Academic Press, London (1979)

[2.50] Boehm H.P., *Advances in Catalysis*, Academic Press, New York (1966)

[2.51] Kalish, R., Carbon **37** (1999) 781

[2.52] Goss J.P., Eyre R.J. and Briddon P.R., Physica Status Solidi B **9** (2008) 1679

[2.53] Wentorf R.H. and Bovenkerk H.P., Journal of Chemical Physics **36** (1959) 1987

[2.54] Teraji T., Wada H., Yamamoto M., Arima K. and Ito T., Diamond and Related Materials **15** (2006) 602

[2.55] Lagrange J.-P., Deneuville A., Gheeraert E., Diamond and Related Materials **7** (1998) 1390

[2.56] Yamanaka S., Watanabe H., Masai S., Daisuke T., Okushi H. and Kajimura K., Japanese Journal of Applied Physics, **37** (1998) L1129

[2.57] Fontaine F., Uzan-Saguy C., Philosoph B. and Kalish R., Applied Physics Letters **68** (1996) 16

[2.58] Prins J.F., Physical Review B **44** (1991) 2470

[2.59] Goss J.P., Briddon P.R., Rayson M.J., Sque S.J. and Jones R., Physical Reviews B **72** (2005) 3

[2.60] Gheeraert E., Koizumi S., Teraji T. and Kanda H., Science **292** (2001) 1899

[2.61] Koizumi S., Kamo M., Sato Y., Mita S., Sawabe A., Reznik A., Uzan-Saguy C. and Kalish R., Diamond and Related Materials, **7** (1998) 540

[2.62] Katagiri M. and Isoya J., Applied Physics Letters **85** (2004) 26

[2.63] Teukam Z, Chevallier J., Saguy C., Kalish R., Ballutaud D., Barbe M., Jomard F., Tromson-Carli A., Cytermann C., Butler J.E., Bernard M., Baron C. and Deneuville A., Nature Materials **2** (2003) 482

[2.64] Nakazawa K., Tachiki M., kawarada H., Kawamura A., Horiuchi K. and Ishikura T., Applied Physics Letters **82** (2003) 2074

[2.65] Nesladek, M. Semiconductor Science Technology **20** (2005) R19

[2.66] Kajihara S.A., Antonelli A., Bernholc J. and Car R., Physics Review Letters, **78** (2001) 446

[2.67] Jagannadham K., Reed M.L., Lance M.J., Watkins T.R., Verghese K., Butler J.E. and Smirnov A., Diamond and Related Materials **16** (2007) 50

[2.68] Zeisel R., Nebel C.E., Stutzmann M., Sternschulte H., Schreck M. and Stritzker B., Physica Status Solidi A **181** (2000) 45

[2.69] Te Nijenhuis J., Cao G.Z., Smits P.C.H.J., van Enckevort W.J.P., Giling L.J., Alkemade P.F.A., Nesladek M. and Remes Z., Diamond and Related Materials **6** (1997) 1726

[2.70] Ronning C. and Hofsass H., Diamond and Related Materials **8** (1999) 1623; Restle M., Bharuth Ram K., Quintel H., Ronning C., Hofsass H., Jahn S.G., ISOLDE Collaboration and Wahl U., Applied Physics Letters **66** (1995) 2733

[2.71] Uzan-Saguy C., Cytermann C., Fizgeer B., Richter V., Brenner R. and Kalish R., Physica Status Solidi A **193** (2002) 508

[2.72] Spitsyn B.V. and Alexenko A.E., Proceedings of the Second International Symposium on Diamond Materials, edited by Purdes A.J., Angus J.C., Davis R.F., Meyerson B.M., Spear K.E. and Yoder M. (Electrochemical Society, Pennington, NJ, 1991), 597

[2.73] Sachdev H., Haubner R. and Lux B., Diamond and Related Materials **6** (1997) 494

[2.74] Ueda K. and Kasu M., Diamond and Related Materials **18** (2009) 121

[2.75] Yan C.X., Dai Y., Huang B.B., Long R. and Guo M., Computational Material Science **44** (2009) 1286

[2.76] Boccara A.C. and Fournier D., Optics Letters, **5** (1980) 9

[2.77] Nesladek M., Meykens K. and Stals L.M., Physical Review B **54**, (1996) 8

[2.78] Zammit U., Madhusoodanan K.N., Foglietta S., Marinelli M., Mercuri F. and Scudieri F., Photoacustic and Photothermal Phenomena: 10th International

Conference **463** (1999) 283

[2.79] Hearne S.M., Trajkov E., Jamieson D.N., Butler J.E. and Prawer S., Journal of Applied Physics **99** (2006) 113703

[2.80] Robertson J. and O'Reilly, Physical Review B **35** (1987) 2946

[2.81] Bredas J.L. and Street G.B., Journal of Physics C **18** (1985) L651

[2.82] Nebel C.E., Semiconductor Science Technology **18** (2003) S1

[2.83] Hammersberg J., Isberg J., Johansson E., Lundstrom T., Hjorstam O. and Bernhoff H., Diamond and Related Materials **10** (2001) 574

[2.84] Balducci A., Marinelli M., Milani E., Morgada M.E., Tucciarone A., Verona-Rinati G., Angelone M. and Pillon M., Applied Physics Letters **86** (2005) 022108

[2.85] Zhou D., Applied Physics Letters **82** (1997) 4546

[2.86] Proffitt S.S., Probert S.J., Whitfield M.D., Foord J.S., Jackman R.B., Diamond and Related Materials **8** (1999) 768

[2.87] Ye H., Sun C.Q., Huang H. and Hing P., Applied Physics Letters, **78** (2001) 1826

[2.88] Williams O.A. and Nesladek M., Physica Status Solidi, **A203**, (2006) 3375

[2.89] Jiao S., Sumant A., Kirk M.A., Gruen D.M., Krauss A.R. and Auciello O., Journal of Applied Physics **90** (2001) 118

[2.90] Liu C., Xiao X., Wang J., Shi B., Adiga V.P., Carpick R.W., Carlisle J.A. and Auciello O., Journal of Applied Physic **102** (2007) 074115

[2.91] Williams O.A., Curat S., Gerbi J.E., Gruen D.M. and Jackman R.B., Applied Physics Letters **85** (2004) 1680

[2.92] Gruen D.M., Annual Review of Material Science, 29:211-59 (1999)

[2.93] Borst T.H. and Weis O., Physica Status Solidi, **A154** (1996) 423

[2.94] Borst T.H. and Weis O., Diamond and Related Materials **4**, (1995) 948

[2.95] Ye H., Hing P. and Jackman R.B., Journal of Applied Physics **94** (2003) 7878

[2.96] Nesladek M., Bergonzo P., Hubik P., Mares J.J. Kristofik J., Kindl D., Williams O.A. and Gruen D.M., Diamond and Related Materials, **15** (2006) 607

[2.97] Wang S.H. and Swain G.M., Journal of Physical Chemistry C **111**, (2007) 3986

[2.98] El Tall O., Jaffrezic-Renault N., Sigaud M. and Vittori O., Electroanalysis **19** (2007) 1152

[2.99] Synthesis, properties and applications of ultrananocrystalline Diamond Eds, Gruen D.M., Shenderova O.A. and Vul A.Y. (Nato Science Series, vol. 192, Spinger, Netherlands 2005, ISBN 10-1-4020-3321-4)

[2.100] Shenderova O.A., Zhirnov V.V. and Brenner D.W., Crit. Rev. Solid State Mater. Sci. **250-251** (2002) 227

[2.101] Baidakova M. and Vul A.Y., Journal of Physics D: Applied Physics 40 (2007) 6300

[2.102] Krüger A., Kataoka F., Ozawa M., Fujino T., Suzuki Y., Aleksenskii A.E., Vul A.Y. and Osawa E., Carbon **43** (2005) 1722

[2.103] Panich A.M., *et al*., *Nuclear magnetic resonance stu*dy *of ultrananocrystalline diamond*, Eur. Phys. JB

[2.104] Barnard A., *From nanodiamond to nanowires: Synthesis, properties and Applications of Ultrananocrystalline Diamond* vol 192 ed Gruen D *et al.* (Dordrecht: Springer)

[2.105] Stumm P. and Drubold D.A., Solid State Commun. **93** 617

[2.106] Alexenskii A.E. *et al*., Tech. Phys. Lett. **23** 874

[2.107] Alexenskii A.E. *et al*., Phys. Solid. State **43** 145

[2.108] Ivanov-Omskii V.I. *et al*., Phil. Mag. B **73** 715

[2.109] Belobrov P.I. *et al*., Dokl. Phys. **46** 459

[2.110] National Materials Advisory Board, *Status and Applications of Diamond and Diamond-like Materials: an Emerging Technology*, NMAB-445, National Academy Press, Washington, DC (1990)

[2.111] Available at: www.kobelco.co.jp/showroom/np0802e/np08021e.htm

[2.112] Landstrass M.I., Plano M.A., Moreno M.A. and McWilliams S., Diamond and Related Materials **2** (1993) 1033

[2.113] Liao M. and Koide Y., Applied Physics Letters **89** (2006) 113509

[2.114] McKeag R.D., Chan S.S and Jackman R.B., Applied Physics Letters **67** (1995) 15

[2.115] Binari S.C., Marchywka M., Koolbeck D.A., Dietrich H.B. and Moses D., Diamond and Related Materials **2** (1993) 1020

[2.116] Polyakov V.I., Druz B.L., Karabutov A.V., Rossukanyi N.M., Rukovishnicov A.I., Ostan E., Hayes A., Frolov V.D., Konov V.I., Diamond and Related Materials **7** (1998) 821

[2.117] Lefeuvre E., Castex M.-C., Achard J., Tardieu A., Beuille C. and Schneider H.*.,* Diamond and Related Materials **12** (2003) 1804

[2.118] McKeag D. and Jackman R.B., Diamond and Related Materials **7** (1998) 513

[2.119] Lansley S.P., Gaudin O., Whitfield M.D., McKeag R.D., Rizvi N. and Jackman R.B.*,* Diamond and Related Materials **9** (2000) 195

[2.120] From Element Six L.t.d., available at: www.e6cvd.com

[2.121] Balducci A., De Sio A., Marinelli M., Milani E., Morgada M.E., Pace E., Prestopino G., Pucella G., Scoccia M., Tucciarone A., Verona-Rinati G., Diamond and Related Materials **14** (2005) 1980

[2.122] Balducci A., Marinelli M., Milani E. and Morgada M.E., Applied Physics Letters, **86** (2005) 193509

[2.123] Teraji T., Yoshizaki S., Wada H., Hamada M., and Ito T., Diamond and Related Materials **13** (2004) 85

[2.124] Brescia R., De Sio A., Donato M.G., Faggio G., Messina G., Pace E., Pucella G., Santangelo S., Sternschulte H. and Verona Rinati G., Physica Status Solidi A **199** (2003) 113

[2.125] Iwakaji Y., Kanasugi M., Maida O. and Ito T., Applied Physics Letters **94** (2009) 223511

[2.126] *Properties and growth of diamond* Gordon Davies (ed.) INSPEC, Institution of Electrical Engineers, London, UK (1998) ISBN: 0-85296 875 2

[2.127] Mortet V., Williams O.A., and Haenen K., Physica Status Solidi A **205** (2008) 1009

[2.128] Williams O.A., Mortet V., Daenen V., Haenen K, Journal of Nanoscience and Nanotechnology **9** (2009) 3483

[2.129] Looi H.J., Foord J.S. and Jackman R.B., Applied Physics Letters **72** (1998) 353

[2.130] Looi H.J., Pang L.Y.S., Molloy A.B., Jones F.H., Foord J.S. and Jackman R.B. Diamond and Related Materials **7** (1998) 550

[2.131] Hayashi K., Yamanaka S., Okushi H. and Kajimura K., Applied Physics Letters **68** (1996) 376

[2.132] Aoki M. and Kawarada H., Japanese Journal of Applied Physics **33** (1994) 708

[2.133] Sung Gi R.S., Ishikawa T., Tanaka S., Kimura T, Akiba Y., Iida M., Japanese Journal of Applied Physics **36** (1997) 2057

[2.134] Wang Q., Qu S.L., Fu S.Y., Liu W.J., Li J.J. and Gu C.Z., Journal of Applied Physics **102** (2007) 103714

[2.135] Metzger L., Fischer F. and Mokwa W., Sensors and Actuators, A **133** (2007) 259

Chapter 3

Experimental methods

3.1 Impedance spectroscopy

Impedance Spectroscopy (IS) is a powerful technique to characterize the electrical properties of materials and their interfaces with electrically conducting electrodes. The technique may be used to investigate the dynamics of bound or mobile charges in bulk or interface regions of any kind of ionic solids, or liquid materials, semiconductors, mixed ionic-electronic materials and insulators (dielectrics). The technique measures the impedance as a function of frequency automatically in the range of 1 mHz to 10 MHz and is easily interfaced to computer. The technique was comprehensively reviewed by MacDonald [3.1].

Complex impedance measurements are capable of separating the various contributions to the total conductivity due to bulk, grain boundary and electrode and therefore form the backbone of the present work.

3.1.1 Impedance theory

Electrochemical impedance is the frequency-dependent complex valued proportionality factor, which is a ratio between the applied potential and current signal. The objective of impedance experiments is to determine the values of the various elements in the equivalent circuit or simply to confirm that a given electrochemical system fits a particular equivalent circuit model. For the sake of simplicity, the impedance plots for the resistor-capacitor (*RC*) in parallel with a series resistor network (figure 3.1), will be considered in some detail. The reason for choosing this circuit is because several electrochemical systems are actually modelled using this network [3.1].

The term resistance and impedance both imply an obstruction to current or electron flow. When dealing with a direct current (DC), only resistors provide this effect. However, in the case of an alternating current (AC) circuit elements such as capacitors and inductors can also influence the electron flow. These elements can affect not only the magnitude of an AC wave-form, but also its time-dependent characteristics or phase. In DC theory, where the frequency equals 0 Hz, a resistance is defined by Ohm's Law:

$$V = IR \tag{3.1}$$

where V is the applied potential, I is the resulting current, R is the resistance.

In the case of an AC current, where the frequency exceeds zero, this is represented by:

$$\mathbf{V} = I\mathbf{Z} \qquad (3.2)$$

Where **V** is the wave form amplitude, I is the resulting current, **Z** is the impedance, which is basically the AC equivalent of the resistance.

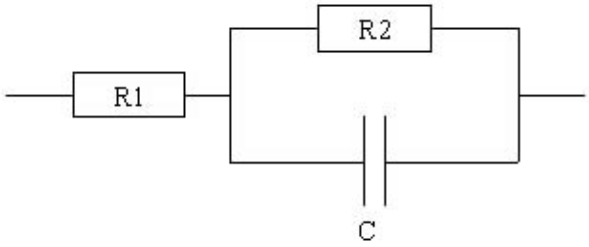

Figure 3.1: equivalent circuit of an impedance measurement with one time constant [3.1]

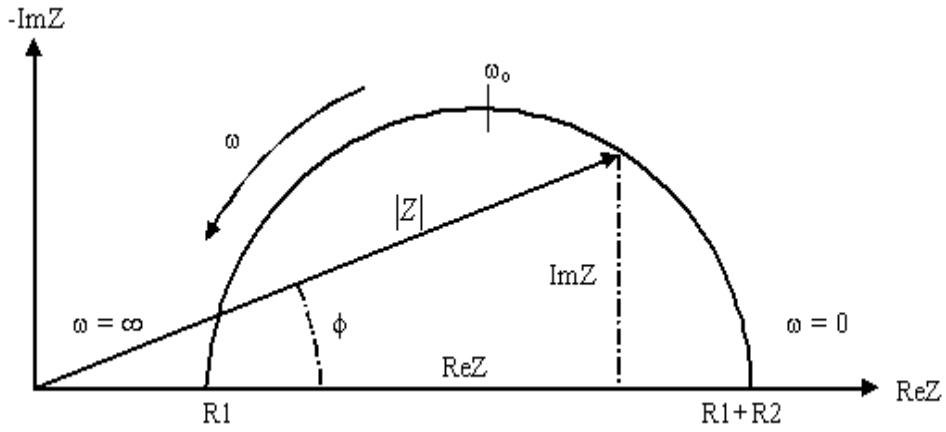

Figure 3.2: Cole-Cole plot in the complex plane, $\omega_o = 1/(R_2C)$

The plot in figure 3.2 is based on a vector diagram, corresponding to a sine wave I. The current sine wave can be described by the following equations:

$$I = A \sin(\omega t + \phi) \qquad (3.3)$$

$$\omega = 2\pi f \qquad (3.4)$$

where A is the maximum amplitude, ω is the frequency in radians/sec, f is the frequency in Hz, ϕ is the phase shift in radians.

The impedance Z(ω) is a complex number that can be represented either in polar co-ordinates or in Cartesian coordinates:

$$Z(\omega) = |Z| \exp(j\phi) \tag{3.5}$$

$$Z(\omega) = ReZ + j\ ImZ \tag{3.6}$$

where ReZ and ImZ are the real part and the imaginary part of the impedance, respectively. [3.1] The relationships between theses quantities are:

$$|Z|^2 = (ReZ)^2 + (ImZ)^2 \tag{3.7}$$

$$\phi = \tan^{-1} ImZ / ReZ \tag{3.8}$$

$$ReZ = |Z| \cos\phi \tag{3.9}$$

$$ImZ = |Z| \sin\phi \tag{3.10}$$

Figure 3.1 shows the equivalent circuit of a material with a resistive and capacitive element, whose impedance is:

$$Z(\omega) = \frac{V}{I} = R_1 + \frac{1}{\frac{1}{R_2} + jC\omega} = R_1 + \frac{R_2}{1 + \omega^2 C^2 R_2^{\ 2}} - \frac{j\omega C R_2^{\ 2}}{1 + \omega^2 C^2 R_2^{\ 2}} \tag{3.11}$$

where V is the voltage, I is the current, R_1 and R_2 are the resistance values of the equivalent circuit and *C* is the capacitance value of the equivalent circuit. [3.1]
The impedance modulus is given by:

$$|Z(\omega)| = \sqrt{(R_1 + \frac{R_2}{1 + \omega^2 C^2 R_2^{\ 2}})^2 + (\frac{\omega C^2 R_2^{\ 2}}{1 + \omega^2 C^2 R_2^{\ 2}})^2} \tag{3.12}$$

The high frequency intercept yields R_1, whereas the low frequency $R_1 + R_2$, meaning that at high frequencies the capacitor conducts the current easily, whereas at low frequencies the current flow via the capacitor is impeded. [3.1] The current therefore flows through R_1 and R_2, and the impedance is given by the sum of the two resistors:

$$|Z(\omega)| = R_1 + R_2 \text{ when } \omega \rightarrow 0 ,$$
$$|Z(\omega)| = R_1 \text{ when } \omega \rightarrow \infty$$

At intermediate frequencies the impedance has a value between R_1 and $R_1 + R_2$, thus possessing both real and imaginary components. This gives rise to the semicircular shaped Cole-Cole plot, described by the equation:

$$\left[Z' - (R_1 + \frac{R_2}{2})\right]^2 + Z''^2 = (\frac{R_2}{2})^2 , \tag{3.13}$$

which is actually the equation of a circle with radius $r = R_2 / 2$ and centre coordinates $C(R_1 + R_2/2, 0)$. $Z(\omega)$ is plotted in figure 3.2 in terms of a Cole-Cole plot in the complex plane with the negative imaginary parts in the positive part of the real axis.
At the peak of the semicircle, the following condition is obtained:

$$\omega_{max} R_2 C = 1 \tag{3.14}$$

and hence:

$$C = \frac{1}{2\pi f_{max} R_2} \tag{3.15}$$

Knowing the value of R_2 and the frequency f_{max}, the value of the capacitance can be determined. It is possible to obtain all the three parameters (R_1, R_2 and C) from the Cole-Cole plot as shown in figure 3.2, providing a sufficient frequency range is investigated.
The application of Impedance Spectroscopy to the characterization of polycrystalline materials started after Bauerle [3.2] showed that for Zirconia with platinum electrodes the individual polarizations of grain interiors, grain boundaries, and electrodes could be resolved in the admittance plane. He presented an equivalent circuit for his results, in which its components correspond to grain interiors, grain boundaries, and electrode connected in series. However, estimation of the circuit parameters was made rather complicated by Bauerle's choice of the admittance plane. Many subsequent researchers

have therefore preferred to work in the impedance plane, i.e. Cole-Cole plot, where a more direct relationship exists between the spectrum and the circuit [3.3, 3.4]. The level of agreement between experiment and simulation is quite satisfactory for the grain interior and grain boundary arcs both in terms of shape and distribution of frequencies on the arcs, therefore supporting the view that equivalent circuits can be a valid way of representing the data.

3.1.2 Conductivity models

The impedance plots of polycrystalline materials can be related to their microstructure by means of physical models of the grain interior, grain boundary and the electrode behaviour. The physical models used to describe the electronic materials are reviewed in detail with their respective circuit equivalents [3.5].

The early model used to describe the properties of a two-phase mixture is the series layer model. The model describes that the two phases are assumed to be stacked in layers parallel to the measuring electrodes, with total thickness of each phase made proportional to volume fractions X_1 and X_2. This model shows a linear mixing rule for the complex resistivity (ρ), which is the sum of the individual phase resistivity (ρ_1 and ρ_2):

$$\rho = X_1\rho_1 + X_2\,\rho_2 \tag{3.16}$$

In the parallel circuit model the two phases are assumed to be stacked across the electrodes. For this model, the complex conductivity (σ) rather than resistivity follows a linear mixing rule:

$$\sigma = X_1\sigma_1 + X_2\sigma_2 \tag{3.17}$$

The widely used physical model is a more realistic one, which treats the microstructure as an array of cubic shaped grains with flat grain boundaries of finite thickness as shown in figure 3.3 [3.6].

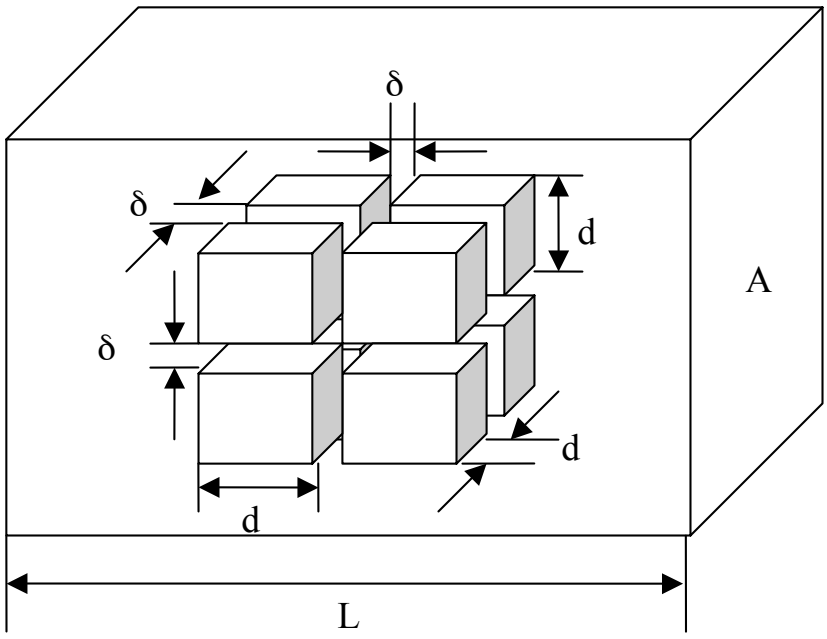

Figure 3.3: Brick layer model of idealized polycrystalline structure in which grains of dimensions d^3 are separated by grain boundaries of width δ [3.7].

The volume fraction of grain boundaries is 3δ/d (δ is grain boundary thickness and d is grain size) [3.5]. The current flow is assumed to be one-dimensional and the current path at the corners of the grains is neglected. In this case the two paths available to the current are either through the grains and across the grain boundary, or along grain boundaries, as depicted in figure 3.3. Depending on the relative magnitudes of grain and grain boundary conductivity one of the two paths may dominate. This model has been applied to many material systems and according to this model the bulk resistivity and the grain boundary resistivity may have different response [3.6].

In the brick layer model, the grain interior response will be displaced from the grain boundary response depending on the relaxation rate of charged species within each region. It is normal to compare the relaxation rates of different processes in terms of rate constant or relaxation time (τ), this can be defined as:

$$\tau = RC \tag{3.18}$$

In terms of grain interior rate constant, τ_{gi} can be expressed as follows:

$$R_{gi} = L / A\sigma_{gi} \tag{3.19}$$

$$C_{gi} = \varepsilon_0\varepsilon_{gi} / L \tag{3.20}$$

Therefore:

$$\tau_{gi} = \varepsilon_0 \varepsilon_{gi} / \sigma_{gi} \qquad (3.21)$$

where L is the sample length, A is the cross sectional area, ε_o is the permittivity of free space (8.854×10^{-12} F/m), and σ_{gi} and ε_{gi} are the electrical conductivity and relative dielectric constant of the grain interior respectively. [3.7]

The grain boundary relaxation time constant τ_{gb} can be expressed as follows [3.7];

$$R_{gb} = L\delta / A\sigma_{gb}d \qquad (3.22)$$

$$C_{gb} = A\varepsilon_0\varepsilon_{gb}d / L\delta \qquad (3.23)$$

Therefore:

$$\tau_{gb} = \varepsilon_0 \varepsilon_{gb} / \sigma_{gb} \qquad (3.21)$$

where d is the grain size, δ is the grain boundary width, and σ_{gb} and ε_{gb} are the specific electrical conductivity and relative dielectric constant of the grain boundary, respectively. The resistance of the grain boundary is normally associated with the presence of a second phase or a constriction resistance, which can also result in a space-charge region at the grain boundary. The capacitance of this region is thus associated with the polarization at the interface.

By applying the brick-layer model and classic identification criteria comprehensively discussed in the literature [3.1, 3.8, 3.9, 3.10, 3.11, 3.12], bulk (at high frequencies) and grain boundary (at low frequencies) contributions to the total material impedance were in each case distinguished.

This can be explained by the different relaxation rate of charged species within each region or the different RC relaxation time of the elements. The defects, non-diamond phases and impurities are thought to accumulate preferentially within the grain boundaries [3.13]. The grain boundaries may induce dipole moments that respond to an applied field with a delay [3.14]. Thus the grain boundary contributions with a long relaxation time usually happen at low frequencies and the grain bulk contributions with a short relaxation time at high frequencies. In most cases, the sufficient difference in the capacitance of the RC

equivalent circuit rather than the resistance results in the two semicircles being separated on the complex Cole-Cole plane [3.15].

The capacitance values of the grain boundary and grain interior are reported to be of the order of 10^{-9} F and 10^{-12} F, respectively, for many polycrystalline material systems, for example, zirconia [3.5], bismuth titanate [3.16] ferroelectrics [3.17], and polycrystalline diamond [3.18].

The reason different materials show similar capacitance values (10^{-9} F for grain boundaries and 10^{-12} F for the grain interiors) when analyzed in the Cole-Cole plot may be explained by recalling the definition of the capacitance itself, as shown in equations (3.20) and (3.23): L is the sample length within the order of one millimetre, A is the cross-sectional area within the order of 10 mm^2, ε_o is the permittivity of free space (8.854×10^{-12} F/m), and ε_{gi} is the relative dielectric constant of the grain interior of the sample. For high purity diamond, the dielectric constant is reported to be approximately 5.7 [3.19]. Thus equation (3.20) indicates that the grain interior capacitance for diamond is estimated around 0.5 pF.

The same A and L values can be applied to the grain boundary capacitance in equation (2.23). In addition, the grain-boundary-induced dipole polarization may cause the dielectric constant (ε_{sgb}) to be slightly higher than that of grain bulk (ε_{gi}), but probably on the same magnitude order [3.14]. Furthermore, the grain size of a typical polycrystalline material is usually on the order of μm, where the effective grain boundary width is expected to be on the order of nm [3.20]. Thus, the estimated grain boundary capacitance for a polycrystalline diamond is around 0.5 nF.

To gain further insight into these quantitative estimations, the ratio of the grain interior capacitance and grain boundary capacitance may be considered as follows:

$$C_{gi} / C_{gb} \approx \delta / d \qquad (3.25)$$

Equation (3.25) indicates that the ratio of the grain capacitance and grain boundary capacitance is proportional to the ratio of the grain boundary width (δ) and grain size (d). In other words, the difference between the grain interior capacitance and grain boundary capacitance mainly originates from the geometric effect of the sample. This effect may be controlled by the following factors such as grain size, anisotropy, and porosity [3.1]. The typical geometric characteristic within a polycrystalline material leads to the grain boundary capacitance being normally two or three orders of magnitude higher than the grain interior capacitance.

The above discussion gives an explanation of the origin of the classic procedures and identification criteria for the grain boundary and grain bulk contributions in an ideal condition. In practice, it is difficult to calculate the theoretical capacitance of grain interior and grain boundaries for diamond because the in-plane electrode measurement makes it unlikely to define the specific length and area of each sample. Cross-section electrode measurements allow the geometric parameters to be solved easily, but most impedance data cannot be detected across the samples due to the extremely high resistance in diamond. So the conduction path identification criteria used in this thesis are emphasized on practical and empirical interpretations of materials based on the brick-layer model discussed here.

In the current work, a Solartron impedance analyzer SI1260 with a high impedance input module 1296 was used; during measurement, the samples were placed in a stainless steel electrically shielded chamber (figure 3.4 and 3.5), which could be pumped down a pressure 10^{-3} Torr to perform measurements in vacuum.

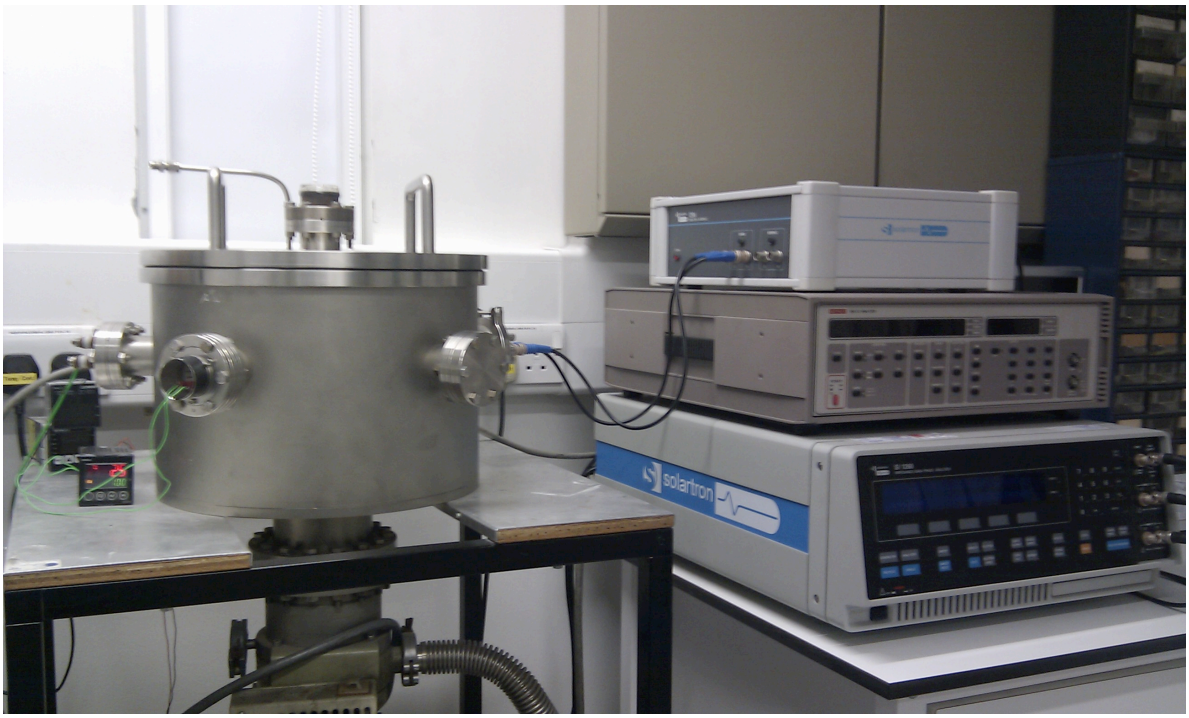

Figure 3.4: Solartron impedance analyzer SI1260 with a high impedance input module 1296 and stainless steel chamber at the Diamond Electronics laboratory at the London Centre for Nanotechnology

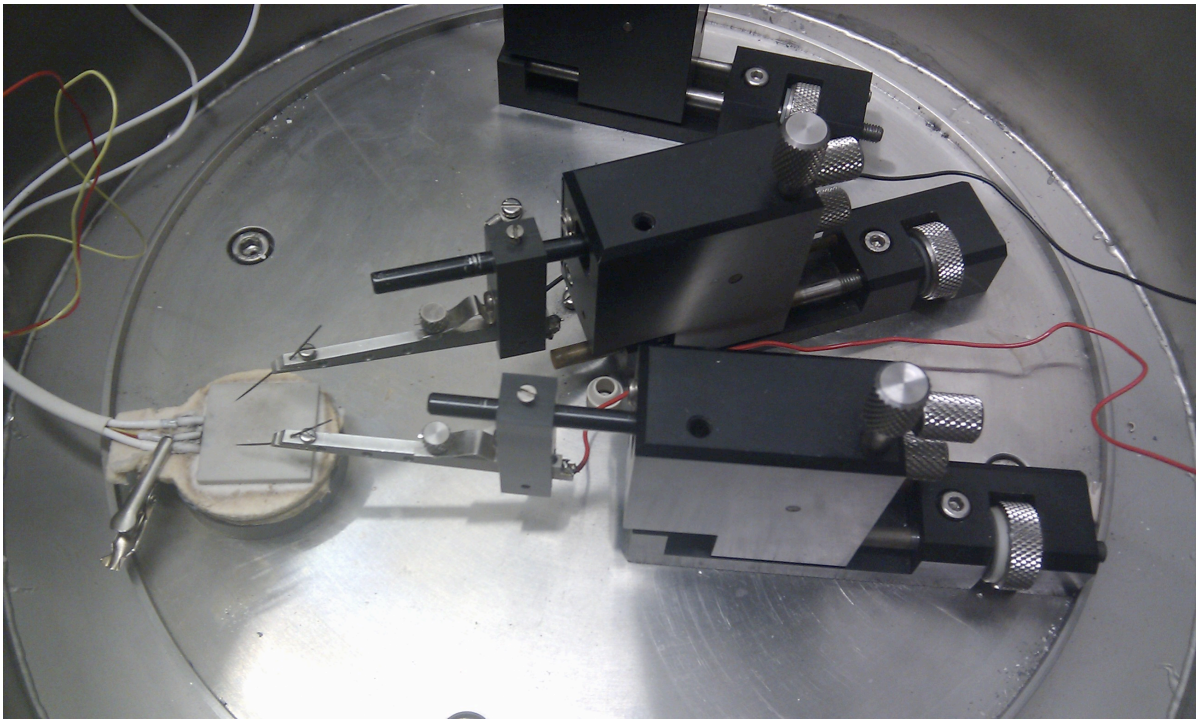

Figure 3.5: Details of the probing system within the stainless steel chamber used for impedance measurements

3.2 Hall effect measurements

Hall Effect measurement is an electro-magnetic characterisation used to determine some of the electrical properties of semiconductors and metals. It gives information on the carrier type, the carrier concentration and the mobility. If measurements are carried out over a temperature range, information about scattering mechanism of carriers, activation energy of dopants and factors governing the resistivity of a material can be gathered [3.28].

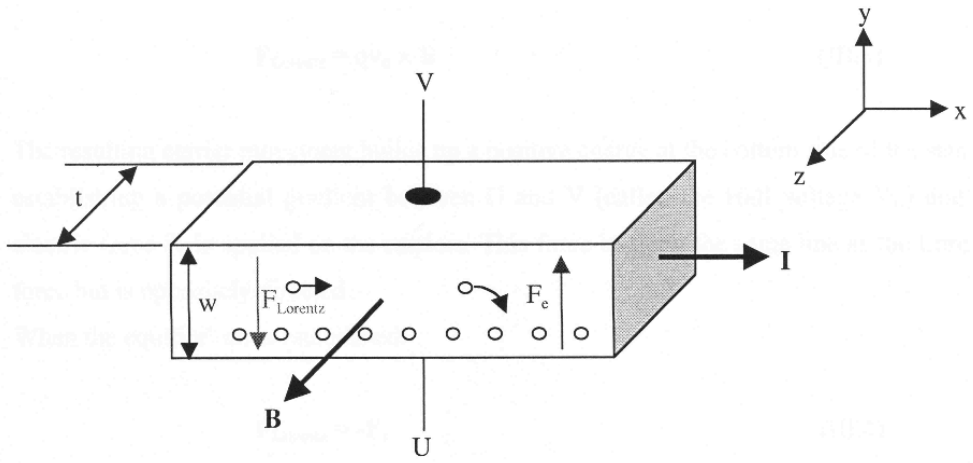

Figure 3.6: Hall effect in a p-type sample [3.28]

Figure 3.6 shows a p-type semiconductor with a carrier (hole) moving from left to right as a current I flows in the x-direction. This current is given by:

$$I = wtpqv_{dx} \tag{4.2}$$

where w is the width of the bar, t is the thickness, p is the density of holes, q is the electric charge and v_{dx} is the average drift velocity of carriers in the x direction.
When a magnetic field B is applied in the z-direction in conjunction with the current flow, a force called the Lorentz force deflects the carriers away from the current line towards the bottom of the sample as indicated in figure 3.6 by the hole with the curved arrow. This force is expressed as:

$$\mathbf{F_{Lorentz}} = q\mathbf{v_d} \times \mathbf{B} \tag{4.3}$$

The resulting carrier movement builds up a positive charge at the bottom side of the sample establishing a potential gradient between U and V (called Hall voltage V_H) and an

electric force F_e is applied on the carriers. This force is along the same line as the Lorentz force but is oppositely directed.
When the equilibrium is established:

$$\mathbf{F_{Lorentz}} = \mathbf{-F_e} \tag{4.4}$$

The Hall voltage can thus be derived:

$$\mathbf{F_{Lorentz}} = \mathbf{-F_e}$$
$$q\mathbf{v_d} \times \mathbf{B} = -q\mathbf{E}$$
$$\mathbf{E} = -V_H / w$$
$$v_{dx}B_z = V_H / w$$

therefore:

$$V_H = v_{dx}B_z w \tag{4.5}$$

Combining (4.4) and (4.5):

$$V_H = B_z I / tpq \tag{4.6}$$

From the above expression the density p of free carriers can be determined and from the sign of the Hall voltage the type of carriers can be identified.
The Hall mobility μ_H of the carriers is deduced from equation (4.7) provided the resistivity ρ of the material is known:

$$\mu_H = 1 / pq\rho \tag{4.7}$$

Equation (4.7) holds only under the assumption of energy-independent scattering mechanisms otherwise the Hall mobility has to be modified by a factor r, the Hall scattering factor. This factor depends on the scattering mechanism in the semiconductor and generally lies between 1 and 2. It is also a function of the magnetic field and temperature.

Hence taking into account the scattering factor r, the Hall mobility becomes:

$$\mu_H = r\,\mu_p \qquad (4.8)$$

where μ_H is the Hall mobility and μ_p is the conductivity mobility of the holes.
Conductivity mobilities can therefore differ significantly from the measured Hall mobilities. However the factor r was taken as unity in this work since the scattering mechanisms in diamond are not clearly identified.
The resistivity ρ of the material needs to be known to determine the carrier mobility. The four-point probe method is commonly used to measure the resistivity. The probes are arranged in line and are equidistantly spaced. A voltage drop is then measured between the two inner probes while a current is passed through the outer electrodes [3.25].
The sheet resistivity $\rho = \rho / t$ (expressed in Ω / cm) is normally used in calculations to determine the mobility when the thickness of the sample is not well defined. Using (4.6) and (4.7):

$$\mu_H = V_H\, t / B_z\, I\, \rho = V_H / B_z\, I\, \rho_s \qquad (4.9)$$

The Hall "bar" or the bridge type configuration [3.25] is normally the preferred way to derive the resistivity, the carrier concentration and the Hall mobility. However this geometrical configuration may not be convenient for characterizing thin films of material as it is difficult to process the required configuration using such thin films.
A more general geometry was developed by Van der Pauw [3.26, 3.27]. The Hall effect measurement evaluation is based on a conformal mapping of arbitrary shaped samples (figure 3.7) without the need to know the current flow paths in the sample. The following conditions must however be met:

1. The contacts are at the circumference of the sample.
2. The contacts are sufficiently small.
3. The sample is uniform in thickness.
4. The surface of the sample is singly connected, i.e. the sample does not contain isolated holes.

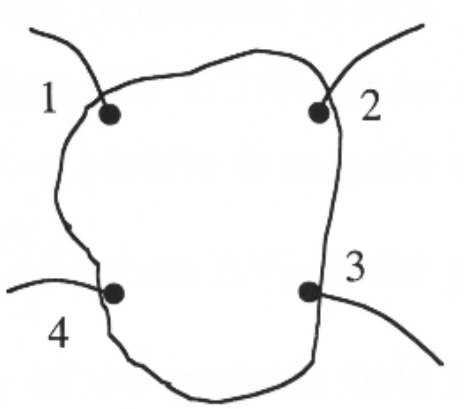

Figure 3.7: typical contact position in the van der Pauw configuration [3.28]

With reference to figure 4.17 the resistivity ρ is given by:

$$\rho = (\pi t / \ln 2) (R_{12,34} + R_{23,41}) / 2 F \qquad (4.10)$$

where t is the thickness of the sample, $R_{12,32} = V_{34} / I_{12}$, $R_{23,41} = V_{41} / I_{23}$, with $V_{xy} = V_y - V_x$ and I_{xy} being the current entering the sample through contact x and leaving through contact y; F is a correction factor and is a function of the ratio $R_{12,34} / R_{23,41}$. It is a measurement of the deviation from the symmetric situation, e.g. circular or square samples would have F = 1 [3.28].

Hall Effect measurements were performed to determine carrier densities and mobilities within the films studied. A Lakeshore Cryogenics System (1T electromagnet) was used to determine sheet resistance and carrier densities using the 'van der Pauw' approach, whereby four ohmic-like metal contacts (Au coated with Ag paste) are placed on the top side of the NCD film and in the four corners of square samples. Measurements were performed in a He atmosphere between 300 and 600 K. It is important to note that this system is capable of sequentially switching the direction of the applied electromagnetic field, enabling the Hall voltage to be accurately determined without the problems of background drift often associated with Hall measurements of wide band-gap materials.

This equipment allows data acquisition at temperatures ranging from 10 K to 800 K under a magnetic field of 10.4 kG. In practice the field was switched from positive to negative values. As a result twice the Hall voltage was measured: $V_H = \Delta V_{12} / 2$, where ΔV_{12} is the potential difference between contacts 1 and 2 when the polarity of the magnetic field is changed from positive to negative with the current flowing from contact 3 to 4 [3.28].

The measurements were performed in such a way to maximize the signal-to-error ratio.

In the current work, a Lakeshore Cryogenics System 1 Tesla electromagnet was used to carry out Hall measurements (figure 3.8)

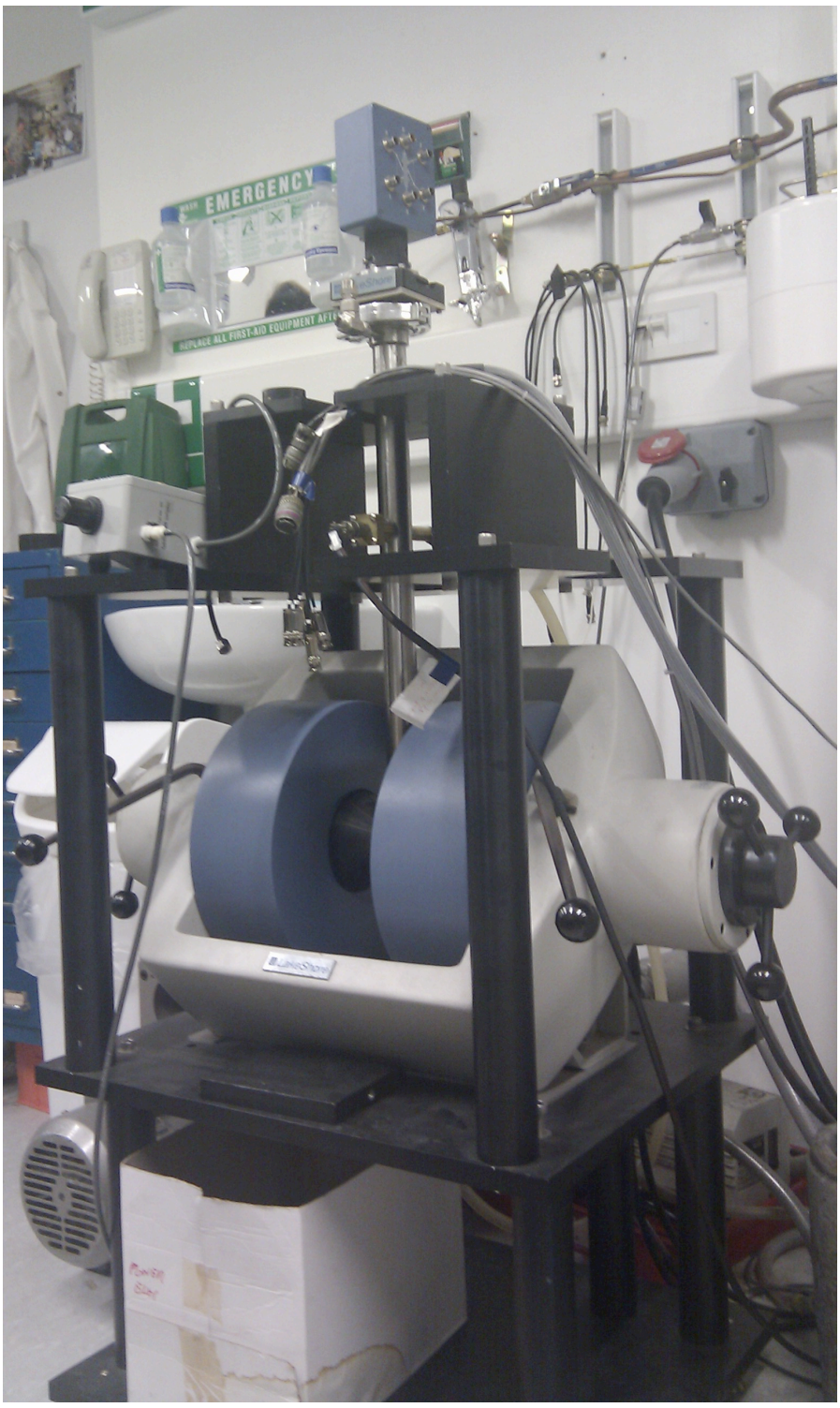

Figure 3.8: Lakeshore Cryogenics System 1 T electromagnet used for Hall measurements in the Diamond Electronics laboratory at the London Centre for Nanotechnology

3.3 Fourier Transform Infrared Spectroscopy

Fourier Transform Infrared Spectroscopy is a measurement technique that allows recording infrared spectra.

3.3.1 Vibrational spectroscopy

When two or more atoms are bonded together to form a molecule many different modes of mechanical vibration are possible. A diatomic molecule with two atoms of mass m_1 and m_2 can be treated as two particles bonded together by a spring with a force constant k. The frequency of vibration is given by:

$$f = (1/2\pi) \times (k/\mu)^{-1/2} \qquad (5.2)$$

where μ is the reduced mass of the two particles such that $\mu = m_1m_2/(m_1 + m_2)$ [3.29]. The diatomic molecule can also have different modes of rotation. It happens that the frequency of molecular vibrations usually lies in the infrared region of the electromagnetic wave spectrum. Infrared absorption spectroscopy can therefore be used to study the various modes of mechanical vibrations in molecule. It happens that in polyatomic molecules the frequencies of mechanical vibrations can be used to identify the various types of bonds and functional groups present in the molecule. This is the basis of the popularity of infrared absorption spectroscopy in both organic and inorganic chemistry [3.30].

For infrared spectroscopy, the selection rule is that the electric dipole moment of the molecule must change during vibration in order for a particular vibration mode to be infrared active. Symmetric vibrations are therefore forbidden because the electric dipole moment will not change. The symmetric stretch mode of carbon dioxide, for example, is not IR active [3.30].

3.3.2 Terminology

In infrared spectroscopy the term “wavenumber”, which is defined as the reciprocal of the wavelength and thus proportional to the frequency, is widely used. Wavenumber is expressed in cm^{-1}. Transmittance T is defined by $T = I/I_0$, where I is the intensity of light transmitted through the sample and I_0 is the intensity of light incident on the sample. Absorbance A is defined by $A = \log (1/T)$. The infrared spectrum obtained by FTIR spectrometer is in the form of either transmittance T or absorbance A plotted against wavenumber (figure 3.9).

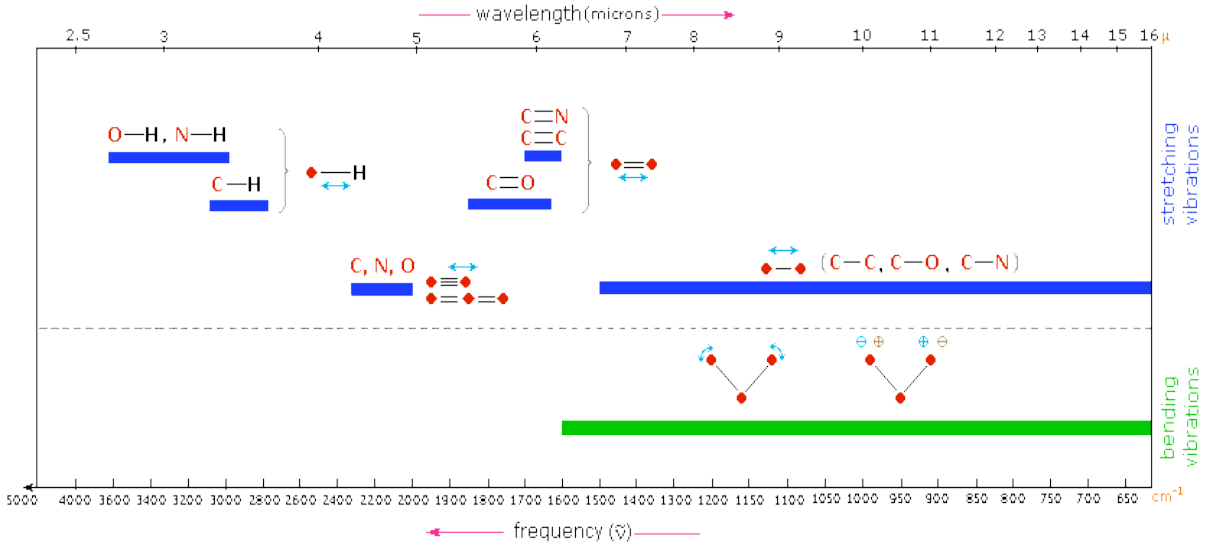

Figure 3.9: Stretching and bending absorptions within the infrared range [3.31]

3.3.3 Fourier transfer infrared spectrometry

The principle behind Fourier Transform Infrared Spectroscopy (FTIR) is essentially based on the Michelson Interferometer (figure 3.10).

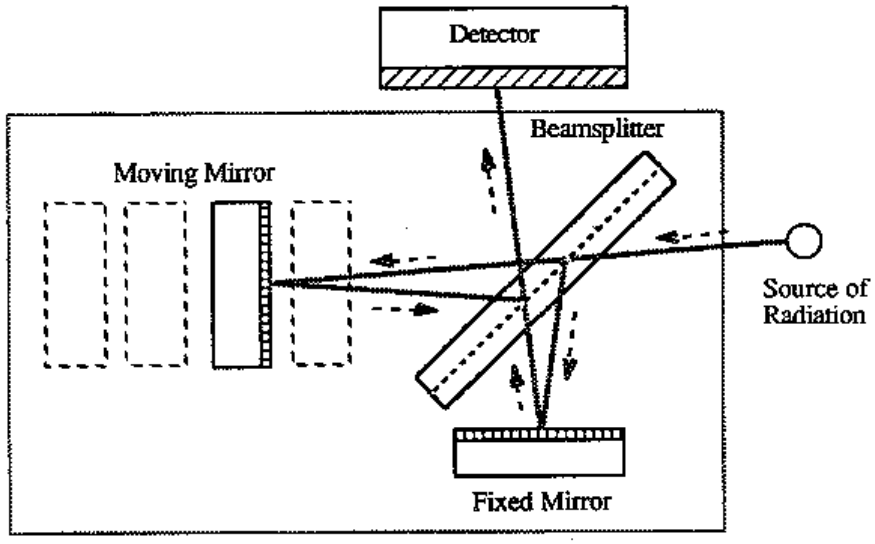

Figure 3.10: schematics of Michelson's interferometer [3.31]

The Michelson interferometer consists of a beamsplitter, a fixed mirror and a moving mirror. Collimated radiation from the broadband infrared source is directed into the interferometer and impinges on the beamsplitter. The beamsplitter splits the incoming beam into two beams of equal intensity. Approximately half of the infrared radiation from

the source is transmitted through the beamsplitter and directed onto the fixed mirror, whereas the other half reflects off the beamsplitter and is directed onto the fixed mirror. The beams reflect off the surfaces of the two mirrors and recombine at the beamsplitter, where constructive and destructive interference occurs depending on the position of the moving mirror relative to the fixed mirror. The resulting beam passes through the sample where selective absorption takes place and then continues onto the detector. The scan in FTIR spectroscopy is achieved by the mechanical displacement of the moving mirror assembly. The detected signal as a function of the position of the moving mirror is called on"interferogram", and is fed to a computer. A data-processing technique called Fourier Transform turns this raw data into the desired result, i.e. the sample's spectrum [3.30].

3.3.4 Transparent substrates

When FTIR is applied to thin films relevant to microelectronics, the infrared absorption spectrum of a thin solid film or an infrared-transparent substrate is needed.

Even though silicon is a very good infrared material in terms of transparency, it is not perfect due to five factors: 1) infrared absorption due to lattice vibrations: in monocrystalline silicon, its atoms can have collective lattice vibration modes known as phonons; various absorption peaks in the infrared absorption spectrum of silicon are assigned to various combinations of phonons; 2) infrared absorption due to impurities; 3) free-carrier absorption: in semiconductors, electrons at the bottom of the conduction band can absorb infrared radiation to go up to energy levels slightly higher than the bottom of the conduction band; 4) plasma resonance, defined as the collective vibration of electrons or holes with respect to the fixed atoms in semiconductors; the substrate is transparent for frequencies above the plasma resonance frequency. In semiconductors, the plasma resonance frequency lies within the infrared region; 5) surface roughness: silicon substrates are usually highly polished only on one side, and it has been proved that the rough side can scatter infrared light significantly [3.29].

Potassium Bromide (KBr) does not influence the infrared spectrum in the wavenumber range 4000 – 400 cm^{-1}. This technique can be used when the sample material can be crushed or ground. Two milligrams of sample is mixed with 200 mg of KBr powder. The mixture is pressed into a tablet, which is then used for analysis [3.32]. This technique was used by the author in the current work to analyse DND powder.

FTIR has been extensively used to investigate the presence of various functional groups on the surface of DND [3.33-3.36].

3.4 Atomic Force Microscope (AFM)

Atomic Force Microscopy is a type of high resolution scanning probe microscopy capable of imaging almost any kind of surface, including insulators, with a resolution in the order of fractions of a nanometer [3.37]. For this reason it was chosen to investigate the surface profile of the highly smooth polished CVD single crystal diamond used to build the photoconduction devices studied in the current work.

As a technique, it was used by Cheng and co-authors [3.38] to investigate the validity of a series of novel methods for polishing the surface of CVD diamond.

Their best result consisted in obtaining an average surface roughness of less than 20 nm after prolonged treatment. The minimum roughness peak (Ra) was less than 10 nm as shown in figure 3.11.

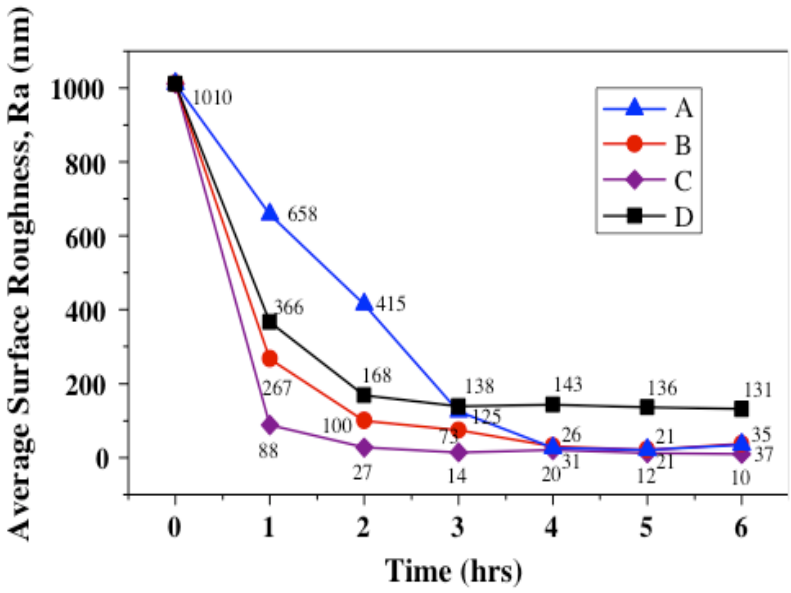

Figure 3.11: Average surface roughness of polished CVD diamond films [3.38]

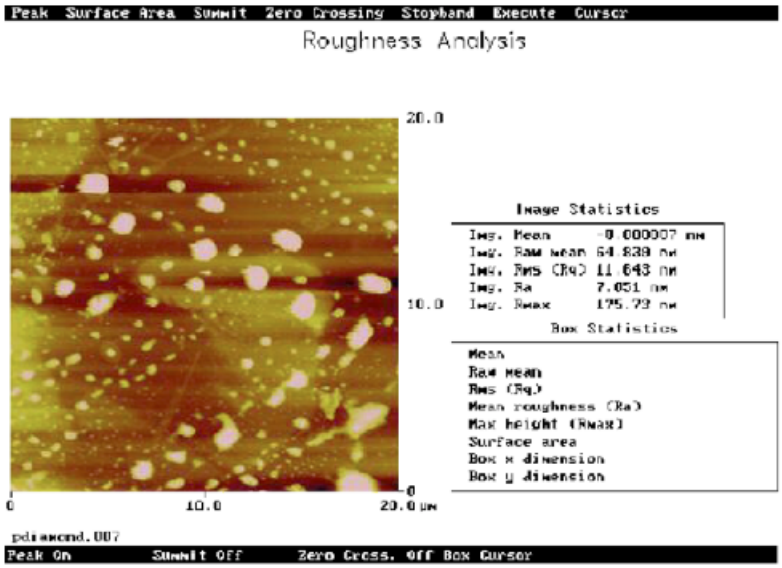

Figure 3.12: Atomic Force Microscope (AFM) image of polished CVD diamond film [3.38]

Terry and co-authors [3.39] used AFM to compare mechanically and manually polished CVD diamond surfaces whose crystals bore different orientations. Their results are summarized in table 3.1.

Face	Groove widths after mechanical polish (µm)	Groove widths after manual polish (µm)	Groove widths after mechanical polish (nm)	Groove widths after manual polish (nm)	Small roughness after mechanical polish (µm)	Small roughness after manual polish (µm)
(100)	0.1 to 1.7	0.05 to 0.4	0.1 to 4.8	0.2 to 4.5	0.03	0.014
(110)	0.05 to 0.7	0.05 to 1.2	0.13 to 7.2	0.13 to 5	0.05	0.015
(111)	0.05 to 0.7	0.05 to 0.5	0.1 to 1.1	0.05 to 1	0.04	0.03

Table 3.1: Approximate ranges of most of the observed polished surface roughness on the three low index faces [3.39]

Their study gives evidence of roughness profiles perpendicular (figure 3.13b and figure 3.13e) and parallel (figure 3.13c and figure 3.13f) to the polishing grooves. In the case of the manually polished (100) oriented substrate, the following profiles were obtained:

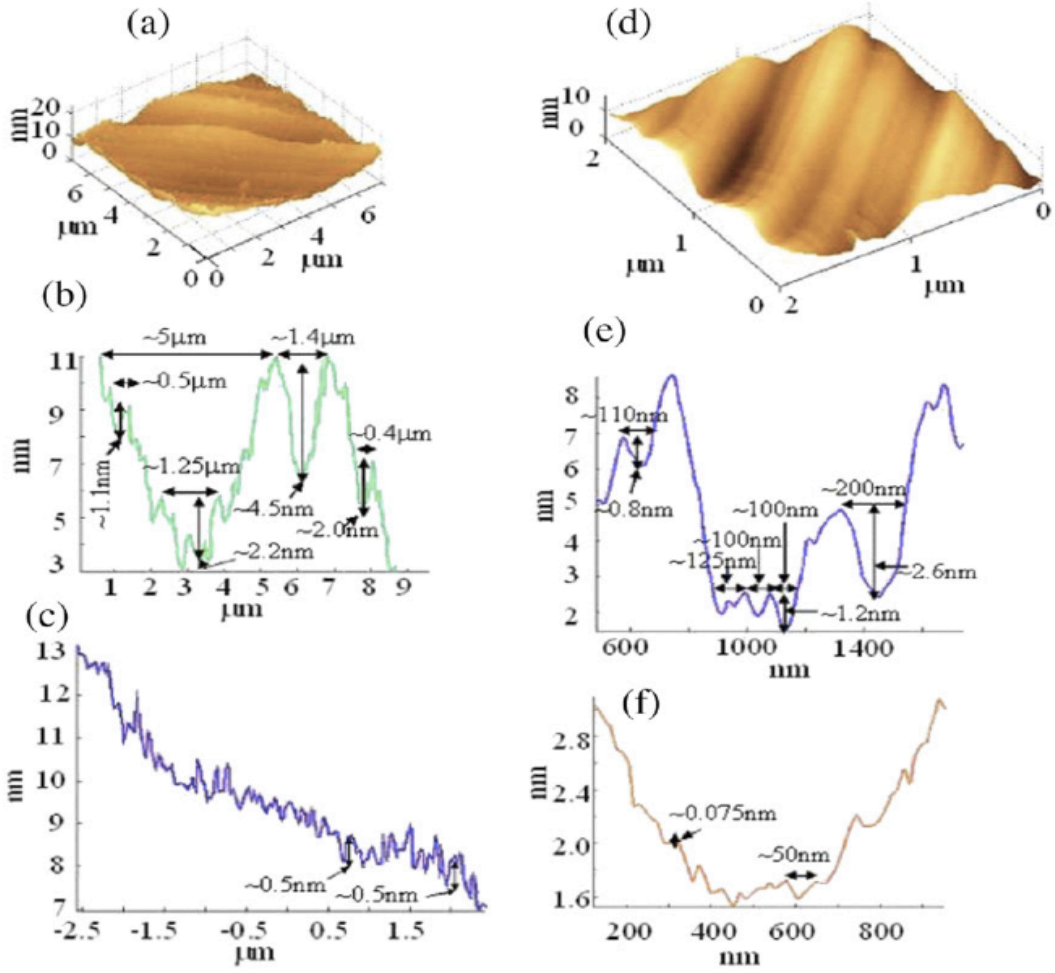

Figure 3.13: A (100) surface polished both mechanically and manually. Figures (a) and (d) show the 3-dimensional AFM images for the mechanically and manually polished surfaces respectively, while graphs (b) and (e) are the line profiles obtained perpendicular to the polishing grooves respectively. Graphs (c) and (f) are similar to graphs (b) and (e), but obtained along or inside the polishing grooves [3.39]

Mechanically polished (100) surfaces were found to be below 1.5 nm on average, while the manually polished surfaces ranged in RMS roughness up to 2.5 nm. The line profiles shown in figure 3.13c and figure 3.13f showed that the roughness decreased on average from 0.5 to 0.25 nm following manual polishing.

3.5 Surface preparation

3.5.1 Single-crystal diamond

Single crystal diamond substrates were subjected to wet treatments that are known to leave the surface free from contamination and in an oxidised state avoiding so-called “surface conductivity”. The procedure used is described below [3.40]:

1. Acetone, Isopropanol and de-ionised H_2O rinse in ultra-sonic bath for 1 minute, respectively.
2. Immersion in a 1:1 solution of HCl (conc.) and HNO_3 (conc.) at 45 ^{0}C for 15 minutes.
3. Immersion in a solution of 2.5% non-residual soap and 97.5% de-ionised H_2O, in an ultra-sonic bath for 5 minutes.
4. Immersion in de0ionized water in an ultra-sonic bath
5. Immersion in a 1:1 solution of H_2O_2 (conc.) and H_2SO_4 (conc.) at 100 ^{0}C for 25 minutes.
6. Same as in 3.
7. Same as in 4.
8. DC plasma treatment, 95% Helium and 5% Oxygen, at 0.5 Torr and 200 W for 2 minutes.
9. Same as in 8, but on the other side of the sample.
10. Immersion in molten $NaNO_3$ (350 ^{0}C).
11. Same as in 3.
12. Same as in 4.
13. Same as in 10.
14. Same as in 3.

3.5.2 Polycrystalline diamond

Polycrystalline diamond is grown on Silicon, which does not withstand the strong acid treatment given to single-crystal diamond.
Therefore, only step 1 of the cleansing procedure was used in this case.

3.6 Metal Deposition

The method used to deposit the electrodes was thermal deposition, an inexpensive and simple technique that nonetheless produces high quality metal layers, particularly suitable for depositing metals such as Gold, Chromium and Aluminium, [3.41, 3.42]. The thermal evaporator used was an Edwards A360 Bell Jar (figure 3.14); having loaded the machine with diamond substrates, deposition was initiated once a base pressure of approximately 10^{-7} mBar was achieved.

Figure 3.14: Edwards A360 Bell Jar in the London Centre for Nanotechnology

When choosing the metals to build the device electrodes the desirable characteristics of a metallization system were taken into account: good adhesion to the substrate, low stress, good electrical conductivity and minimal reactions at subsequent temperatures [3.43]. Gold and Chromium were chosen as metals to create the device electrodes. Gold protects the surface from the environmental attack and helps to ensure bonding ability. It has good soldering ability and is an extremely inert metal, which protects it from oxidation. However, since Gold is a noble metal, it has poor adhesion to diamond, which is chemically inert [3.43].

There are two classes of metals that are known to form carbides with diamond at high temperature: refractory metals such as Titanium, Tungsten and Molybdenum and transition metals such as Chromium, Nickel and Iron. Chromium has been extensively used in many MCM technologies as an adhesion promoter and diffusion barrier metal.

The thickness of the Chromium layer was chosen to be 10 nm, whereas the thickness of the Gold layer was chosen to be 200 nm. Metals were deposited at a rate of approximately 0.5 nm/s. In the adhesion study of different metals to CVD diamond conducted by Meyyappan and co-authors [3.43], these figures yielded maximum adhesion compared to all the other set values (table 3.2).

The value of 11.8 klbf/in^2 is considered excellent by the authors.

Deposition rate (Å/s)	Thickness (Å)	Adhesion (klbf in^2)
5	5000	4.96
5	3000	11.82
10	5000	9.45
15	5000	9/09
15	1000	10.28
5	1000	9.85
5	5000	5.85
5	3000	11.17

Table 3.2: Adhesion values of evaporated Au/Cr/diamond samples [3.43]

3.7 Photolithography

Standard photolithographic methods for defining device geometries on a smooth, flat semiconductor surface are a well-developed and characteristic technology [3.42]. Every diamond substrate was subjected to the initial degrease treatment in step 1 of the procedure described in 6.3.2. Substrates were then placed on a hotplate at 140°C for 20 minutes; in order to assure temperature uniformity, they were covered by a clean Petri dish. After a cooling period of approximately 5 minutes, substrates were then place in a closed container together with a few drops of Hexamethyldisilazane (HMDS) 98% for 15 minutes without letting the drops come in contact with the samples. HMDS enhanced adhesion between the photoresist and the sample surface. The photoresist used was Microposit S1805, suitable for manufacturing patterns in the order of the tens of microns [3.44].

After placing a single substrate on the spinner platform, a drop of S1805 photoresist was dropped on the substrate with a glass pipette. Based on empirical knowledge, aimed at achieving as much resist uniformity as possible, the initial spinning velocity was 1000 rpm, maintained for 2 seconds, then 4000 rpm following a rapid ramp and maintained for 30 seconds. This creates a 0.5 μm thick layer of photoresist.

The substrates were then placed on a hotplate, covered by a clean Petri dish, at 115°C for 60 seconds in order to harden the photoresist. A thermocouple was used to check the temperature to ensure it did not fall above or below the standard, as otherwise it would compromise the quality of the photoresist which is absolutely necessary in the following steps.

When photolithography is performed on large Silicon substrates, nearly perfect photoresist uniformity in their active area is normally achieved. However, single-crystal diamond samples are much smaller than Silicon, in this case being 4.2 × 4.2 mm. Such small

dimensions caused the formation of a photoresist edge bead after spinning. In order to eliminate such beading that would have otherwise compromised photoresist uniformity, a 2.5 × 2.5 mm piece of Silicon was placed on top of each substrate prior to exposure to UV light. UV light was then shone on the substrates for more than 2 minutes exceeding 600 mJ/cm^2 and then immersed in MF319 ion-free developer until total disappearance of the photoresist edge bead, by visual inspection. This time interval is typically below 1 minute. Rinsing in de-ionised water and blowing dry with N_2 followed.

A Karl-Suss MJB3 aligner (figure 3.15) was used to align each sample with the desired mask pattern that was previously selected.

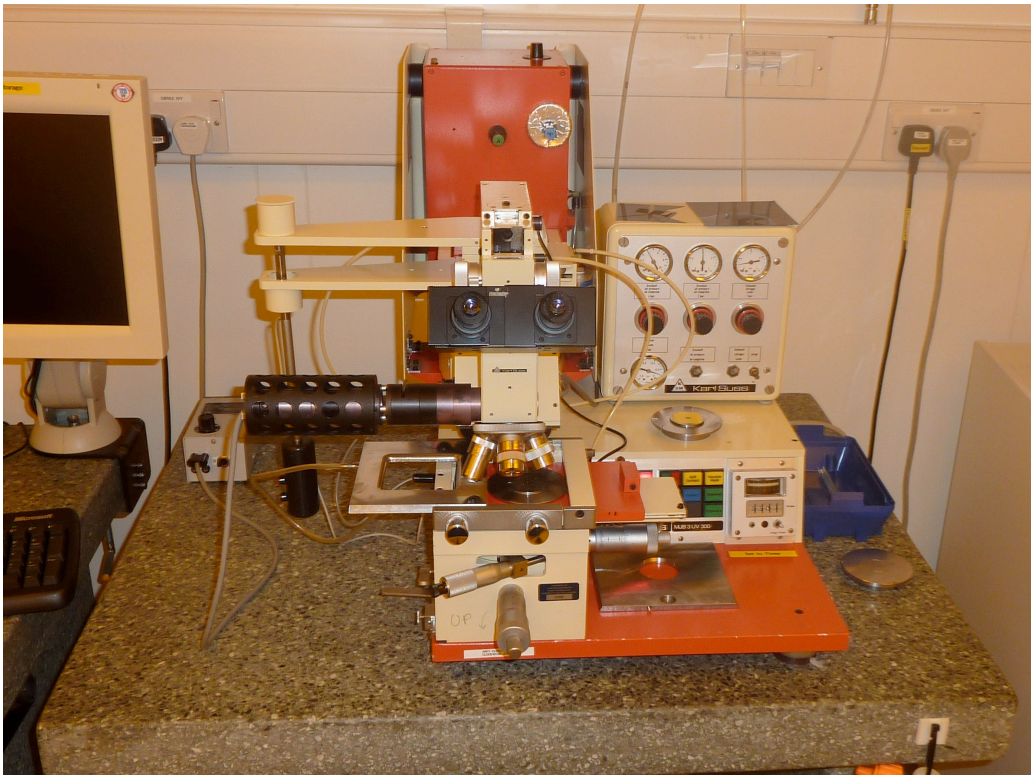

Figure 3.15: Karl Suss MJB3 aligner in the London Centre for Nanotechnology

The substrates were then exposed to UV light for exactly 1 second; such a time interval was empirically worked out by means of trial and error in previous attempts, in which the developing time was fixed and then the exposure time was slightly increased or decreased.

3.8 Wet-etching

Following exposure to UV radiation, samples were then immersed in a MF319 developer (Sodium Hydroxide) for about 40 seconds with mild agitation, then rinsed for 1 minute in de-ionised water and dried with Nitrogen.

Diamond substrates were then subjected to wet etching; samples were first immersed in Gold etchant (Iodine) with mild agitation for about 30 seconds, then in Chromium etchant until disappearance by visually inspection (typically after 45 seconds). Acetone was used to remove the photoresist, followed by Isopropanol and de-ionised water to maintain the surface radical-free.

References

[3.1] MacDonald JR, *Impedance Spectroscopy*, Wiley, New York (1987)

[3.2] Bauerle J.E., Journal of Physics and Chemistry of Solids **30** (1969) 565

[3.3] Armstrong R.D., Journal of Electroanalytical Chemistry **53** (1974) 389

[3.4] Schouler E.J.L., Journal of the Electrochemical Society 128 (1981) C124

[3.5] Khan N., PhD Thesis, University of London (1990)

[3.6] Tuller H.L., Solid State Ionics **131** (2000) 143

[3.7] Maier J, Progress in Solid Status Chemistry **23** (1995) 171

[3.8] Van Dijk T, and Burggraaf A.J., Physica Status Solidi A **63** (1981) 229

[3.9] Verkerk M., Middlehuis B.J. and Burggraaf A.J., Solid State Ionics **6** (1982) 159

[3.10] Godickemeier M, Michel B., Orliukas A., Bohac P., Sasaki K., Gauckler L., Heinrich H., Schwander P., Kostorz G., Hofmann H. and Frei O., J. Mater. Res. (1994) 1228

[3.11] Fleig J., Solid Status Ionics **131** (2000) 117

[3.12] M'Peko J.C., Spavieri D.L. and de Souza M.F., Applied Physics Letters **81** (2002) 2827

[3.13] Nistor L.C., Landuyt J.V., Ralchenko V.G., Obraztsova E.D. and Smolin A.A., Diamond and Related Materials **6** (1997) 159

[3.14] Daniel Vera V.*, Dielectric Relaxation*, Academic Press, London (1967)

[3.15] Hodge I.M., Ingram M.D. and West A.R., Journal of Electroanalitycal Chemistry **58** (1975) 429

[3.16] Huanosta A., Alvarez-Fregoso O. and Amano E., Journal of Applied Physics **69** (1991) 404

[3.17] Kumar M.M. and Ye Z.G., Journal of Applied Physics **90** (2001) 934

[3.18] Garcia I., Olias J.S., Rueda F.A. and Vazquez A.J., Diamond and Related Materials **6** (1997) 1210

[3.19] Veerasamy V.S., Diamond and Related Materials, **2**, (1992) 782

[3.20] Aoki M., Chiang Y.M., Kosacki I., Lee L.J., Tuller J. and Liu Y.P., Journal of American Ceramics Society **79** (1996) 1169

[3.21] Volger J., Progress in Semiconductors **4** (1960) 209

[3.22] Vendik I.B., Vendik O.G., Deleniv A.N., Kondratiev V.V., Goubina M.N. and Kholodniak D.V., IEEE Transactions On Microwave Theory and Technology **48** (2000) 1247

[3.23] Vendik O.G., Zubko S.P. and Nikolski M.A., Technical Physics **44** (1999) 349

[3.24] Hench L.L. and West J.K., *Principles of Electronic Ceramics*, Wiley, New York (1989)

[3.25] Schroder D.K., *Semiconductor Material and Device Characterization*, 2nd ed. (Wiley, New York, 1998)

[3.26] Van der Pauw L.J., Phil. Res. Rep., **13**, 1 (1958)

[3.27] Van der Pauw L.J., Phil. Tech. Rev., **20**, 220 (1958)

[3.28] Curat S, PhD thesis, University of London (2006)

[3.29] Meloan C.E., *Elementary infrared spectroscopy*, Macmillan, New york, (1963)

[3.30] Lau W.S., *Infrared Characterization for Microelectronics*, World Scientific Publishing Co. Pte. Ltd. (1999)

[3.31] Available at: http://www.cem.msu.edu

[3.32] Available at: http://www.sintef.no/Home/Materials-and-Chemistry

[3.33] Jiang T., Journal of Chemical Society, Faraday Transactions, **92** (1996) 3401

[3.34] Mironov E., Koretz A. and Petrov E., Diamond and Related Materials **11** (2002) 872

[3.35] Mitev D., Dimitrova R., Spassova M., Minchev Ch. And Starev S., Diamond and R elated Materials **16** (2007) 776

[3.36] Koshcheev A.P., Russian Journal of Physical Chemistry A **82** (2009) 10

[3.37] (2002-2010) *Atomic Force Microscopy.* Available at: http://www.nanoscience.com/education/afm.html

[3.38] Cheng C.Y., Tsai H.Y., Wu C.H., Liu P.Y., Hsieh C.H. and Chang Y.Y., Diamond and Related Materials **14** (2005) 622

[3.39] Terry T.E., van der berg N. and Makau N.W., Diamond and Related Materials, **17** (2008) 127

[3.40] Williams O.A. and Jackman R.B., Journal of Applied Physics **96** (2004) 3742

[3.41] Jaeger R. C., *"Film Deposition. Introduction to Microelectronic Fabrication",* Upper Saddle River, N.J. Prentice Hall, 2002

[3.42] Sze S.M., *Semiconductor devices: Physics and Technology*, New York, Wiley,

[3.43] Meyyappan I., Malshe A.P., Naseem H.A. and Brown W.D., Thin Solid Films **253** (1994) 4072002

[3.44] Rohm and Hass. (2006). *Microposit SI800 G2 Series Photoresists.* Available at: http://home.snafu.de/microresist/products/room_haas/pdf/Microposit_S1800_G2_Serie.pdf

Chapter 4

Nanocrystalline diamond as an electronic material

4.1 Introduction

In the group of wide band gap materials (including silicon carbide and gallium arsenide), diamond can be considered extreme in its intrinsic electronic properties as shown in figure 4.1. The unmatched combination of highest bulk thermal conductivity, high carrier mobility and high breakdown voltage makes diamond suitable for applications in environments too demanding for other materials and devices. Diamond electronic devices such as high-power diodes and high-frequency field effect transistors can be expected to show outstanding performance [4.1].

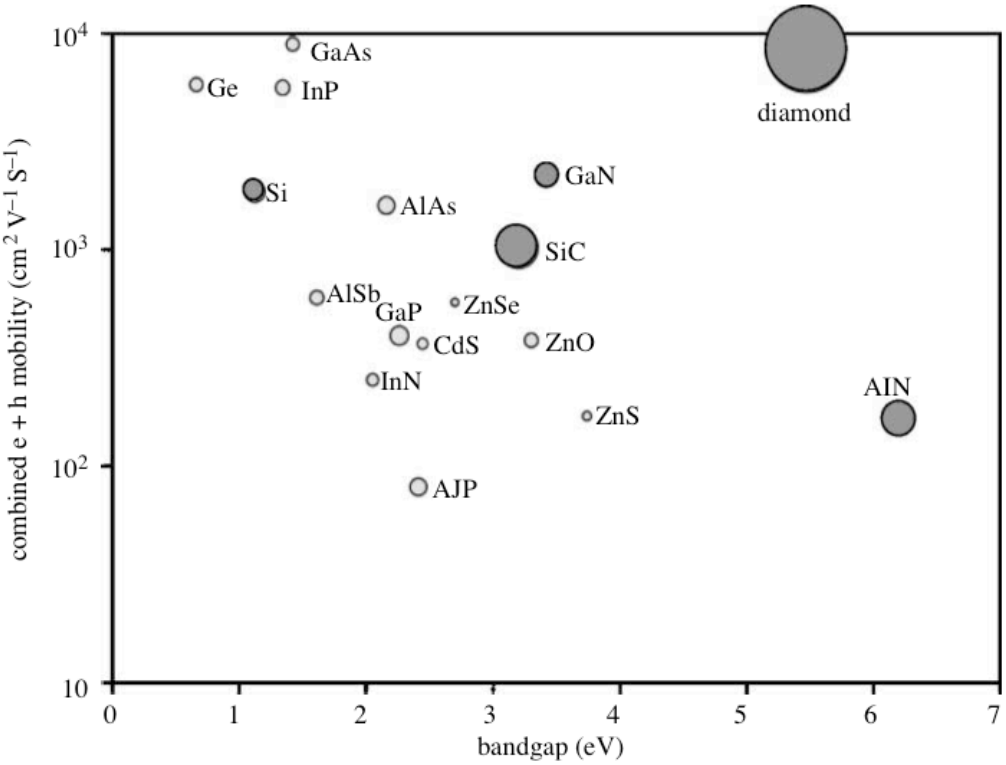

Figure 4.1: Comparison of diamond's combined carrier mobility, band-gap and thermal conductivity with other semiconductors (the area of each circle is proportional to the material's thermal conductivity) [4.1]

There are also potentially important passive uses for diamond within electronics, for example as a more thermally effective insulator layer than SiO_2 within 'silicon-on-insulator' (SOI) technologies. As circuits become smaller and more complex, self-heating effects in SOI devices occur due to the poor thermal conductivity of the buried silicon dioxide (SiO_2) layer. To overcome this problem a thinner oxide insulator could be used, but that would increase substrate parasitic capacitances. Diamond has a thermal conductivity twenty times higher than silicon, four times higher than copper and one thousand times higher than silicon dioxide, so it is expected that self-heating effects in devices fabricated

on silicon on diamond (SOD) material could be suppressed [4.2].

The use of chemical vapour deposition (CVD) methods for the formation of homoepitaxial diamond films is well established; the technique has been reviewed in chapter 2. Understanding and monitoring CVD-grown single-crystal diamond is useful for the fabrication of a wide range of electrical and mechanical devices, for which it is critical to carefully introduce dopants or defects to give the grown films the desired properties [4.3].

High-quality CVD single-crystal diamond crystals have been grown to sizes of up to 9×9 mm, which is currently the largest available [4.4]. Despite such remarkable achievements, even the largest diamond wafer cannot find extensive applications in the electronic industry. Only wafers as large as those available with Silicon can permit the fabrication of high-power devices necessitating large areas, within which large current intensities can flow. Moreover, large wafers can permit the fabrication of multiple devices within a single substrate, making the manufacturing process more practical and reducing costs.

Attempts to grow CVD diamond on non-diamond substrates such as silicon led to polycrystalline materials (PCD) whose properties are strongly influenced by the presence of numerous grain boundaries, which are expected to have a significant influence on the charge transport in devices fabricated from this material [4.5].

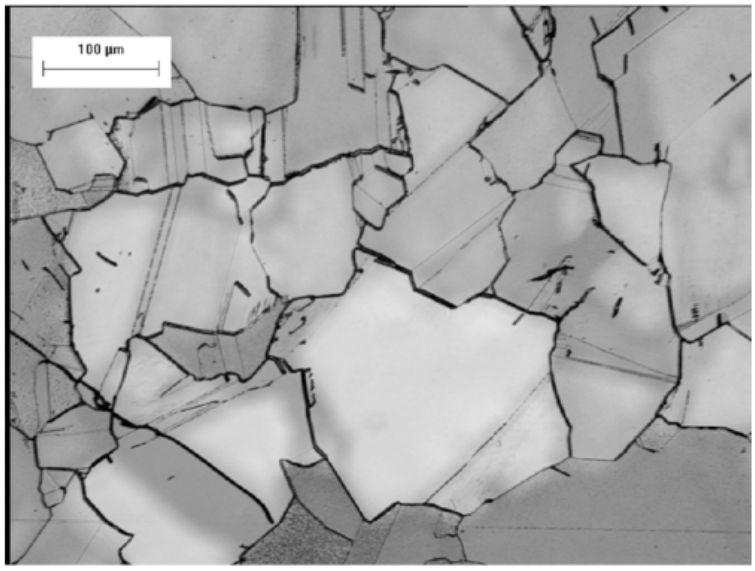

Figure 4.2: Optical microscope image of microcrystalline diamond (MCD) with an average grain size of 110 µm, and maximum grain size approximately 350 µm. The sample was annealed at 900°C in air to enhance the contrast between the boundaries of the grains and their interior [4.5]

PCD films with grain boundaries less than 100 nm in size are called nanocrystalline diamond (NCD). The detrimental effect that grain boundaries have on the properties of

NCD due to their graphitic content was fully discussed in chapter 2

When considering the growth of NCD it is important to classify the nucleation density at the onset of growth of the film since this will control the grain boundary density. Attempts to grow fully dense NCD, where any non-diamond carbon material centred at the grain boundary regions is minimised, have focused on the use of a nanodiamond seeding process to enhance the nucleation density of the NCD as it begins to grow, followed by high quality diamond growth condition. Philip and co-authors [4.6] reported the elastic and thermal properties of NCD films displaying columnar structure with grain size less than 100 nm in diameter and film thickness of the order of 1 to 5 μm; these films were produced using an ultrasonic seeding method using explosively formed nanodiamond powder, which promotes nucleation densities from 10^{10} to greater than 10^{12} cm^{-3}. The grain size and optical quality of the films were characterized by scanning electron microscopy and Raman measurements; surface acoustic wave (SAW) method and travelling wave technique (TWT) were used to characterize the elastic and thermal properties of the films.

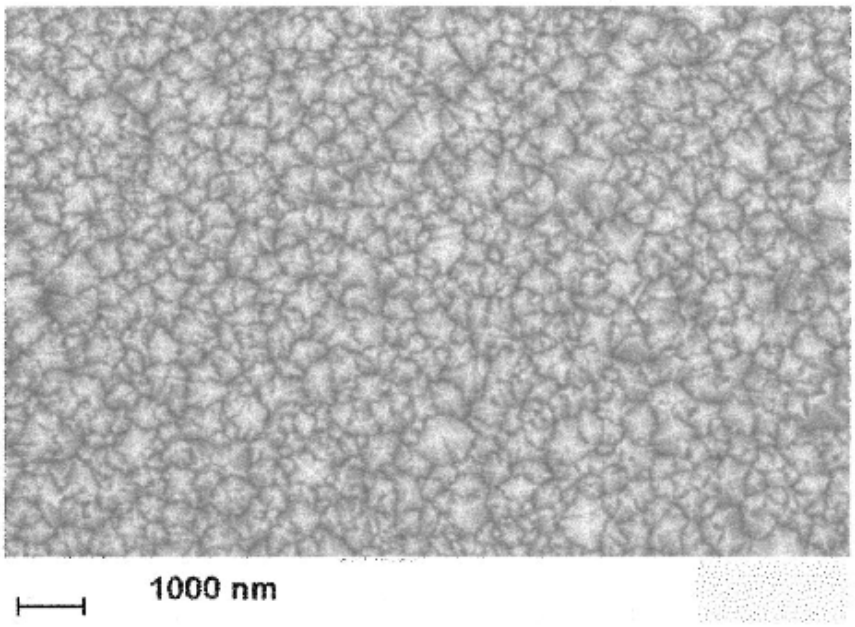

Figure 4.3 Scanning electron microscope image of a portion of the growth surface of the film [4.6]

For films grown with nucleation densities greater than 10^{12} cm^{-3}, the Young Modulus and thermal diffusivity were more than twice that of NCD films grown with a lower nucleation density (less than 10^{10} cm^{-3}), with values approaching those of high quality large grain CVD diamond.

These results imply high density seeding followed by optimised (high-quality) growth

conditions can successfully lead to the formation of near-to fully dense NCD materials, which have found utility in microelectromechanical systems (MEMS) [4.7] and nanoelectromechanical systems (NEMS) [4.8] devices.

This chapter reports on the electronic properties of a highly dense form of NCD (both intrinsic and lightly boron-doped) grown by Dr. James E. Butler in the Naval Research Laboratories (Washington DC, USA) using a novel seeding technique.

In its intrinsic form the NCD films studied behave as a near-to-ideal dielectric material. The films were investigated using a technique (Impedance Spectroscopy) capable of differentiating between the electrical conduction that occurs within the grains in the NCD and that occurring in between the grain boundaries, allied to Hall effect measurements. In this way it was possible to show that in the form of state-of-the-art fully dense NCD used here, boron within 'grain boundaries' behaves in a similar fashion to boron within grain interiors, supporting the idea that this material can be considered for electronic applications.

4.2 Experimental methods

4.2.1 Growth conditions

The NCD films investigated in this chapter were kindly provided by the Naval Research Laboratories, (Washington DC, USA). Such films were grown on silicon substrates with a thermally produced oxide layer of around 100 nm. The purpose of the oxide layer was to isolate the NCD from the silicon during electrical measurements. The oxide-coated silicon layer was ultrasonically treated with nanocrystalline diamond powder suspension in ethanol leading to a nucleation density greater than 10^{12} cm^{-3}.

For intrinsic NCD microwave enhanced plasma CVD was carried out with a microwave power of 800 W and a substrate temperature of 750°C using a gas flow of 300 sccm of H_2 and 0.8 sccm of CH_4. The CVD system had not been previously used for boron-doping experiments, ensuring that the films grown were free from any boron contamination. The resultant NCD films were approximately 1.5 μm thick with a grain size of the order of 100 nm. Similar conditions were used in a boron-contaminated CVD system for the growth of boron-doped films; the resultant NCD films were approximately 1.6 μm thick with a grain size of the order of 50 – 100 nm. More detailed information on the seeding and growth process can be found elsewhere [4.6]. As-grown films were first cleaned by boiling in acid solutions to remove any residual surface conductivity due to organic contaminants and

adsorbate-hydrogenated surface complexes [4.9, 4.10].

4.2.2 Impedance spectroscopy and Hall effect measurements

Impedance spectroscopy has been previously deployed to study the properties of single crystal and polycrystalline diamond films to some effect [4.11 – 4.15]. This technique, fully reviewed in chapter 3, involves the measurement of the real and imaginary components of the films impedance as a function of both frequency and temperature. The impedance as a complex number, can be defined as:

$$Z(\omega) = Re(Z) + Im(Z)$$

where the real part refers to resistive contributions and the imaginary part to the capacitive. Hence any contributions to the over all impedance measured that have strongly differing RC components can be identified. In a typical impedance spectroscopic IS analysis, the impedance is measured as a function of frequency, and the real component plotted against the imaginary component as the frequency is changed. These so-called "Cole–Cole" plots may then reveal differing semi- circular responses for each RC component of the film. In the present case, a Solartron impedance analyzer SI1260 with a high impedance input module 1296 was used, operating over the range 10 – 10^7 Hz. Silver-paste coated Au-evaporated contacts were made to the top side of the NCD films, which were then placed in an electrically shielded measurement chamber. Impedance measurements were recorded between room temperature and 400°C.

Hall effect measurements were also performed to determine carrier densities and mobilities within the films studied. A Lakeshore Cryogenics System 1 Tesla electromagnet was used to determine sheet resistance and carrier densities using the van der Pauw approach, whereby four Ohmic-like metal contacts Au coated with Ag paste were placed on the top side of the NCD film and in the four corners of square samples. Measurements were performed in a helium atmosphere between 300 and 600 K. It is important to note that this system is capable of sequentially switching the direction of the applied electromagnetic field, enabling the Hall voltage to be accurately determined without the problems of background drift often associated with Hall measurements of wide band-gap materials.

4.3 Results

4.3.1 Intrinsic NCD

Impedance spectroscopy was firstly carried out in air atmosphere between room temperature and 400°C. The measurements recorded at room temperature and 100°C were affected by moisture in the environment and therefore are not reported. The measurement at 400°C could not be recorded due to a temporary failure in the apparatus. The Cole-Cole plot recorded at 150°C is shown in figure 4.4.

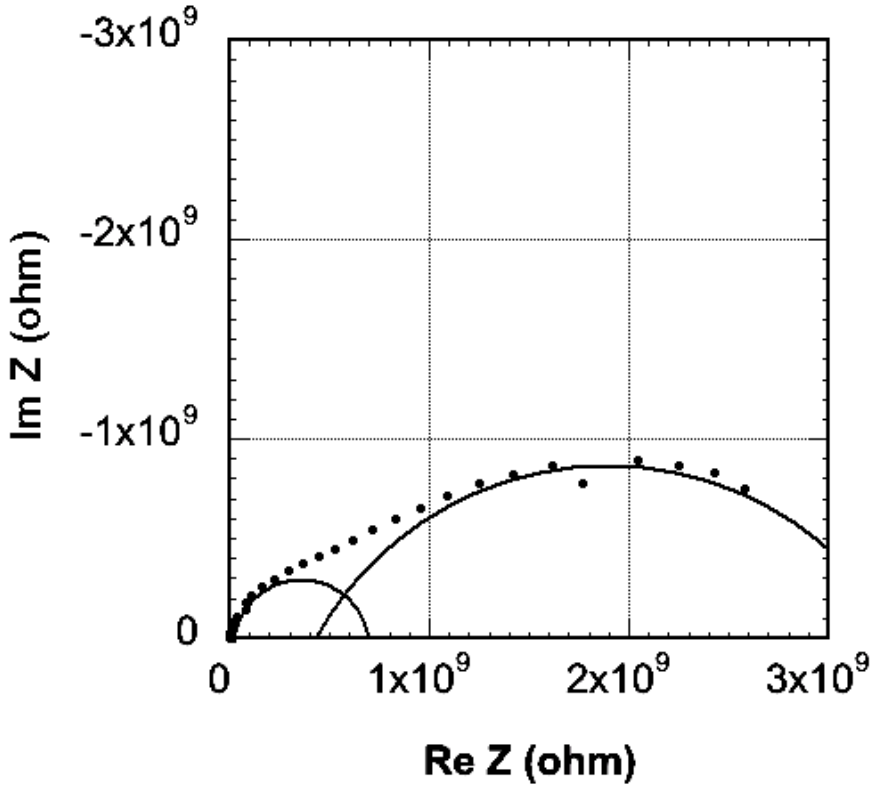

Figure 4.4: Cole-Cole plot recorded for the as-grown intrinsic NCD film at 150°C

It is evident in figure 4.4 that two overlapping semi-circular responses are present. Mathematical fitting on this assumption enables the R and C components for the two semicircular responses to be determined as reported as in table 4.1. The semi-circular response at lower frequency displays a capacitance value of the order of 9 pF, whereas the higher has a capacitance of around 0.1 nF.

Fig. 4.5 shows similar data, but now recorded at 250°C, 300°C and 350°C; in all cases two overlapping semi-circular responses can still be seen.

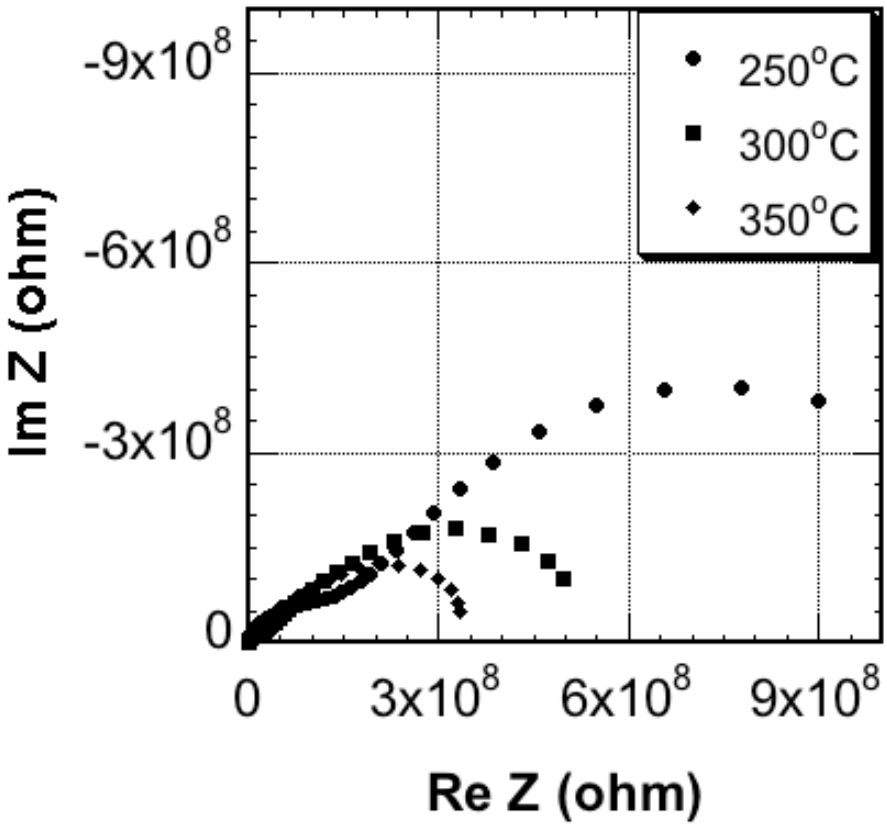

Figure 4.5: Cole-Cole plot recorded for the as-grown intrinsic NCD film at 250°C, 300°C and 350°C

Interestingly the effect of increasing temperature is to reduce the size of responses in the Cole-Cole plot, meaning that the film resistance is decreasing. Table 4.1 reports the resistance and capacitance values for these cases derived again from fitting two semicircular responses to the data.

T (C)	R-GI (Ω^9)	R-GB (Ω^9)	C-GI (F^-12)	C-GB (F^-12)
150	0.8800	3.35	9.15	115
250	0.1650	1.18	17.6	884
300	0.0310	4.79	9.57	814
350	0.0085	2.83	6.70	88.3

Table 4.1: Resistance and capacitance values determined for grain interiors (GI) and grain boundaries (GB) regions of the NCD films investigated here, determined by mathematical fitting to the Cole-Cole plots, as a function of film temperature

Figure 4.6 shows impedance data recorded at room temperature before and after the previous measurements, which were all performed in air. After performing the measurement at 400°C, the sample was left cooing down up to room temperature, at which point the measurement marked as '(ii)' in figure 4.5 was taken. It can be seen that whilst two semi-circular responses are present in both data sets, after heating the impedance of the film has increased even when measured at the same temperature.

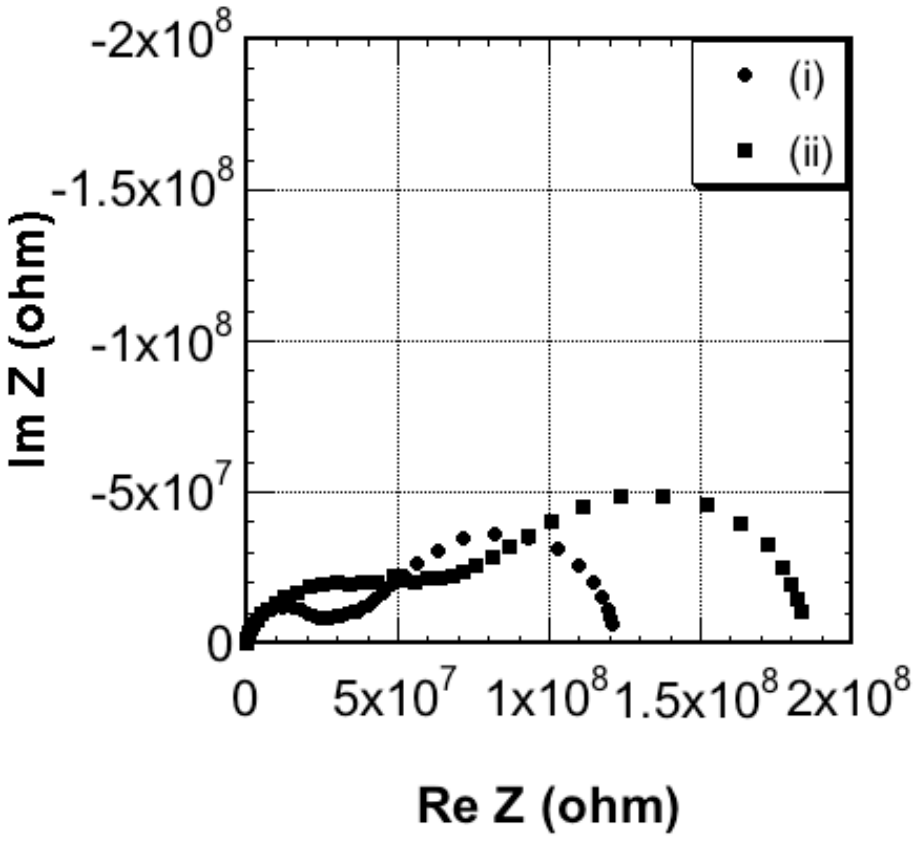

Figure 4.6: Cole Cole recorded for the as-grown intrinsic NCD film at room temperature for the (i) as-grown and (ii) after several heat cycles to 400°C.

To elucidate the effect of air during these heating cycles, measurements were next performed *in vacuo* (10^{-3} mbar) as shown in figure 4.7. In this case Cole-Cole plots are presented for an NCD film at 400°C and for the same film, which has been temperature cycled between room temperature and 400°C *in vacuo* several times.

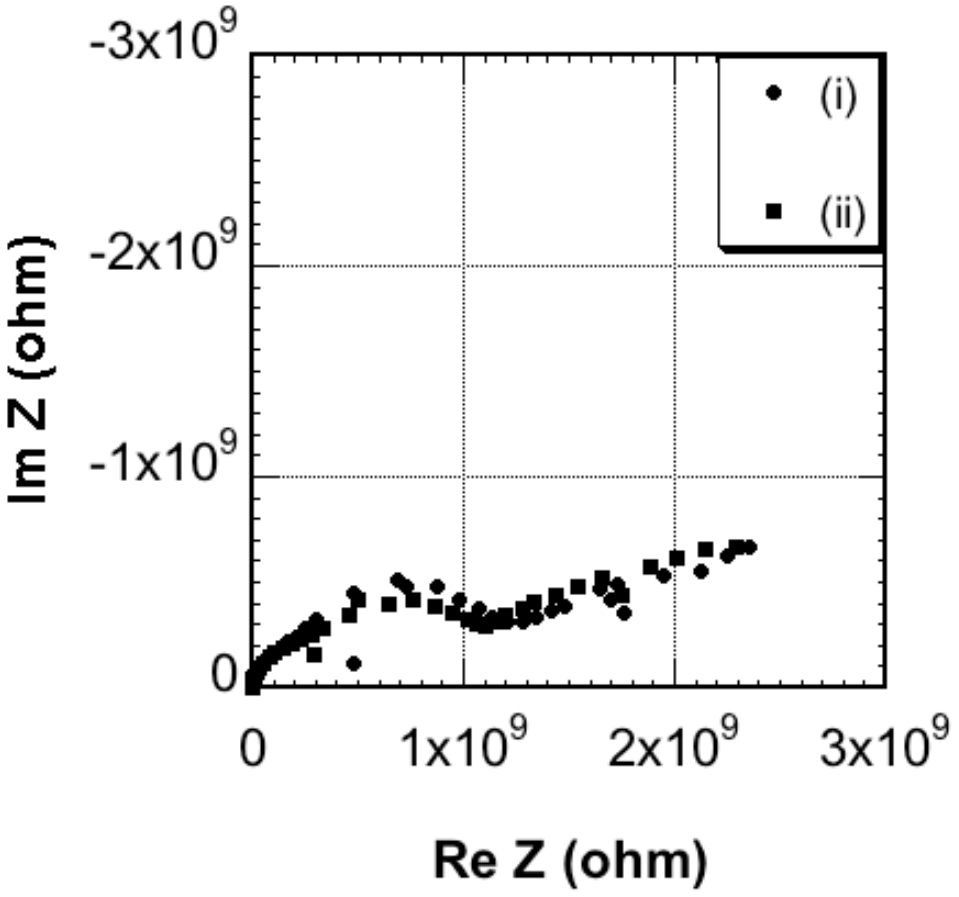

Figure 4.7: Cole-Cole plots for an NCD sample carried out at 400°C for (i) as-grown and (ii) after several heat cycles between room temperature and 400°C *in-vacuo.*

It can be seen that the data points overlie each other indicating that the changes observed during heating in air are no longer occurring. Further heating of the same NCD film but now once again in air (at 400°C) for more than one hour resulted in the complete loss of semi-circular characteristic in the Cole-Cole plots up to a temperature of 250°C.

Figure 4.8 shows the magnitude of the impedance measured at room temperature for such a film plotted directly as a function of frequency; it can be seen that a near-straight line response is apparent in this log-log plot. Measurements carried out at higher temperature showed a slight decrease in the film resistivity above 250°C.

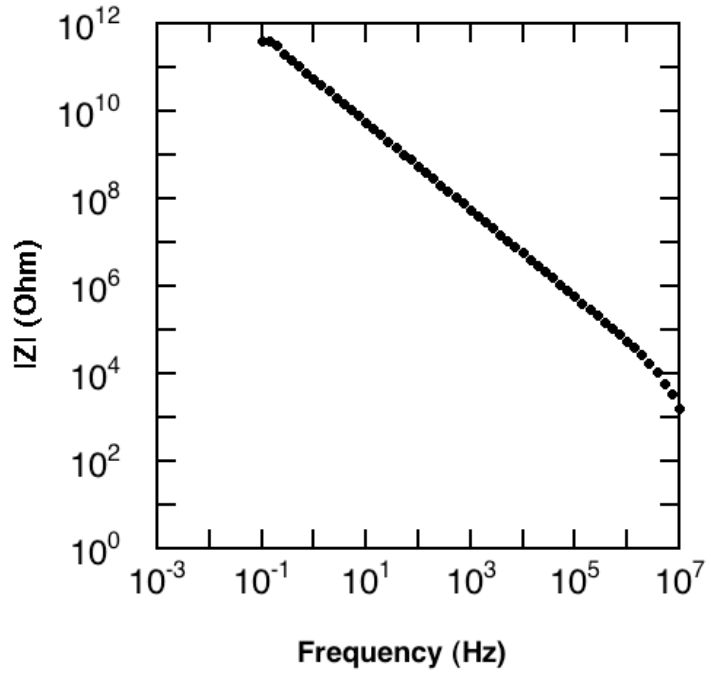

Figure 4.8: Impedance magnitude (recorded at room temperature) plotted as a function of applied frequency for an intrinsic NCD film that has been oxidised in air at 400°C for 1h

Figure 4.9 shows an Arrhenius plot revealing the activation energy for this conduction process to be 0.85 eV.

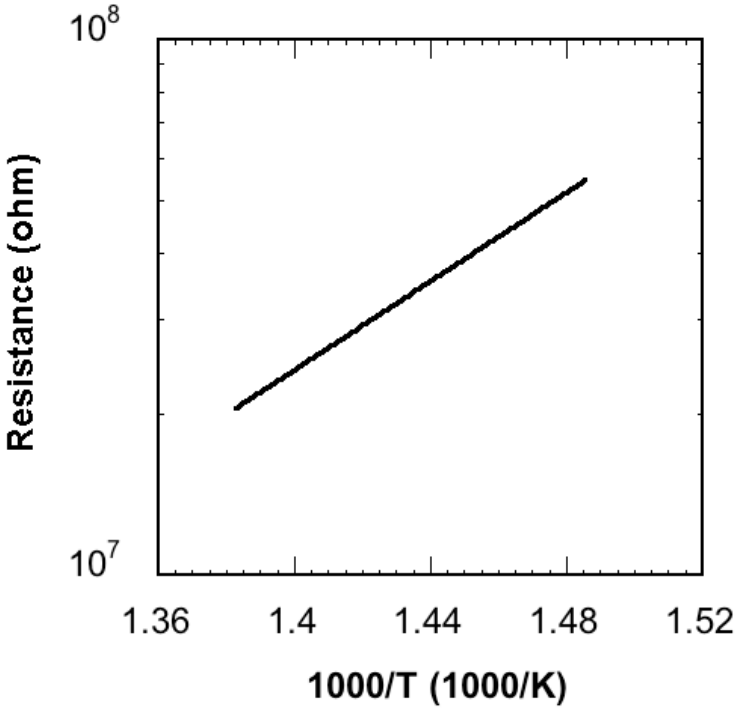

Figure 4.9: Arrhenius plot for the thermally activated conduction process seen in an intrinsic NCD film at temperatures above 250°C

An important characteristic of an insulating film is the dielectric loss tangent tan(δ), determined as a function of AC frequency, which is defined as the ratio between the imaginary part of the complex dielectric constant (ε'') and its real component (ε'). It can be showed that this value is equal to the ratio of the real part of the complex impedance (Z') divided by its imaginary component (Z").

The complex permittivity, as discussed in chapter 3, is given by:

$$\boldsymbol{\varepsilon} = \varepsilon' - i\varepsilon'' = (C / \varepsilon_0) - (1 / \varepsilon_0 \omega R), \tag{4.1}$$

where ε_0 is the permittivity of air, C is the capacitance, ω is the angular frequency and R is the resistance, so that tan(δ) can be written as:

$$\tan(\delta) = |\varepsilon''| / |\varepsilon'| = |(1 / \varepsilon_0 \omega R)| / |(C / \varepsilon_0)| = |1 / \omega RC|, \tag{4.2}$$

The impedance as a complex number is:

$$\mathbf{Z} = Z' + Z'' = R / (1 + \omega^2 R^2 C^2) + \omega R^2 C / (1 + \omega^2 R^2 C^2) \tag{4.3}$$

$$|Z'| / |Z''| = |R / (1 + \omega^2 R^2 C^2| / |\omega R^2 C / (1 + \omega^2 R^2 C^2)| = |1 / \omega RC| \tag{4.4}$$

Therefore:

$$\tan(\delta) = |\varepsilon''| / |\varepsilon'| = |Z'| / |Z''| \tag{4.5}$$

Figure 4.10 shows tan(δ) plotted as a function of the impedance measurement frequency for the NCD film investigated here, measured at room temperature.

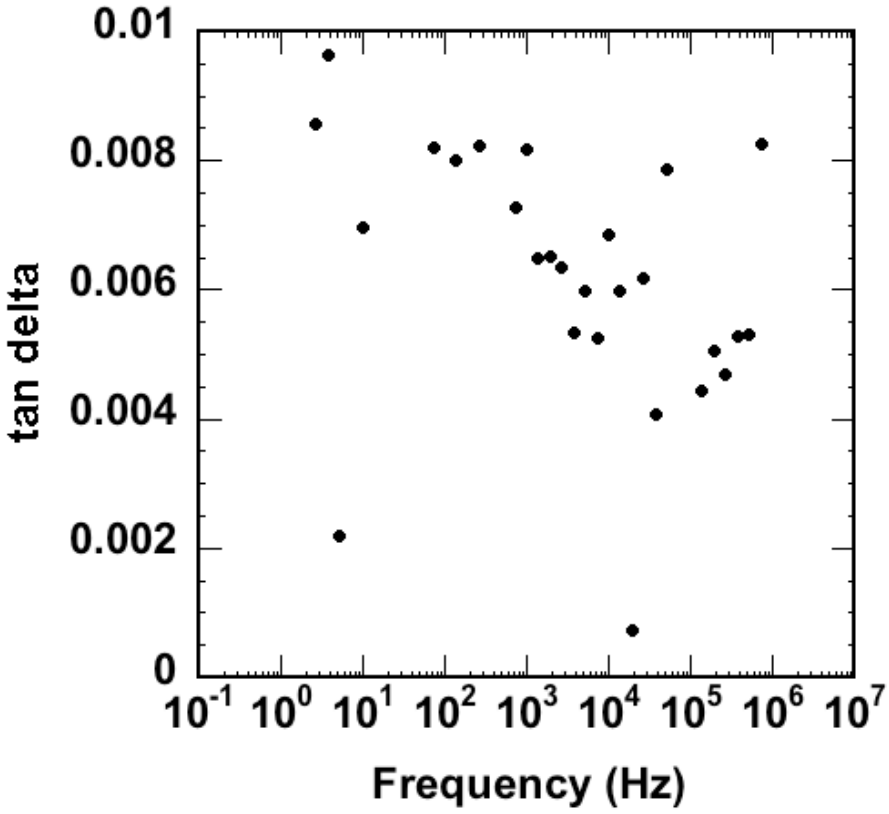

Figure 4.10: Plot of loss tangent as a function of frequency

Whilst there is some scatter in the data, it is evident that the value lies within the range of ~0.004 - 0.008 for frequency varying between 10 and 10^7 Hz.

4.3.2 Boron-doped NCD

Cole-Cole plots recorded for an as-grown Boron-doped NCD sample is shown in figure 4.11. Measurements were recorded over the temperature range 25 – 400°C *in-vacuo.*

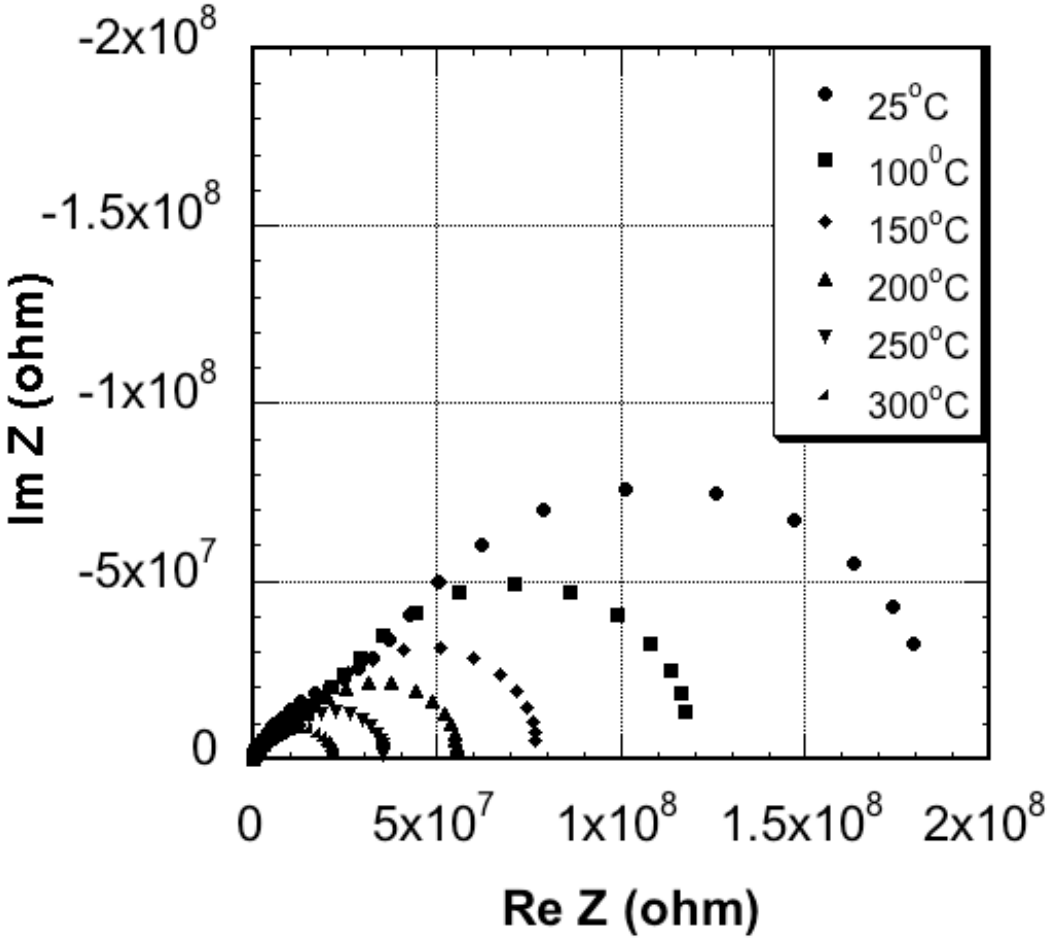

Figure 4.11: Cole-Cole plot for Boron-doped NCD films plotted as a function of measurement temperature

For the room temperature data (250°C) it is visually apparent that a single semi-circle cannot be fitted to the data. Indeed, mathematical fitting reveals the presence of two overlapping semicircular responses being responsible for the curve shape that is obtained. Upon heating, the Cole-Cole plot is seen to progressively reduce in intensity whilst still comprising two overlapping semicircular responses.

Figure 4.12 shows the effect of repeating the measurement on the same sample, again *in vacuo*, a second time, with typical Cole-Cole plots recorded at 200°C and 250°C for sequential measurements on the same sample.

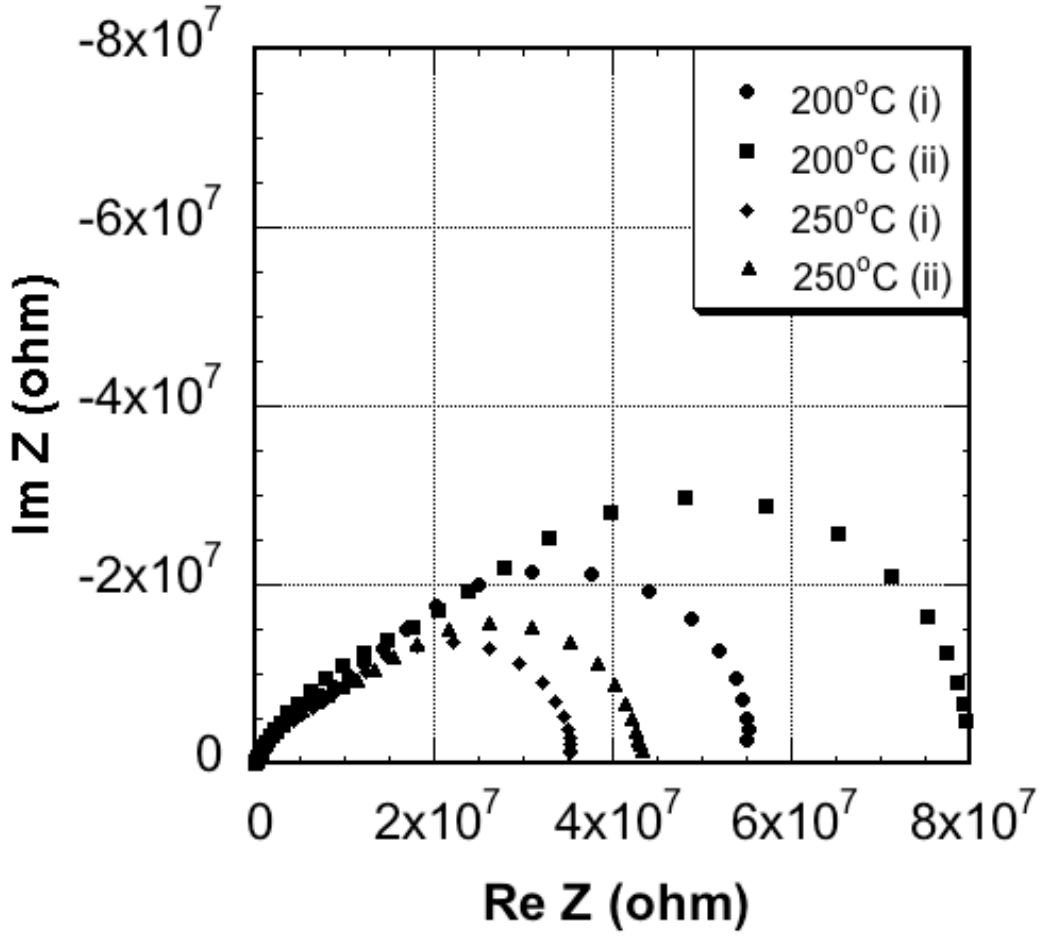

Figure 4.12: Cole-Cole plot for sequential measurements at two chosen temperatures

In both cases a reduction in the overall intensity can be seen as the temperature is increased, indicating a reduction of film resistance with increasing temperature as before. However, whilst the high frequency component of the Cole-Cole plot (on the left side of the graph) remains unchanged between the first and second experiments, the lower frequency component increases in magnitude.

Figure 4.13 shows comparable data for 300°C and 350°C; in this case no difference is apparent between sequentially recorded data sets. Further heating (to 400°C for prolonged durations) affected no further changes in the impedance measurements.

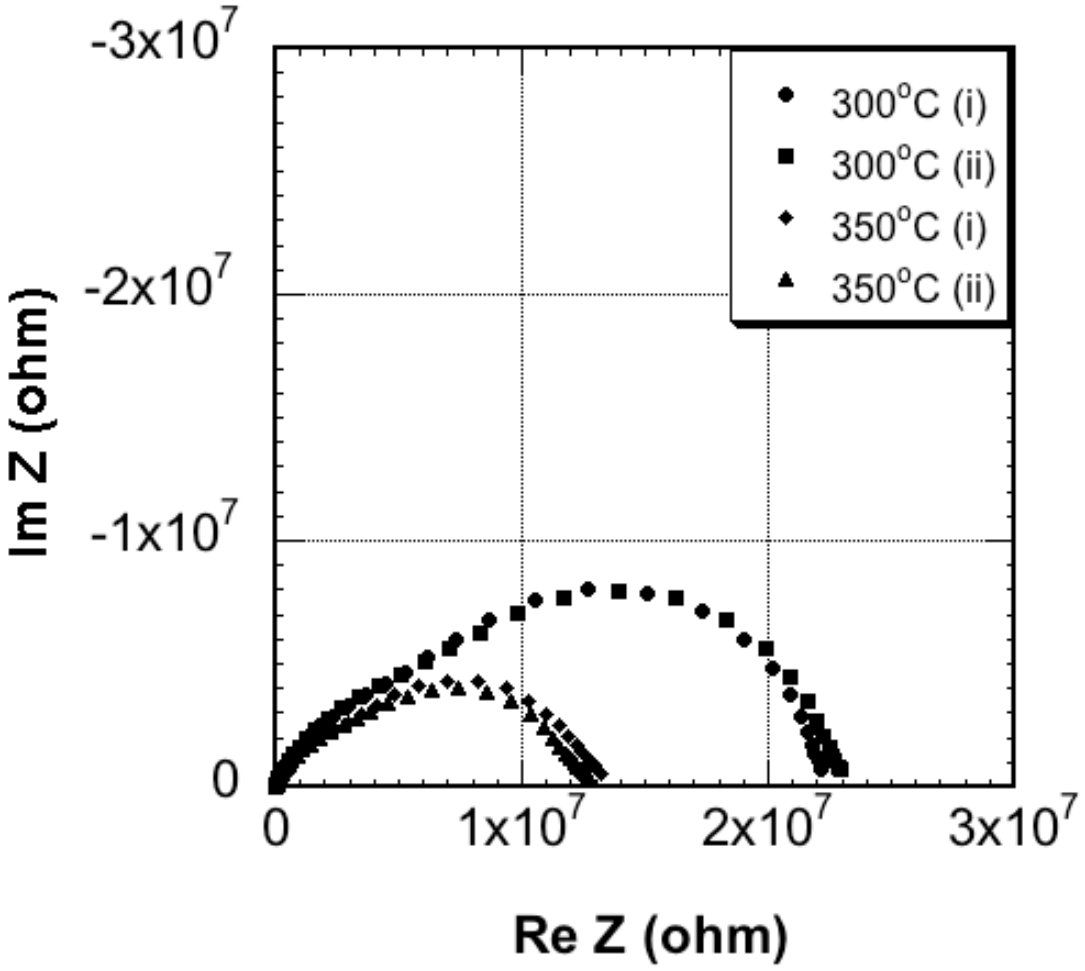

Figure 4.13: Cole Cole plots for sequential measurements at higher temperatures following film stabilization

Interestingly, neither did heating in air as opposed to vacuum. Mathematical fitting at this point enables the R and C components for the two semicircular responses to be determined as reported as in table 4.2.

T (C)	R_1 (M)	R_2 (M)	C_1 (nf)	C_2 (nf)
25	13	18	0.1	1.7
75	9	10	0.2	1.4

Table 4.2: Boron-doped NCD: the resistance and capacitance values determined for the high frequency (R_1, C_1) and low frequency (R_2, C_2) components of the Cole-Cole plots recorded at 25°C and 75°C following film stabilization

It should be noted that the semicircular response at higher frequency (on the left side of the impedance plots, (C_1)), displays a capacitance value of the order of 0.1 nF, whereas the lower frequency component (C_2) has a capacitance of >1 nF.

To investigate the thermal activation energy underlying each of the semicircular responses, a logarithmic plot of the value of R_1 (high-frequency component) and R_2 (low-frequency component) for each vs. 1/T is presented in figure 4.14.

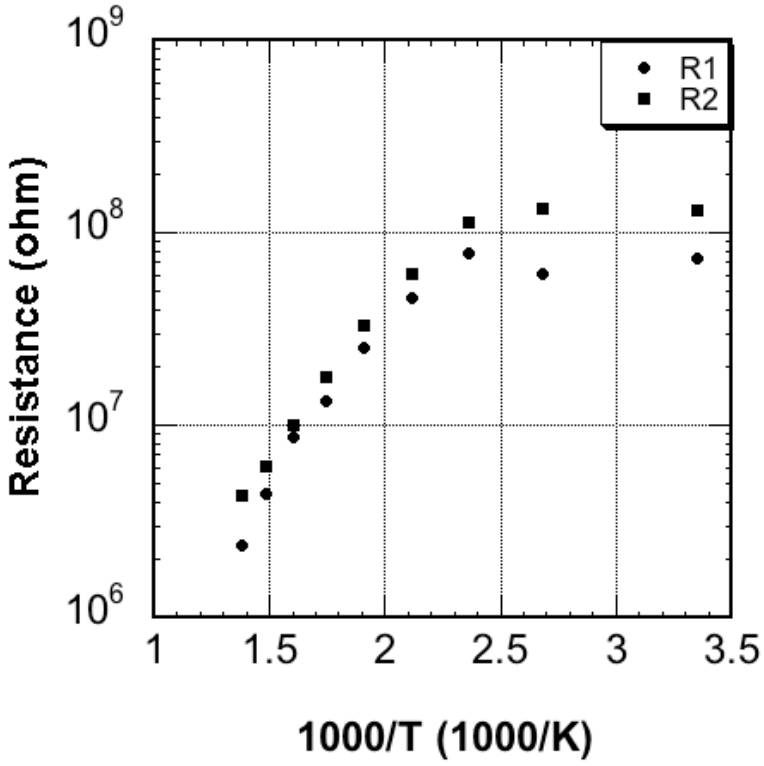

Figure 4.14: Logarithm of film resistance determined from fitting to higher frequency (R_1) and low frequency (R_2) components of the Cole-Cole plots following film stabilization, as a function of 1/T

It is interesting to note that both semicircular responses lead to very similar values in this graph; in both cases the slope gives a value for E_a of 0.38 eV at temperatures above 100°C. Hall effect measurements were carried out on the stabilised films.

Figure 4.15 shows the sheet carrier density determined for a typical film plotted as a function of temperature; the material is p-type with values in the range 10^{13} – 10^{14} cm^{-3}, with the higher values arising at higher temperatures.

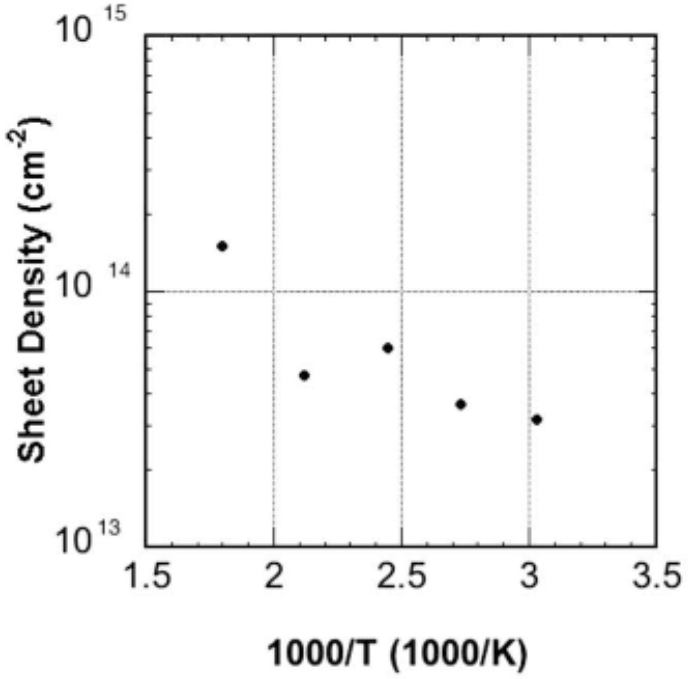

Figure 4.15: Hall effect measurement revealing the sheet carrier density (cm^{-2}) for the stabilized Boron-doped films plotted as a function of 1/T

Values for mobility can be determined from this data when combined with measurements of the sheet resistivity, as shown in figure 4.16. Whilst there is considerable scatter within the data set, values lie in the range 10 – 50 cm^2 / Vs with a general trend to be increasing with increasing temperature.

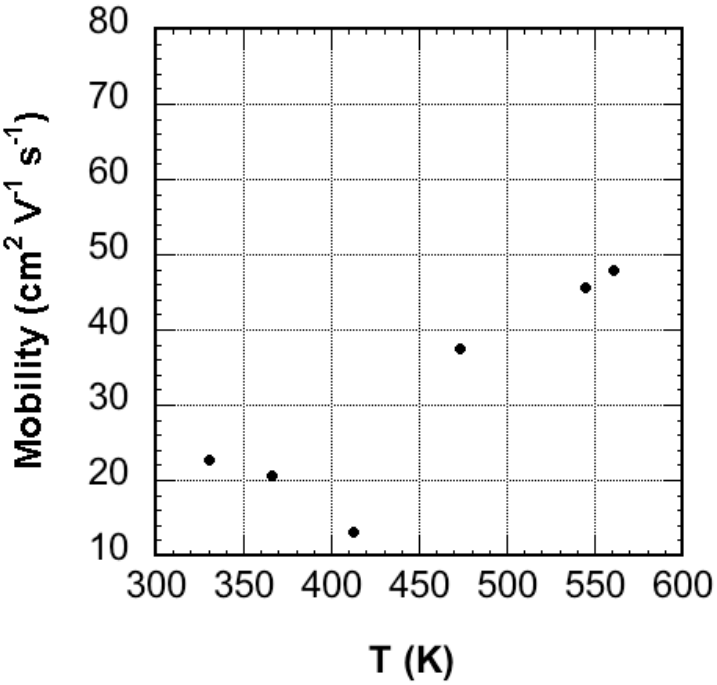

Figure 4.16: Calculated Hall mobility for the stabilized boron-doped NCD films

4.4 Discussion

4.4.1 Intrinsic NCD

For polycrystalline materials it is well established that capacitance values of around picofarad levels arise from the contribution to the impedance measurement from grain interiors, whilst nanofarad level responses can be attributed to grain boundaries [4.16]. It is therefore clear that in the present case both grains and grain boundaries within the NCD films are contributing to the electrical characteristics being measured. As the films are heated the capacitance values remain within the regions attributable to these distinct regions. However, after heating the impedance of the film has increased even when measured at same temperature. This suggests that the increase in film resistance observed in figure 4.18 and figure 4.19 is due to thermally provoked changes within the NCD films as opposed to being simply the result of increased temperature. The data contained in figure 4.21 confirms that the changes being provoked are due to the presence of air during heating. Hydrogen-terminated diamond surfaces are known to display p-type electrical conductivity of the order of 10^{-4} to 10^{-5} Ω^{-1} at room temperature [4.17]. Meier and co-authors [4.17] argued that chemisorbed hydrogen is a necessary but not sufficient condition for surface conductivity in diamond. The authors showed that when hydrogenated diamond samples were annealed in ultra-high vacuum at 410°C for 15 minutes their conductance value of 10^{-6} – 10^{-4} A/V dropped at 10^{-10} A/V, while hydrogenation remained intact (in fact hydrogen desorption does not commence below 700°C [4.17]). Having then masked one half of the sample surface and having desorbed hydrogen from the other half, re-exposure to air raised the conductance level of the masked part of the samples by four orders of magnitude (figure 4.17).

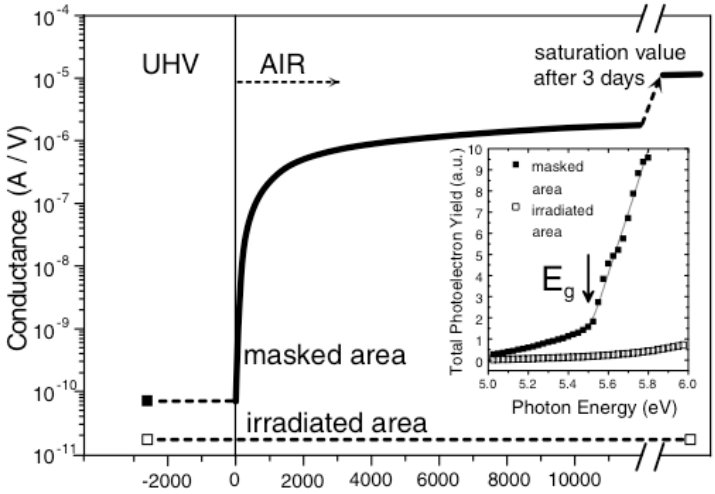

Figure 4.17: Surface conductance of the hydrogenated (masked) and hydrogen-free part of a homoepitaxial diamond (100) layer in UHV and following subsequent exposure to air [4.17]

These results showed that a component from the air is necessary for surface conductivity of hydrogenated diamond to manifest. However, hydrogenated diamond has a negative electron affinity value of -1.3 eV [4.18], whereas electron affinities of molecular atmospheric species are around 2.5 eV: electron transfer from diamond into air would thus appear unfeasible. The authors however pointed out that the thin water layer that forms naturally on all surfaces exposed to air has a chemical potential $\mu_e = \mu_0 + 0.18 = -4.26$ eV, and therefore can act as a surface acceptor for diamond. The difference in the chemical potential between the electrons of the liquid layer and in the diamond (Fermi level E_F) causes an electron transfer from the wet layer to the diamond surface (or hole transfer from the diamond to the liquid layer) that has the effect of decreasing the electron affinity of the hydrogenated diamond side of the interface and increasing that of the liquid layer, until equilibrium conditions are reached and the chemical potential is the same on both sides of the interface [4.17].

The authors also showed that surface conductivity was lost upon heating in air at temperature below 200°C, as in figure 4.18.

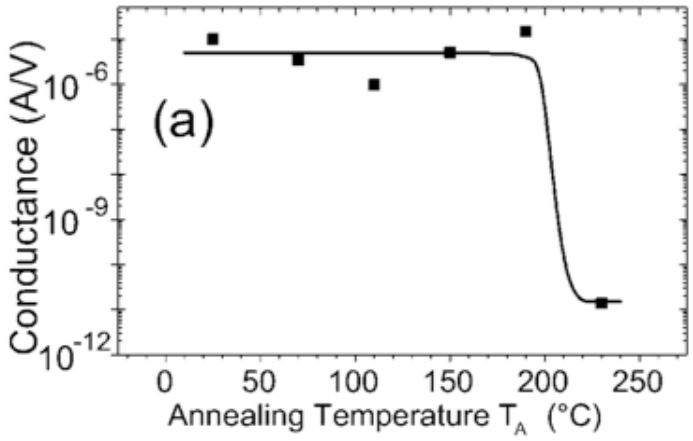

Figure 4.18: Surface conductance of hydrogenated single-crystal diamond as a function of annealing temperature in air [4.17]

The 'oxidation' process of hydrogenated diamond (100) single-crystal surfaces have been studied using scanning tunnel microscopy by Nakamura and Ito [4.19]. They reported the formation of surface ethers (comprising H, C and O atoms) at temperatures around 350°C, with fully oxidised diamond surfaces being evident following heating in oxygen at 500°C. It is therefore likely that the surfaces produced here following heating in air at 400°C will be oxidised. It is also known that polycrystalline diamond can contain hydrogen within grain boundaries [4.20] and therefore the oxidation of grain boundary material, either non-

diamond carbon or hydrogen, could also be occurring. In the present case conduction due to surface conductivity can be ruled out, as the acid treatments used prior to all measurements remove this effect. Indeed, films that had become fully resistive (more than one hour annealing at 400°C in air) were subjected to a further acid treatment to confirm that surface conductivity did not return to the film following this process. Thus, it can be concluded that following the oxidation treatment, whatever the form of the grain boundaries within the annealed NCD films, they are not electrically conductive, despite the fact that such grain boundaries must be highly networked within such fine grain material. The most plausible explanation for this observation is that they are being sufficiently oxidised to at least reduce the susceptibility of the grain boundaries to hydrogen-terminated so-called surface conductivity (through the formation of ethers or similar), or that non-diamond carbon within the grain boundaries is being oxidised. Given the high quality growth conditions employed here, the former explanation is favoured.

It is encouraging that the properties of the film stabilize, displaying an extremely high level of resistivity. Indeed, at this point the films are behaving as a near-ideal dielectric. This behaviour is dissimilar to all previous reports of impedance measurements on NCD films where a contribution to the conduction process from the grain boundaries persists even following the mild oxidation carried out here. Indeed, in some cases the grain boundaries dominate the conduction process with little evidence for conduction within the grain interiors being found [4.11].

Extrapolation of the line displayed in figure 4.8 to zero frequency enables the DC resistivity of the film to be determined, revealing a value greater than 10^{13} ohm/sq. This value is typical for the highest quality polycrystalline CVD material [4.21] and remarkably close to values obtained for single crystal diamond. This is an excellent result given that this is an NCD material.

The thermally activated conduction process (0.85 eV) observed at temperatures above 250°C is extremely close to the 0.84 eV activated conduction process reported by Gonon and co-workers [4.22] for undoped thick commercially available CVD diamond films.

The authors firstly performed current-voltage measurements on the films at room temperature between -100 V and 100 V, from which they calculate an activation energy value of 0.84 eV for the conduction process. After fitting the experimental data points according to several different models from I-V measurements, and successively from conductivity-frequency measurements they realised that the conduction process occurring in the films is best described by a Hill-type hopping conduction mechanism [4.22].

Hill conduction is a field-activated type of conduction involving discrete levels (at E_i from

the valence band) whose overlap of the Coulombic potentials is sufficient to permit carrier-hopping from site to site. This conductivity is frequency-dependent and follows an ω^p law with p given by:

$$p = 1 - 6kT / [E_i + kT\ln(\omega\tau)]$$

where τ is the inverse of a phonon frequency, k is the Boltzmann constant, T is the temperature, and ω is the frequency of measure [4.23].

Carriers hop over a potential barrier $E_p = E_i - \beta^2 / es$, where s is the distance between two centres, e is the electric charge, and $\beta = e^{3/2}(\pi\varepsilon\varepsilon_0)^{-1/2}$ is the Poole-Frenkel constant for the material, equal to 3.23×10^{-4} $eVcm^{1/2}/V^{1/2}$ for diamond.

The activation energy is given by:

$$E_a = E_p - eVs / 2d = E_i - E_p = E_i - \beta^2 / es - eVs / 2d$$

with d being the thickness of the films. Since E_a was deducted experimentally (0.84 eV), the authors calculated $E_i = 0.91$ eV, meaning that the discrete acceptor states for this type of conduction were 0.91 eV above the valence band with a density around 10^{17} cm^{-3} [4.22].

Huang and co-authors [4.24] have proposed a similar mechanism to explain the conduction in their films.

The AC impedance values obtained for these films are also very good. The data contained in figure 4.10 show only a small change in the value of the dielectric loss over the frequency range of $10 - 10^7$ Hz. It should be remembered that the loss tangent is a measure of the ratio of the power dissipated in the dielectric to the power stored, implying low numbers are desirable.

Lu and co-authors [4.25] investigated the dielectric properties of very large grain thick freestanding diamond films (0.3 – 1.5mm). Over the frequency range we have investigated here they observed an increasing value of tan(δ) from 0.05 to 0.085, whilst in our case the trend in the data is the opposite with values of 0.08 decreasing to around 0.004. The decreasing trend is a desirable feature since it shows the dielectric loss is decreasing with increasing frequency. In another report on the use of commercially available thick CVD polycrystalline diamond films, Ibarra and co-workers [4.26] measured a dielectric loss tangent of around 0.01 falling to around 0.001 at 10MHz. In this case the trend is similar to the one that observed in the current work, decreasing with increasing frequency. Heidger

and co-authors [4.27] reported loss tangent values as high as 0.25 in thick free standing polycrystalline CVD films; the value could be reduced by using oxygen within the methane/hydrogen MWPECVD gas mixture used for film growth, but this led to a decrease in the films resistivity. It must be stressed that these reports are all for high quality large grain size CVD diamond and hence further underline the excellent properties being displayed by the nanocrystalline film studied here. Preliminary measurements indicate that these excellent RF properties are maintained at higher temperatures.

4.4.2 Boron-doped NCD

The Cole-Cole plots presented in figures 4.11 – 4.14 clearly indicate the presence of two conduction processes within these films. As stated above it is conventionally considered that the observation of widely separated capacitance values for two semicircular responses arising from a polycrystalline film (typically pF to nF) can be explained in terms of grain interior and grain boundary contributions respectively [4.16]. It is therefore interesting to note that in the current case the capacitance values listed in table 4.2 differ by only a single order of magnitude, implying a more similar physical origin for the reactance of the conduction processes than has been previously noted for nanocrystalline diamond films. It may also be noted from table 4.2 that the resistance of each process is broadly comparable. The Cole-Cole plots presented in figure 4.11 show an overall decrease in magnitude with increasing temperature, indicating a reduction in the resistance of the film is occurring. However, since this decrease appears to be pronounced for the lower frequency side of the curve, one of the conduction processes is changing more with temperature than the other. An explanation for this observation can be found in the plot shown is figure 4.12, where it is it clear that successive heat cycles yielded differing results, with the lower frequency component of the curve being increased in intensity the more the film is subjected to heat treatments. Since this component of the curve (C_2) is the one with the largest capacitance value, it seems reasonable to conclude that the region that is being affected by heating is the more ‘grain-boundary-like’ part of the film. The plots presented in figure 4.13 indicate that the film stabilises following these heat treatments, whilst clearly preserving two distinct conduction routes within the film. The thermal activation of both, noted as R_1 and R_2 in figure 4.14 and table 4.2, is similar at a value of 0.38 eV for each. That this is the energy conventionally associated with the activation of boron acceptor states within diamond when at modest doping concentrations [4.28] cannot be coincidental; this provides strong evidence for the association of both conduction routes with the presence of substitutional boron within diamond.

Theoretical studies of the likely location of boron within NCD, carried out by Barnard and Sternberg [4.29], predicted that the Boron will locate at the grain boundaries within thin film NCD samples. However, for certain crystalline arrangements sub-surface substitutional boron was considered to be energetically more favourable than extreme sites at surfaces, edges or corners of crystals. The crystal sizes modelled were considerably smaller than in the current experimental case. It can therefore be proposed that grain interior doping is being supported due to the grain size in the current films, but that this is being supplemented by grain boundary doping in the form of sub-surface boron substitutions. Such a case would then explain the slight variation in environment for the boron acceptors that gives rise to the C_1 and C_2 values determined (and hence two semicircular responses in the Cole – Cole plots), but the coincident thermal activation energies of 0.38 eV for the two similar R_1 and R_2 values. The instability of the film characteristics (as revealed in figure 4.12) presumably arises from thermally provoked changes during initial heating of the samples used. The acid pre-treatments used are known to leave the surface free from organic contamination and so called 'surface conductivity' caused by the presence of hydrogenated surface sites [4.30], so these effects can be ruled out. The NCD films were produced from hydrogen-rich plasmas and following high temperature growth, cooled down in hydrogen. The most likely explanation for the changes observed is therefore the loss of hydrogen from the NCD films during the treatments (in vacuum or air), or a change to the nature of any hydrogen trapped within the film. Whichever the case, the subsequent stability of the films during all further experimentation shows that simple heat treatments to 'as-grown' films are sufficient to overcome this problem. This behaviour is dissimilar to previous reports of impedance measurements on NCD films [4.13, 4.14] where a contribution to the conduction process from the grain boundaries persists following similar treatments. Indeed, in some cases the grain boundaries dominate the conduction process with little evidence for conduction within the grain interiors being found [4.11]. The carrier (hole) sheet densities measured by Hall effect can be converted to volume density by consideration of the thickness of the films being analysed. This leads to values in the 10^{17} cm^{-3} range at temperatures where the boron is expected to be fully ionised. Single crystal diamond has been reported to display hole mobility values of several hundred cm^2/Vs in this doping regime [4.31], but NCD would be expected to display much lower values due to increased opportunities for carrier scattering. Nesladek and co-workers [4.32] reported values in the range 0.2 – 0.5 cm^2 / Vs for NCD films with a carrier concentration of around 10^{20} cm^{-3}. This is to be expected, as hopping conductivity will dominate in this case. In a recent paper by Gajewski and co-

workers [4.33], mobilities greater than 2 cm^2 / Vs were reported for NCD material at room temperature with a boron concentration of 2.7×10^{19} cm^{-3}. The higher mobility values determined here, in the range of 10 – 50 cm^2 / Vs, are to be expected given the lower boron concentration (of the order of 10^{17} cm^{-3}). Nonetheless such high values are indicative of band-conduction processes, and add further weight to the argument that the boron within all regions of the NCD films being studied is behaving as a classical dopant, being relatively unaffected by the presence of grain boundaries. The density of free carriers and the high mobility values also indicate the very high quality of the NCD film grown here; any significant impurity concentrations, of, say, nitrogen, would be likely to reduce the values determined for both. The trend in mobility with temperature (figure 4.16) is curious; with mobility initially decreasing from room temperature to around 100°C, before increasing to the maximum temperature studied. In a polycrystalline material it is possible to calculate an incorrect mobility value from Hall measurements, if there is a component of the conductivity measured that does not contribute to the Hall voltage, i.e. is not due a single carrier type. This could be possible if de-trapping processes at higher temperatures gave rise to a source of carriers. However, in the current case the Impedance measurements have clearly indentified that both conduction processes display an activation energy of 0.38 eV which is most normally associated with a boron acceptor state. A detailed explanation of the relationship of mobility with temperature is beyond the scope of the current study, but is most likely to be associated with the presence of deep trap states.

4.5 Conclusion

Impedance Spectroscopy measurements have been carried out on the form of NCD created by seeding the diamond nuclei with nanocrystalline diamond particles, and deposited using optimised microwave plasma enhanced CVD process conditions. The resultant highly dense NCD films show electrically conduction to be occurring both through the diamond grains and the grain boundaries. However, following mild oxidation treatments the contribution to the conduction process from the grain boundaries can be eradicated leaving a highly resistive material whose DC characteristics rival those of thick free-standing CVD polycrystalline diamond plates. Furthermore the AC dielectric properties show a very low loss tangent indicating the lack of polarisable defects in this form of NCD material. In addition, Impedance Spectroscopy and Hall Effect measurements have been carried out on boron-doped NCD. Electrical conduction can be seen to be occurring through two distinct

pathways that may be associated with the diamond grains and a region that is ‘grain boundary-like’. However, both forms of conduction display characteristics associated with band-conduction from boron acceptor states, and lead to carrier mobility values that are high for a nanocrystalline material. Further work is required to understand in detail the mobility measurements recorded. Since NCD can be grown over large areas and the film thickness controlled in the range of 50 – 100 nm, it would appear that this material may be useful for several future micro- and nano-device technologies that would rely on the active use of either insulating or semiconducting (p-type) diamond.

References

[4.1] Balmer R.S., Friel I., Woollard S.M., Wort C.J.H., Scarsbrook G.A., Coe S.E., El-Hajj H., Kaiser A., Denisenko A., Kohn E. and Isberg J., Philosophical Transactions of the Royal Society **366** (2008) 251

[4.2] Edholm B., Soderbarg A., Olsson J., Johansson E., Japanese Journal of Applied Physics **34** (1995) 4706

[4.3] Lang A.R., Makepeace A.P.W., Alexander W.B., McCormick T., Pehrsson P.E. and Butler J.E., Journal of Crystal Growth **200** (1999) 446

[4.4] From Element Six L.t.d., available at: www.e6.com

[4.5] Hammersberg J., Isberg J., Johansson E., Lundstrom T., Hjorstam O. and Bernhoff H., Diamond and Related Materials **10** (2001) 574

[4.6] Philip J. and Hess P., Journal of Applied Physics **93** (2003) 2164

[4.7] Wang J., 17th Int. IEEE Micro Electro Mechanical Systems Conference, Maastricht, The Netherlands, Jan. 25-29, 2004, 641

[4.8] Baldwin J.W., Zalalutdinov M.K., Feygelson T., Patel B.B., Butler J.E. and Houston B.H., Diamond and Related Materials **15** (2006) 206

[4.9] Baral B., Chan S.S.M. and Jackman R.B., Journal of Vacuum Science and Technology **A14** (1996) 2303

[4.10] Williams O.A. and Jackman R.B., Journal of Applied Physics **96** (2004) 3742

[4.11] Ye H., Hing P. and Jackman R.B., Journal of Applied Physics **94** (2003) 7878

[4.12] Ye H., Gaudin O., Jackman R.B., Muret P. and Gheerart E., Physica Status Solidi A **199** (2003) 92

[4.13] Ye H., Gaudin O. and Jackman R.B., Journal of Material Science Technology **21** (2005) 879

[4.14] Ye H., Yan H.X. and Jackman R.B., Semiconductor Science Technology **20** (2005) 296

[4.15] Curat S., Ye H., Gaudin O., Koizumi S. and Jackman R.B., Journal of Applied Physics **98** (2005) 073701

[4.16] Macdonald J.R., *Impedance Spectroscopy* (Wiley, New York) 1987

[4.17] Maier F., Ristein J. and Ley L., Physical Review B **64** (2001) 165411

[4.18] Bachmann P.K., Leers D. and Lydtin H., Diamond and Related Materials **1** (1991) 1

[4.19] Nakamura J. and Ito T., Applied Surface Science **244** (2005) 301

[4.20] Maclear R.D., Butler J.E., Connell S.H., Doyle B.P. Machi I.Z., Rebuli D.B., Sellschop J.P.F., Sideras-Haddad E., Diamond and Related Materials **8** (1999) 1615

[4.21] Brandon J.R., Coe S.E., Sussmann R.S., Sakamoto K., Sporl R., Heidinger R. and Hanks S., Fusion Engineering and Design **53** (2001) 553

[4.22] Gonon P., Deneuville A., Fontaine F. and Gheeraert E., Journal of Applied Physics **78** (1995) 11

[4.23] Hill R.M., Philosophical Magazine **23** (1971) 59

[4.24] Huang B. and Reinhard D.K., Applied Physics Letters **59** (1991) 12

[4.25] Lu F.X., Zhang H.D., Tong Y.M., Yang J.X., Li C.M., Chen G.C. and Tang W.Z., Diamond and Related Materials **13** (2004) 1714

[4.26] Ibarra A., Gonzalez M., Vila R. and Molla J., Diamond and Related Material **6** (1997) 856

[4.27] Heidger S., Frie-Carr S., Jordan B. and Wu R., Proceedings of the IEEE 1998 National Aerospace and Electronics Conference, Naecon, 1998, 247

[4.28] Borst T.H. and Weis O., Physica Status Solidi A **154** (1996) 423

[4.29] Barnard A.S. and M. Sternberg, Journal of Physical Chemistry B **110** (2006) 19307

[4.30] Looi H.J., Pang L.Y.S., Molloy A.B., Jones F., Foord J.S. and Jackman R.B., Diamond and Related Materials, **7**, (1998) 550

[4.31] Thonke K., Semiconductor Science Technology **18** (2003) S20

[4.32] Nesladek M., Bergonzo P., Hubik P., Mares J.J. Kristofik J., Kindl D., Williams O.A. and Gruen D.M., Diamond and Related Materials, **15** (2006) 607

[4.33] Gajewski W., Achatz P., Williams O.A., Haenen K., Bustarret E., Stutzmann M. and Garrido J., Physical Reviews B **79** (2009) 045206

Chapter 5

The influence of ammonia on the electrical properties of detonation nanodiamond

5.1 Introduction

Ammonia is a natural gas that is found throughout the atmosphere. Approximately 4 billion years ago it was present in large quantities together with methane as well as hydrogen and helium. Most of this primordial atmosphere was lost into space during the history of the planet; today ammonia's concentration in the atmosphere ranges from low-ppb to sub-ppb, most of which is emitted by direct or indirect human activity [5.1].

The largest source of ammonia in the overall nitrogen cycle (figure 5.1) is ammonification, a series of metabolic processes in which organic nitrogen (manure from agriculture, wildlife and leaves) is decomposed by bacteria and fungi. The released ammonium ions and gaseous ammonia is again converted to nitrite and nitrate by bacteria.

Another source of ammonia is combustion from chemical plants and motor vehicles.

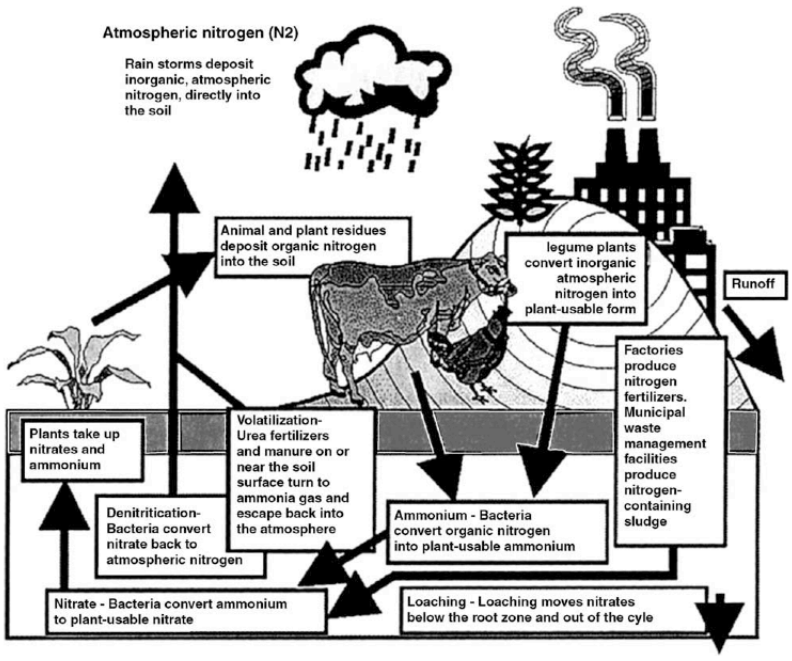

Figure 5.1: Nitrogen cycle (Copyright University of Missouri)

Generally, the detection and measurement of ammonia concentrations is required in order to avoid exposure to higher-than-allowed limits.

The lower limit of human ammonia perception by smell was estimated to be around 50 ppm, corresponding to 40 $\mu m/m^3$ [5.2]. However, even at lower concentrations ammonia is irritating to the respiratory systems, eyes and skin [5.3, 5.4]. The long term allowed concentration that people may work in is set at 20 ppm. Immediate and severe irritation of nose and throat follows exposure to 500 ppm. Pulmonary oedema follows exposure to

1000 ppm, with symptoms taking up to 24 hours before manifesting. Exposure to extremely high concentrations such as 5,000 – 10,000 ppm can be lethal within 5 – 10 min [5.1]

The detection and measurement of ammonia is mainly required in four areas [5.1]:

- Environmental: ammonia levels can exceed permissible levels in certain areas (such as intensive farming) and be dangerous for both humans and animals.

- Automotive industry: exhaust gases need monitoring as they are a major source of pollution in urban areas.

- Chemical industry: industries, fertilised factories and refrigeration systems make use of high purity ammonia, therefore potential leaks can be life-threatening.

- Medical applications: ammonia levels in exhaled air need to be analysed in order to diagnose certain diseases.

Ammonia sensors need to be fast, specific, reliable, sensitive, inexpensive and have the possibility for miniaturization [5.5, 5.6].
However, the minimum amount of ammonia to be detected varies considerably with the four areas of application mentioned above. For this reason, ammonia sensors will be required to be built with different specifications in order to satisfy the required sensitivity and time response, as well as temperature range.
Table 5.1 summarizes such specification in each of the four areas of application considered.

Application	Detection limit	Required response time	Temperature range	Remarks
Environmental: monitoring ambient conditions / measures in stables	0.1 ppb to > 200 ppm / 1 to > 25 ppm	Minutes / ~ 1 min	0-40 C / 10-40 C	Reduce environmental pollution / Protect livestock animals and farmers
Automotive: measure ammonia emission from vehicles	4 to 2000 g/min (soncentration unknown)	Seconds	Up to 300 C	Ammonia emission is not regulated at this time
Passenger cabinet air control	50 ppm	~ 1 s	0-40 C	Automotive air quality sensor mainly aim on Nox and Co levels
Detect ammonia slip	1-100 ppm	Seconds	Up to 600 C	Control Urea injection in SCR Nox reduction
Chemical: leakage alarm	20-1000 ppm	Minutes	Up to 500 C	Concentration can be very high at ammonia plans and can even be explosive
Medical: breath analysis	50-2000 ppb	~ 1 min	20-40 C	Diagnosis of peptic ulcer caused by bacteria, small gas volumes

Table 5.1: Specifications for ammonia sensors in different areas of application [5.1]

Commercial ammonia detectors are based on different principles [5.1]:

- Metal-oxide gas sensors, based on the principle of conductance change due to chemisorption of gas molecules to the sensing layer.

- Catalytic ammonia sensors, based on change of the charge carrier concentration in the catalytic metal triggered by a change in concentration of ammonia.

- Conducting polymer gas detectors, based on the reduction of a polymer film following a chemical reaction with ammonia.

- Spectrophotometric ammonia detectors, where the coloration of an analyte is caused by the reaction with ammonia and certain agents.

- Optical absorption ammonia detectors, in which the spectrum of the light reaching the detector is altered due to the composition of ammonia.

- Indirect gas analyser using non-selective detectors: the sensor includes a selection mechanism that allows only the gas of interest to influence the medium surrounding it. Gas permeable membranes are employed to achieve gas diffusion separation.

Table 5.2 summarises the properties of commercially available ammonia sensors.

Principle	Lower detection limit	Response time	Temperature range	Remarks
Metal-oxide WO3	1 ppm	~ 1 min	400 C	Low selectivity drift
Catalytic metal (Palladium, conducting polymer	1 ppm	~ 1 min	Up to 600 C	Low selectivity
Polyaniline	1 ppm	~ 3 min	Up to 150 C (regeneration)	Irreversible reactions
Optical gas sensors:				For ammonia in water
Nessler	50	~ 1 min	37 C	Expensive setup
Colourometric	1 ppt	~ 5 min		Large and expensive
Absorption spectroscopy	1 ppb	~ 5 min		
pH-transitions and EC detectors	100 ppt	~ 20 min	0-40 C	Fluidic system

Table 5.2: Parameters of different types of ammonia sensor systems [5.1]

The electrical properties of DND are currently poorly understood. In the current study, Impedance Spectroscopy (IS) has been used to investigate the electronic properties of DND in some detail, and then investigate the changes occurring when DND is exposed to ammonia. The results are discussed both in terms of what changes occur to the DND surfaces when in contact with NH_3 and the prospects for DND to be a suitable material for chemical sensing applications.

5.2 Experimental methods

Detonation nanodiamond powder (SuperSyndia SSX 0 – 3.5) was investigated in the 'as-received' condition. SEM images of a typical particle are shown in figure 5.2.

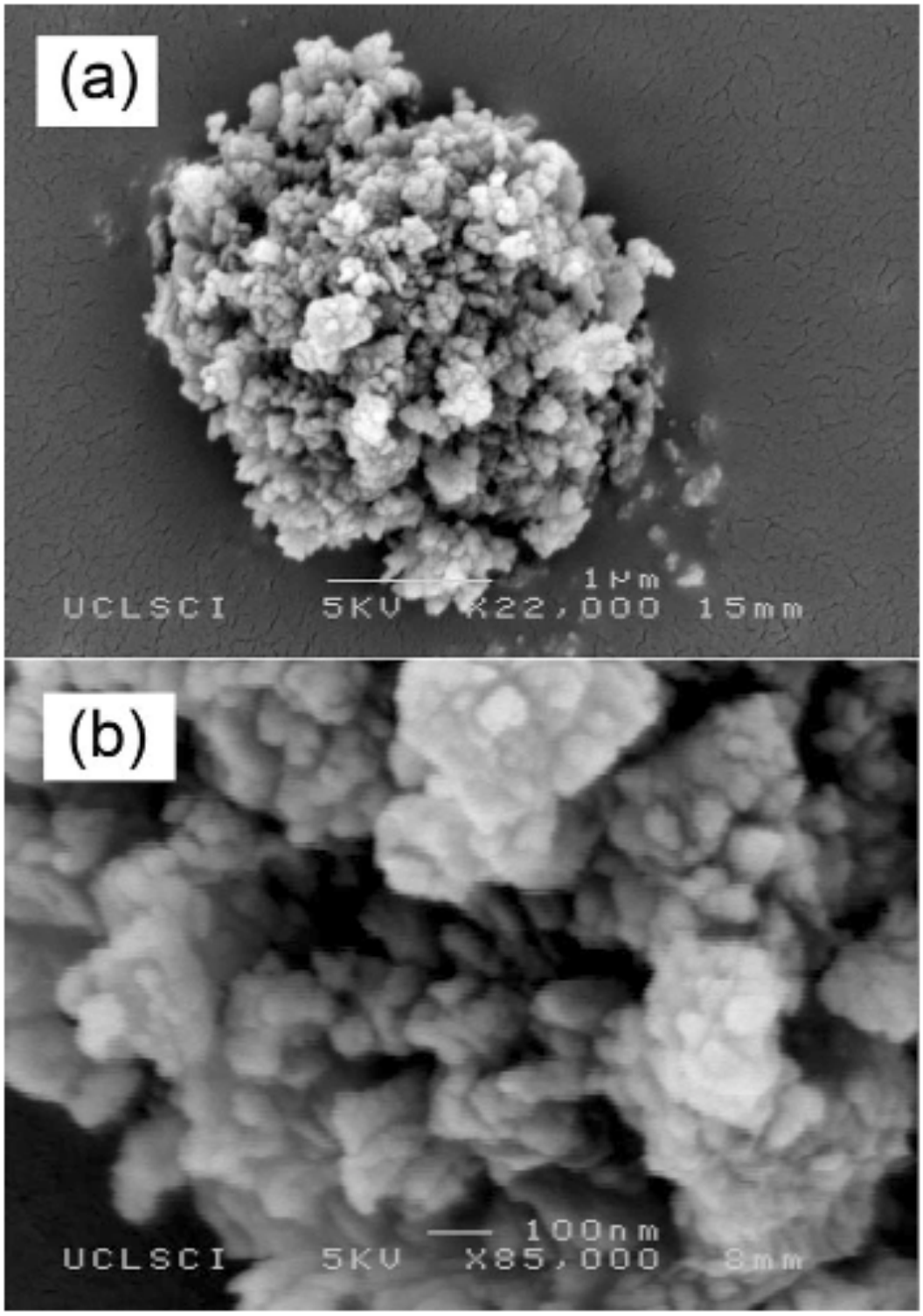

Figure 5.2: **Scanning electron microscope pictures of the DND used revealing (a) typical 'grain' size and (b) the densely agglomerated nature of the DND crystals**

In figure 5.2(a) a typical agglomerated 'grain' can be seen to have an overall dimension of the order of 3 μm, whilst in figure 5.2(b) it is just possible to discern extremely small crystals aggregated to grains of 30-100 nm sizes, which in turn make up the 3-μm particle. It was impractical to carry out Impedance spectroscopy on a single particle; hence a multiplicity of grains were placed between two Tantalum discs. The total powder thickness between the plates was approximately 0.5 mm. Tantalum was chosen as the metal for the discs due to its refractory properties; a drop of silver paste was applied on top of each disc and then dried in a furnace at 100°C for 5 minutes in order to assure a good contact between electrical probes and discs, and to drive off any water vapour.

In the present case, Impedance spectroscopy was performed over the frequency range 0.1 Hz–10 MHz Solartron 1260 impedance system with Solartron 1296 dielectric interface. The voltage applied between the Ta plates was 5 V, giving a field-strength of 100 V/cm. All experiments were carried out inside a stainless steel vacuum chamber (base pressure: 10^{-3} mbar), which allowed both electrical screening and control of the ambient gas. Exposure to NH_3 involved heating ammonium hydroxide (50% NH_3) by weight and drying the resultant gas through calcium oxide.

5.3 Results

5.3.1 Untreated DND

Measurements were initially recorded for the DND powder prior to exposure to ammonia. Figure 5.2(a) shows the impedance magnitude plotted against the measurement frequency at room temperature in both air and vacuum; it can be seen that the DND material trapped between the electrodes has a very high DC resistance (greater than $10^{11}\Omega$) and that the AC resistance remains very high beyond a measurement frequency of 1 MHz.

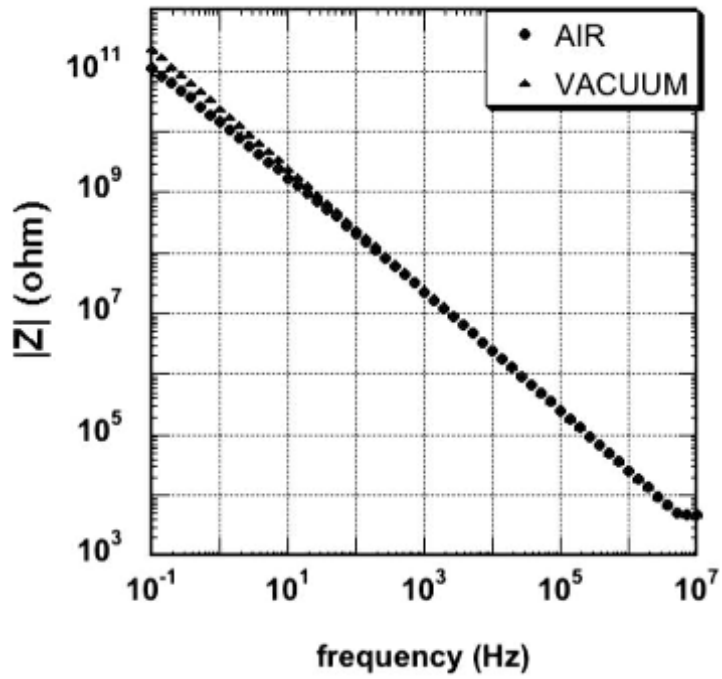

Figure 5.2(a): Real impedance plotted against measurement frequency for DND powder measured in air and vacuum at room temperature

The DC resistance value can be seen to be around one or two factors lower in the case of the air measurement compared to vacuum, but this difference is lost once the measurement frequency exceeds 100 Hz.

Figure 5.2(b) shows similar data, recorded in air, but at temperatures of 400°C and 550°C.

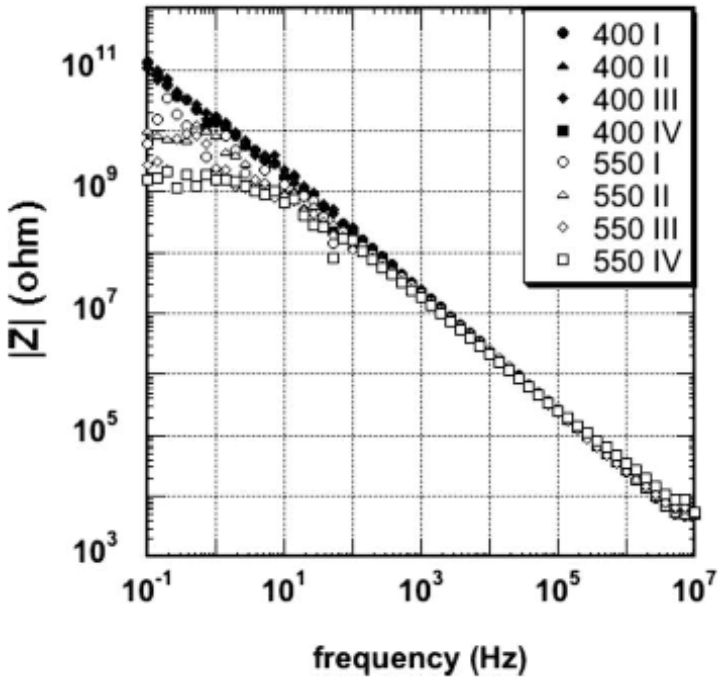

Figure 5.2(b): Real impedance plotted against measurement frequency for DND powder measured at 400°C and 550°C in air

In each case the measurement was performed several times. Interestingly, the measurements at 400°C are both stable when repeated and almost identical to those recorded at room temperature. However, at 550°C the curves can be seen to decrease in resistivity with increasing measurement cycle, with the DC resistance falling by almost two orders of magnitude.

Electrical conduction through the films could only be measured at temperatures of 350°C and above; figure 5.3(a) shows Cole-Cole plots, measured in air, recorded at 350, 400 and 450°C.

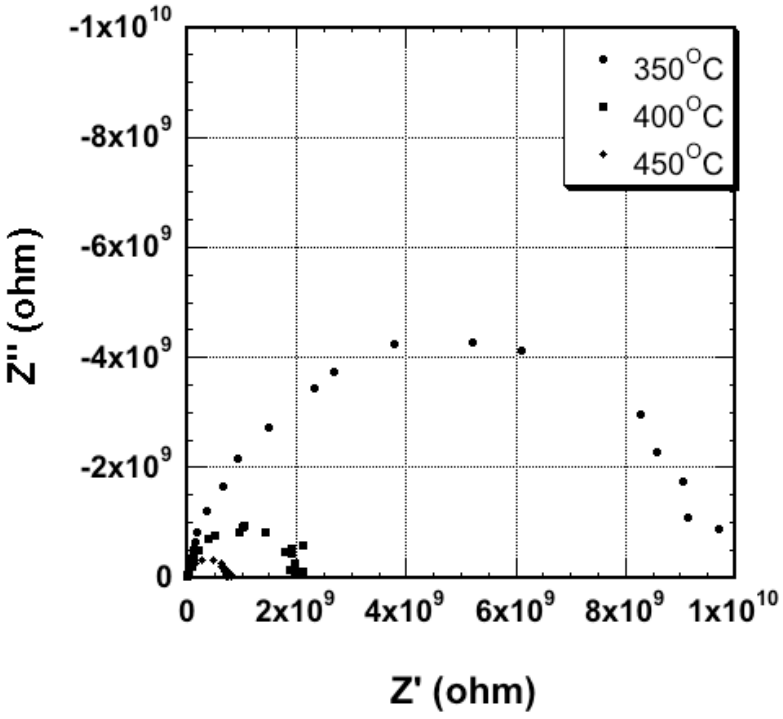

Figure 5.3(a): Cole-Cole plots for DND powders measured in air at (a) 350-450°C

Single semicircular responses can be seen which decrease in overall size with increasing temperature.

Similar data are shown in figure 5.3(b) but now for measurements at 450-550°C, where the same trend of decreasing semicircle magnitude with increasing temperature can be seen.

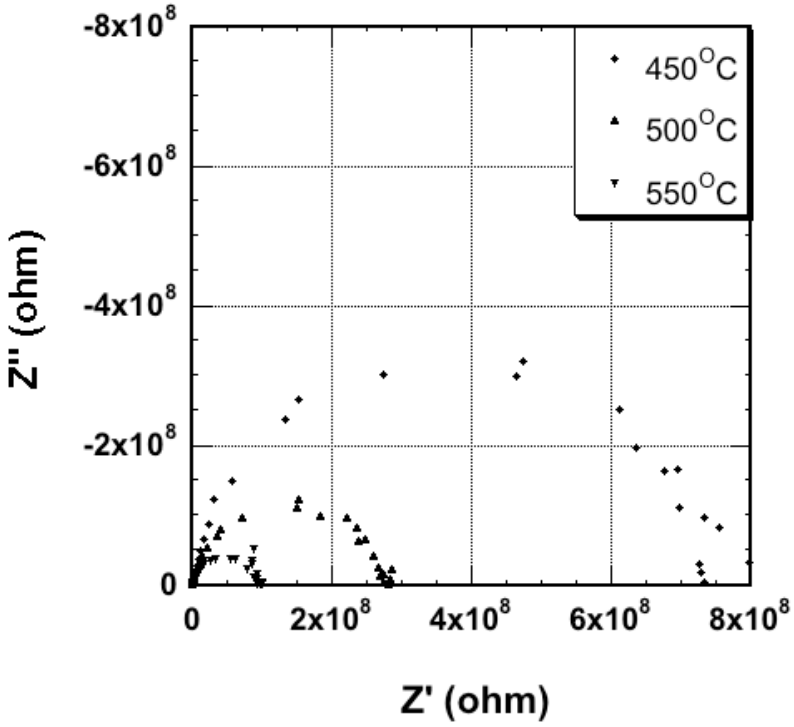

Figure 5.3(b): Cole-Cole plots for DND powders measured in air at 450-550°C

Measurements continued to be made throughout this temperature range. Figure 5.3(c) shows data recorded at 450-550°C after a total of four measurement cycles.

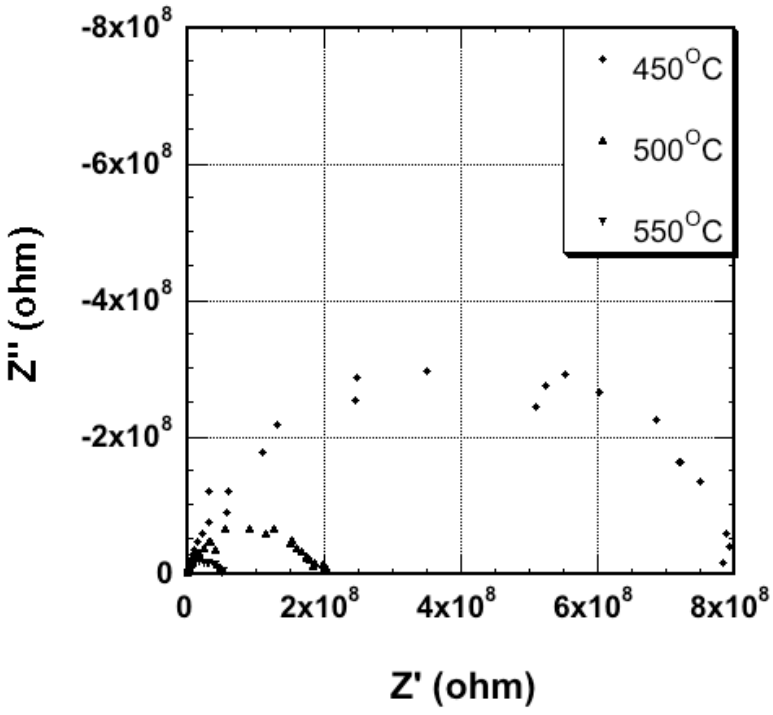

Figure 5.3(c): Cole-Cole plots for DND powders measured in air at 450-550°C after several measurement cycles.

The trend with temperature remains the same, but the overall magnitude of the semicircular response can be seen to have decreased since the first measurements were performed at these temperatures.

5.3.2 Ammonia-treated DND

DND powder was exposed to ammonia vapour (30 min) and the impedance measurements repeated. Interestingly, at room temperature it was now possible to observe two semicircular responses in the Cole-Cole plot, where none were seen prior to ammonia exposure (figure 5.4(a)).

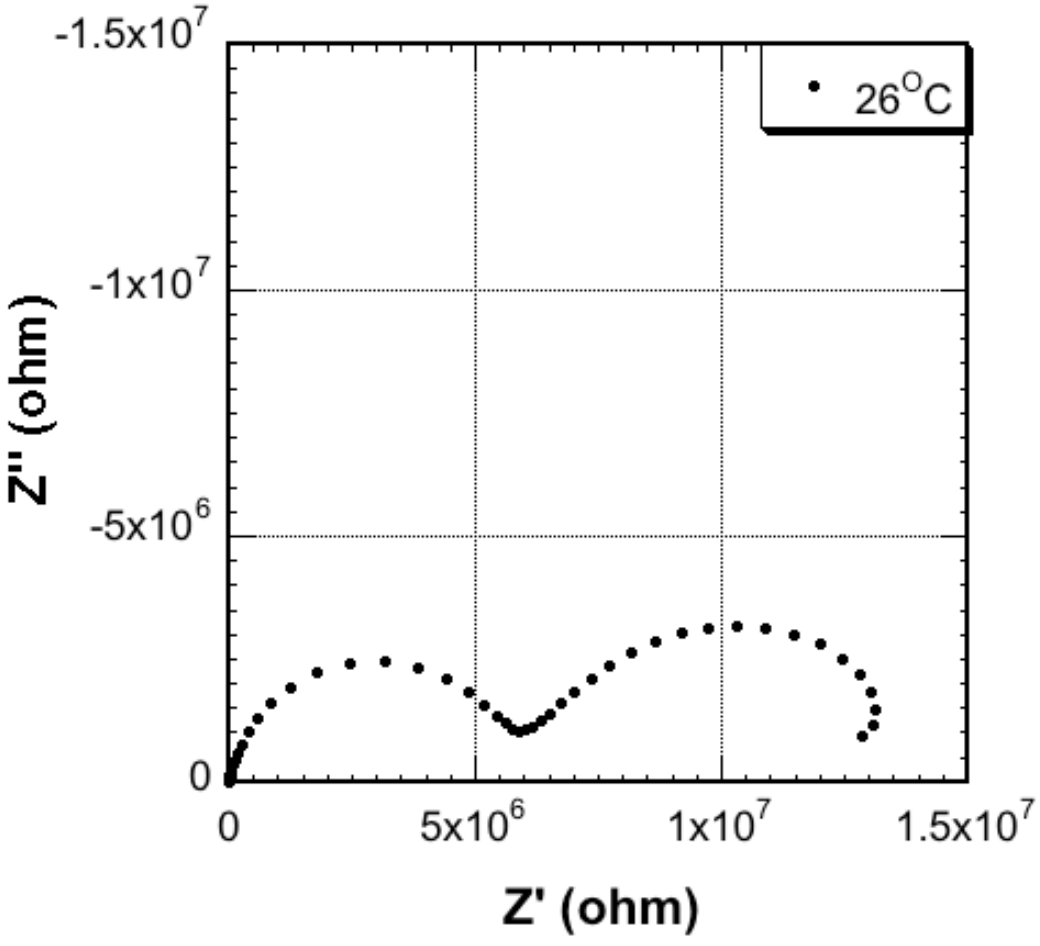

Figure 5.4(a): Cole-Cole plots for DND powders exposed to ammonia vapour (thirty minutes) measured in air at room temperature.

The resistivity range of both semicircles is now much lower than that observed for the DND prior to ammonia exposure, being 1-10 MΩ. Heating the ammonia-treated DND

powder led to the loss of these semicircles, and the return of characteristics typical for the unexposed DND (figure 5.4(b), 100-300°C, figure 5.4(c), 400-550°C).

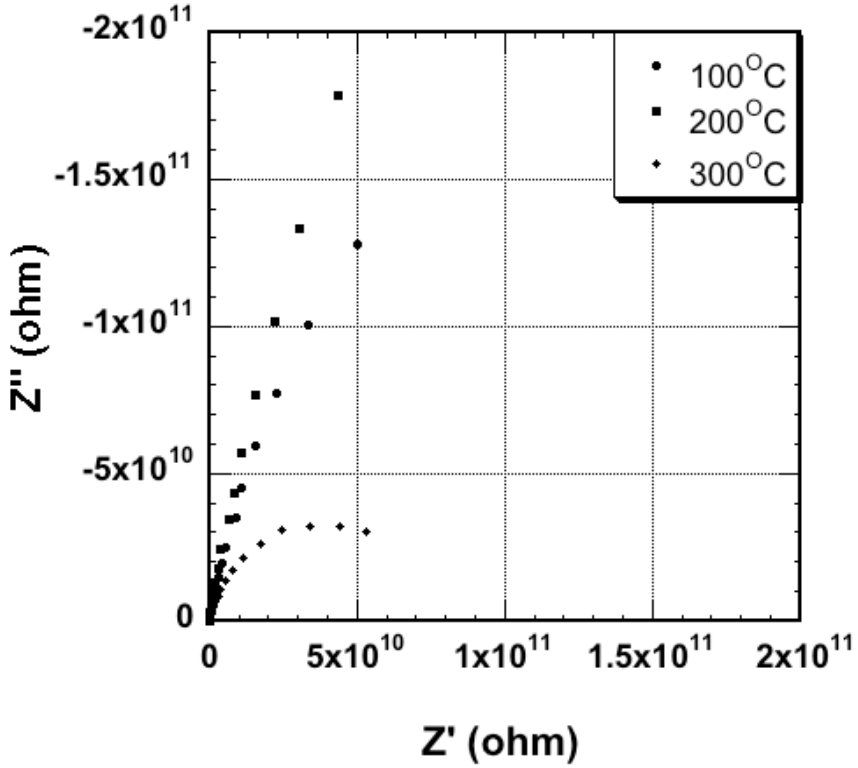

Figure 5.4(b): Cole-Cole plots for DND powders exposed to Ammonia vapour (30 minutes) measured in air at 100°C, 200°C and 300°C

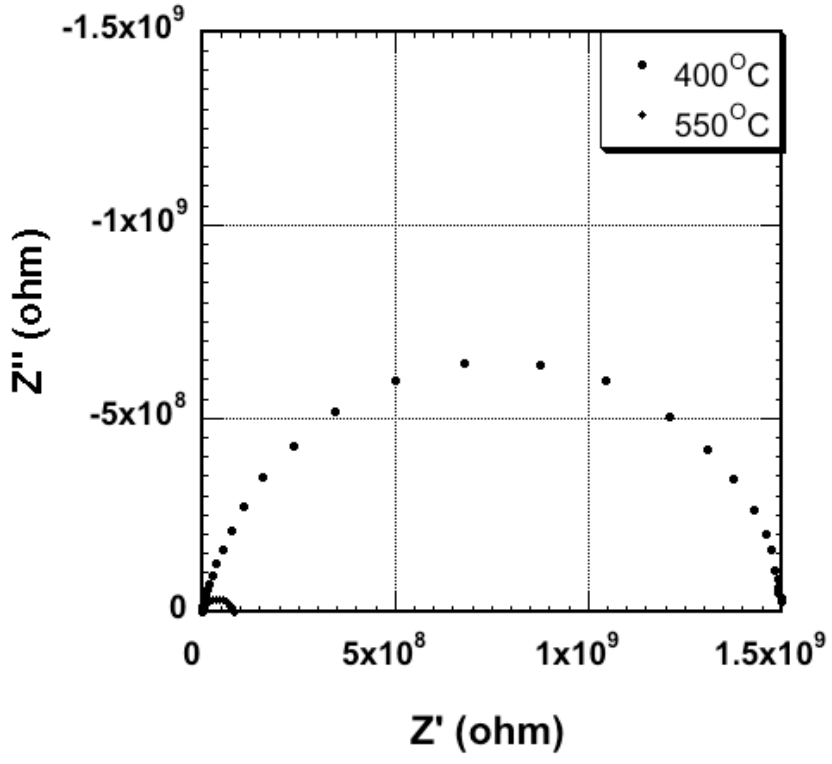

Figure 5.4(c): Cole-Cole plots for DND powders exposed to ammonia vapour (30 min) measured in air at 400°C and 550°C

These characteristics could be observed after repetitive ammonia exposure-heating cycles. Impedance Spectroscopy was then performed at room temperature after heating an ammonia-exposed sample for one minute at 100, 200, 300, 400 and 550°C, as shown in figure 5.5(a) (100°C) and 5.5(b) (150-550°C).

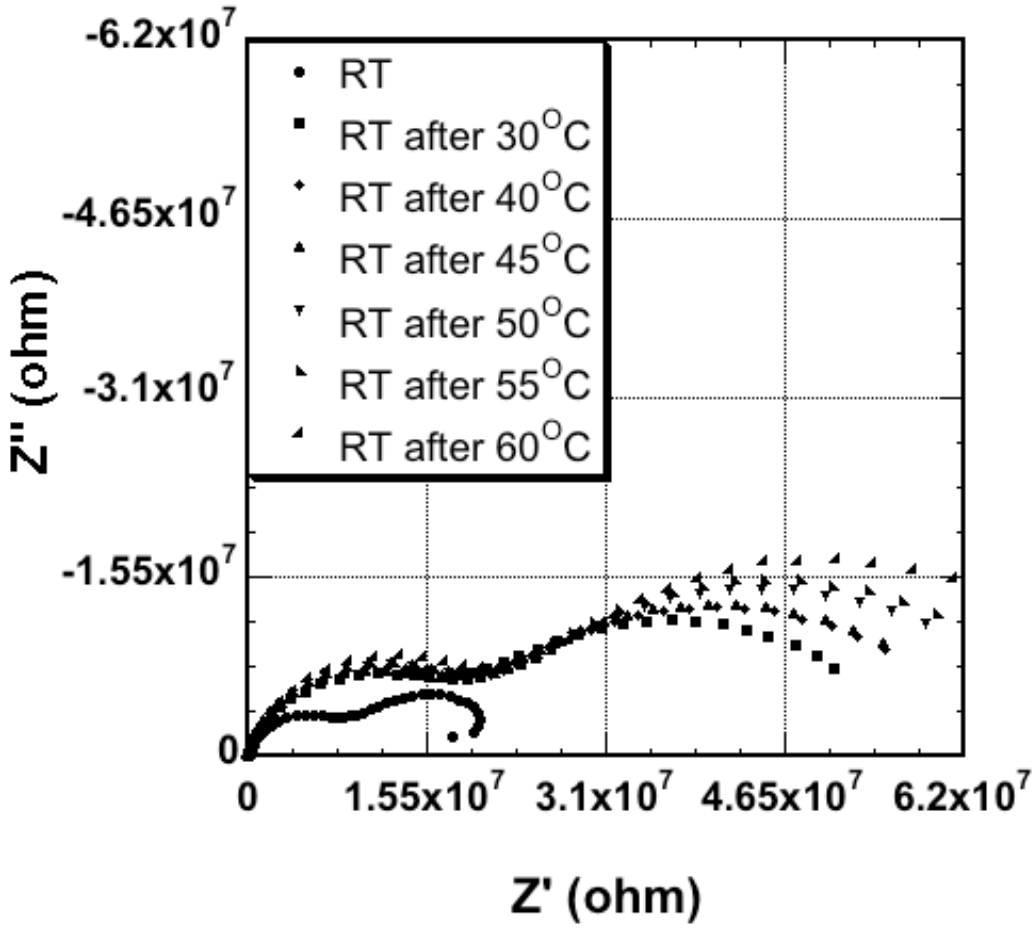

Figure 5.5(a): Cole-Cole plots for DND powders exposed to ammonia vapour measured in air at room temperature after heating for one minute at 30-60°C.

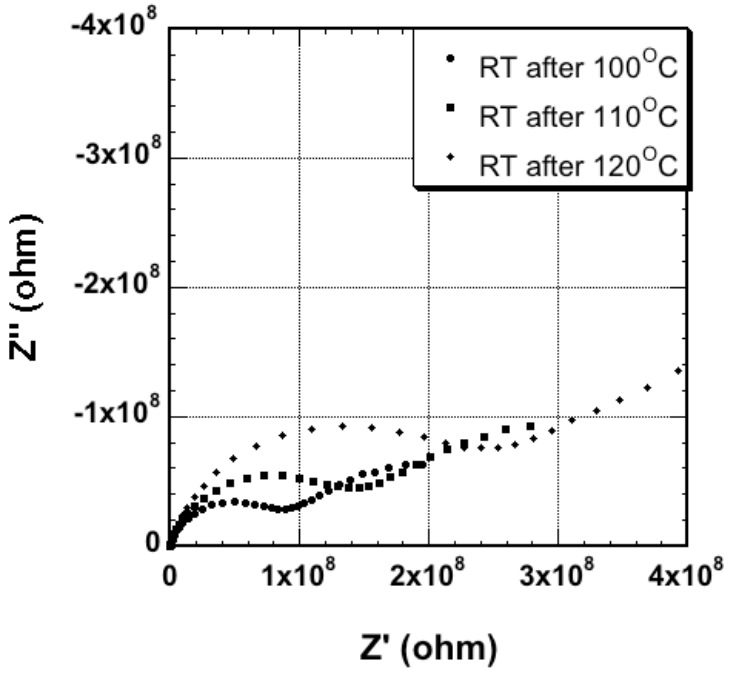

Figure 5.5(b): Cole-Cole plots for DND powders exposed to ammonia vapour measured in air at room temperature after heating for one minute at 100-120°C.

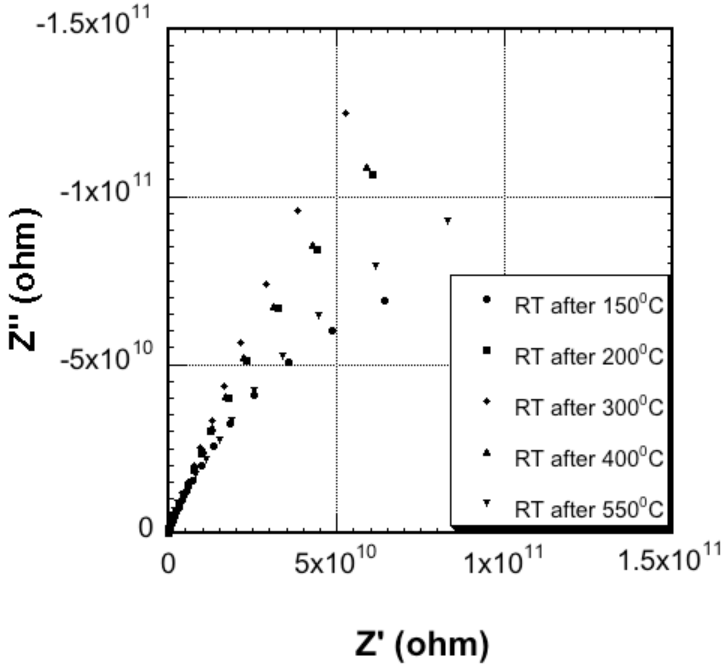

Figure 5.5(c): Cole-Cole plots for DND powders exposed to ammonia vapour measured in air at room temperature after heating for one minute at 150-550°C.

	Low frequency response	Low frequency response	High frequency response	High frequency response
Temperature (C)	**C (pF)**	**R (MΩ)**	**C (nF)**	**R (MΩ)**
30	31.5	0.212	2.78	0.453
40	29.6	0.223	3.35	0.518
50	28.4	0.228	4.38	0.567
60	27.9	0.246	4.93	0.641
70	28.2	0.296	5.40	0.780
80	28.3	0.385	5.73	1.045
90	28.5	0.541	6.19	1.494
100	27.9	0.960	5.64	2.415
110	28.8	1.560	2.60	4.502
120	29.0	2.665	5.97	14.85

Table 5.3: Resistance and Capacitance values determined from fits to the impedance data contained in figures 5.5(a) and 5.5(b)

The activation energy for both semicircular responses, derived from this data (figure 5.21), gives values that are similar, although they strongly vary with the temperature range (40-90meV, below 60^0C, ~0.5 eV, above).

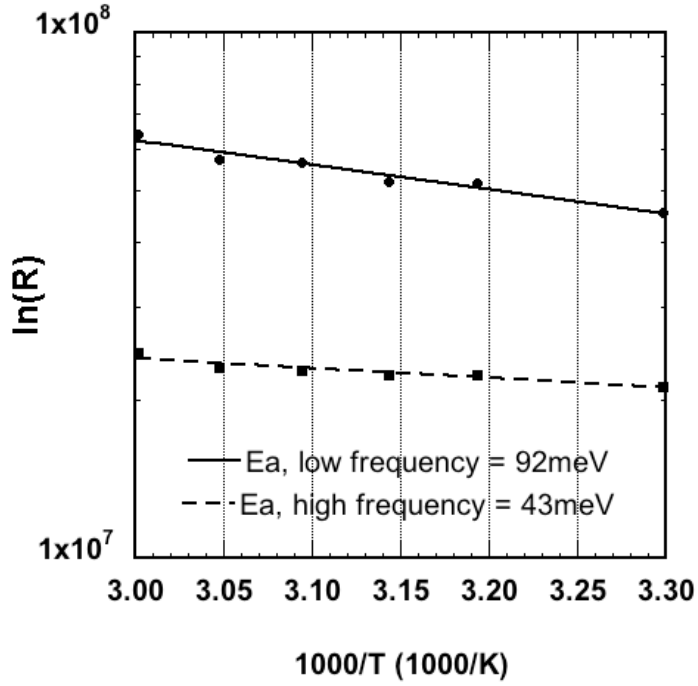

Figure 5.21(a): Arrhenius plots showing activation energy for semicircular responses in figure 5.5 at temperatures between (a) 30 – 60°C

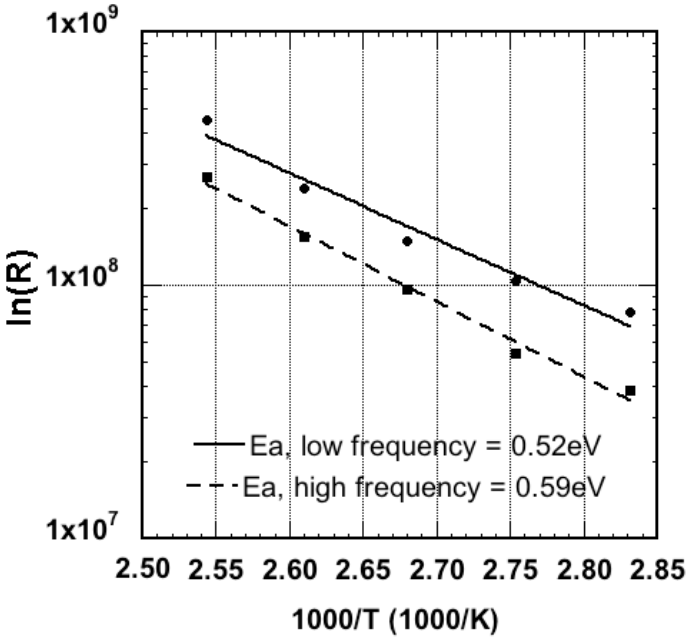

Figure 5.21(b): Arrhenius plots showing activation energy for semicircular responses in figure 5.5 at temperatures between 80 and 120°

5.4 Discussion

Extrapolation of the line displayed in figure 5.2(a) to zero frequency enables the DC resistivity of the film to be determined, revealing a value greater than 10^{13} ohm/sq. This value is typical for the highest quality polycrystalline CVD material[18] and remarkably close to values obtained for single crystal diamond. This is an excellent result given that this is nanostructured detonation powder, which has often been considered to comprise a composite of sp^3, sp^2 and impurity species, as was discussed in the introduction section. An important characteristic of an insulating film is the dielectric loss tangent (tan (δ)), determined as a function of AC frequency. The loss tangent was calculated for the data showed in figure 5.2a and it was found to be around 0.3 at 0.1 Hz, falling to 0.02 at 1 MHz for the air measurements, and 0.04 falling to less than 0.01 for measurements in vacuum.

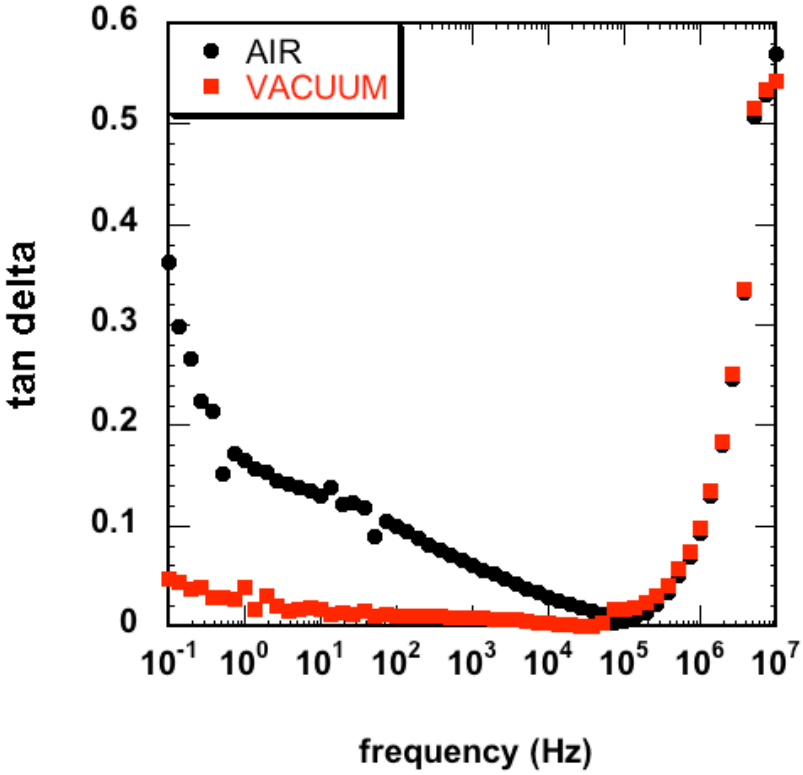

Figure 5.6: Loss tangent calculate for the data in figure 5.2a (untreated DND, room temperature)

It should be remembered that tan(δ) is a measure of the ratio of the power dissipated in the dielectric to the power stored, implying low numbers are desirable. Lu and co-authors [5.7] investigated the dielectric properties of very large-grain thick freestanding diamond films

(0.3 – 1.5 mm) (figure 5.7). Over the frequency range we have investigated here they observed an increasing value of tan(δ) from 0.005 to 0.0085, whilst in our case the trend in the data is the opposite up to frequencies of 10^5 Hz.

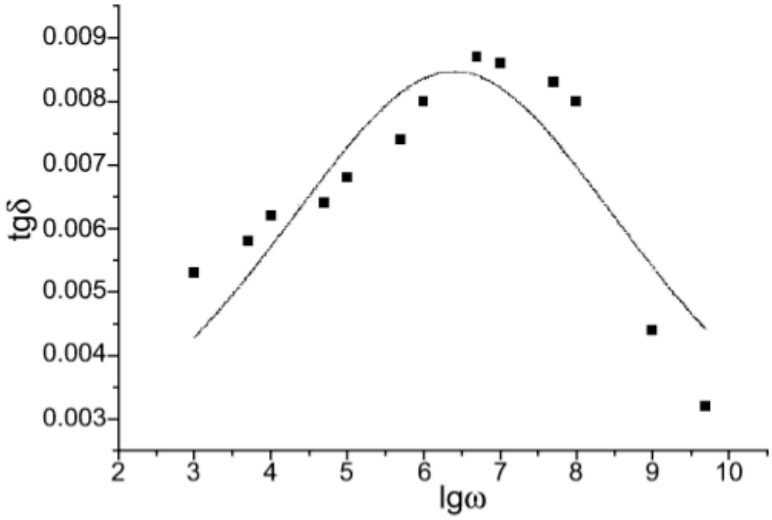

Figure 5.7: Frequency dependence of dielectric loss for a high quality freestanding diamond film [5.7]

The decreasing trend is a desirable feature since it shows the dielectric loss is decreasing with increasing frequency.

In another report on the use of commercially available thick CVD polycrystalline diamond films, Ibarra and co-workers [5.8] measured a dielectric loss tangent of around 0.01 falling to around 0.001 at 10MHz (figure 5.8).

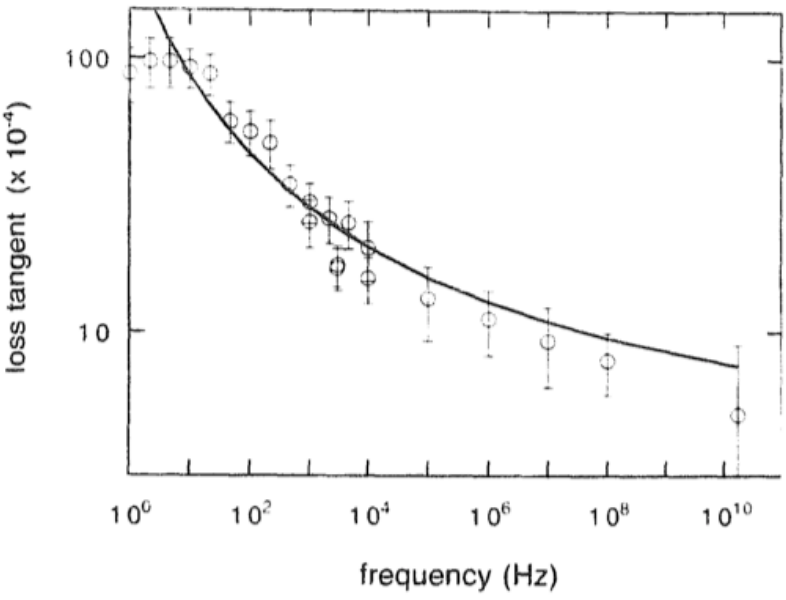

Figure 5.8 Frequency dependence of loss tangent for CVD diamond [5.8]

In this case the trend is similar to the one we observe here; decreasing with increasing frequency, and with similar values, at least for the measurement performed in vacuum. The DND samples can be considered as a three-dimensional network of nanodiamond particles. They are not continuous films, rather they contain many interfaces formed by the surface of the nanodiamond particles and voids where the irregular particles are not perfectly packed. Due to the large specific surface area of the nanodiamond particles, the interfaces should play an important role in the electronic properties of the material. It is thus surprising that the dielectric properties are similar to single crystal diamond, indicating that this particular DND powder is principally an sp^3 material, even at the boundaries between the agglomerated nanocrystals. The most likely reason for the difference in the values (both in terms of impedance and tan(δ)) is the presence of adsorbates on exposed surfaces of the powder when the measurements are carried out in air at room temperature. The fact that little change is evident in the data recorded at 400°C (figure 5.2(b)) indicates good stability of this dielectric material to this temperature. That this is not so at 550°C, figure 5.2(b) shows that changes to the film are now occurring, as the reduction in impedance values (and an increase in the value of tan(δ)) is not reversible. The most obvious explanation would be the onset of sp^2 formation in the DND powder at this temperature; this is discussed further below.

The Cole-Cole plots in figure 5.3 indicate that electrical conduction through the films can be detected at temperatures greater than 350°C. The reduction of the magnitude of the semicircular response with increasing temperature indicates that the powder sample becomes more conductive as the temperature increases, which is expected behaviour. The fact that only a single semicircular response is seen is interesting. In previous studies of diamond using impedance spectroscopy, more than one semicircular response has often been observed [5.7-5.10], indicating more than one conduction path. In the case of polycrystalline and nanocrystalline diamond, this observation has been attributed to conduction through both the grains and grain boundaries. The fact that only one semicircle is observed here indicates that only a single conduction path exists. Mathematical fitting to the semicircles can lead to the values of R and C associated with it to be determined. For the data contained in figure 5.3 for 350°C the capacitance values all lie in the pF range. It has been previously shown that grain interior conduction displays capacitance values of this order, whereas grain boundary conduction more often displays nF values [5.11]. Hence, it is possible to suggest that the surfaces and interfaces between the nm-scale diamond crystals within the agglomerated particles are not supporting a second form of electrical conduction when compared to that derived from the crystal interiors at this

temperature. However, for the semicircles measured at 550°C after a number of measurement cycles display capacitance values in the 1-10 nF range, indicative of grain-boundary type conduction. It is known that heating diamond in air at temperatures greater than around 400°C leads to oxidation of the diamond surface [5.9], typically increasing the resistivity values determined in any subsequent measurements. This is clearly not the case here. Instead, it can be suggested that the nm-scale crystals that are agglomerated to form the μm size particles, are not stable in the sp^3 form as they are heated to 550°C, and that some degree of sp^2 formation, presumably at the boundaries between the agglomerated crystals, is now occurring. An Arrhenius plot derived from the data in figure 5.3 gives an activation energy for this conduction process of 1 – 1.5 eV, depending on the number of measurement cycles.

The observation of conduction paths, as witnessed by the presence of room temperature semicircular responses in the Cole-Cole plots (figure 5.5 and 5.6) with relatively low resistances, suggests that ammonia has modified the electrical properties of the DNDs. That there are two semicircular responses indicates two differing conduction paths, which are differentiated by their respective capacitance values, whilst having similar resistivity levels (table 5.3). It is very interesting to note that at this temperature pF and nF responses suggest a grain-boundary like conduction process is being accompanied by a grain-interior like conduction. Heating the ammonia exposed DNDs above room temperature increases the resistivity associated with both conduction paths (figure 5.5), which are eventually lost completely. The activation energies (meV) associated with both appear at modest temperatures, but when the ammonia-exposed DNDs are subjected to higher temperatures a relatively high activation energy (0.5 eV) appears to be associated with further loss of conductivity within these states.

The ability for diamond surfaces to display differing levels of surface conductivity depending on the chemical nature of the surface termination (typically hydrogen or oxygen) has been extensively reported [5.11-5.12], and that Ammonia can affect this property [5.13]. In the latter case hydrogenated diamond surfaces became less conductive when exposed to ammonia, and more when exposed to NO_2. Given the observations made here regarding the highly resistive nature of the DNDs prior to ammonia exposure, the presence of any form of hydrogen-termination, which would lead to surface conductivity, can be ruled out. Instead it would appear that exposure to ammonia strongly increases the conductivity of this form of diamond. This process is clearly reversible as the conduction is lost upon heating. The presence of the two conduction paths would imply that an ammonia-derived adsorbate may be affecting the sub-surface region, causing band-bending

and a form of surface transfer doping [5.15], and that this is accompanied by a grain boundary conduction caused by ammonia exposure.

The mechanism of surface transfer doping, proposed by Strobel and co-authors, is similar to the surface conductivity of hydrogenated diamond reported by Meier and co-authors, which has been discussed in chapter 4. The authors evaporated C_{60} molecules in ultra-high vacuum (UHV) on homoepitaxial hydrogen-terminated diamond, oxygen-terminated diamond and silica glass. With increasing C_{60} surface coverage, conductance increased by more than six orders of magnitude in the case of hydrogenated diamond, whereas no increase in conductance was detected with any other sample. The results are showed in figure 5.9.

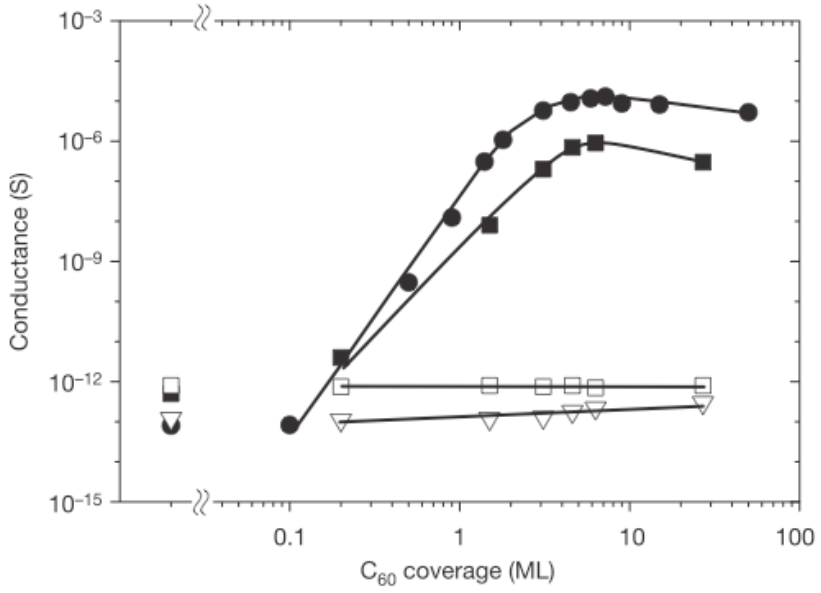

Figure 5.9: Conductance of hydrogenated diamond (filled squares and circles), oxygenated diamond (open squares), silica glass (open triangles) upon evaporation of C_{60} in UHV. 1 ml (monolayer) corresponds to an areal density of 1.15×10^{14} C_{60} molecules per cm^3 [5.15]

The fact that conductance increased only in the case of hydrogenated diamond samples indicates, similarly as in the study of Meier and co-authors in chapter 4 [4.17], that surface hydrogenation is a necessary condition but not sufficient for diamond surface conductivity to occur.

Strobel and co-authors explained the increased conductance in hydrogenated samples by means of a transfer doping mechanism whereby electrons are transferred from the diamond to the C_{60} layer, so that an equal amount of electrons and holes reside on the diamond side of the interface and on the C_{60} layer.

In the present work, ammonia exposure appears to lead to the creation of a chemisorbed species that can be removed at modest temperatures, which strongly modifies the electronic properties of the DND. It is thought that the most likely origin of this conductivity is a form of surface transfer doping, suggesting that the adsorbates will only be required in monolayer concentrations.

The activation energy associated with conduction loss at higher temperatures (0.5 eV) is most likely due to desorption of surface attached ammonia-derived species; this energy is typical of the bond-strength of chemisorbed species [5.16]. The co-presence of water or a water-derived species cannot be ruled out, but the exposure to water vapour alone did not give rise to similar observation. Indeed, the FTIR data (figure 5.10 and 5.11) provide some evidence for the presence of ammonia-derived chemisorption on the DNDs; the peak that appears near to 850 cm^{-1} having been previously linked with NH_2 species [5.17].

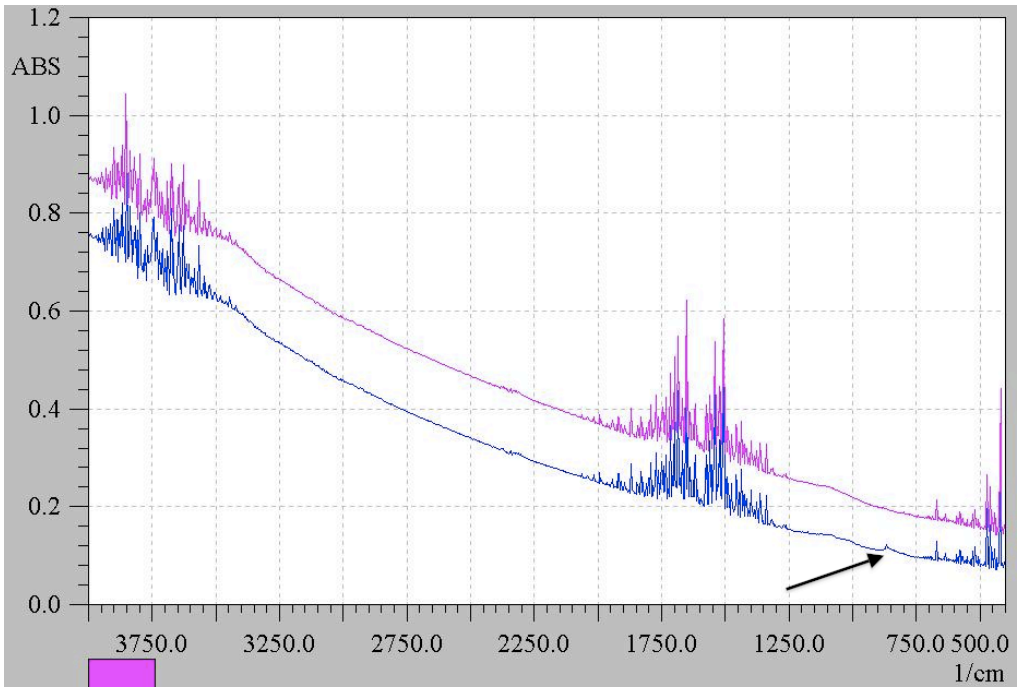

Figure 5.10: FTIR data showing an absorbance peak near 850 cm^{-1}

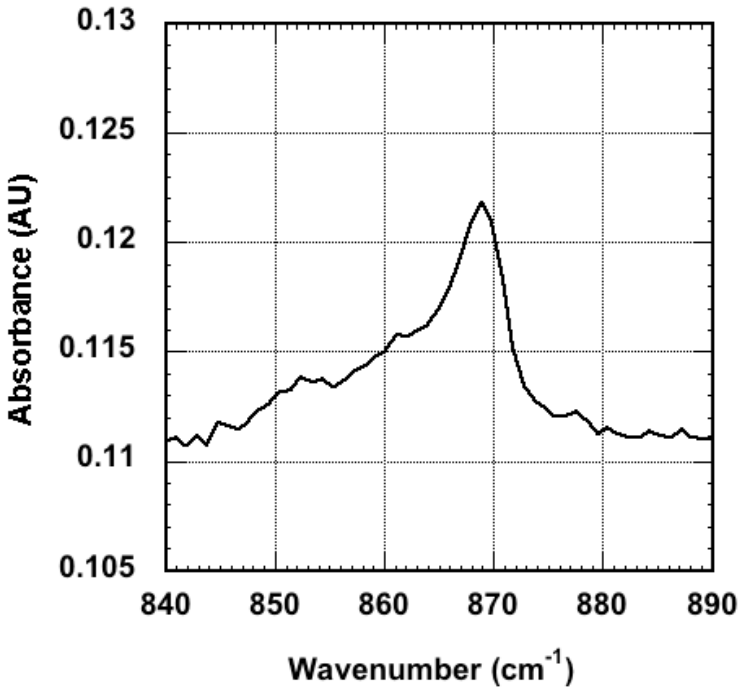

Figure 5.11: Detail of the peak in figure 5.10

The work performed here does not directly relate to the use of DNDs for ammonia sensing, in that controlled flux experiments have not been carried out. However, the observation that ammonia exposure strongly modifies the electronic properties of the DNDs is encouraging. The high surface area offered by the use of compacted DND powders would also enable high sensitivity to be achieved.

5.6 Conclusion

The commercially supplied form of detonation nanodiamond studied here has been found to be highly resistive, and capable of performing as a near ideal dielectric at temperatures below 350°C. This is contrary to some previous observations on other DND types, and challenges the idea that the nm-sized detonation-formed diamond crystals agglomerate together via a network of non-sp^3 carbon that is impervious to annealing and/or acid treatments. Indeed, the measurements performed here suggest that only one form of electrical conduction occurs within these materials, which is grain-interior-like at temperatures below 350°C, but may be due to surface/interface conduction at higher temperatures. This implies that these diamond powders may be suitable for several applications where chemically functionalising nanometre-scale sp^3 material is desirable, and for those requiring a dense dielectric powder material under either DC or microwave frequency conditions. At temperatures above 350°C the film resistivity begins to decline irreversibly indicating a limitation to the operational temperature for the powder within any application. This change is most likely to be caused by the onset of sp^2 formation on the surfaces of the nm-scale diamond crystals.

Once exposed to ammonia, ammonia-derived species (most likely to be NH_2) appear to chemisorb reversibly to the DNDs with desorption activation energy of 0.5 eV. The presence of the ammonia-derived species creates two parallel conduction paths, with relatively high conductivity, which appears to relate to grain interior conduction and grain boundary conduction. It seems reasonable to speculate that the former occurs through a form of surface transfer doping. Since the resistivity of the DNDs is changed by around 10^7 orders upon ammonia exposure, it would appear that there may be a promising future for DND-based solid-state ammonia sensors based on this approach.

References

[5.1] Timmer B., Olthuis W., van den Berg A., Sensor Actuators B **107** (2005) 666.

[5.2] Budavari S. *et al*., *The Merck Index, An encyclopedia of Chemicals, Drugs and Biologicals*, 12th ed., Merck, 1996

[5.3] Close L.G., Catlin F.I., Cohn A. M., Acute and chronic effects of ammonia burns on the respiratory tract, Arch. Otolaryngol. **106** (3) 151

[5.4] Leung C.M., Foo C.L., *Mass ammonia inhalation burns-experience in the management of 12 patients*, Ann. Acad. Med. Singapore **21** (1992) 624

[5.5] Lopez de Mishima B.A., Lescano D., Molina Holgado T. and Mishima H.T., Electrochim. Acta **43** (1998) 395

[5.6] Bendahan M., Lauque P., Seguin J.-L., Aguir K., Knauth P., Sensors B **95** (2003) 170

[5.7] Lu F.X., Zhang H.D., Tong Y.M., Yang J.X., Li C.M., Chen G.C. and Tang W.Z., Diamond and Related Materials, **13** (2004) 1714

[5.8] Ibarra A., Gonzalez M., Vila M. and Molla J., Diamond and Related Materials, **6** (1997) 856

[5.9] Kuznetsov V.L., Butenko Y.V., Chuvilin A.L., Romanenko A.I. and Okotrub A.V., Chemical Physics Letters **336** (2001) 397

[5.10] Ye H., Williams O.A., Jackman R.B., Rudkin R. and Atkinson A., Physica Status Solidi A-Applications and Material Science **193** (2002) 462

[5.11] L. L. Hench and J. K. West, *Principles of Electronic Ceramics* (Wiley, New York, 1989), Chapter 5

[5.12] V. Mortet, O. A. Williams, and K. Haenen, Physica Status Solidi A **205** (2008) 1009

[5.13] Williams, Oliver A., Mortet, Vincent, Daenen, Michael, Haenen, Ken Journal of Nanoscience and Nanotechnology, **9** (2009) 3483

[5.14] Looi H.J., Foord J.S., Jackman R.B. Applied Physics Letters **72** (1998) 353

[5.15] Strobel P., Riedel M., Ristein J. and Ley L., Nature **430** (2004) 439

[5.16] Chua,L.H., Jackman R.B., Foord J.S., Chalker P.R., Johnston, C., Romani, S. Journal of Vacuum Science and Technology A**12** (1994) 3033

[5.17] Alexenskii A.E., Osipov V. Yu., Vul' A. Ya., Ber B. Ya., Smirnov A.B., Melekhin V.G., Adriaenssens G. J. and Iakoubovskii K., Physics of the Solid State **43** (2001) 145

Chapter 6

Deep UV Diamond Photodetectors

6.1 Introduction

Ultra-violet (UV) photodetectors are a subject of increasing interest due to a variety of current and potential applications in industrial and scientific arenas. Some of these are covert space-to-space communications, jet engine monitoring, chemical/reagent detection, plant growth, ozone and flame/engine monitoring [6.1].

Existing methods for detecting deep UV include either a semiconductor photodiode or the combination of a photomultiplier tube and a vacuum photodiode. The latter arrangement has the disadvantage of being fragile, requires a bias potential of several hundred volts and usually offers broadband sensitivity ranging from the infrared to the UV, depending upon the photocathode/glass envelope combination deployed [6.2].

The most widespread photodiodes for deep UV detection available on the market are 'UV enhanced' Silicon devices; the spectral responsitivity of a typical device of this kind is reproduce in figure 6.1 and shows a broadband sensitivity in which the response to deep UV illumination at 200 nm is approximately 55% of the signal generated by a similar intensity of green light at 500 nm. The device has an active area of 5.8 mm^2 and operates at bias voltages of 5 V with a dark current of 3 pA at 10 V reverse bias, a peak DC current of 10 mA, and a maximum illumination intensity of 100 W/cm^2 [6.3].

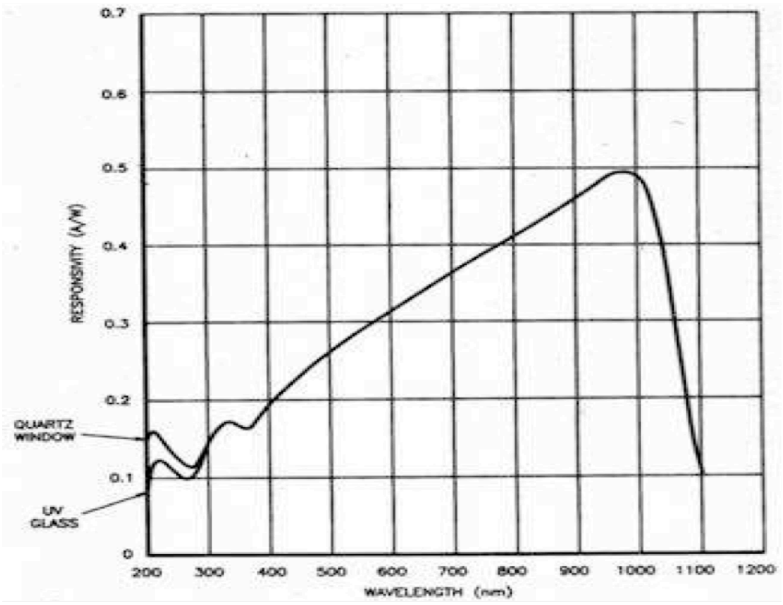

Figure 6.1: Spectral responsitivity of a typical UV enhanced Silicon photodiode [6.3]

When light with the appropriate wavelength impinges on the semiconductor, electron-hole pairs are generated, changing the material conductivity. The electric field in the device

causes the electrons and holes to move in opposite directions, leading to current. The carriers are present in the system until they recombine or are collected at the contacts [6.4]. However, no amplification occurs and the resulting external quantum efficiency (EQE) remains below 1.

Silicon-based detectors present the disadvantage of not being 'visible blind', that is, they remain sensitive to visible wavelengths responding strongly to excitation. Moreover, due to the narrow band gap of Silicon, these detectors require external filters that often reduce their efficiency to levels of 20% or lower [6.1].

Diamond is an ideal material for the fabrication of high performance deep UV photodetection devices due to its outstanding properties. Kania and authors [6.5] presents a summary of these properties. Diamond has a large band gap energy that permits windowless operation of diamond-based devices in many applications, as well as operation at high temperature whilst maintaining a low noise. Diamond is also radiation hard and chemically inert, suggesting applications in harsh environments where Silicon detectors would not operate. The high saturated-carrier-velocity permits high speed and high count-rate of diamond detectors, a characteristic that is fundamental in high event-rate applications as it reduces the effects of pulse pile-up or the summation of multiple events into an apparent single event. Another critical property is that diamond is biocompatible with human tissue, a property that is important in dosimetry application. A comparison of diamond and silicon properties is summarized in table 6.1.

Property	Diamond	Silicon
Density (g/m^3)	3.5	2.32
Band gap (eV)	5.5	1.1
Resistivity (Ω cm)	> 10^12	10^5
Breakdown voltage (V/cm)	10^7	10^3 (pn junction)
Electron mobility (cm^3/Vs)	1800	1500
Hole mobility (cm^3/Vs)	1200	500
Saturation velocity (μm/ns)	220	100
Dielectric constant	5.6	11.7
Energy per e-h pair (eV)	13	3.6
Atomic number	6	14

Table 6.1: Comparison of the electrical properties of diamond and silicon [6.5]

In particular, diamond 5.5 eV band-gap energy makes it an ideal material for the fabrication of photodetection structures, which respond to deep UV light (< 225 nm). The structure of a diamond photodetection device would be much simpler compared to the

more complex reverse biased p-n junction Silicon diodes that are required to minimize dark current [6.5].

Illumination of diamond with photons of energy greater than 5.5 eV leads to the absorption and the generation of an electron in the conduction band and hole in the valence band. Until recombination of this electron-hole pair occurs, the electron will remain in the conduction band and will cause an increase in the material electrical conductivity; the application of electrodes which allow an electric field to be placed across the diamond will result in a current flow. As opposed to Silicon photodiodes, in a diamond photodetector the electron may go around the circuit several times before it recombines with a photogenerated hole, and hence the current can be larger due to photogenerated carriers alone, i.e. photodetectors can display gain [6.6].

In order to be considered for industrial and scientific applications, additional factors needs to be considered for potential diamond photodetection devices to be employed in industrial and scientific applications; such factors include speed of response, sensitivity, stability and manufacturability. However it would be practically difficult to amply satisfy all these criteria as the devices are being manufactured; for this reason, a minimum of four criteria were taken in consideration in the design phase, leaving the following to an optimization phase following the manufacture.

These basic criteria are:

- To display ‘visible blindness’.
- To obtain satisfactory performance at $V_B <= 30$ V.
- To display dark currents in the order of picoamperes.
- To make use of commercially available CVD diamond.

Single crystal diamond SCD grown by CVD methods has recently become a commercially available material [6.7], awakening interest in the use of this form of diamond for the fabrication of UV photodetectors rather than PCD. Despite an extensive literature on the use of homoepitaxial single crystal layers grown on natural or high pressure high temperature substrates as photoconductive devices, as discussed in chapter 2, the direct use of a CVD grown single crystal has attracted little attention. This chapter describes the fabrication of devices made on commercially supplied SCD, and shows how the defect passivation treatments discussed above can be used to modify the surface of this form of SCD resulting in extreme levels of sensitivity to deep UV while maintaining good UV to visible light discrimination and dark current levels.

6.2 Experimental methods

SCD substrates produced by Element Six Ltd and supplied by Diamond Detectors Ltd were subjected to wet treatments that are known to leave the surface free from contamination [6.8] and in an oxidized state avoiding so-called "surface conductivity." 20 Standard lithographic methods were used to pattern the metal electrodes 15 nm Cr, 300 nm Au, into an interdigitated array of 15 electrode pairs, spaced by 25 μm on a 25 μm pitch. Contact pads connected to each electrode pair were 300×300 μm in size. In choosing the design of the device, the successful work of McKeag and co-authors [6.5, 6.6] with a similar design was taken into consideration. The limiting factors were the small size of the CVD diamond substrate (4×4 mm) and the even smaller available surface left after the elimination of the photo-resist edge beads. The total available surface area (2.5 mm^2) allowed for a maximum of 15 electrodes to be built. The electrode pitch of 25 μm assured that the interdigitated array could be easily lithographed. A smaller pitch would increase the risk of generating imperfect electrodes, as well as possible reflection of a higher electric field [6.9]. The size of the contacts pads made sure the device could be probed without too much difficulty, when metal probes needed to be placed on them for the photoconductive measurements.

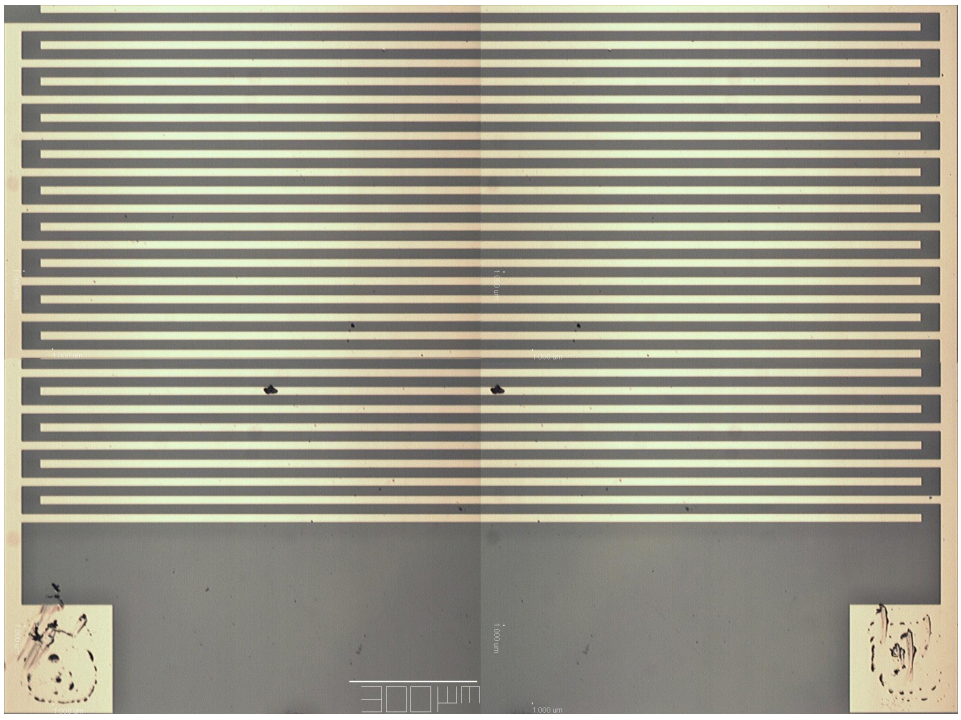

Figure 6.1: Optical micrograph of a typical UV photodetector fabricated by the author

Defect passivation, performed previously in a similar fashion by McKeag and co-authors [6.5] involved treating the fabricated devices in a methane environment at 700 °C for approximately 15 minutes, followed by annealing in air at 400 °C for 1 hour. To record the photoconductive response of the devices, the contact pads were probed and connected to a Keithley voltage source-picoammeter model 487. Illumination from a monochromated Xe lamp source with dual gratings enabled 180–800 nm wavelength light to be selected Amko A1020. Impedance spectroscopy was performed over the frequency range 0.1 Hz–10 MHz using a Solartron 1260 Impedance system with Solartron Dielectric Interface (figure 3.4) All experiments were carried out inside a stainless steel vacuum chamber base pressure 10^{-3} mbar, which allowed both electrical screening and control of the ambient gas (figure 3.5).

6.3 Results

6.3.1 Atomic Force Microscopy

Atomic force microscopy (AFM, Veeco Dimension V) was carried out and the surface was found to be free of contaminants. A typical image is shown in figure 6.3 The flat region of the substrate can be seen to be grooved with a periodicity of 0.05 – 0.1 μm, regular protrusions from the surface are also apparent with a vertical dimension of around 10 nm (not exaggerated Z-scale). The roughness of the surface can be found to have an RMS value of around 3.5 nm, although this drops to around 0.3 nm when the measurement along the protrusions. This data is consistent with the study of Terry and co-authors [3.39].

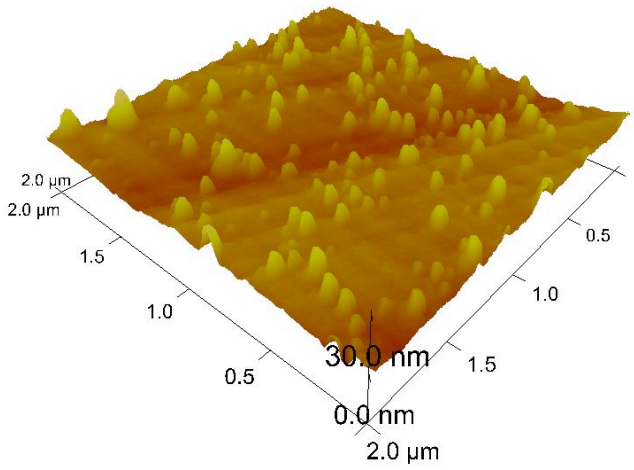

Figure 6.3: Typical AFM scan of the cleaned single-crystal diamond substrates

However, the two sides of each of the CVD diamond samples were found to have different roughness profiles, as shown in figure 6.4 and figure 6.5.

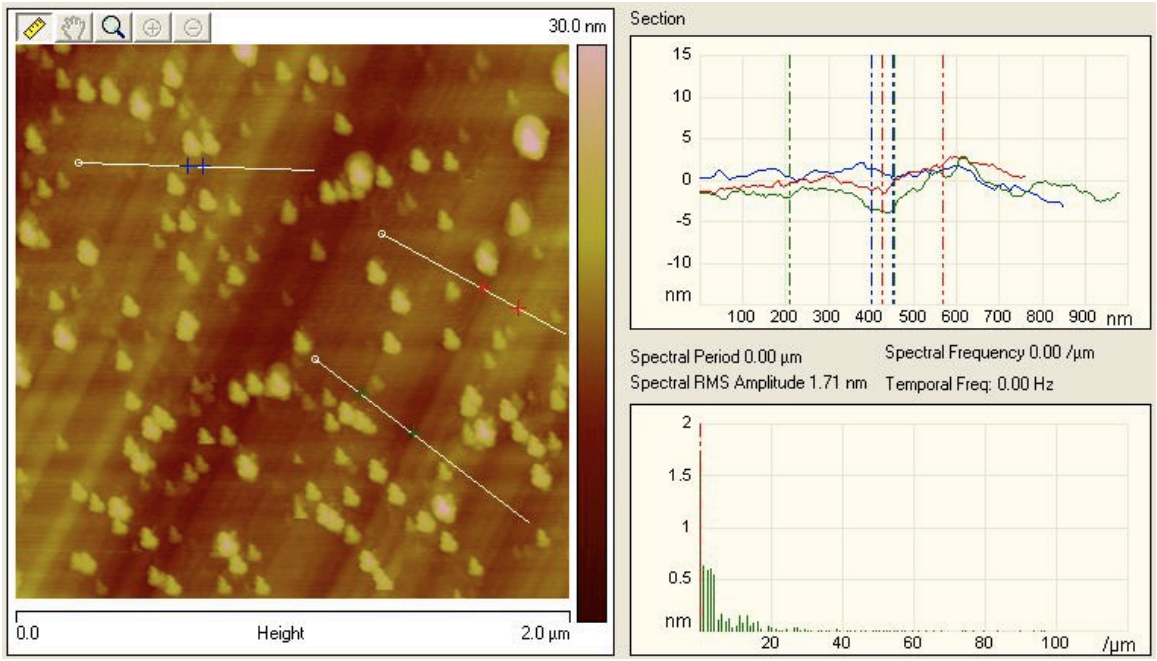

Figure 6.2: Typical AFM of the cleaned single-crystal diamond substrates, smoother side

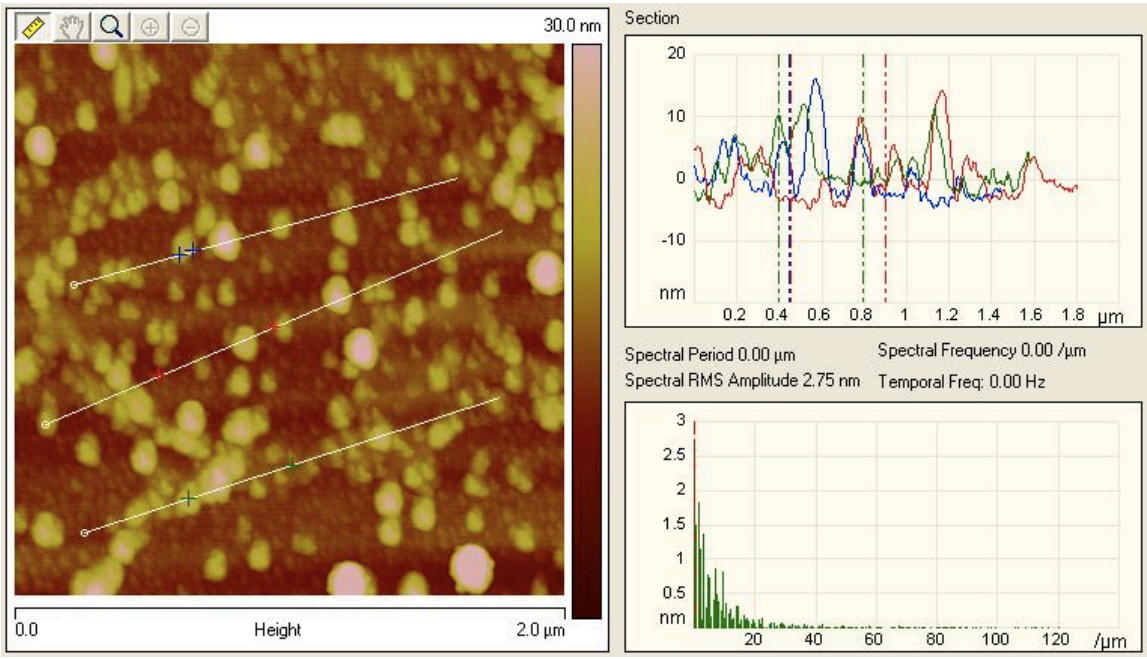

Figure 6.3: Typical AFM scan of the cleaned single-crystal diamond substrates, rougher side

6.3.2 Spectral responses

The spectral response of both the "as-fabricated" and passivated devices are shown in figure 6.6, where responsivity A/W is plotted as a function of illumination wavelength, for a device bias of 30 V. In the case of the as-fabricated device the peak responsivity at 210 nm is around 0.1 A/W, with the visible response being some six orders less, in the noise of the measurement system. While there is a sharp decline in responsivity at the band edge of four orders, some photoconductive signal persists until around 450 nm. In contrast, the treated device shows a peak responsivity of approximately 10 A/W, while retaining six orders of magnitude discrimination between deep U.V and visible light; however, the visible responsivity value remains above noise levels at 10^{-4} A/W. Figure 6.7 shows the 210 nm responsivity value plotted against device bias level (left axis) and the same data expressed as external quantum efficiency EQE or Gain, right axis. The device displays a responsivity of some 100 A/W at a bias level of 90 V, equivalent to an EQE of around 700. A bias level of no more than 90 V could be applied as the photocurrent had increased beyond a level the picoammeter was able to record (> 2.2 mA). Across this measurement range the background dark current remained in the nA range.

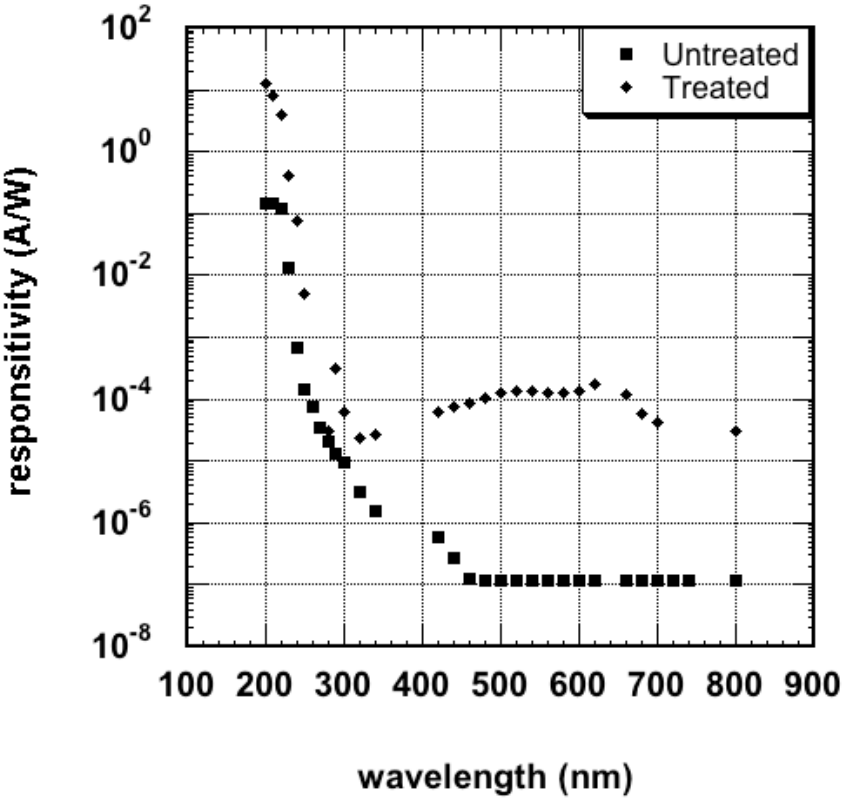

Figure 6.6: Responsitivity (A/W) plotted as a function of device illumination wavelength for untreated and treated single-crystal photoconductive devices, biased at 30 V.

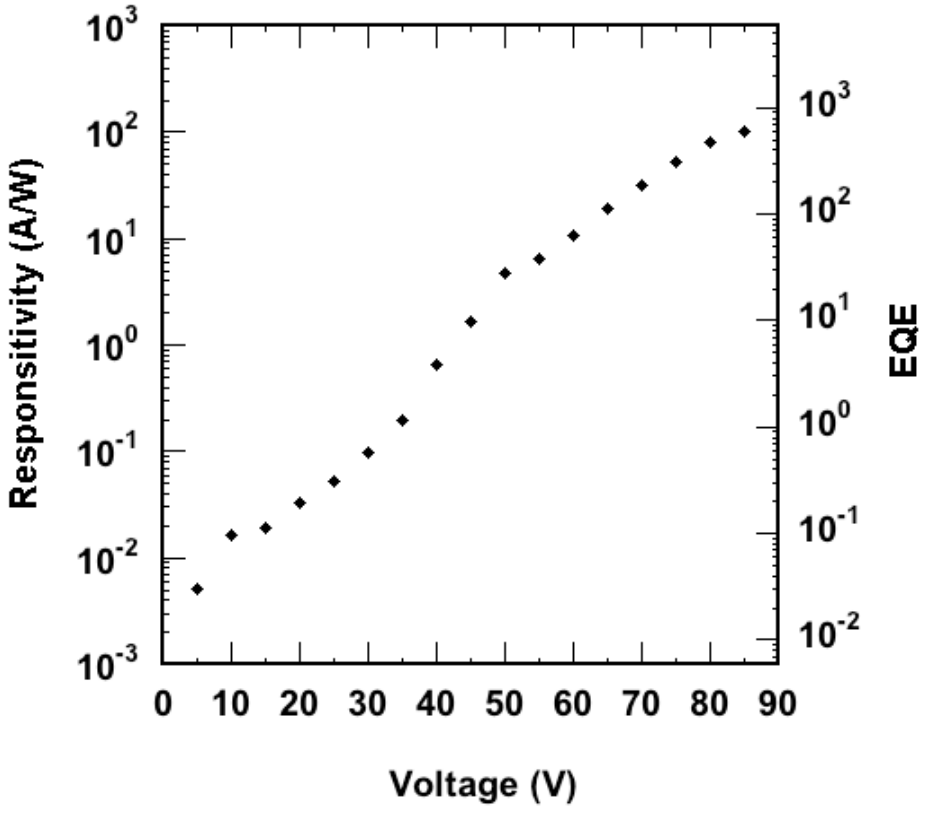

Figure 6.7: Responsitivity (A/W) plotted as a function of device bias, left axis, and converted to external quantum efficiency (EQE), right axis

Photoconductive measurements performed on another device belonging to the same batch was then given multiple annealing cycles; the photoresponse of the device was recorded after each anneal cycle and compared to the as-fabricated one. The concept behind putting the device under multiple anneal treatments was to further enhance its performance and to gain insight on how such an anneal process affects the surface of the diamond substrates. Only two anneal cycles could be performed as after a third the contact pads of the device were too damaged to be probed, as much of the gold had been removed due to repeated scratching by the tungsten probes. Figure 6.8 shows the photoresponse after one and then two anneal cycles, compared to the as fabricated.

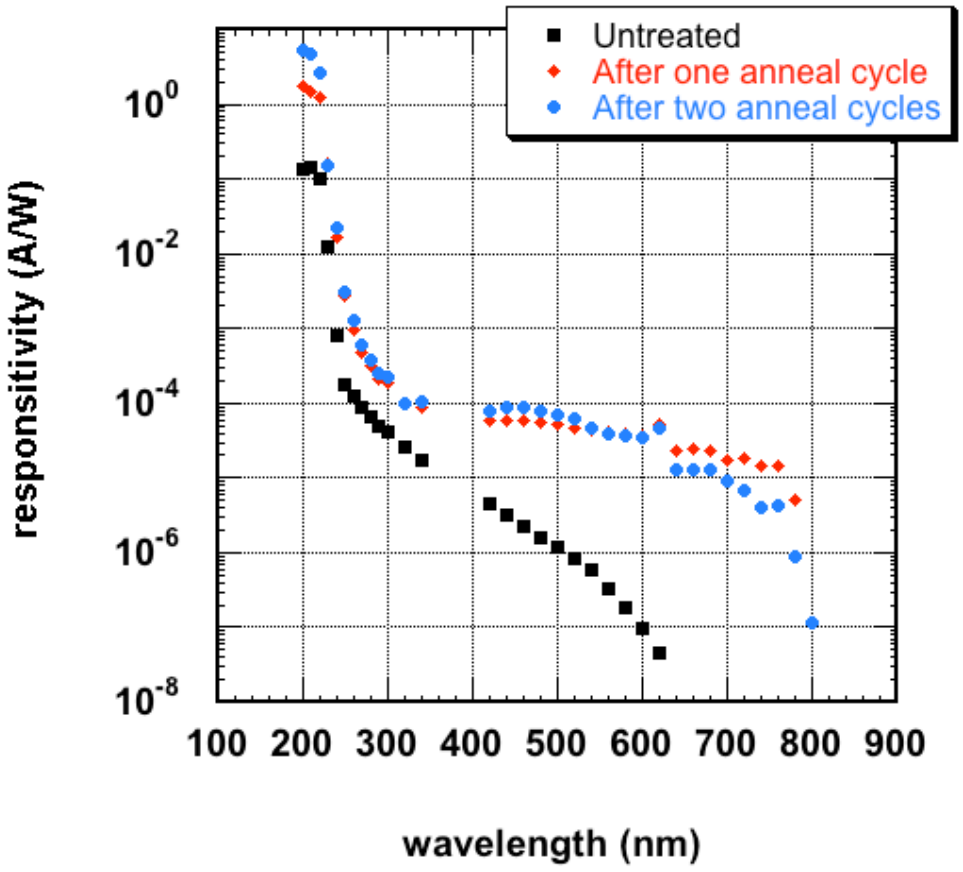

Figure 6.8: Responsitivity (A/W) plotted as a function of device illumination wavelength for untreated single-crystal photoconductive devices, for a device after one passivation cycle and for a device after two passivation cycles (biased at 30 V).

The second anneal cycle shows to have improved the device responsitivity, although its peak value only matches what was previously obtained after one anneal cycle only.

In figure 6.9 the measured photocurrent is plotted as a function of time, as the illumination source (210 nm) was turned on and then off. The as-fabricated device, within the time

resolution that can be discerned from this simple experiment, shows an immediate rise in photocurrent upon illumination and a similarly instant decrease in the measured signal back to its original value when the light is turned off. In the case of devices treated both once and twice, this appeared not to be the case with some background signal persisting long after illumination has ceased.

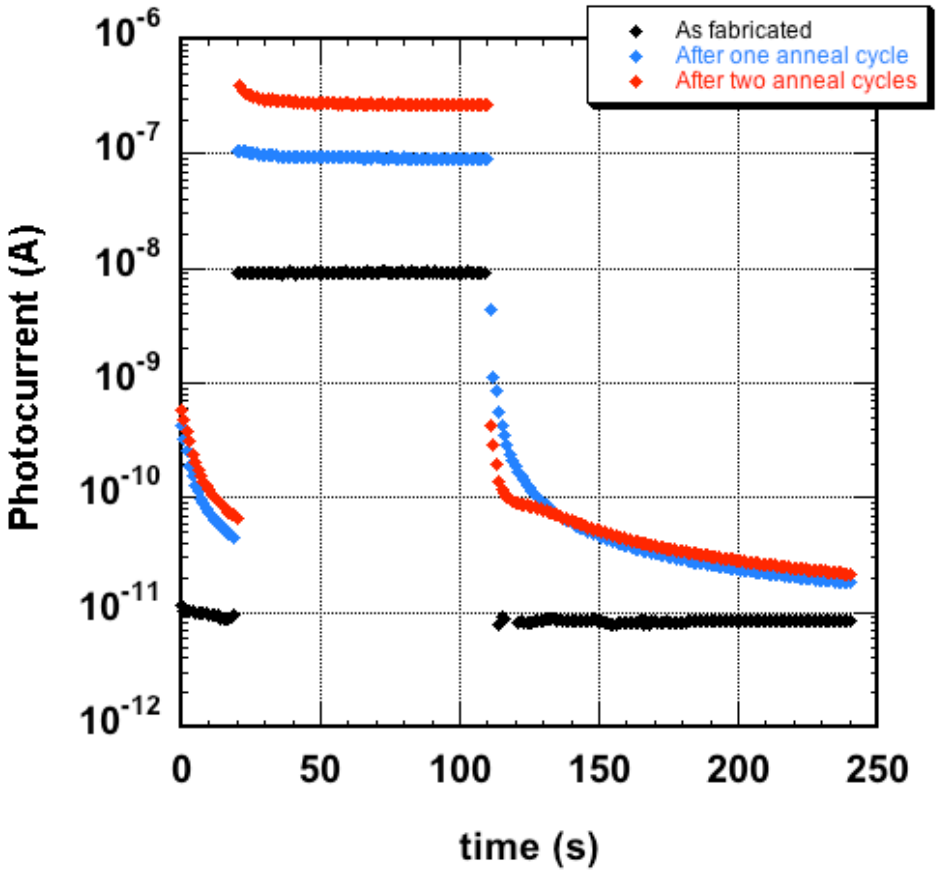

Figure 6.9: Photocurrent plotted as a function of time at a wavelength of 210 nm

6.3.3 Impedance spectroscopy

Impedance spectroscopy was used to isolate different contributions to the overall conductivity of diamond samples and was used here to give some insight into the changes being imparted to the SCD by use of the passivation treatment. The real and imaginary components of the impedance value were measured as a function of frequency, and plotted against each other in a so-called ‘Cole-Cole’ plot.

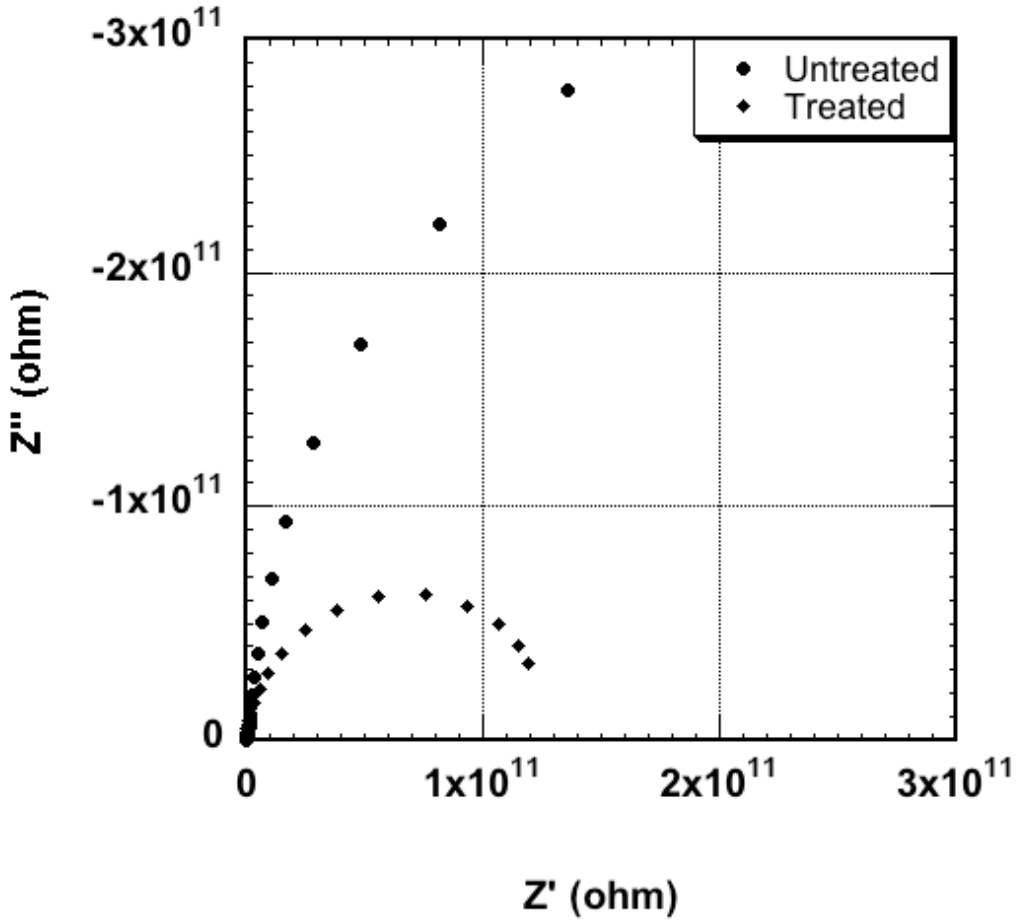

Figure 6.10: Cole-Cole plot (real impedance Z' vs. imaginary component of impedance Z'') for the treated and untreated device.

The presence of a semicircular response indicates the presence of a conduction path within the sample analysed with characteristic values of resistance and capacitance (R and C in parallel); observation of multiple semicircles arises through the presence of several conduction paths [6.13]. Figure 6.35 shows the Cole-Cole plots for both treated and untreated devices. Whilst only the initial part of a semicircle is apparent for the untreated device, a complete semicircle can be seen for the treated structure. The difference can be seen to arise from the different impedance values, and mathematical fitting to these curves gives R and C values of 8×10^{11} Ω and 0.5 pF (untreated) and 1×10^{11} Ω and 3 pF (treated). Figure 6.11 shows similar data measured at higher frequencies; whilst the plot for the treated device appears unchanged, a second semicircular response can be determined from the shoulder to the main feature on the untreated device. Mathematical fitting (shown) gives R and C values of 4×10^{9} Ω and 0.3 pF, respectively.

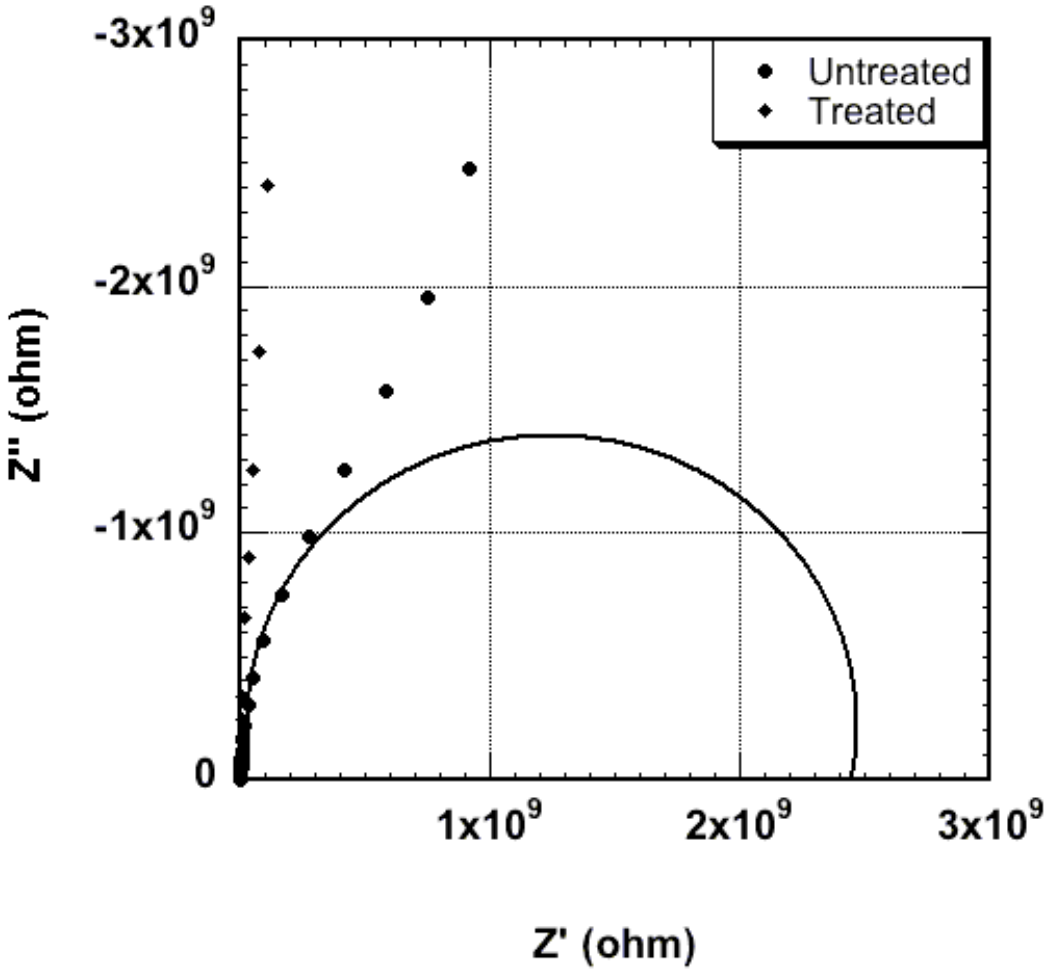

Figure 6.11: Cole-Cole plot for the treated and untreated device as in figure 6.35, but recorded at high frequencies

6.4 Discussion

The changes in the spectral response curve shape and absolute responsivity following the use of the passivation treatment are marked (figure 6.6 and 6.7). The untreated device shows some responsivity to wavelengths as long as 450 nm; the shape of the spectral response curve is similar to that reported by Balducci and co-workers [2.121, 2.122] when investigating the photoconductive response of high-quality CVD grown, thick (150 μm) homoepitaxial layers showed in figure 2.42 and 2.43. The form of sub-band gap response indicates the presence of defects and trap states within the material. In contrast, the treated device shows a much sharper decline in responsivity at wavelengths greater than 220 nm, although some photoconduction persists at all measured wavelengths, indicative of non-diamond carbon. The responsivity (and EQE) values obtained in the present work represent state-of-the-art performance of deep UV diamond photodetectors.

In the case of Balducci and co-workers [2.121, 2.122], their photoconductive device showed the highest responsivity when tested at 220 nm, whereas in the current work it was at 210 nm. EQE was calculated at those wavelengths, respectively. The measured values of EQE (figure 6.7) are much higher compared to Balducci's (figure 2.43) at all voltages tested.

In the work of Liao and Koide [2.133] the highest responsitivity obtained is approximately 10 at a bias of 20 V (at a wavelength of 220 nm) in figure 2.33, which is higher than the one obtained in the present work at the same voltage. However, the photodetector presented in this work obtains higher value of responsitivity than Liao and Koide at biases higher than 60 V (figure 2.34), as shown in figure 6.7.

Responsivity (and EQE) values remain considerably higher than other reports using homoepitaxial films, such as in the work of Brescia [2.124] and Iwakagi [2.125], where the performance of similar planar photoconductive devices was analysed.

The enhanced performance of the diamond photodetectors presented in this present work relies on the effect of the passivation treatments applied. The changes the single crystal substrates underwent made them at least as good as the very best homoepitaxial films.

The mobility-lifetime product ($\mu\tau$) can be evaluated from the following expression for a photoconductor [6.10]:

$$G = \mu\tau V / L^2 \qquad (6.1)$$

Where V is the applied voltage and L the gap between the electrodes. In the current case the $\mu\tau$ product can be calculated to be around 5×10^{-5} cm^2/V. This value is similar to that found by Liao and Koide [2.133], further highlighting the high quality, in terms of carrier generation and transport, of the SCD substrates used here following treatment. The penetration depth of 210 nm light in diamond is of the order of 3 μm [6.11], suggesting that the passivation treatment used here results in material changes potentially within this depth.

The observation of two semicircular responses in the IS measurements on the untreated SCD devices (figure 6.10 and figure 6.11) is indicative of two conduction paths within the material. In polycrystalline materials it is well established that pF range capacitance levels are associated with grain interior conduction, where as nF range capacitance is suggestive of grain boundary conduction [6.12]. The capacitance levels for the two processes measured for the untreated device are both in the pF regime, as to be expected for SCD; they principally differ in terms of the resistivity associated with each, which changes by

around two orders of magnitude. In the case of the treated device, the IS component associated with the higher resistivity in the untreated case remains, whilst the lower resistivity component has been removed. The most likely explanation is that the treatment eradicates disordered material in the surface region that is responsible for the lower resistivity conduction process.

Given that the treatment considerably enhances the EQE, and hence the μτ product, it can be inferred that this region is responsible for the relatively poor characteristics displayed by the 'as-fabricated' untreated devices.

Further insight into how the anneal treatment described above caused defect passivation (and therefore the increase of Gain and EQE values) was gained by Gaudin and co-workers [6.13]. Planar photoconductive devices comprising of a series of interdigitated electrodes with a spacing of 25 μm and a pitch of 50 μm were built using free-standing polycrystalline thin film diamond. The photoresponse of the as-fabricated devices was analysed and compared to that of devices that underwent heat treatment including anneal for 1 hour in methane atmosphere at 700°C followed by 1 hour anneal in air at 400°C. The photoresponse of the devices (bias = 10 V) and gain as a function of the field strength is reported below in figure 6.12:

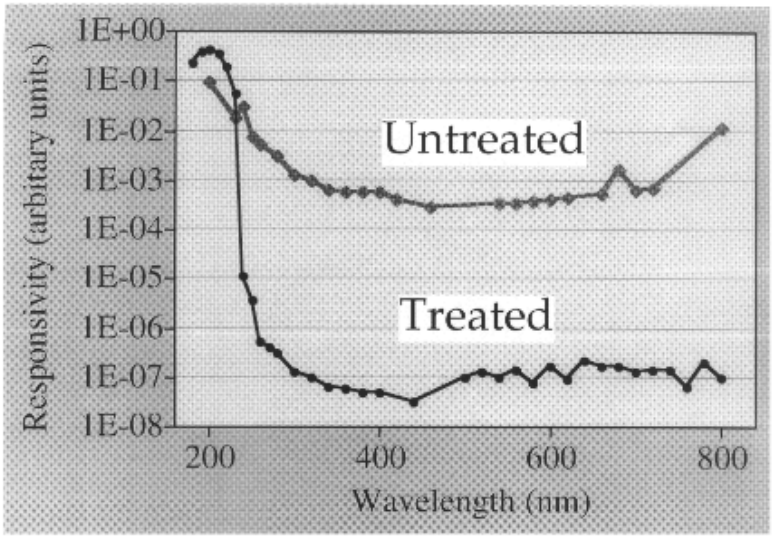

(a)

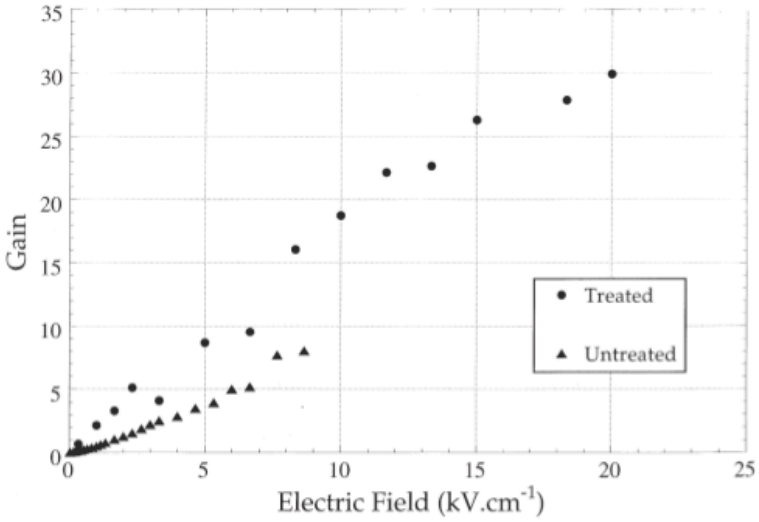

(b)

Figure 6.12: (a) Spectral response of treated and untreated thin-film diamond photodetectors. (b) Gain (external quantum efficiency) for treated and untreated detectors plotted as a function of applied electric field strength [6.13]

Furthermore, TSC (thermally stimulated current) measurements were conducted. Such measurements involved placing unpackaged devices inside a vacuum system on a block whose temperature could be varied from 100 to 700 K. Following cooling, devices were charged by illumination from a Xenon lamp and then heated whilst the dark current was measured at a bias of 10 V.

Figure 6.13 is representative of two successive TSC measurements for an untreated device compared to the TSC curve for a treated device. The strong α peak appeared to have shifted from 580 K in the first measurement to 550 K in the second. For the treated device, a weaker β peak centred at 260 K was observed.

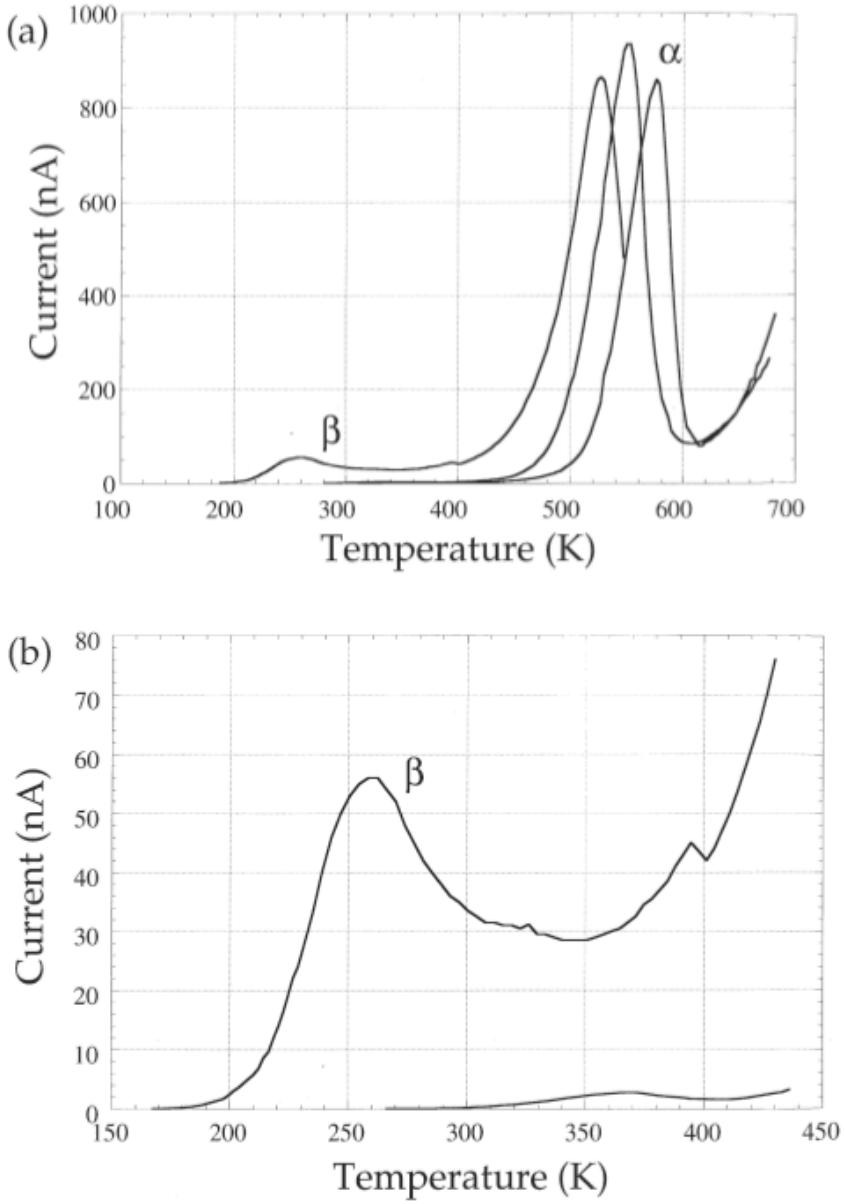

Figure 6.13: (a) TSC curve recorded over the temperature range 100-690 K, revealing two peaks labelled α and β. For the α peak, the highest temperature peak is derived from the first TSC experiment on an untreated device, with the neighbouring feature emerging on the second run on the same device. The lowest-temperature α peak derives from a treated device, as does the β peak. (b) TSC curves recorded over the temperature range 150-450 K for the treated (upper curve) and untreated (lower curve) devices [6.13]

The heat treatments seemed to have little effect on the α peak, to which an activation energy of 1.1 eV was assigned following a variety of methods; the β peak, to which an activation energy of 0.6 eV was assigned, appeared only in the treated devices and was also recorded by Gorokhovsky and co-workers [6.14] when performing TSC measurements on single-crystal diamond.

The appearance of the β peak was considered to be the introduction of a shallow trap by means of the anneal treatments the devices underwent,

The work of Souw and co-authors [6.15] also backed up such findings. They presented a detailed study of trap states in CVD polycrystalline diamond films using Photoconduction and TSC methods. They proposed that states existed between 0.6 eV and 2.1 eV from the valence band edge, to which the letter "M" and "S" was assigned, respectively. Whilst the deep S trap would behave as an effective recombination centre, the shallow M trap would be fully occupied under most illumination conditions. They proposed that the S state was associated with a charged vacancy complex (C^0–H^0–$C^{\text{dangling bond}} \rightarrow C^0$–$H^0$-$C^+ + e^-$), whilst the M state was a neutral carbon-vacancy defect ($V^-_c \rightarrow V^0_c + e^-$); they also proposed that the M and S state could be in equilibrium.

Gaudin and co-workers could not detect such a peak at 2.1 eV as it was beyond the thermal range of their experiments, but they noted that the presence of such a state would have led to significant (extrinsic) conductivity in the visible range, which was not present after treating the device with the same anneal cycle that was also used in the present work. Gaudin and co-workers therefore assumed to have been able to minimise, with the applied heat treatments, traps in this region of the bandgap. The transformation of the S into M state, (seen in the TSC curves at 0.6 eV) may account for this effect, whilst at the same time producing shallow traps that would increase the gain in a photoconductive device. Moreover, they proposed that the M and S state could be in equilibrium.

As seen in figure 6.9, the background signal persisting after illumination in the case of the treated devices is often termed "persistent" photoconductivity and it is most commonly associated with the presence of deep traps that are occupied upon illumination, taking some time to release their charge after illumination has ceased. This observation is interesting since photoconductive gain relates the carrier lifetime as well as mobility and applied electric field. If it were to be the case that these traps, for example, captured a photo-generated electron but its subsequent release was back into the conduction band as opposed to recombination then an effective increase in carrier lifetime would have been achieved. Thus, whilst this observation alone cannot unambiguously assign the origin of the gain been observed following treatment, it can be argued that such effects may at least be contributing to it. Whilst the data in figure 6.9 is insufficiently time-resolved to comment in detail on the persistent photoconductivity observed, changes following the second treatment indicate that such a process is continuing to modify the defect structure within the near-to-surface region of the diamond samples.

6.5 Conclusion

Previously developed treatments that passivated defects in PCD material, leading to enhanced deep UV photoconductive device performance have been found to act similarly to improve SCD devices, formed from commercially purchased diamond. The quality, in morphological and electrical terms, of PCD varies significantly between laboratories and commercial suppliers. In contrast, high quality SCD substrates are a more stable platform for device fabrication. Reports on the use of such material have been encouraging but have involved the growth of a high quality homepitaxial film on the substrate prior to device fabrication. In the current study extreme sensitivity to deep UV light has been achieved without the need for this process, by application of a simple defect passivation treatment. This should enable relatively low-cost high-performance diamond UV photodetection devices to be realized in the near future.

References

[6.1] Sandvik P., Mi K., Shahedipour F., McClintock R., Yasan A., Kung P. and Razeghi M., Journal of Crystal Growth **231** (2001) 366

[6.2] Verdeyen J.T., *Laser Electronics* 3rd Edn, Prentice Hall, New Jersey, 1995

[6.3] Silicon Photodetectors, Product catalogue: European edition 2, Centronic Ltd., King Henry's Drive, Croydon, CR9 0BG, United Kingdom

[6.4] Singh J., *Semiconductor Devices: an introduction*, Mc Graw-Hill, 1994

[6.5] McKeag R.D., Chan S.S.M. and Jackman R.B., Applied Physics Letters **67** (1995) 2117

[6.6] McKeag R.D., Marshall R.D., Baral B., Chan S.S.M. and Jackman R.B., Diamond and Related Materials **6** (1997) 374

[6.7] From Element Six L.t.d., www.e6cvd.com

[6.8] Baral B., Chan S.S.M. and Jackman R.B., Journal of Vacuum Science Technology A **14** (1996) 2303

[6.9] Binari S.C., Marchywka M., Koolbeck D.A., Dietrich H.B. and Moses D., Diamond and Related Materials, **2** (1993) 1020

[6.10] Bube R.H., *Photoelectronic Properties of Semiconductors,* Cambridge, New York, 1992

[6.11] R. Brescia, A. De Sio, E. Pace and M.C. Castex, Diamond and Related Materials, **13** (2004) 938

[6.12] Hench L.L. and West J.K., *Principles of Electronic Ceramics*, Wiley, New York, 1989, Chapter 5

[6.13] Gaudin O., Watson S., Lansley S.P., Looi H.J., Whifield M.D. and Jackman R.B., Diamond and Related Materials, **8** (1999) 886

[6.14] Gorokhovatsky *et al.,* Proc. 8th Int. Symp. Elect. (ISE-8), IEEE, New York, 1994

[6.15] Souw E.-K., Meilunas R.J., Szeles C., Ravindra N.M., Tong F.-M., Diamond and Related Materials, **6** (1997) 1157

Chapter 7
Concluding remarks

The present work investigated and discussed the fundamental electrical properties of highly dense nanocrystalline diamond films (NCD) and detonation nanodiamond (DND), pointing at possible future applications for which these materials can be employed. Another diamond-based application investigated was deep UV photodetectors, built by the author with commercially supplied high-quality single-crystal diamond.

Impedance spectroscopy measurements were carried out on a form of NCD created by seeding the diamond nuclei with NCD particles and deposited using optimized microwave plasma enhanced CVD process conditions. The resultant highly dense NCD films showed electrically conduction to be occurring through the diamond grains interiors as well as through grain boundaries.

Following mild oxidation, further Impedance measurements showed conduction through the grain boundaries to have disappeared, leaving a highly resistive material lacking polarizable defects, whose DC characteristics rival those of thick free standing CVD polycrystalline diamond plates.

Hall measurements conducted on the same type of NCD but highly doped with Boron revealed a remarkably higher value of mobility compared to previous lower values recorded on other type of NCD.

The commercially supplied form of detonation nanodiamond (DND) studied in the present work was found to be highly resistive and capable of performing as a near-to-ideal dielectric at temperatures below 350°C, opposite to previous observations on other DND types. At temperatures above 350°C, the film resistivity begins to decline irreversibly indicating a limitation to the operational temperature for the powder within any application.

The results obtained from Impedance Spectroscopy showed the presence of a single conduction path, which is grain-interior-like below temperatures of 350°C but may be due to surface/interface conduction at higher temperatures.

Once exposed to Ammonia, Ammonia-derived species appeared to chemisorb reversibly to the DNDs. The presence of the Ammonia-derived species created two parallel conduction paths, with relatively high conductivity, which appear to be related to both grain interior and grain boundary conduction. It seemed reasonable to speculate that the former occurs

through a form of surface transfer doping. Since the resistivity of the DNDs is changed by around seven orders of magnitude upon Ammonia exposure, there may be a promising future for DND-based solid-state Ammonia sensors based on this approach.

The spectral response of deep UV single-crystal diamond photodetectors over the wavelength range 180-800 nm were recorded and analysed. Previously developed treatments that passivated defects in polycrystalline diamond (PCD) material, leading to enhanced deep UV photoconductive device performance, have been found to act similarly to improve the single-crystal diamond (SCD) devices studied in the present work. High-quality SCD substrates are a more stable platform for device fabrication compared to PCD's, which varies significantly between laboratories and commercial suppliers. Extreme sensitivity to deep UV light has been achieved through the application of a simple defect passivation treatment. This should enable relatively low cost high performance diamond UV photodetection devices to be realized in the near future.

Further work will include:

- *in-situ* observation of the grain boundaries using high-resolution transmission electron microscope in order to gain insight into the role of the non-diamond material on the insulating properties of the type of NCD studied.

- exposure of the type of DND to Nitric Acid fumes followed by rounds of Impedance Spectroscopy and FTIR in order to gain further insight into the structure of DND and further exploring its potential in future applications as a sensor.

- application of multiple rounds of heat treatments to the manufactured deep UV diamond photodetectors in order to assess their maximum capability with UV light detection, making them increasingly attractive in industrial applications.